Springer Theses
Recognizing Outstanding Ph.D. Research

Su-Ying Chien

Rheological and Seismic Properties of Solid-Melt Systems

A Mechanical Spectroscopy Study

Springer

Springer Theses

Recognizing Outstanding Ph.D. Research

For further volumes:
http://www.springer.com/series/8790

Aims and Scope

The series "Springer Theses" brings together a selection of the very best Ph.D. theses from around the world and across the physical sciences. Nominated and endorsed by two recognized specialists, each published volume has been selected for its scientific excellence and the high impact of its contents for the pertinent field of research. For greater accessibility to non-specialists, the published versions include an extended introduction, as well as a foreword by the student's supervisor explaining the special relevance of the work for the field. As a whole, the series will provide a valuable resource both for newcomers to the research fields described, and for other scientists seeking detailed background information on special questions. Finally, it provides an accredited documentation of the valuable contributions made by today's younger generation of scientists.

Theses are accepted into the series by invited nomination only and must fulfill all of the following criteria

- They must be written in good English.
- The topic should fall within the confines of Chemistry, Physics, Earth Sciences, Engineering and related interdisciplinary fields such as Materials, Nanoscience, Chemical Engineering, Complex Systems and Biophysics.
- The work reported in the thesis must represent a significant scientific advance.
- If the thesis includes previously published material, permission to reproduce this must be gained from the respective copyright holder.
- They must have been examined and passed during the 12 months prior to nomination.
- Each thesis should include a foreword by the supervisor outlining the significance of its content.
- The theses should have a clearly defined structure including an introduction accessible to scientists not expert in that particular field.

Su-Ying Chien

Rheological and Seismic Properties of Solid-Melt Systems

A Mechanical Spectroscopy Study

Doctoral Thesis accepted by
the University of Cambridge, UK

Springer

Author
Dr. Su-Ying Chien
Department of Earth Sciences
University of Cambridge
Cambridge
UK

Supervisor
Prof. Simon Redfern
Department of Earth Sciences
University of Cambridge
Cambridge
UK

ISSN 2190-5053 ISSN 2190-5061 (electronic)
ISBN 978-3-319-03097-5 ISBN 978-3-319-03098-2 (eBook)
DOI 10.1007/978-3-319-03098-2
Springer Cham Heidelberg New York Dordrecht London

Library of Congress Control Number: 2013953246

Printed on acid-free paper

Springer is part of Springer Science+Business Media (www.springer.com)

Parts of this thesis have been published in the following journal and conference articles:

White, R.S., Redfern, S.A.T., & Chien, S.-Y. (2012) Episodicity of seismicity accompanying melt intrusion into the crust. *Geophysical Research Letters*, 39, L08306

Chien, S.-Y., Redfern, S.A.T., & White, R.S. (2012) Glass transition and crack percolation in basalt: implications for microseismicity. *2012 Annual Congress of Geological Society of Taiwan and Chinese Taipei Geophysical Society, 17–18th May 2012, Taoyuan, Taiwan*, Program with abstracts

Chien, S.-Y., Salje, E.K.H., & Redfern, S.A.T. (2010) Microstructure, shear modulus and attenuation in igneous rocks approaching melting at seismic frequencies, *2010 AGU Fall Meeting, 13–17th December 2010, San Francisco, California, USA*, Program with abstracts

Chien, S.-Y., Redfern, S.A.T., Chen, C.-J., & Kung, J. (2010) Lithology, anisotropy, pore pressure and acoustic velocity in fluid-saturated sandstones at pressure, *2010 Western Pacific Geophysics Meeting, 22–25th June 2010, Taipei, Taiwan, Program with abstracts*

Supervisor's Foreword

The role of mineral and rock properties in controlling the behaviour of the bulk Earth has long been acknowledged by geoscientists. Mineral physicists have, over recent decades, contributed to the wider Earth Sciences by providing key data and models that explain the properties of the solid Earth, and feeding these results into the wider or complementary studies of geophysicists and geochemists. Understanding the seismic properties of planetary interiors, for example, has been achieved through an appreciation of the material properties of the minerals and rocks forming those interiors. Rheological properties of the Earth from core to crust can be interpreted in terms of physical processes in the crystals and polymineralic assemblages forming the key materials of interest. Approaches adopted may be computational or experimental, with atomistic scale modelling forming one part of the toolbox of the mineral physicist, but careful experiment forming the other.

In this volume, the experimental approach to understanding the materials properties of the Earth is adopted. The focus is on complexities of response due to energy dissipation processes. This is important because as seismic waves pass through the Earth there is gradual loss of intensity which is, in large part, due to anelastic processes occurring within the minerals of the interior. By characterising these processes it becomes possible to interpret the attenuation of seismic waves as a probe of the deep Earth, additional to bare velocity data. This work describes the results of experiments designed to characterise anelastic processes occurring in real complex natural geological samples. Different experimental approaches have been adopted to understand the responses of these systems under varying conditions, and the complex responses observed interpreted and compared with the model systems of previous studies. The work highlights the complexity of natural minerals and rocks, but has additional important findings. It also demonstrates the effective conditions under which laboratory analogue studies can mimic the behaviour of real geo-materials. Work on the response of real partially molten igneous rocks is applied to the observed behaviour of magma progressing through intrusive dykes on Iceland, for example, but also found to be directly analogous to highly synthetic laboratory systems.

The role of mechanical noise in the experimental data is considered, and shown to be similar to the noise behaviour of seismicity in the bulk Earth, with torsion

pendulum experiments in the lab mimicking rather precisely the power law distribution of noise seen by scaling relationships for earthquake magnitudes. It is this link between laboratory and planet that characterises the studies described in this volume, and which will provide a starting point for further research into the physics of mechanical properties of minerals and planets.

Cambridge, September 2013 Prof. Simon A. T. Redfern

Preface

The complexity of physical processes operating on and within Earth are linked to the dynamics of our planet. The natural laboratory of our planetary home has provided countless examples of phenomena that have tested the ideas of the fundamental sciences. Thus, mineral physics on the one hand seeks to illuminate the Earth by explaining why it behaves as it does, from an atomistic perspective. But on the other hand the behaviour of minerals and rocks itself has on many occasions led to developments in physics, materials science, chemistry and even biology, as models and theories are developed in the light of that behaviour. Hence, empirical models and experimental approaches in mineral and rock physics can play an important role to link the theory and application of geophysical observations of the Earth system. With improvements in state-of-art instrumentation and techniques, more sophisticated and subtle behaviours are revealed, themselves leading to new models and explanations. How do rocks react to seismic frequency stress and how do they respond to temperature and pressure? The theme of this work is a response to these fundamental questions.

The role of melting and its importance in controlling the behaviours of the boundaries between crystalline mineral grains in a polymineralic rock assemblage is one important aspect of this study. To examine these phenomena, basaltic and gabbroic rocks with similar chemical composition, but different grain sizes have been compared, and their anelastic and viscoelastic properties determined experimentally as the melting transition is approached on heating, and reversed on cooling. Analogue systems, such as resin- and water-saturated sandstones, have also been used for additional understanding of the physical behaviours of liquid–solid systems. This volume comprises eight chapters, with the main experimental results presented in Chaps. 4–7. Each chapter contains its own fundamental context and discussions. The study will attract a wide variety of readers with a basic understanding of petrology, solid-state physics and geophysics. This study should provide a starting point for others following in the subject area, and my hope is that such studies will be as enjoyable as mine have been.

There are many individuals who I wish to thank for their help in the work I have undertaken. I would particularly like to thank to my Supervisor Prof. Simon Redfern, who introduced me to the study of anelastic properties in minerals and rocks, for his advice, guidance, support and patient help throughout my studies. I am also grateful for the help of colleagues in the Department of Earth Sciences at

Cambridge, including Prof. Ekhard Salje, Dr. Sally Gibson and Dr. John Maclennan, as well as Dr. Geoffrey Bromiley from the University of Edinburgh and Dr. Jennifer Kung of National Cheng Kung University, Taiwan for their helpful suggestions and advice. In addition, I would like to thank Dr. Richard Harrison and Dr. Nathan Church for their support and help with Igor software and Dr. Iris Buisman, Dr. Giulio Lampronti and Mr. Martin Walker for their support with sample analysis. Additionally, I want to thank my peers and friends for their support and friendship, especially those in the Department of Earth Sciences and those from the Cambridge Taiwanese Society and Jesus College. My work and life in Cambridge was enjoyable and colourful. In particular, my sincere and deep thanks are given to my family. This work would never have started without their understanding and constant support.

I am grateful to the Ministry of Education in Taiwan, the Cambridge Overseas Trust, the Department of Earth Sciences, Jesus College and the Cambridge Philosophical Society, who have provided financial support to enable me to accomplish my research.

Cambridge, September 2013 Su-Ying Chien

Symbols

Q^{-1}	Inverse quality factor or loss factor (identical to tanδ)
δ	Phase angle by which strain lags behind stress (also known as loss angle)
tanδ	Loss tangent or mechanical loss (identical to Q^{-1})
v	Poisson's ratio
v_0	Frequency at $1/T = 0$
ρ	Density
B	The Skempton pore pressure coefficient
R	Gas constant
R_0	Hypothetical mean rate for $M_{th} = 0$
H', R'	Constants related to the coupling between solid and fluid stress and strain
H_1, H_2	Functions of sliding crack orientation angle, numbers of sliding cracks and wing crack length
F	Force
F_D	Dynamic force applied in the dynamic mechanical analyser (DMA)
D	Displacement
u_D	The amplitude of detection due to the dynamic force in the DMA
$u_{i,j}$	Displacement vector in a deformation-diffusion process
η	Viscosity
η_{ss}	Steady-state viscosity in the Andrade model
η_0	Viscosity at $1/T = 0$
$\dot{\gamma}_{ss}$	Strain rate for steady-state creep
ε_{ij}	Second-rank strain tensor
ε	Volumetric strain
ε_s	Exponent for magnitude distribution of AE energies
σ_{ij}	Second-rank stress tensor
σ_0	Stress at $t = 0$
$s^*(\omega)$	Complex (frequency-dependent) compliance

s_{ijkl}	Fourth-rank compliance tensor
s_1	Amplitude of the component of strain in phase with the stress
s_2	Amplitude of the component of strain that is 90° out of phase with stress
ς	Fluid volume per unit volume of porous material
$q_{i,i}$	Rate of fluid volume crossing a unit area of porous solid (in direction x_i)
A_s	Amplitude of acoustic emission (AE)
E_s	Magnitude of acoustic emission (AE) energies
E	Young's modulus
E_{act}	Activation energy of a relaxation process
E_{HTB}	Activation energy of high-temperature background
$E_1(\omega)$	Real part of the dynamic Young's modulus
$E_2(\omega)$	Imaginary part of the dynamic Young's modulus
$\|E\|$	Absolute dynamic Young's modulus
G	Shear modulus
M_{th}	Magnitude of earthquake on a logarithmic scale
M	Stiffness modulus
$M^*(\omega)$	Complex (frequency-dependent) stiffness modulus
M_U	Unrelaxed stiffness modulus
M_R	Relaxed stiffness modulus
$M_1(\omega)$	Real part of $M^*(\omega)$
$M_2(\omega)$	Imaginary part of $M^*(\omega)$
$\|M\|$	Absolute dynamic stiffness modulus
$J^*(\omega)$	Complex (frequency-dependent) compliance
J_U	Unrelaxed compliance
J_R	Relaxed compliance
$J_1(\omega)$	Real part of $J^*(\omega)$
$J_2(\omega)$	Imaginary part of $J^*(\omega)$
$\|J\|$	Absolute dynamic compliance
K	Bulk modulus
K_U or K_{dry}	Bulk modulus of the undrained solid (or dry rock)
K_p	The bulk modulus for the pore volume
K_f	The bulk modulus of the fluid
K_m	The bulk modulus of the constitutive mineral
K_s	The bulk modulus of the solid material
K_s', K_s''	Bulk moduli associated with α and β
K_{IC}	Critical fracture toughness of pre-existing crack (sliding crack)
c_{ijkl}	Fourth-rank stiffness tensor
c	Distribution factor for a relaxation peak
$r(c)$	Distribution function for a relaxation peak

$Z_A(\tau_s)$	Normalised functions for size distribution exponent of AE activities
$Z_E(\varepsilon_s)$	Normalised functions for magnitude distribution exponent of AE energies
z_s	Ratio of $\tau_s - 1$ and $\varepsilon_s - 1$
HTB	Activation energy of apparent high-temperature background ($= nE_{\mathrm{HTB}}$)
Δ	Relaxation strength
ω	Angular excitation frequency
ω_r	Angular resonance frequency
T	Temperature
T_P	Temperature of the Debye relaxation peak
T_M	Melting temperature
T_0	Temperature parameter in the Vogel–Fulcher–Tammann relation
P_s	Compressive pressure on solid phase of the material
p or P_p	Pore (fluid) pressure
P or P_c	Total pressure (isotropic compressive stress) or conning pressure
P' or P_d	Terzaghi effective pressure ($= P - p$) or differential pressure
P_e	Effective pressure
P_{cr}	Critical pressure for the onset of grain crushing
P^*	Critical effective mean pressure for grain crushing
V_P	Compressional wave velocity
V_S	Shear wave velocity
V_{S1}, V_{S2}	Velocities of two perpendicularly polarised shear waves
V_m	Total volume of a porous material
V_{mp}	Volume of interconnected pore space
V_{ms}	Volume of the solid phase and the isolated pore space
V_{mf}	Volume of fluid which fully circulates in the sample
ΔV	Activation volume
Δ_z	The burst size of crackling noise for a single crack propagation
ΔW	Dissipated energy in a full stress cycle per unit volume
δW	Work increment associated with strain increment under stress
W	Maximum stored energy per unit volume
W_r	Down-dip width of rupture for large earthquakes
L_r	Length of rupture along the strike of fault for large earthquakes

l_c	Length of a sliding crack (or a pre-existing crack)
l	Sample length
h	Sample thickness
d	Sample width
ϕ	Porosity
ϕ_θ	Phase lag measured in the inverted forced torsion pendulum (IFTP)
α	Ratio of fluid pore volume change to solid volume change
α_{IFTP}	Numerical coefficient associated with sample dimensions in the IFTP
α_z, β_z	Numerical constants for size distribution in a single crack propagation
β	Effective stress coefficient in the poroelastic model
β_{IFTP}	Numerical coefficient associated with sample dimensions in the IFTP
β_n	Constant for transient part of the Andrade model
K_b	Compressibility of the bulk material
K_s	Compressibility of the solid phase in the material
K_p	Compressibility of the pore phase in the material
θ	Torsion angle of sample in the IFTP
θ_0	Torsion angle at $\omega t = \phi_\theta$
t	Time
t_P	Travel time of compressional wave
t_S	Travel time of shear wave
t_{S1}, t_{S2}	Travel time of two perpendicularly polarised shear waves
t_0	Travel time of waves propagation through ultrasonic transducers and buffer assembly in the 400 MP_a ultrasonic piezoelectric oscillator (UPO)
t_i	Measured travel time in the 400 MPa UPO ($i = P$, S1 or S2)
t_θ	Rescaled waiting-time between two earthquakes ($i = P$, S1 or S2)
b_{th}	Exponent for Gutenberg-Richter Law
m_d, α_d	Empirical exponents for grain-size-dependent internal friction power law
m_n	Exponent for Q^{-1} α $1/\tau_n$ under grain boundary diffusion creep
n	Exponent for high-temperature background exponent for transient part in the Andrade model
n_{Pe}	Empirical effective pressure coefficient
n_k	Effective stress coefficient for velocities in the pore-clay model

α_θ, γ_θ, b_θ	Exponents of waiting-time distributions for earthquakes
τ_s	Exponent for size distribution of AE activities
τ	Relaxation time
τ_σ	Relaxation time at constant stress
τ_ε	Relaxation time at constant strain
τ_{A}	Relaxation time for transition between elastic and anelastic behaviour
τ_{V}	Relaxation time for transition between anelastic and viscous deformation
τ_n	Relaxation time for the steady-state process in the Andrade model
τ_0	Limit relaxation time $\left(= v_0^{-1}\right)$
τ_{z}	Exponent for the scaled size distribution of single crack propagation

Contents

Chapter 1
Introduction

1.1 Motivation

Our understanding of rheological properties of the Earth's interior is largely based on a combination of mineral physics data and direct geophysical observations. Hence seismic velocities and attenuation may be interpreted if we understand how they depend on the mechanical properties of matter. For example, the travel-times and amplitudes of seismic waves propagating through the Earth can be interpreted in terms of mineralogical models when we know the properties of minerals and rocks at depth. Seismic velocities and attenuation depend on the mechanical properties of the matter through which waves propagate: in particular the elastic moduli and their time (or frequency) dependence (reflected in the anelastic inverse quality factor, Q^{-1}, also called loss factor). Anelastic relaxation in minerals and rocks is one of the main origins of seismic attenuation. Others include reflection and scattering by velocity or density heterogeneities in Earth's interior. To interpret seismic attenuation due to anelasticity, it is essential to understand the anelastic properties of the minerals and rocks through which the waves pass. It has long been recognised that different anelastic relaxation processes occur at specific vibration frequencies, as shown in Fig. 1.1. In other words, seismic energy loss can be associated with different resonant relaxation processes inside minerals and rocks which occur at specific frequencies, controlled by discrete atomistic or microstructural processes.

So, seismic attenuation due to anelastic relaxation is affected by the mechanical properties of materials, but these also change with temperature, pressure and frequency. The mechanical properties of the Earth's interior are further complicated because rocks are multi-phase or even multi-state (such as fluid saturated porous rocks or partially-molten rocks). Therefore, understanding the microstructural relations between fluid and solid states and their effect on the mechanical properties of minerals and rocks is crucial when interpreting seismic studies of the Earth's interior.

Many experimental studies attempting to understand seismicity of heterogeneous multi-phase rocks have simplified the problem by focusing on single-phase homogeneous samples. These experimental data are then typically compared with geological

S.-Y. Chien, *Rheological and Seismic Properties of Solid-Melt Systems*,
Springer Theses, DOI: 10.1007/978-3-319-03098-2_1,

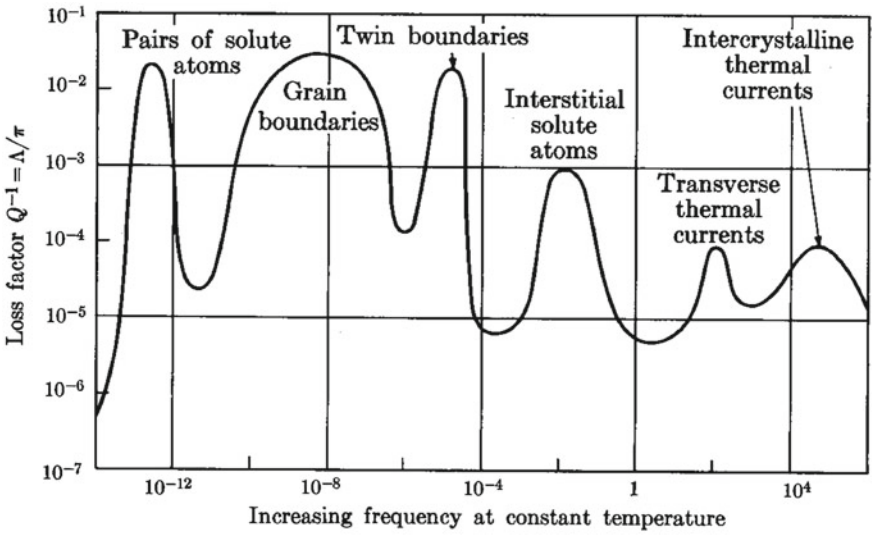

Fig. 1.1 Various anelastic relaxation processes inside materials characterised by loss factors Q^{-1} with increasing frequency at constant temperature. After [1]

observations of multiphase heterogeneous assemblages, in an attempt to interpret real Earth problems using various empirical averaging schemes, e.g. Hashin-Shtrikman [2] or Voigt-Ruess type approaches. Laboratory data, obtained from single phase samples and then empirically averaged, rarely fit perfectly with seismic observations [3].

Some theoretical models make simple assumptions to simulate the energy losses of solids, but typically these do not work well at predicting the real attenuation of complex sample assemblages [4, 5]. Most attenuation experiments on porous rocks have been conducted using high frequency (kHz to MHz) methods at ambient conditions. These typically overestimate the elastic modulus (the unrelaxed modulus) compared with the low frequency observations (mHz to Hz) from seismic studies of rocks at depth (at high temperature and high pressure).

Further complexity arises when one recognises that solid-liquid mixtures are common in Nature: a partially-molten rock is just one example of such a fluid-bearing system. Laboratory attenuation studies of upper mantle minerals have been carried out; for example, the studies of the viscoelastic behaviour of melt-free and basaltic melt-bearing specimens of fine-grained synthetic polycrystalline olivine at high-temperature and seismic frequency [6, 7]. In addition, a recent study of Dobson et al. predicts that mean diameter for olivine grain size in upper mantle is 1.2 mm and is 19 mm for perovskite grain size in the lower mantle [8]. The extrapolation of Jackson et al.'s results, however, fails to explain the observed attenuation in the Earth, either due to an underestimate of the influence of partial melting or due to differences in

the distribution of grain sizes of the order of millimetres (or more) in the lithosphere rather than of microns in the laboratory experiments [9].

In the partially-molten rocks, the small amount of melt is often accommodated in the vicinity of pores, cracks or grain boundaries and results in relaxation processes associated with their interactions. Ultrasonic measurements (kHz to MHz) of minerals have been extensively made for many upper mantle mineral candidates [10, 11]. Of these, the study of Sato et al. [11] of peridotite at high temperature (to 1553 K) and pressure (to 0.73 GPa) pointed out the major dissipation of seismic wave energy that occurs at the grain boundaries, possibly due to grain boundary relaxation or high-temperature background attenuation, which are related to grain boundary damping [11].

In addition, Gribb and Cooper [12] showed that the shear modulus of olivine polycrystalline samples, measured by torsion apparatus at $1 - 10^{-2}$ Hz and around 1473–1558 K, decreases strongly with increasing temperature, which is suggested as a result of grain boundary diffusion [12]. The energy dissipation from laboratory ultrasonic data, though, is unlikely to be caused by the same relaxation processes in the minerals and rocks as those pertinent to seismic wave propagation, and measured by low-frequency laboratory apparatus since they are at such a different frequency. Moreover, smaller grain size in the rock results in more grain boundaries and larger grain size in the rock leads to fewer grain boundaries. This is important when considering whether grain boundary sliding is a significant anelastic process in the deep Earth.

As a partially-molten rock cools, the melt may transform into glass if the rocks undergo a rapid cooling. For instance, when partially-molten rocks are emplaced to the Earth's crust (such as through an intrusive dyke system), silicate glass-crystal mixtures form in rapid cooling systems. In the study of White et al. [13] of the mid-crust of Iceland, many small earthquakes are recorded episodically around the propagating dyke area [13]. They proposed several mechanisms to explain the faulting systems in Iceland, where the movements of the melts in the propagating dyke may be the cause for the flipping of faults along and parallel to the dyke plane as well as the fractures near the dyke tip. However, the episodical microseismicity is still not well understood.

Nucleation and propagation of microcracks may be important when a dyke propagates and cools. As cracks form and propagate in minerals and rocks, they may percolate and result in the macroscopic brittle failure of materials. Consequently, acoustic waves can be emitted and recorded by sensitive microphones as acoustic noise [14]. The behaviour of crackling noise then provides a new insight into the nature of the damage process in such solids. In a slow process, materials respond with discrete events of a variety of size (crackles) with size distributions that adhere to a power law regardless of the scale. The most famous example is the frequency-magnitude relationship (Gutenberg-Richter Law) for earthquakes, such that small earthquakes are common and large earthquakes are rare.

If melts form and are forced into the crack tip of a propagating dyke, pore pressure is generated when fluids (gas or melts) in cracks and pores are compressed. Higher pore pressure opens cracks while increasing confining pressure closes them. As a

result, rock properties, such as velocities, are controlled by pore fluid pressure as well as by confining pressure [4, 15, 16]. The question then arises as to how the changes of pore fluid pressure affect the rock properties.

To test and untangle these issues and questions, two different grain sizes of rocks (basalt and gabbro) have been used and studied at temperatures at which partial melting occurs. This allows us to understand the effect of grain size on the internal friction (attenuation). The inverted forced torsion pendulum is employed to carry out this experiment because it is a powerful tool to study anelastic properties (shear modulus and internal friction), the time-dependent elastic properties, of partially-molten rocks. Besides this experiment, crystalbond-saturated and water-saturated sandstones are also used as analogues for further understanding of rock properties in the glass-crystal system as well as in the pore pressure environment, using the dynamic mechanical analyser and ultrasonic methods. The results are discussed in terms of thermal relaxations (Chap. 4), the glass transition (Chap. 5), noise behaviour (Chap. 6) and fluid pressure (Chap. 7).

1.2 Theoretical Foundations

1.2.1 Anisotropic Elasticity

The origins of elasticity may be traced back to the famous law of Robert Hooke [17]: *ut tensio sic vis*, or "as the extension, so the force". This describes the linear relationship between stress and recoverable strain for a solid body. The constitutive equation of Hooke's law can be formulated for an isotropic medium [1] as

$$F = MD \tag{1.1}$$

where F is force (which can be a torque, or couple) while D is displacement (or angle of twist, or bend), respectively. M is a modulus such as the tensile modulus, torsion modulus, or bending modulus, depending on the type of the applied force.

Elastic materials can show anisotropic responses to different directions of applied force. The result for linear anisotropic elasticity [18] in a three-dimensional symmetric matrix tensor given the generalized Hooke's law in the form

$$\sigma_{ij} = c_{ijkl}\varepsilon_{kl} \tag{1.2}$$

and

$$\varepsilon_{ij} = s_{ijkl}\sigma_{kl} \tag{1.3}$$

where σ_{ij} and ε_{ij} are second-rank stress and strain tensors, respectively, and c_{ijkl} and s_{ijkl} are fourth-rank stiffness and compliance tensors, respectively (i, j =1, 2, 3). In Voigt notation (also known as matrix notation [19], this simplifies two suffixes into

one suffix in a matrix), we have $\sigma_m = c_{mn}\varepsilon_n$ and $\varepsilon_m = s_{mn}\sigma_n$ $(m, n = 1, 2, \ldots, 6)$. Material symmetry reduces the number of independent elements in a single crystal. Based on the different symmetries, the independent components can be reduced to two components in an isotropic system (c_{11} and c_{12}, or s_{11} and s_{12}) or up to 21 components in triclinic crystal.

For homogeneous isotropic elastic materials, the matrix of compliance elements (s_{mn}) can be expressed [20] in terms of Young's modulus (E), shear modulus (G) and Poisson's ratio (ν):

$$s_{11} = 1/E, s_{12} = -\nu/E \text{ and } 2(s_{11} - s_{12}) = 1/G \tag{1.4}$$

which are themselves related:

$$G = E/2(1 + \nu) \tag{1.5}$$

Polycrystalline aggregates of crystals in random orientations, or homogenous aggregates of different crystals are often treated as isotropic materials. The quantities (E, G and ν) and bulk modulus (K) are also related to seismic velocities [21]. For homogeneous isotropic elastic materials, the bulk modulus (K) and shear modulus (G) can eventually be expressed in terms of the density (ρ) and group velocities of elastic waves (compressional, V_P, and shear, V_S,) as:

$$K = \rho(V_P^2 - \frac{4}{3}V_S^2) \tag{1.6}$$

and

$$G = \rho V_S^2 \tag{1.7}$$

Pores and cracks, however, affect velocities in natural rocks. Their existence may contribute to anisotropy even in homogenous rocks. Even though the effect of porosity can often be ignored below a few kilometres depth, stress-aligned fluid-saturated microcracks may occur in the crust or in the upper mantle or indeed at the core-mantle boundary, resulting in seismic anisotropy. Shear waves split into the fast and slow components when they propagate through anisotropically microcracked homogeneous rocks. A review by Crampin and Peacock [22] indicates that it is highly likely that the distributions of stress-aligned fluid-saturated microcracks are the cause of observed stress-aligned shear-wave splitting (seismic anisotropicity) within certain regions of the Earth as shown in Fig. 1.2.

1.2.2 Anelasticity

Anelasticity was originally described by W. Voigt [24] in the late nineteenth century. It was not until 1948, however, that the first formal theory of anelasticity of material

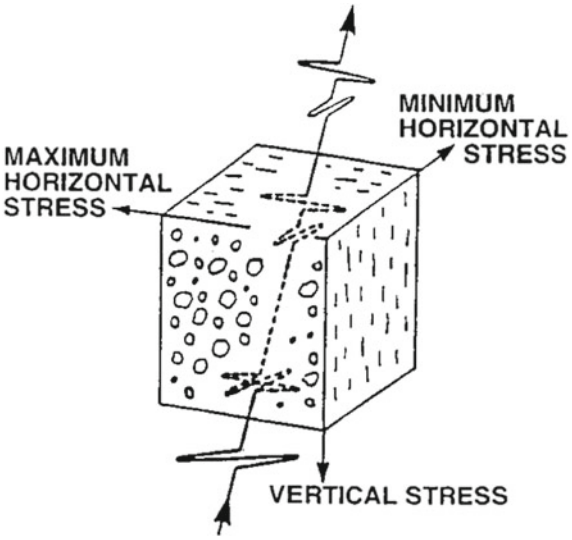

Fig. 1.2 Schematic illustration of shear-wave splitting for wave propagation through a distribution of stress-aligned fluid-filled intergranular microcracks. From [23]

was introduced in Zener's book [1] for metals. This was then extended in discussions of anelasticity in crystalline solids by Nowick and Berry [25]. To derive the equations of anelasticity in an anisotropic material, each compliance s_{mn} (or each c_{mn}) becomes time-dependent, and hence also a complex and frequency-dependent quantity, $s^*(\omega)$. The compliance modulus, $J^*(\omega)$, is constrained to vary between extreme values: the unrelaxed compliance (J_U) for $\omega \to \infty$ and the relaxed compliance (J_R) for $\omega \to 0$.

Anelasticity results from time-dependent materials response with a recoverable stress-strain relationship. In order to formulate the anelastic equations, the Voigt model or Maxwell model (Fig. 1.3) may be employed [26]. A standard anelastic solid can be expressed as a three-component system with a Voigt unit and a spring in series (Voigt-type) or with a Maxwell unit and a spring in parallel (Maxwell-type) (Fig. 1.4). The Voigt-type model is usually used to describe creep behaviour with $J_R\sigma + \tau_\sigma J_U\dot{\sigma} = \varepsilon + \tau_\sigma\dot{\varepsilon}$, while the Maxwell-type model corresponds to stress relaxation in a material with $\sigma + \tau_\varepsilon\dot{\sigma} = M_R\varepsilon + M_U\tau_\varepsilon\dot{\varepsilon}$, where $\dot{\varepsilon}$ and $\dot{\sigma}$ are first time derivatives of strain and of stress, J_R and M_R are relaxed compliance and stiffness moduli, J_U and M_U are unrelaxed compliance and stiffness moduli, and τ_σ and τ_ε are the relaxation times at constant stress and at constant strain given by $\tau_\varepsilon \equiv \tau_\sigma(J_U/J_R) = \tau_\sigma(M_R/M_U)$.

It is of interest to understand the relationship between stress and strain of standard anelastic solids when these quantities are periodic. In dynamic experiments, the stress and strain behave as $\sigma(\omega) = \sigma_0 e^{i\omega t}$ and $s^*(\omega) = (s_1 - is_2)e^{i\omega t}$, where s_1 is the amplitude of the component of strain in phase with the stress and s_2 is the amplitude of the component that is 90° out of phase. Dividing complex strain by stress, the complex compliance can be obtained as $J^*(\omega) = J_1(\omega) + iJ_2(\omega)$, where $J_1(\omega) \equiv \varepsilon_1/\sigma_0$ is the real part of $J^*(\omega)$ and $J_2(\omega) \equiv \varepsilon_2/\sigma_0$ is the imaginary

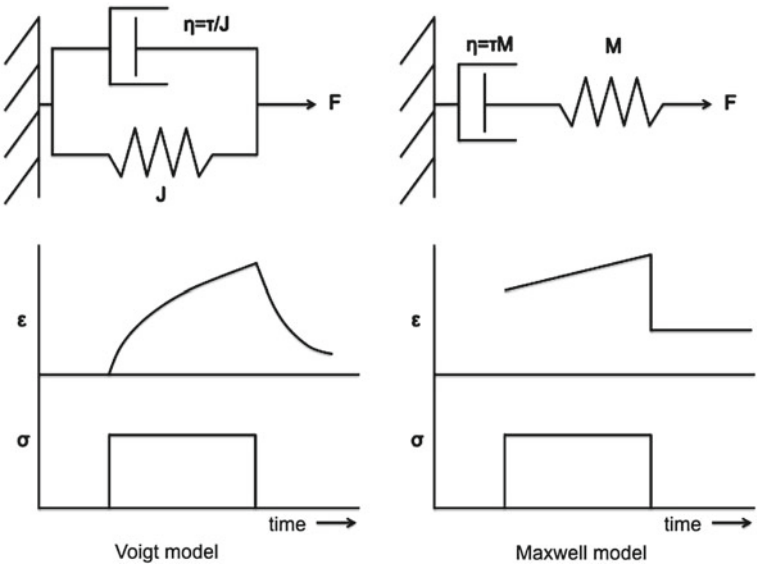

Fig. 1.3 Schematic illustration of a Voigt model and a Maxwell model: The Voigt model comprises a spring and a dashpot in parallel, which reflects creep and recovery under application and removal of a stress. In the other hand, a spring and a dashpot are in series for the Maxwell model, which behaves as a material undergoing linear viscous creep with stress applied and a permanent strain remaining after the removal of the stress (η: viscosity). After [25]

part of $J^*(\omega)$. The complex compliance $J^*(\omega)$ can be illustrated as a vector diagram on the complex plane (Fig. 1.5). It is clear to see that $|J|^2 = J_1^2 + J_2^2$ and $tan\delta = J_2/J_1$, where $|J|$ is the absolute dynamic compliance. Similarly, the complex modulus $M^*(\omega)$ and the absolute dynamic modulus, $|M|$, may be obtained and $tan\delta = M_2/M_1$. Hence,

$$J_1 = M_1/|M|^2 = [M_1(1 + tan^2\delta)]^{-1} \tag{1.8}$$

and

$$J_2 = M_2/|M|^2 \text{ or } M_2 = J_2/|J|^2 \tag{1.9}$$

The quantities J_1 and J_2 also correspond to the energy stored and the energy dissipated in a cycle of vibration (they are referred to as storage compliance and loss compliance, respectively). The energy dissipated in a full cycle per unit of volume can be expressed by $\Delta W = \pi J_2 \sigma_0^2$ and the maximum stored energy per unit volume is $W = \frac{1}{2} J_1 \sigma_0^2$. The ratio of the energy dissipated to the maximum stored energy, $\Delta W/W = 2\pi(J_2/J_1) = 2\pi tan\delta$, is often called the specific damping capacity, which is also proportional to loss factor ($Q^{-1} = \Delta W/2\pi W$) with a factor of 2π. The tangent of the loss angle ($tan\delta$), also called loss tangent or mechanical loss, is shown to be identical to inverse quality factor (Q^{-1}). Since the tangent of the

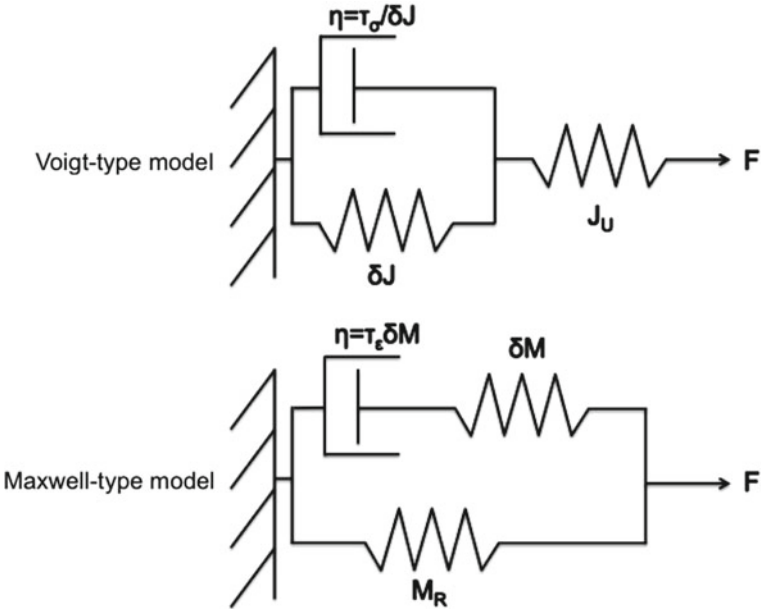

Fig. 1.4 Schematic illustration of three-parameter models: the Voigt-type model and the Maxwell-type model, where the relaxation of the modulus $\delta M \equiv M_U - M_R$ and the relaxation of the compliance $\delta J \equiv J_R - J_U$ with a relation of $\delta M = \delta J / J_U J_R$. After [25]

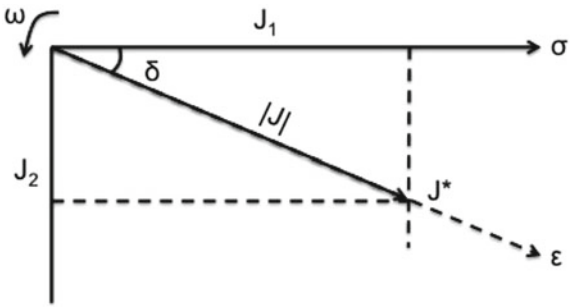

Fig. 1.5 The conventional vector diagram for the complex quantity, $J^*(\omega)$, illustrating the phase relations between stress, strain, and the complex compliance (the entire diagram rotates about the origin with angular frequency, ω). The phase angle (δ), also known as loss angle, is the angle by which strain lags behind stress. After [25]

loss angle ($tan\delta$) provides the fractional energy loss per cycle due to the anelastic behaviour, the loss angle (δ) is often known as the internal friction of the material [25].

Substituting the above definitions of complex stress and strain into the formula for a three-parameter Voigt-type model, gives $J^*(\omega)$, $J_1(\omega)$ and $J_2(\omega)$ as

$$J^*(\omega) = J_U + \frac{\delta J}{1 + i\omega\tau_\sigma} \tag{1.10}$$

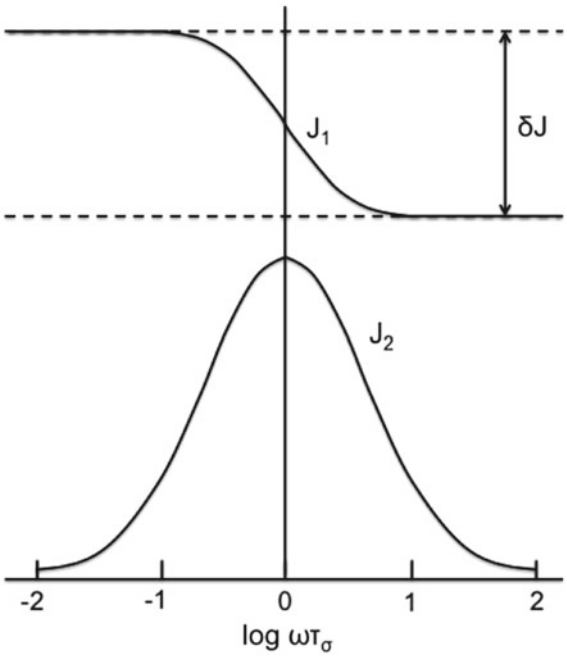

Fig. 1.6 Comparison of $J_1(\omega)$ and $J_2(\omega)$ as functions of $log\omega\tau_\sigma$ for a standard anelastic solid. After [25]

$$J_1(\omega) = J_U + \frac{\delta J}{1 + (\omega\tau_\sigma)^2} \tag{1.11}$$

$$J_2(\omega) = \delta J \frac{\omega\tau_\sigma}{1 + (\omega\tau_\sigma)^2} \tag{1.12}$$

Equations 1.10, 1.11, and 1.12 are commonly known as the Debye equations, which are first derived by Peter Debye [27] to explain dielectric relaxation phenomena. The quantity $J_1(\omega)$ varies from J_U at high frequencies ($\omega\tau_\sigma \geqslant 1$) to J_R at low frequencies ($\omega\tau_\sigma \leqslant 1$). The quantity $J_2(\omega)$ has its maximum value at $\omega\tau_\sigma = 1$ and symmetrically decreases to very small values at both high and low frequencies ($\omega\tau_\sigma \geqslant 1$ or $\omega\tau_\sigma \leqslant 1$). Thus, the quantity $J_2(\omega)$ can be plotted against $log\omega\tau$ as a peak function, a Debye peak with width of $\Delta(log_{10}\omega\tau_\sigma) = 1.144$ at half maximum (Fig. 1.6).

The internal friction $\delta(\omega)$ can also be expressed as a Debye peak in the case when $\delta J \ll J_U$ (and hence $tan\delta(\omega) \cong \delta(\omega) \cong J_2/J_1$), where $\Delta = \delta J/J_U$ is the relaxation strength and τ_σ and τ_ε become equal at $\Delta \ll 1$, therefore the subscript to τ can be ignored.

$$\delta(\omega) \cong \frac{\delta}{J_U} \frac{\omega\tau_\sigma}{1 + (\omega\tau_\sigma)^2} \cong \Delta \frac{\omega\tau}{1 + (\omega\tau)^2}, \Delta \ll 1 \tag{1.13}$$

Zener [1] also shows that $\delta(\omega)$ can be expressed as a Debye peak without any calculations from relaxation strength, using the geometric mean of the two relaxation times $\bar{\tau} = (\tau_\sigma \tau_\varepsilon)^{1/2}$. Consequently, the two expressions can be related, as shown in equation 1.14, which is a Debye peak whose maximum ($tan\delta_{max} = \Delta/2(1+\Delta)^{1/2}$) occurs at $\omega\bar{\tau} = 1$. Equation 1.12 becomes equivalent to Eq. 1.13 if and only if $\Delta \ll 1$ and hence $tan\delta_{max} = \Delta/2$.

$$tan\delta = \frac{\delta J}{(J_U J_R)^{1/2}} \frac{\omega\bar{\tau}}{1+(\omega\bar{\tau})^2} = \frac{\Delta}{(1+\Delta)^{1/2}} \frac{\omega\bar{\tau}}{1+(\omega\bar{\tau})^2} \tag{1.14}$$

From Eqs. 1.11 and 1.12, Cole and Cole [29] proposed to plot a form of Argand diagram in which $J_2(\omega)$ is shown against $J_1(\omega)$, also called Cole-Cole plot that satisfies the Kronig-Kramers relations [28], that each point is referred to one frequency [29]. Therefore, the relationship between $J_1(\omega)$ and $J_2(\omega)$ can be given as:

$$\left(J_1(\omega) - \frac{J_R + J_U}{2}\right)^2 + (J_2(\omega))^2 = \left(\frac{J_R - J_U}{2}\right)^2 \tag{1.15}$$

The Cole-Cole plot corresponds to a semicircle with radius $(J_R - J_U)/2$ centred at a distance $(J_R + J_U)/2$ from the origin (Fig. 1.7).

Generally, multiple relaxation processes (more than one single relaxation time) occur in natural systems. A modified distribution function is, therefore, required under these conditions. Cole and Cole (1941) introduced a distribution factor, c, into the Debye equations:

$$J^*(\omega) = J_U + \frac{\delta J}{1 + i\omega\tau^c}, \quad 0 < c \leq 1 \tag{1.16}$$

$$\frac{J_1(\omega) - J_U}{\delta J} = \frac{1 + (\omega\tau)^c cos(\frac{c\pi}{2})}{1 + 2(\omega\tau)^c \cos(\frac{c\pi}{2}) + (\omega\tau)^{2c}} \tag{1.17}$$

$$\frac{J_2(\omega)}{\delta J} = \frac{(\omega\tau)^c cos(\frac{c\pi}{2})}{1 + 2(\omega\tau)^c \cos(\frac{c\pi}{2}) + (\omega\tau)^{2c}} \tag{1.18}$$

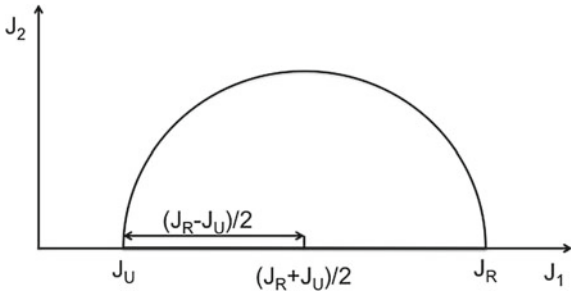

Fig. 1.7 Cole-Cole plot for a single relaxation time model

For $c = 1$, Eq. 1.16 is equivalent to Eq. 1.10, i.e. a pure Debye relaxation. If $0 < c < 1$, the dispersion curve from Eq. 1.17 becomes broader and symmetrical about $\omega\tau = 1$; the loss curve from Eq. 1.18 is lower in amplitude but broader. Mechanical loss in the multi-relaxation systems (with a distribution of relaxation times) can also be expressed by Fuoss-Kirkwood distribution [30] with an introduced distribution factor (Fig. 1.8):

$$tan\delta(\omega) = \Delta \frac{(\omega\tau)^c}{1 + (\omega^2\tau^2)^c}, 0 < c \leq 1 \tag{1.19}$$

To illustrate the relationship between $J_1(\omega)$ and $J_2(\omega)$ in multi-relaxation systems, several empirical distribution functions have been used in dielectric studies [31]. The best-known empirical approach is perhaps the modified Cole-Cole distribution function that is given as an equation, which corresponds to a depressed circle with the centre at $\left(\frac{J_R+J_U}{2}, -\frac{J_R-J_U}{2} cotan(\frac{c\pi}{2})\right)$ and a radius $\frac{J_R-J_U}{2} cosec(\frac{c\pi}{2})$:

$$\left(J_1(\omega) - \frac{J_R + J_U}{2}\right)^2 + \left(J_2(\omega) + \frac{J_R - J_U}{2} cotan\left(\frac{c\pi}{2}\right)\right)^2 = \left(\frac{J_R - J_U}{2} cosec\left(\frac{c\pi}{2}\right)\right)^2 \tag{1.20}$$

The Debye equations are obtained as a function of frequency from Eqs. 1.10 to 1.20 and the relaxation time has been considered as a constant at a constant temperature. However, the motion of the microstructural defects, triggering most of the relaxations processes, is thermally activated with an associated energy barrier. Therefore, the relaxation time is given [26] as

$$\tau = \tau_0 e^{E_{act}/RT} \tag{1.21}$$

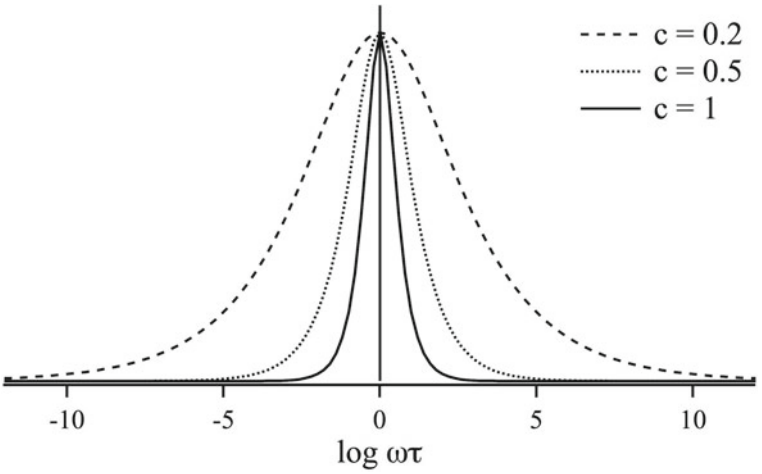

Fig. 1.8 $tan\delta(\omega)$ as a function of $log\omega\tau$ for c=0.2, 0.5 and 1

in which the limit relaxation time $\tau_0 = \nu_0^{-1}$ where ν_0 corresponds to the attempt frequency. The probability that the activation barrier is overcome follows Maxwell-Boltzmann statistics and is given by $e^{E_{\text{act}}/\text{R}T}$, where E_{act} is the activation energy (kJ/mole), R is gas constant and T is the absolute temperature. The distribution in relaxation time, τ, can be considered in terms of a distribution in τ_0 or in E_{act} or in both of them, which makes the relaxation more complicated. Here, τ_0 and E_{act} are considered as constant. The dynamic response functions (Debye equations) are then expressed as a function of temperature by substituting Eq. 1.21 into Eqs. 1.10–1.12 at constant frequency as

$$ln\omega\tau = ln\omega\tau_0 + \frac{E_{\text{act}}}{\text{R}}\left(\frac{1}{T}\right) \tag{1.22}$$

For the case of single Debye relaxation, the peak position, where $ln\omega\tau = 0$ corresponds to a temperature, T_P, given by $ln\omega\tau_0 + (E_{\text{act}}/\text{R})(1/T_P) = 0$. If the different Debye peak positions (at different temperatures) are measured at different frequencies, the activation energy for this single relaxation process can be obtained from the slope $(E_{\text{act}}/\text{R})$ in a plot of $ln\omega$ versus $1/T_P$ from

$$ln\left(\frac{\omega_2}{\omega_1}\right) = \frac{E_{\text{act}}}{\text{R}}\left(\frac{1}{T_{P_2}} - \frac{1}{T_{P_1}}\right) \tag{1.23}$$

The internal friction can also be considered in terms of τ as a function of temperature [26], and a Debye relaxation occurs as a function of temperature as expressed by Eq. 1.24.

$$tan\delta = \frac{\Delta}{2}cosh^{-1}\left[\frac{E_{\text{act}}}{\text{R}}\left(\frac{1}{T} - \frac{1}{T_P}\right)\right] \tag{1.24}$$

This can be extended to incorporate a distribution of relaxation processes by incorporation of a distribution function, $r(c)$ (Fig. 1.9):

$$tan\delta = \frac{\Delta}{2}cosh^{-1}\left[\frac{E_{\text{act}}}{r(c)\text{R}}\left(\frac{1}{T} - \frac{1}{T_P}\right)\right],\ r(c) \geqslant 1 \tag{1.25}$$

At relatively high temperatures, above $0.6T_M$ (T_M = melting point), internal friction generally exhibits an exponential rising background, sometimes with superimposed relaxation peaks. This high-temperature background is more evident in polycrystalline materials than in the single crystals. The internal friction that gives rise to the high-temperature background appears to follow a law $tan\delta = \text{A}exp(-E_{\text{HTB}}/\text{R}T)$, in which A is a material-related pre-factor and E_{HTB} is an activation energy. Schoeck et al. [32] proposed this high temperature damping is caused by a broad spectrum of diffusion-controlled relaxation processes (for E_{HTB}) and gives the relation as

$$tan\delta = \frac{\text{A}}{(\omega e^{E_{\text{HTB}}/\text{R}T})^{\text{n}}} \tag{1.26}$$

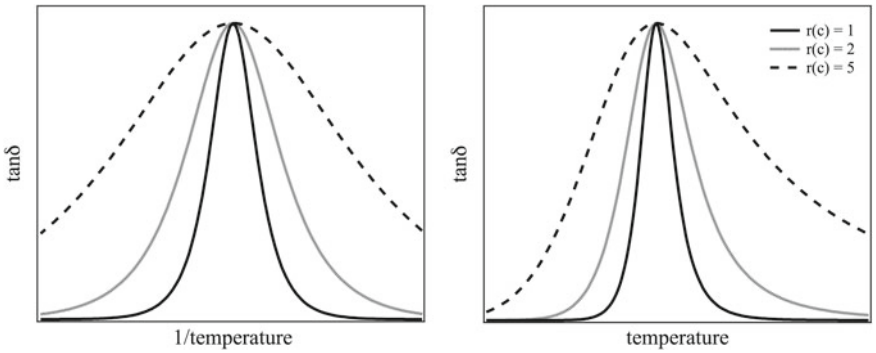

Fig. 1.9 $tan\delta(\omega)$ as a function of inverse temperature (*left*) and temperature (*right*) for $r(c)$=1, 2 and 5

where A and n are essentially constant over a limited range of temperature.

1.2.3 Poroelasticity

The presence of fluids in porous solids modifies their mechanical behaviour and is described by the general topic of poroelasticity. An appreciation of poroelasticity is important when considering the properties of partially molten rocks. It is also extensively treated in studies of oil reservoir rock systems. The earliest theory of poroelasticity is Terzaghi's one-dimensional consolidation in 1923 [33] and extended to three-dimensions by Rendulic in 1936 [34]. This discusses the influence of pore fluid on the quasi-static deformation of soils. However, when a freely moving fluid is present in a porous rock, the reaction of fluid can affect the mechanical response of the rock and vice versa: the compression of a porous rock increases the pore pressure and the rise of the pore pressure causes additional stress on the surrounding rock. To bring coherence between these two basic interactions between the fluid and solids, linear poroelasticity has been developed by Biot in 1935 [35] and extended to three-dimensions in 1941 [36].

In Biot's theory, two strain quantities, ε_{ij} and ζ, are introduced to describe the coupled deformation-diffusion processes within the Biot's poroelastic theory. ε_{ij} is the small strain tensor of solids, positive for extension, which can be expressed in terms of a solid displacement vector u_i as $\varepsilon_{ij} = \frac{1}{2}(u_{i,j} + u_{j,i})$. ζ is the variation of fluid volume per unit volume of porous material and its positive response to an increase of fluid in the porous solid, which also gives the rate of fluid volume crossing a unit area of porous solid (in direction x_i) as $-q_{i,i} = \delta\zeta/\delta t$ [37]. For a linear isotropic poroelastic material, the work increment (δW) associated with strain increments in the presence of the total stress tensor (σ_{ij}) and the pore pressure (p) is given by $\delta W = \sigma_{ij}\delta\varepsilon_{ij} + p\delta\zeta = \varepsilon_{ij}\delta\sigma_{ij} + \zeta\delta p$. In the linear poroelasticity, the

coupled effects only appear in the volumetric stress-strain relationship, which can be expressed as

$$\varepsilon = -\left(\frac{P}{K} - \frac{p}{H'}\right) \tag{1.27}$$

$$\zeta = -\left(\frac{P}{H'} - \frac{p}{R'}\right) \tag{1.28}$$

where ε is the volumetric strain, P is the mean or total pressure (isotropic compressive stress), H' and R' are constants, which characterise the coupling between the solid and fluid stress and strain, and K is the bulk modulus of the drained elastic solid.

Rice and Cleary [38] reformulate Biot's theory and emphasise two limiting behaviours of a fluid-filled porous material in the drained (when excess pore pressure is completely dissipated, $p = 0$) and undrained conditions (when the fluid cannot escape the porous rock, $\zeta = 0$). Under the drained condition, the volumetric strain in Eq. 1.27 becomes

$$\varepsilon = -P/K \tag{1.29}$$

which can be substituted into Eq. 1.28 to obtain

$$\zeta = \alpha\varepsilon, \ \alpha \leq 1 \tag{1.30}$$

where $\alpha = K/H'$ is the ratio of the fluid volume change in the pore space to the volume change of the solid, when the pore pressure is allowed to return to its initial state, $p = 0$. On the other hand, for the undrained condition, Eq. 1.28 can be reformulated as

$$p = BP \tag{1.31}$$

where $B = R'/H'$ is known as the Skempton pore pressure coefficient [39]. Similarly, equation 1.31 can be substituted into Eq. 1.27 to give

$$\varepsilon = -P/K_U \tag{1.32}$$

where the undrained bulk modulus of the solid, $K_U = K(1 + \frac{KR'}{H'^2 - KR'})$, with $K \leq K_U \leq \infty$. Therefore, it is clear that a framework of fluid-filled porous material is stiffer in the undrained condition than in the drained condition. Now, Eqs. 1.27 and 1.28 can be reformulated with physical meaning as

$$\varepsilon = -\frac{1}{K}(P - \alpha p) \tag{1.33}$$

$$\zeta = -\frac{\alpha}{K}\left(P - \frac{p}{B}\right) \tag{1.34}$$

where $B = (K_U - K)/(\alpha K_U)$.

When an extra applied loading, it is possible that either the compressibility of the fluid or the porosity of the rock will change. It is thus desirable to know the volumetric response of the porous rock to loading (total pressure P and pore pressure p). Assuming the total volume of a porous material is the sum of the interconnected pore space of volume and the solid phase plus isolated pores ($V_m = V_{mp} + V_{ms}$), the volume of fluid which freely circulate in the sample under full saturation can be expressed as $V_{mp} = V_{mf}$ and the porosity of the sample is denoted as $\phi = V_{mp}/V_m$. Then, the volumetric response from Eqs. 1.33 and 1.34 to the loading can be expressed as

$$\frac{\Delta V_m}{V_m} = -\frac{1}{K}(P - \alpha p) \tag{1.35}$$

$$\frac{\Delta V_{mp}}{V_{mp}} = -\frac{1}{K_p}(P - \beta p) \tag{1.36}$$

where K_p is the bulk modulus for the pore volumetric strain and β is a dimensionless effective stress coefficient. By invoking the Maxwell-Betti reciprocal theorem [40], that the increase total volume due to a pore pressure is the same as the decrease in the pore volume (with a minus sign) due to a confining pressure, we can obtain $K_p = \frac{\phi}{\alpha}K$ and

$$\alpha = 1 - \frac{K}{K_s'} \tag{1.37}$$

$$\beta = 1 - \frac{K_p}{K_s''} \tag{1.38}$$

where coefficients K_s' and K_s'' are two bulk moduli, which appears to be first discussed by Gassmann [41].

These equations corresponding to the loading can now be used to obtain the dependence of the constants α, β, K and K_U on the porosity and the compressibility of the fluid, solid and pores. If a solid constituent is incompressible ($K/K_s' \ll 1$ and $K/K_s'' \ll 1$), the compressibility of the solid phase is negligible compared to that of the drained bulk material. Then, $\alpha = 1$, $K_U = K(1 + \frac{K_f}{\phi K})$, $B = 1 - (1 + \frac{K_f}{\phi K})^{-1}$, and $K = K_\phi = K_p/\phi$ as $K_\phi^{-1} = K^{-1} - [(1-\phi)K_s']^{-1}$, where K_f is the bulk modulus of the fluid. If both fluid and solid constituents are incompressible ($K/K_s' \ll 1$, $K/K_s'' \ll 1$, and $K/K_f \ll 1$), and the compressibility of the fluid can be further neglected, then $\alpha = B = 1$ and $K_U \to \infty$. In this case, all the poroelastic constants can be treated as their upper bound values. If the fluid constituent is highly compressible ($K_f/K \ll 1$ or $K_f \to 0$), the approximated expressions will be $\alpha = 1$, $B \to 0$, $K_U \to K$ which implies the porous material behaves as an elastic material without fluid.

If a Π-pressure (also named as Π-loading), which corresponds to a confining pressure and a pore pressure of the same magnitude, is applied to an ideal homogenous

and isotropic porous material characterised by fully-connected pores, the material will deform as if all the pores are filled with solid and result in $K_s' = K_s'' = K_s$, where K_s is now identified as the modulus of solid material and two quantities K_s' and K_s'' serve as the definition of the ideal porous material. With this relation, Carroll [42] derived the equations with the compressive solid pressure, P_s:

$$\frac{\Delta V_{ms}}{V_{ms}} = -\frac{P_s}{K_s} \tag{1.39}$$

$$\frac{\Delta \phi}{1-\phi} = -\frac{P'}{K_\phi} \tag{1.40}$$

where $P_s = \frac{1}{1-\phi}(P - \phi p)$ and $P' = P - p$ is known as the Terzaghi effective pressure [33]. Eq. 1.39 presents the volumetric strain of the solid phase which is proportional to the compressive solid stress and Eq. 1.40 shows the Terzaghi effective pressure which controls the porosity variation. For most porous materials, the critical porosity for a sample to collapse under a small stress is approximately 0.5, with an almost linear decay of bulk modulus when porosity is less than this critical value [43]. Therefore, Eq. 1.40 is modified to Eq. 1.41. In the case of Π-loading, no porosity variation will occur in the sample and hence the Terzaghi effective pressure will be zero, i.e. the confining pressure is equal to the pore pressure.

$$\frac{\Delta \phi}{0.5-\phi} = -\frac{P'}{K_\phi} \tag{1.41}$$

Zimmerman et al. [44] suggest that the relationship between the volumetric behaviours of porous rocks and the change of confining pressure and pore pressure is non-linear, and may correspond to the opening/closure of crack-like pores. Under increasing confining pressure and/or dissipation of pore pressure, crack-like pores close progressively (the elongated shapes start first) and the compressibility of the rock will eventually remain constant when all the crack-like pores collapse. Zimmerman *et al.* also demonstrate that only Terzaghi effective pressure controls the bulk and pore compressibility. If the compressibility of the solid phase is independent of stress and there is no porosity variation under Π-loading, the solid phase compressibility (κ_s) is always smaller than the bulk compressibility (κ_b) in a relation of $\kappa_b = \kappa_s + \phi\kappa_p$, where κ_p is the pore compressibility. Therefore, the pore compressibility, as well as the bulk compressibility, is progressively reduced until all the crack-like pores close under increasing confining pressure.

References

1. Zener, C. (1948). *Elasticity and anelasticity of metals*. Chicago: University of Chicago Press.
2. Hashin, Z., & Shtrikman, S. (1963). A variational approach to the theory of the elastic behaviour of multiphase materials. *Journal of the Mechanics and Physics of Solids*, *11*(2), 127–140.

3. Jones, A. G., Evans, R. L., & Eaton, D. W. (2009). Velocity-conductivity relationships for mantle mineral assemblages in archean cratonic lithosphere based on a review of laboratory data and hashin-shtrikman extremal bounds. *Lithos*, *109*(1–2), 131–143.
4. Gist, G. A. (1994). Fluid effects on velocity and attenuation in sandstones. *The Journal of the Acoustical Society of America*, *96*(2), 1158–1173.
5. James Jr, S. W. (1981). Stress relaxations at low frequencies in fluid-saturated rocks: Attenuation and modulus dispersion. *Journal of Geophysical Research*, *86*(B3), 1803–1812.
6. Jackson, I., Fitz Gerald, J. D., Faul, U. H., & Tan, B. H. (2002). Grain-size-sensitive seismic wave attenuation in polycrystalline olivine. *Journal of Geophysical Research*, *107*(B12), 2360.
7. Jackson, I., Faul, U. H., Fitz Gerald, J. D., & Tan, B. H. (2004). Shear wave attenuation and dispersion in melt-bearing olivine polycrystals: 1. specimen fabrication and mechanical testing. *Journal of Geophysical Research*, *109*(B6), B06201.
8. Dobson, D., Ammann, M., & Tackley, P. (2012). The grain size of the lower mantle. *Proceeding of European Mineralogical Conference*, Vol. 1, p. 403.
9. Priestley, K., & McKenzie, D. (2006). The thermal structure of the lithosphere from shear wave velocities. *Earth and Planetary Science Letters*, *244*(1–2), 285–301.
10. Karato, S.-I., & Jung, H. (1998). Water, partial melting and the origin of the seismic low velocity and high attenuation zone in the upper mantle. *Earth and Planetary Science Letters*, *157*(3—-4), 193–207.
11. Sato, H., Sacks, I. S., Murase, T., Muncill, G., & Fukuyama, H. (1989). Qp-melting temperature relation in peridotite at high pressure and temperature: attenuation mechanism and implications for the mechanical properties of the upper mantle. *Journal of Geophysical Research*, *94*(B8), 10,661–10,647.
12. Gribb, T. T., & Cooper, R. F. (1998). Low-frequency shear attenuation in polycrystalline olivine: Grain boundary diffusion and the physical significance of the andrade model for viscoelastic rheology. *Journal of Geophysical Research*, *103*(B11), 27,267–27,279.
13. White, R. S., Drew, J., Martens, H. R., Key, J., Soosalu, H., & Jakobsdóttir, S. S. (2011). Dynamics of dyke intrusion in the mid-crust of iceland. *Earth and Planetary Science Letters*, *304*(3—-4), 300–312.
14. Halász, Z., Timár, G., & Kun, F. (2010). The effect of disorder on crackling noise in fracture phenomena. *Progress of Theoretical Physics Supplement*, *184*, 385–399.
15. King, M. S. (1966). Wave velocities in rocks as a function of changes in overburden pressure and pore fluid saturants. *Geophysics*, *31*(1), 50–73.
16. Nur, A. M., Mavko, G., Dvorkin, J., & Gal, D. (1995). Critical porosity: The key to relating physical properties to porosity in rocks. *SEG Technical Program Expanded Abstracts*, *14*(1), 878–881.
17. Hooke, R. (1678). *de potentia restitutiva*. London: John Martyn Printer.
18. Cowin, S. C. (1989). Properties of the anisotropic elasticity tensor. *The Quarterly Journal of Mechanics and Applied Mathematics*, *42*(2), 249–266.
19. Lovett, D. R. (1999). *Tensor properties of crystals* (2nd ed.). Bristol: Institute of Physics Publishing.
20. Nye, J. (1985). *Physical properties of crystals: Their representation by tensors and matrices*. New York: Oxford University Press.
21. Christensen, N. I. (1982). *Seismic velocities, volume II* (pp. 1–228). Boca Raton: CRC Press.
22. Crampin, S., & Peacock, S. (2008). A review of the current understanding of seismic shear-wave splitting in the earth's crust and common fallacies in interpretation. *Wave Motion*, *45*(6), 675–722.
23. Crampin, S. (1999). Calculable fluid-rock interactions. *Journal of the Geological Society*, *156*(3), 501–514.
24. Voigt, W. (1892). Ueber innere reibung fester körper, insbesondere der metalle. *Annalen der Physik*, *283*(12), 671–693.
25. Nowick, A. S., & Berry, B. S. (1972). *Anelastic relaxation in crystalline solids*. New York: Academic Press.

26. Schaller, R., Fantozzi, G., & Gremaud, G. (2001). *Mechanical spectroscopy Q^{-1} 2001: With applications to materials science. Materials science forum*. Switzerland: Trans Tech Publications.
27. Debye, P. (1912). Einige resultate einer kinetischen theorie der isolatoren. *Physikalische Zeitschrift*, *13*, 97–100.
28. Landau, L. D., & Lifshitz, E. M. (1985). *Statistical physics* (3rd ed.). Oxford: Butterworth-Heinemann.
29. Cole, K. S., & Cole, R. H. (1941). Dispersion and absorption in dielectrics I. Alternating current characteristics. *The Journal of Chemical Physics*, *9*(4), 341–351.
30. Fuoss, R. M., & Kirkwood, J. G. (1941). Electrical properties of solids. VIII. Dipole moments in polyvinyl chloride-diphenyl systems*. *Journal of the American Chemical Society*, *63*(2), 385–394.
31. McCrum, N. G., Read, B. E., & Williams, G. (1967). *Anelastic and dielectric effects in polymeric solids*. New York: Dover Publications Inc.
32. Schoeck, G., Bisogni, E., & Shyne, J. (1964). The activation energy of high temperature internal friction. *Acta Metallurgica*, *12*(12), 1466–1468.
33. Terzaghi, K. (1923). Die berechnung der durchlassigkeitsziffer des tones aus dem verlauf der hydrodynamischen spannungserscheinungen. *Akademie der Wissenschaften in Wien Mathematisch-naturwissenschaftliche Klasse Abteilung*, *132*, 105–124.
34. Rendulic, L. (1936). Porenziffer und porenwasserdrunk in tonen. *Der Bauingenieur*, *17*, 559–564.
35. Biot, M. A. (1935). Le problème de la consolidation des matières argileuses sous une charge. *Annales de la Societe Scientifique de Bruxelles*, *B55*, 110–113.
36. Biot, M. A. (1941). General theory of three-dimensional consolidation. *Journal of Applied Physics*, *12*(2), 155–164.
37. Detournay, E. and Cheng, A. H. D. (1993). *Fundamentals of poroelasticity, volume II, chapter 5*, (pp. 113–171). Oxford: Pergamon Press.
38. Rice, J. R., & Cleary, M. P. (1976). Some basic stress diffusion solutions for fluid-saturated elastic porous media with compressible constituents. *Reviews of Geophysics*, *14*(2), 227–241.
39. Skempton, A. W. (1954). The pore-pressure coefficients a and b. *Géotechnique*, *4*(4), 143–147.
40. Nautiyal, B. D. (2001). *Introduction to Structural Analysis*. New Delhi: New Age International.
41. Gassmann, F. (1951a). Elastic waves through a packing of spheres. *Geophysics*, *16*(4), 673–685.
42. Carroll, M. M., & Katsube, N. (1983). The role of terzaghi effective stress in linearly elastic deformation. *Journal of Energy Resources Technology*, *105*(4), 509–511.
43. Salje, E. K. H., Koppensteiner, J., Schranz, W., & Fritsch, E. (2010). Elastic instabilities in dry, mesoporous minerals and their relevance to geological applications. *Mineralogical Magazine*, *74*(2), 341–350.
44. Zimmerman, R. W., Somerton, W. H., & King, M. S. (1986). Compressibility of porous rocks. *Journal of Geophysical Research*, *91*(B12), 12765–12777.

Chapter 2
Experimental Methods

A variety of dynamic apparati [1, 2] have been employed to measure the mechanical properties of anelastic materials, in which energy is dissipated as a function of time, with a phase lag δ (loss angle) between stress and strain. For material of large energy loss ($tan\delta > 10^{-3}$), subresonant methods are often used to carry out measurements of the transient properties of materials. The subresonant method generally covers the frequency range from 10^{-5} to 100 Hz, due to limitations arising from instrumental resonances. It is also possible to measure the dynamic response function (creep or stress-relaxation) as a function of temperature and frequency. Instruments of this type include the dynamic mechanical analyser [3], torsion pendulum [4], high-resolution inverted torsion pendulum [5] and the variants of torsion pendulum [6, 7]. For low loss angle ($tan\delta < 10^{-3}$), resonant methods are more sensitive to materials properties. The resonant methods are typically used in the frequency range from tens of hertz to megahertz. The piezoelectric ultrasonic oscillator [8] and resonant ultrasound spectroscopy (RUS) [9] are two examples for resonant apparatus. However, subresonant and resonant methods are inappropriate when a sample becomes too soft and unable to support its own weight, either at very low frequency or at very high temperature.

Wave methods (ultrasonic waves) may also be used to obtain the mechanical properties of materials over a frequency range from kHz to GHz (typically above subresonant and resonant methods). The waves are produced by piezoelectric transducers, which are often attached to other devices for velocity measurements in different environments, such as with the 300 MPa hydrostatic pressure vessel for fluid-saturated conditions [10] or with multi-anvil apparatus for phase transitions under mantle condition [11].

In this study, two subresonant methods (inverted forced torsion pendulum and dynamic mechanical analyser, DMA) have been used to investigate creep or stress-relaxation processes in the partially-molten rocks, and one wave method (400 MPa ultrasonic piezoelectric oscillator) was used to measure sound velocities in water-saturated rocks.

S.-Y. Chien, *Rheological and Seismic Properties of Solid-Melt Systems*,
Springer Theses, DOI: 10.1007/978-3-319-03098-2_2,

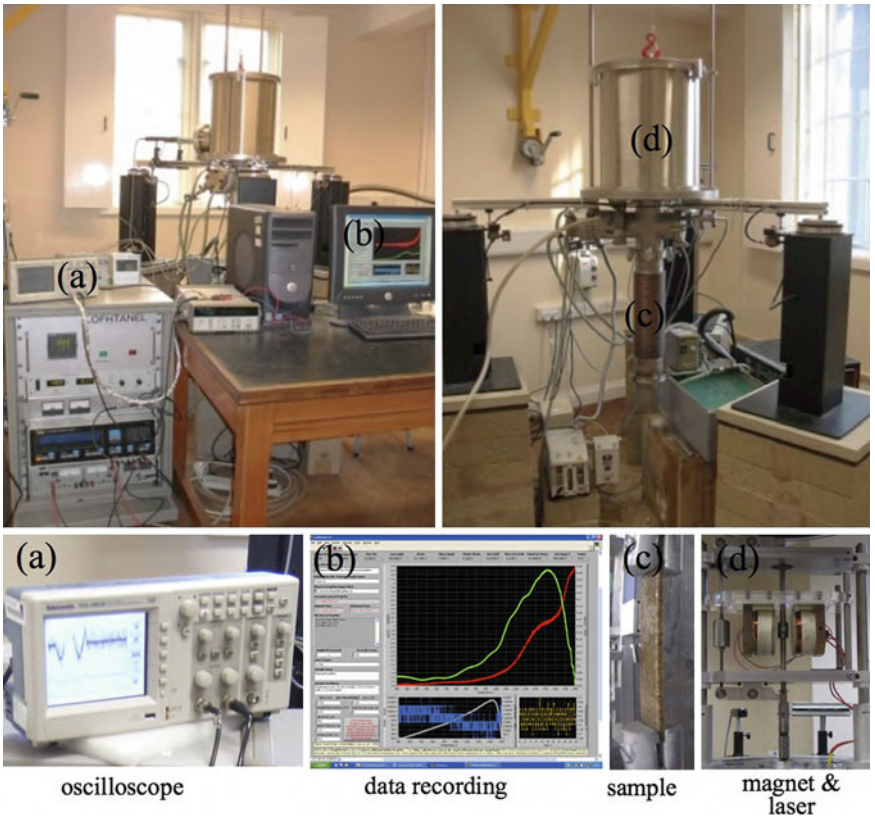

Fig. 2.1 The inverted forced torsion pendulum (*right*) and its electric controls set-up (*left*) used in this work

2.1 Inverted Forced Torsion Pendulum

The inverted forced torsion pendulum operates best at frequencies below 10 Hz (Fig. 2.1). It can be run at higher frequencies but the spectra become complicated by instrumental resonances. The shorter the clamped sample, the higher the resonant frequency of the installation set-up. The $tan\delta$ is measured with a high resolution of 10^{-4} in the inverted forced torsion pendulum, compared to the traditional torsion pendulum which mainly used for materials with high damping ($tan\delta > 0.1$). Strain resolution is of the order of 10^{-7}. The system is operated under low strain of the order of 10^{-4}–10^{-6}. Under these conditions, samples typically display linear mechanical response, as demonstrated by measurement of stress-strain relations for quartz in the DMA used in this study (Fig. 2.2).

The principle of the inverted forced torsion pendulum is sketched in Fig. 2.3. The top end of the rectangular sample is clamped to a rotatable rod that is suspended at

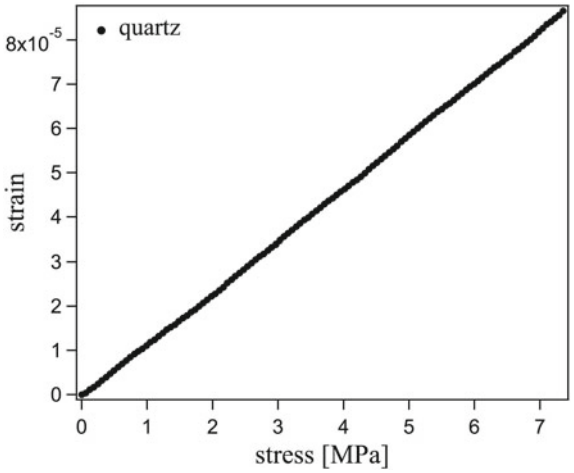

Fig. 2.2 Linear stress-strain relations for quartz in the DMA used in this study

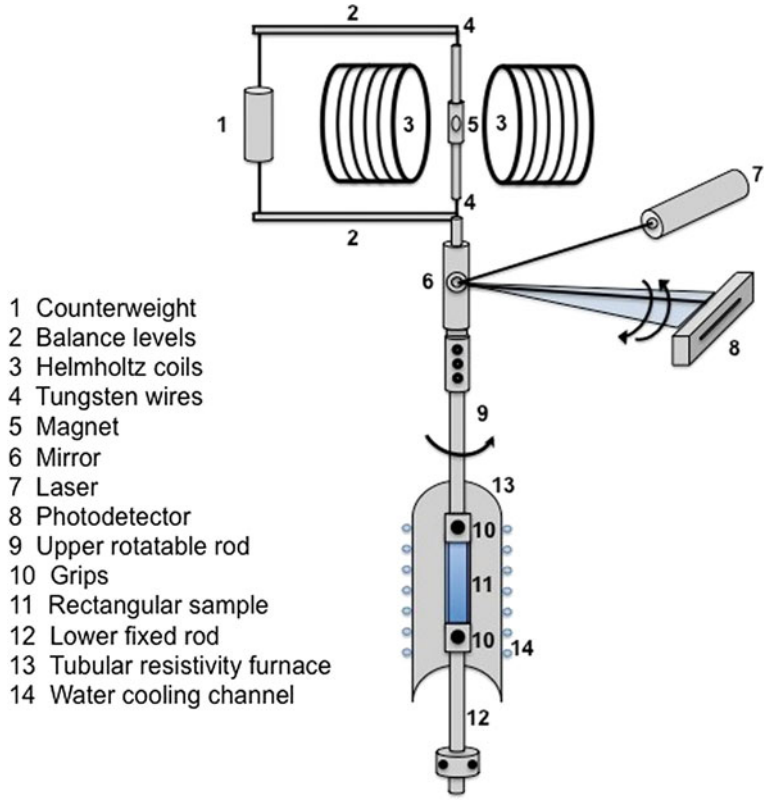

Fig. 2.3 The sketch of the principle of the inverted forced torsion pendulum

its top with thin tungsten wire. The base of the sample is clamped to a fixed rod. Typical sample size is 40 mm in length, 1 mm in thickness and the ideal ratio between width and length is one to five. The tungsten wires are given a required tension by the pairs of balance levels connected with a counterweight. The torsional vibrations of the magnets fixed between the tungsten wires are driven by excited Helmholtz coils. The deflection of the deformed sample is measured by a laser-mirror-detector system. The tubular resistivity furnace surrounds the sample area and a circulated water cooling channel is attached. The rotary and turbo pumps are used to pump out the air in the inverted forced torsion pendulum. The pressure is detected by the sensor on the pressure gouge. For low vacuum environment to 10^{-2} Pa, only the rotary pump is operated. Both rotary and turbo pumps are operated for further high vacuum environment to 10^{-3}–10^{-6} Pa to prevent sample oxidation in the high temperature experiments. The pendulum setup lies on three anti-vibration columns, which contain air beds in the top of the columns (Fig. 2.1 top-right). The air pump is automatically operated to adjust the balance of the pressure in the air beds to avoid the external vibrations from the surrounding environments.

The frequency and amplitude of the AC current supplied to the Helmholtz coils are controlled by the operational power supply. The coils generate a sinusoidally varying magnetic field which rotates the permanent magnet. A four-decade range of frequency is provided from 10^{-3} to 10 Hz in the subresonant mode. The oscillations of the sample due to the torsional rotation are detected through the laser beam reflection on a mirror to give the deflection signals back to the analyser. The Eurotherm PID controller changes the power sent to the furnace to regulate temperature (capable of heating from room temperature to 1600 K) and a thermocouple is used to read the temperature, placed close to the sample. The auto scan of PID was operated initially at 1200 K for calibration at high temperature to obtain the settings for the high-temperature PID: pb(20), ti(51), td(8), res(0.0), HCB(auto), LCB(Auto). Temperature change is found to be stable above 500 K. A two-channel oscilloscope (TDS 210) visualises the signals from the photodetector and frequency analyser to provide the information of loss angle and amplitude as a function of stress and strain. The Lofhtanel software is run in LabView and used to program the electrical control of the installation (as shown in Fig. 2.4) and to visualise the measurements as a function of temperature (isochronal measurements), frequency (isothermal measurements) or time (creep measurements).

The detected strain response (ε) of the sample from deflections is related to the torsion angle (θ), sample thickness (h), sample width (d) and sample length (l) [5] as

$$\varepsilon = \frac{\theta}{l}\frac{\beta_{\mathrm{IFTP}}}{\alpha_{\mathrm{IFTP}}}h \tag{2.1}$$

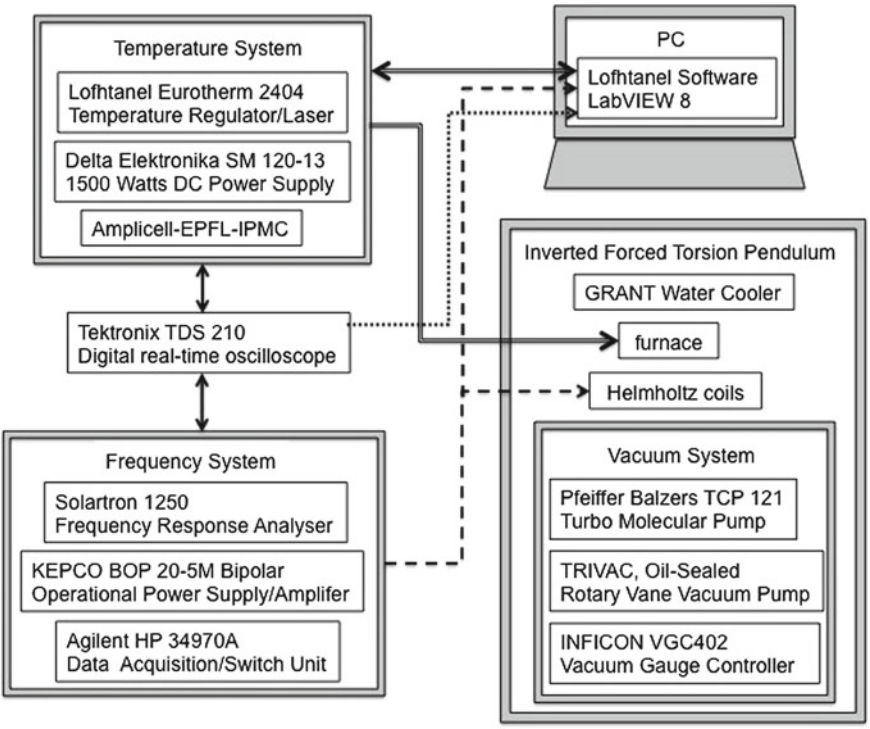

Fig. 2.4 The electric controls scheme of the inverted forced torsion pendulum

where α_{IFTP} and β_{IFTP} are numerical coefficients depending on d/h (Fig. 2.5). Both β_{IFTP} and α_{IFTP} approach 1/3 ($\beta_{\mathrm{IFTP}}/\alpha_{\mathrm{IFTP}} = 1$) when $d/h \to \infty$. The torsion angle is a function of the phase lag (ϕ_θ) as $\theta = \theta_0 e^{-i(\omega t - \phi_\theta)}$ where θ_0 is the pre-factor, ω is the angular frequency of excitation and t is time. The measured phase lag is related to the sample attenuation ($tan\delta$), angular excitation frequency (ω) and angular resonance frequency (ω_r) by

$$tan\phi_\theta = \frac{\omega_r^2}{\omega_r^2 - \omega^2} tan\delta \tag{2.2}$$

The tangent phase lag ($tan\phi_\theta$) can be considered as the loss tangent of the sample ($tan\delta$) when the angular excitation frequency is much smaller than the angular resonance frequency. All data are analysed and presented by Igor. Data errors for absolute measurement (rather than relative changes) arise from error in sample dimension and the external vibration in the surrounding environment.

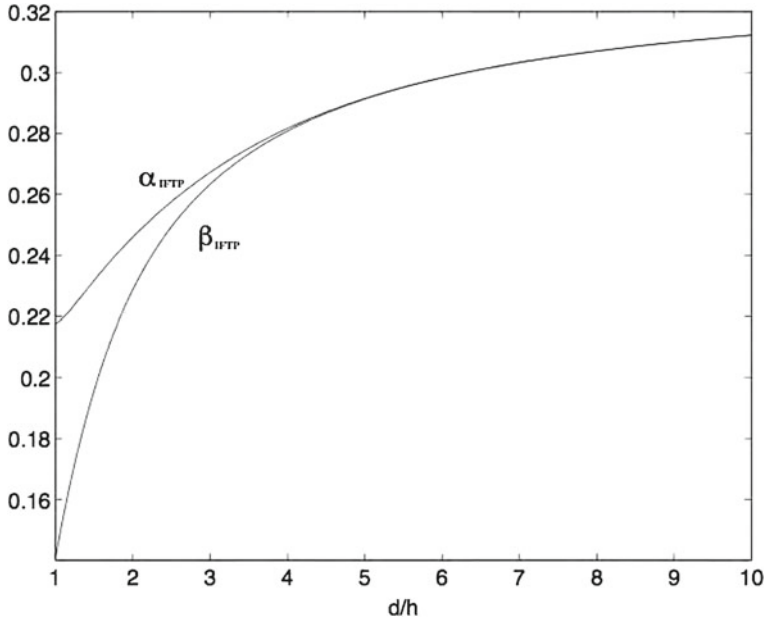

Fig. 2.5 Coefficients α_{IFTP} and β_{IFTP} as a function of d/h for the inverted forced torsion pendulum. From [5]

2.2 Perkin Elmer Dynamic Mechanical Analysis 7e

The three-point bend geometry (as shown in Fig. 2.6) is used in Perkin Elmer Dynamic Mechanical Analysis 7e (see Fig. 2.7) in this study. The height calibration (with a SiO_2 cylinder), eigen deformation calibration and load calibration have been run initially in Dynamic Mechanical Analysis 7e. The $tan\delta$ is measured with a resolution of 10^{-4}. The rectangular sample is placed on the two knife-edges of the bending platform. Typical sample size is 15 mm in length, 1 mm in thickness and 5 mm in width. The force (provided from the attached motor) is transferred to the sample and the deflection of the sample is detected via the probe tip (the central knife edge). The system is operated under low strain of the order of 10^{-4}–10^{-6}. The temperature can be heated to maximum at 350 K and cooled to minimum at 170 K in the furnace, with surrounding liquid nitrogen. A thermocouple is set to be close to the sample. The sample and three knife edges are surrounded by a furnace, which is enclosed in a liquid nitrogen filled container.

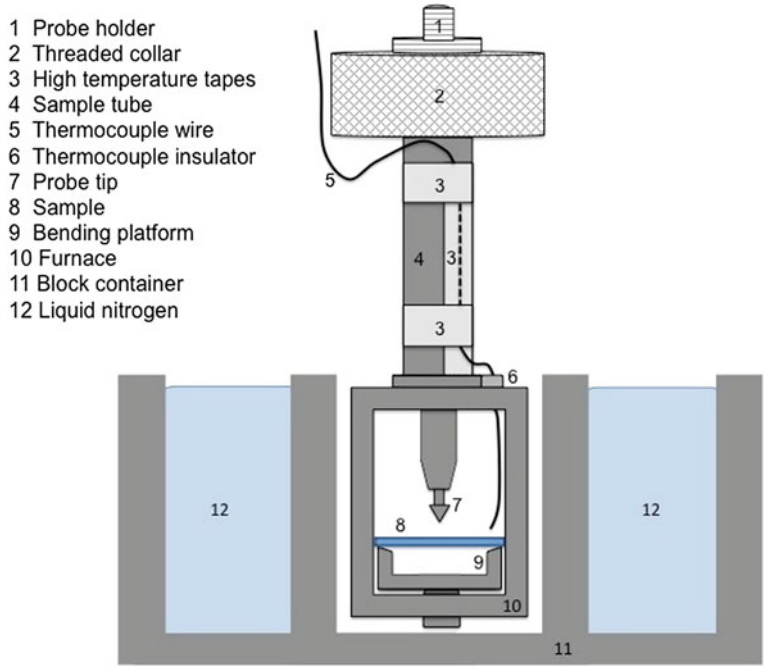

Fig. 2.6 The sketch of three-point bend geometry of the perkin elmer dynamic mechanical analysis 7e (DMA-7e)

The excitation signals are provided on the motor coils to trigger the electromechanical vibration (Fig. 2.8). The applied force has a static component and a dynamic component at frequency in a range of 0.1–50 Hz. The static force is always bigger than the dynamic force in order to keep the sample in contact with the knife-edges at all times. The excited signals for the load and the strain response of the sample are detected by LVDT sensor. The resolution of the deflection of the sample is about 10 nm and the resolution of the phase lag between the applied force and the strain response is about 0.1°. The temperature can be heated up to 350 K by the furnace and cooled down to 100 K by the liquid nitrogen. The accompanying Pyris software is used to program the whole electric control system and also to visualise the measurements as a function of temperature (isochronal) or frequency (isothermal). The mechanical properties measured by DMA and Inverted Forced Torsion Pendulum are effectively isothermal as the experiments correspond to low frequency and reactively long time scales. This is in contrast to data obtained by ultrasonic methods, which provide the adiabatic moduli.

The amplitude of the displacement is affected by both the Young's modulus (E) and shear modulus (G). However, the contribution from the shear modulus is neglected in three-point bend geometry when the length of the sample (l) is much

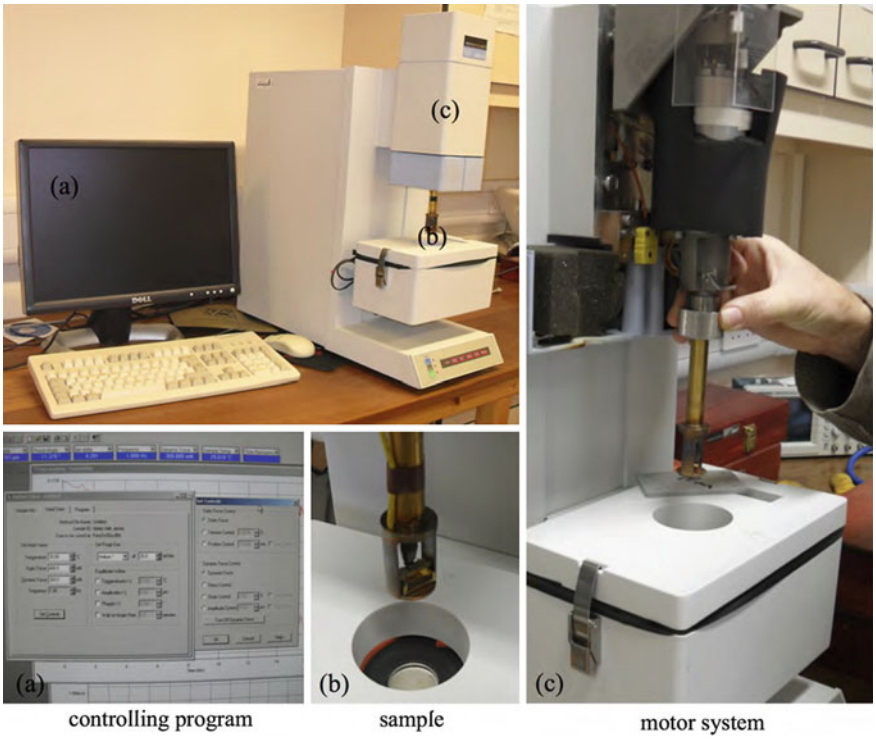

Fig. 2.7 The perkin elmer dynamic mechanical analysis 7e used in this work

bigger than the sample thickness (h) [3]. Under this assumption, the dynamic Young's modulus (along the sample length) is simply related to the dynamic force in the following equation [12]:

$$E = E_1 + iE_2 = \frac{l^3}{4h^3 d}\frac{F_D}{u_D}e^{i\delta} \tag{2.3}$$

where d is the sample width, h is the sample thickness, δ is the phase lag between applied force and strain response, and u_D is the amplitude of deflection due to the dynamic force (F_D). The real ($E_1 = |E|\,cos\delta$) and imaginary ($E_2 = |E|\,sin\delta$) components corresponding to the storage and loss modulus are used to calculate the attenuation by $E_2/E_1 = tan\delta$. All data are analysed and presented by Igor. Data errors may result from error in obtaining sample dimension, hysteresis in motor positioning and external vibrations in the surrounding environment.

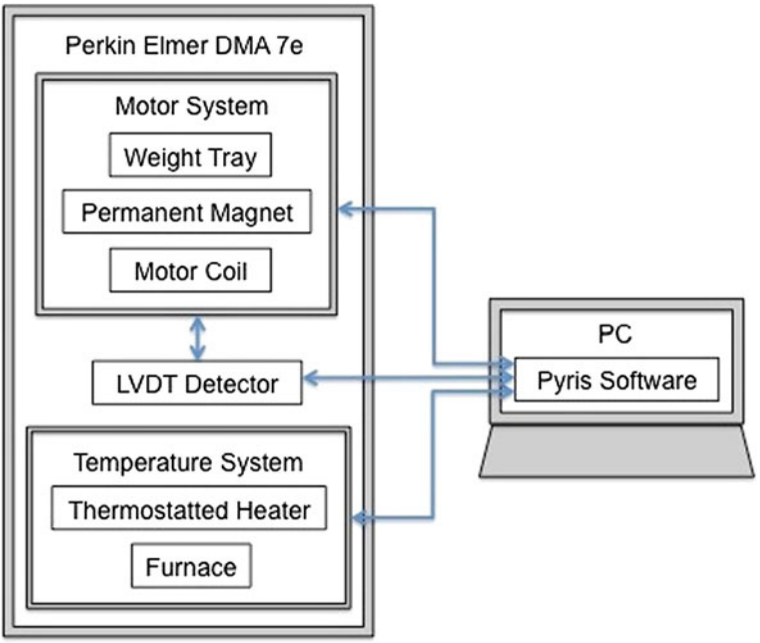

Fig. 2.8 The electronic control scheme of the perkin elmer dynamic mechanical analysis 7e (DMA-7e)

2.3 The 400 MPa Ultrasonic Piezoelectric Oscillator (400 MPa UPO)

The 400 MPa Ultrasonic Piezoelectric Oscillator (see Fig. 2.9) is an installation combined with a 400 MPa hydrostatic pressure vessel with a servo hydraulic pressure intensifier enhanced pressurisation system with up to 200 MPa pore fluid pressure. The measurements were conducted in the Mineral Physics Laboratory at National Cheng-Kung University in Taiwan, where the apparatus is developed from the similar device installed in the Rock and Ice Physics Laboratory (RIPL) at University College London (UCL) [10]. A sketch of the 400 MPa pressure vessel is given in Fig. 2.10. The cylindrical sample is held by a pair of steel buffer rods between two piezoelectric transducers. Typical sample size is 25 mm in length and 24 mm in diameter. The sample and buffer rods are enclosed by a rubber tube, which is in turn enclosed by a second rubber tube also covering part of the transducers. The buffer and transducer rods are drilled with a water channel, one end of which is connected to a hand pump and the other end can be made open to the air by use of a control valve. The whole assembly is placed in the 400 MPa hydrostatic pressure vessel,

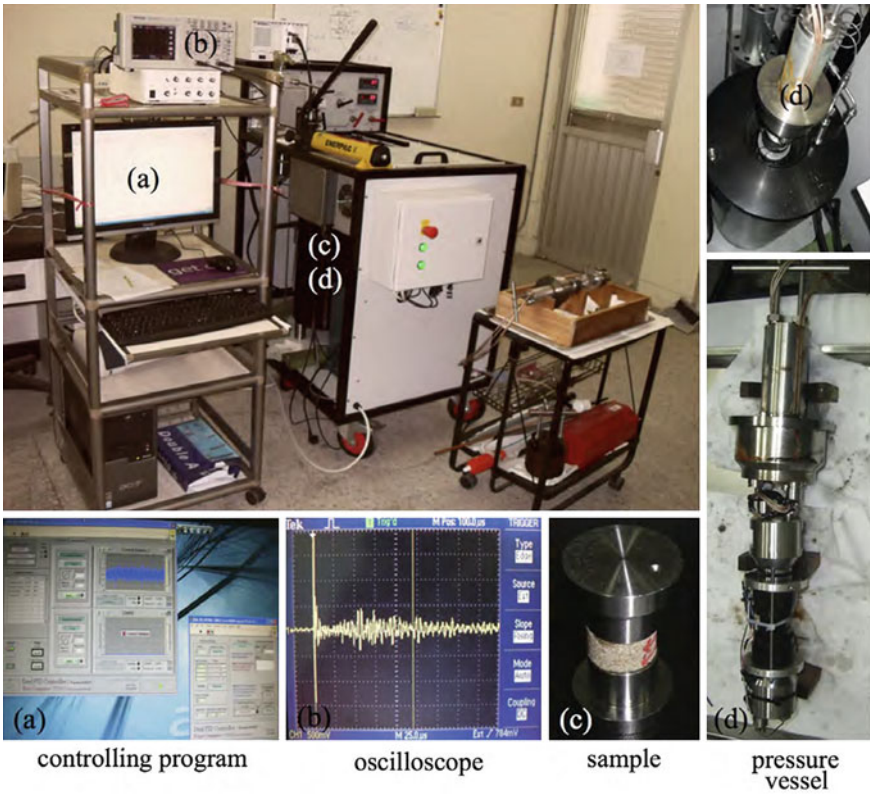

Fig. 2.9 The 400 MPa ultrasonic piezoelectric oscillator (400 MPa UPO) used in this work

which is filled with silicone oil. The pressure vessel is connected to a hand oil pump for experiments requiring low confining pressure and to a 400 MPa servo controlled pressure intensifier for the high confining pressure experiments.

MHz ultrasonic compressional and shear wave pulse signals are generated via a DPR300 Pulser/Receiver and sent to the transmitter (the upper transducer). The waves propagate through the sample and are detected by the receiver (the bottom transducer). The DPR300 Pulser/Receiver also receives these propagating signals. The electronic control scheme is shown in Fig. 2.11. The water pressure (pore fluid pressure) is manually pumped and is read via a pressure transducer. The oil pressure (confining pressure) can be manually pumped below 150 MPa or be increased up to 400 MPa by the servo controlled pressure intensifier via the Dual PID controller and is read via a pressure transducer. A two-channel oscilloscope (TDS 2022) is used to visualise and record the generated pulse signals and the received compressional and shear waves as a function of time, with a resolution of 10^{-9} s. The velocities of the compressional (V_P) and shear waves (V_S) are calculated from the observed time-of-flight (t_P and t_S) and the measured sample length (l) by $V_P = l/t_P$ and

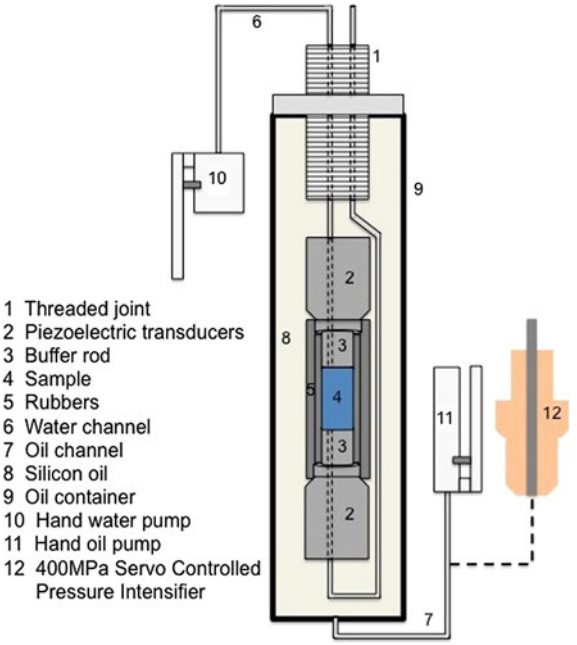

Fig. 2.10 A sketch of the 400 MPa hydrostatic pressure vessel in the 400 MPa Ultrasonic Piezoelectric Oscillator system

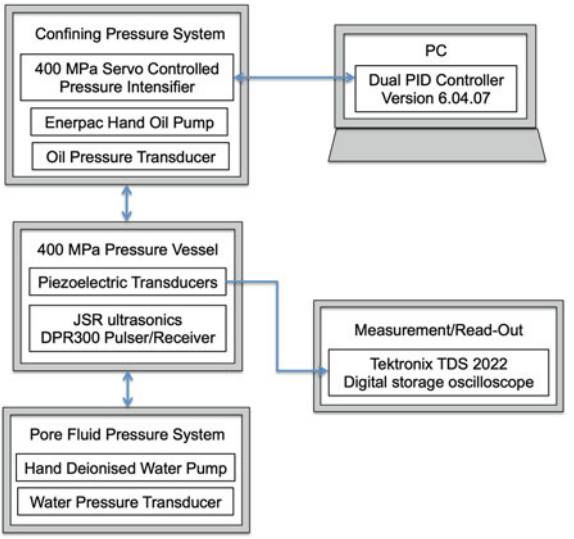

Fig. 2.11 The electric control scheme of 400 MPa ultrasonic piezoelectric oscillator

$V_S = l/t_S$ in the different confining pressures and different pore fluid pressures. All data are analysed and presented by Igor. Data error are mainly due to errors in the sample dimension measurements.

References

1. Lakes, R. S. (2004). Viscoelastic measurement techniques. *Review of Scientific Instruments*, *75*(4), 797–810.
2. Schaller, R., Fantozzi, G., & Gremaud, G. (2001). *Mechanical spectroscopy* Q^{-1}: With applications to materials scienceaterials science. Material science forum (pp. 8, 15, 16, 22). Switzerland: Trans Tech Publications Ltd.
3. Kityk, A. V., Schranz, W., Sondergeld, P., Havlik, D., Salje, E. K. H., & Scott, J. F. (2000). Low-frequency superelasticity and nonlinear elastic behavior of srtio3 crystals. *Physical Review B*, *61*(2), 946–956.
4. Kê, T.-S. (1947a). Experimental evidence of the viscous behavior of grain boundaries in metals. *Physical Review*, *71*(8), 533–546.
5. Fikar, J. (2002). Al-Cu-Fe quasicrystalline coatings and composites studied by mechanical spectroscopy. PhD thesis, Lausanne.
6. D'Anna, G., & Benoit, W. (1990). Apparatus for dynamic and static measurements of mechanical properties of solids and of flux-lattice in type-ii superconductors at low frequency (10^{-5}-10 hz) and temperature (4.7-500 k). *Review of Scientific Instruments*, *61*(12), 3821–3826.
7. Gadaud, P., Guisolan, B., Kulik, A., & Schaller, R. (1990). Apparatus for high-temperature internal friction differential measurements. *Review of Scientific Instruments*, *61*(10), 2671–2675.
8. Marx, J. (1951). Use of the piezoelectric gauge for internal friction measurements. *Review of Scientific Instruments*, *22*(7), 503–509.
9. McKnight, R. E. A., Carpenter, M. A., Darling, T. W., Buckley, A., & Taylor, P. A. (2007). Acoustic dissipation associated with phase transitions in lawsonite, caal2si2o7(oh)2h2o. *American Mineralogist*, *92*(10), 1665–1672.
10. Kolzenburg, S., Heap, M. J., Lavallée, Y., Russell, J. K., Meredith, P. G., & Dingwell, D. B. (2012). Strength and permeability recovery of tuffisite-bearing andesite. *Solid Earth*, *3*(2), 191–198.
11. Li, B., Jackson, I., Gasparik, T., & Liebermann, R. C. (1996). Elastic wave velocity measurement in multi-anvil apparatus to 10 gpa using ultrasonic interferometry. *Physics of the Earth and Planetary Interiors*, *98*(1–2), 79–91.
12. Harrison, R. J., & Redfern, S. A. T. (2002). The influence of transformation twins on the seismic-frequency elastic and anelastic properties of perovskite: dynamical mechanical analysis of single crystal laalo3. *Physics of the Earth and Planetary Interiors*, *134*(3–4), 253–272.

Chapter 3
Sample Characteristics

3.1 Sandstones

Two sandstones have been selected in this study as candidates for pore-fluid-solid experiments and also as analogues for partially-molten rocks: a Darley Dale sandstone from England and a New Red Sandstone from Scotland. Both sandstones were characterised by D8 X-ray powder diffractometer (Fig. 3.1), transmitted light microscopy and scanning electron microscopy (SEM) (Fig. 3.2). Two sandstones were cut into rectangular bars with one-tenth of the samples placed perpendicularly in deionised water for 3 h to assess the relative permeability of the samples. The Darley Dale sandstone was found to be less permeable than New Red Sandstone, as shown in Fig. 3.3. The sandstones for ultrasonic experiments (400 MPa UPO) were cut into cylinders (Fig. 3.4) and samples for DMA experiments are cut into rectangular bars (Fig. 3.5).

Darley Dale sandstone (Fig. 3.2a–c) was collected from Darley Dale, Derbyshire, England, UK. It is a yellow–brown Carboniferous felspathic sandstone with siliceous cement, which has historically been used as a building stone, and therefore has been the subject of much study in the past. For example, Darley Dale sandstone was used to make ashlar blocks to build Leigh Town Hall in Greater Manchester in England. The composition of Darley Dale sandstone is 69 % quartz, 22–26 % feldspar (mainly plagioclase), 3 % mica, and about 6–2 % clay and a few opaque grains. The density of Darley Dale sandstone is on average 2.3 kg/cm^3 with porosity of 13–14 % [1, 2]. Darly Dale sandstone is poorly sorted with grain sizes in the range of 0.04–1 mm, with a mean grain diameter of 0.34 mm. The outlines of the grains are angular to sub-angular and they are irregularly orientated. The pores are also irregularly shaped. Observations of thin sections indicate Darley Dale sandstone has more isolated pores than interconnected pores.

The New Red Sandstone (Fig. 3.2d–f) was collected from the Corrie shore section of the Isle of Arran, Ayrshire, Scotland, UK. It is a Permian aeolian sandstone, with a composition of 79 % quartz and 5 % K-feldspar, 11 % clay, 1 % chlorite/illite and 4 % opaque grains. The grain size varies in the range 0.1–0.3 mm. The New Red

S.-Y. Chien, *Rheological and Seismic Properties of Solid-Melt Systems*,
Springer Theses, DOI: 10.1007/978-3-319-03098-2_3,

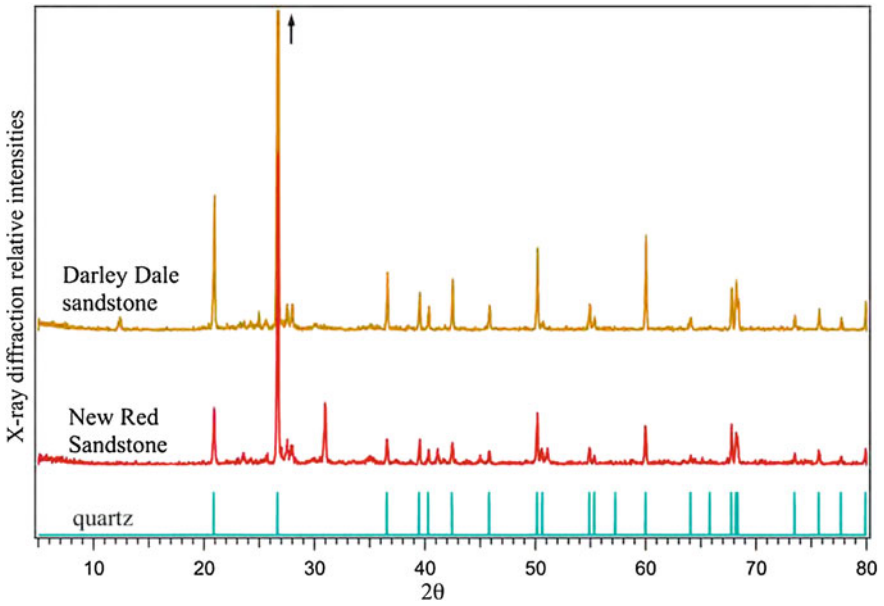

Fig. 3.1 X-ray powder diffraction of two sandstones in this study and the X-ray patterns of quartz as a reference pattern

Sandstones are red because of the presence of Fe-oxides on grain surfaces. The density is approximately 2.2 kg/cm^3 and the porosity is approximately 17 % [3]. Grains are rounded, and cemented by carbonates. The water permeability and rigidity of New Red Sandstones are higher than Darley Dale sandstones, which is consistent with the observation of more interconnected pores in New Red Sandstone than in Darley Dale sandstone.

3.2 Igneous Rocks

Two basalts (Iceland basalt and basalt I13_83493) and one Skaergaard gabbro (Fig. 3.6) were used to carry out studies at high temperature approaching melting. The Fe–Ti oxides of three igneous rocks were magnetically separated and analysed by D8 X-ray diffraction measurements. The X-ray diffraction results show that most of Fe–Ti oxides are the spinel structure minerals (Fig. 3.7). The microstructures and mineral phases of the three igneous rocks were then characterised by transmitted light microscopy and SEM and chemically probed by Cameca SX-100 electron microprobe (Figs. 3.8, 3.9 and 3.10).

Basalt I13_83493 was obtained from the Cambridge University petrological collection. Its origin is unknown. This melanocratic basalt I13_83493 is a hypocrystalline

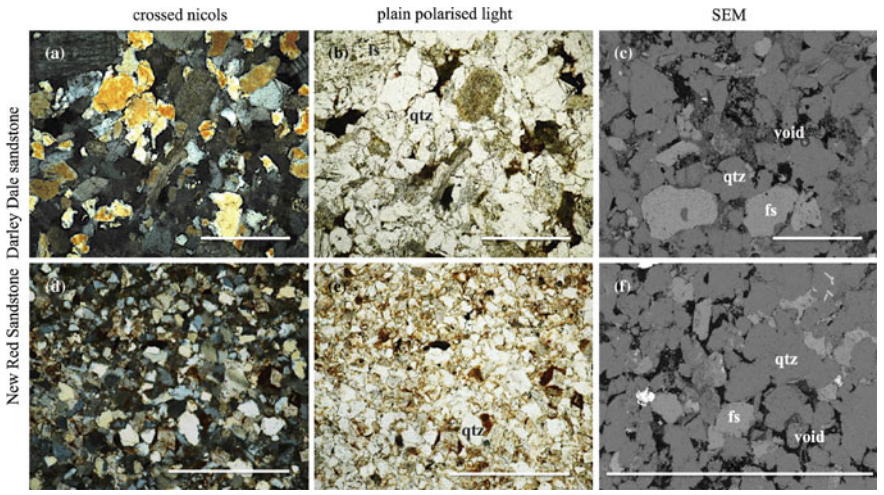

Fig. 3.2 Microstructures of Darley Dale sandstone (*top row*) and New Red Sandstones (*bottom row*) are shown in crossed nicols (**a** and **d**), in plain polarised light (**b** and **e**), and scanning electron microscopy (SEM) images (**c** and **f**). The images of crossed nicols and plain polarised light are taken at the same location and the *yellow colour* of quartz is due to the thickness of the thin section. The *grey* levels in SEM images correspond to different mineral phases and *black areas* are voids (pores). The scale bar is 1 mm in all images. (*qtz* quartz, *fs*feldspar)

Fig. 3.3 Permeability experiments of Darley Dale sandstone and New Red sandstone

igneous rock that exhibits a glomeroporphyritic texture (Fig. 3.8). The thin section observations give an approximately estimation of 2 vol.% phenocrysts (0.4 % olivine and 1.6 % plagioclase) and 98 % fine–grained groundmass. The groundmass contains evenly distributed 55 % olivine + pyroxene, 36 % plagioclase feldspar and 9 % opaques. The chemical compositions, determined by microprobe, for the mineral phases are shown in Table 3.1. A subhedral olivine phenocryst (Fo58) has a diameter of 0.84 mm and the average length of the euhedral plagioclases (Ab22) laths is 0.6 mm, of which the longest is 2.2 mm. The euhedral to subhedral groundmass olivines (Fo44) and pyroxenes (augite, Di78) have similar diameters of 0.2 mm

Fig. 3.4 Darley Dale sandstone and New Red sandstone, cut into cylinders for ultrasonic velocity measurements

Fig. 3.5 Darley Dale sandstones, prepared with crystalbond 509, for DMA experiments

and groundmass plagioclases (Ab36) are 0.2–0.4 mm in length. The opaque phases from optical observation are Fe–Ti oxides, with more ilmenite than magnetite. Small amounts of glass (Di72) are also found, with an augite composition.

The other mesocratic basalt was collected from the Theistareykir segment of the Northern Volcanic Zone in Iceland and provided by John Maclennan. It is from the massive interior of a plagioclase phenocryst bearing basalt flow from the Storaviti lava shield [4]. This flow was erupted between 10,300 and 8,000 years ago. Thin sections and back scattering images of this "Iceland basalt" are shown in Fig. 3.9. The Iceland basalt is a hypocrystalline igneous rock that has a porphyritic texture. The 12 % volume of plagioclase phenocrysts (up to 1.5 mm in length) are situated in a fined-grained groundmass. The composition of the groundmass is composed of roughly 54 % plagioclase feldspar, 42 % olivine + pyroxene and 4 % opaque grains. The chemical composition determined by microprobe for the mineral phases are showing in Table 3.2. The anhedral phenocrysts of plagioclase feldspars (Ab18) have a maximum length up to 2 mm and some glass (Di54) was found inside the plagioclase phenocrysts. Euhedral to subhedral groundmass olivines (Fo70) and pyroxenes (Di77) are 0.1–0.3 mm in diameter. The groundmass plagioclase feldspars (Ab35)

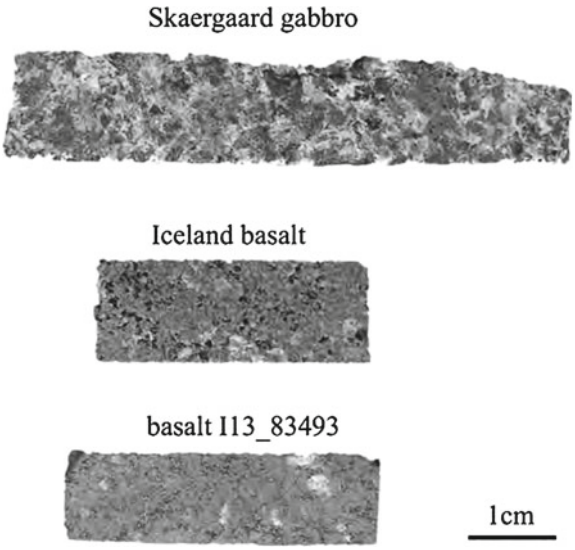

Fig. 3.6 *Rectangular-shaped* igneous rocks, prepared for torsion pendulum experiments

Table 3.1 The chemical compositions[a] for olivine [Fo*xx*], clinopyroxene [Di*xx*$^{(c)}$], feldspar [Ab*xx*] and glass [Di*xx*$^{(g)}$] in basalt I13_83493

Basalt I13__83493 'as received'	
Phenocrysts	
Fo58	$(Mg_{1.17(19)}Fe_{0.83(19)})Si_{0.99(1)}O_4$
Ab22	$(Na_{0.20(7)}Ca_{0.81(8)}Fe_{0.02(0)})(Si_{2.20(8)}Al_{1.76(8)})O_8$
Groundmass	
Fo44	$(Mg_{0.88(17)}Fe_{1.12(17)})Si_{0.98(1)}O_4$
Di78$^{(c)}$	$(Ca_{0.77(4)}Na_{0.02(0)}Mg_{0.90(7)}Fe_{0.27(5)}Ti_{0.02(1)})(Si_{1.90(3)}Al_{0.12(4)})O_6$
Ab36	$(Na_{0.34(8)}Ca_{0.67(8)}Fe_{0.03(0)})(Si_{2.34(8)}Al_{1.61(8)})O_8$
Glass	
Di72$^{(g)}$	$(Ca_{0.71(11)}Na_{0.02(0)})(Mg_{0.84(5)}Fe_{0.39(11)}Ti_{0.03(1)})(Si_{1.92(3)}Al_{0.09(4)})O_6$

Selected raw data are provided in Appendix A

[a] Chemical compositions are averaged from 7 points for phenocryst olivine, 13 points for phenocryst feldspar, 14 points for groundmass olivine, 10 points for groundmass pyroxene, 9 points for groundmass feldspar and 11 points for glass

have length less than 0.5 mm. The opaque phases in optical observations are Fe–Ti oxides that are mostly magnetite with minor ilmenite.

The leucocratic gabbro comes from the 'Lower Zone a' in the lower part of Layered Series in the Skaergaard Intrusion, which was intruded near eastern Greenland during an intense magmatic episode associated with the opening of the North Atlantic about 55–53 Million years ago [5]. The 'Lower Zone a' is the lowest one of three sub-zones in the Lower Zone that are characterised by a poikilitic texture of calcium-rich pyroxene. The composition of rocks in the 'Lower Zone a' is

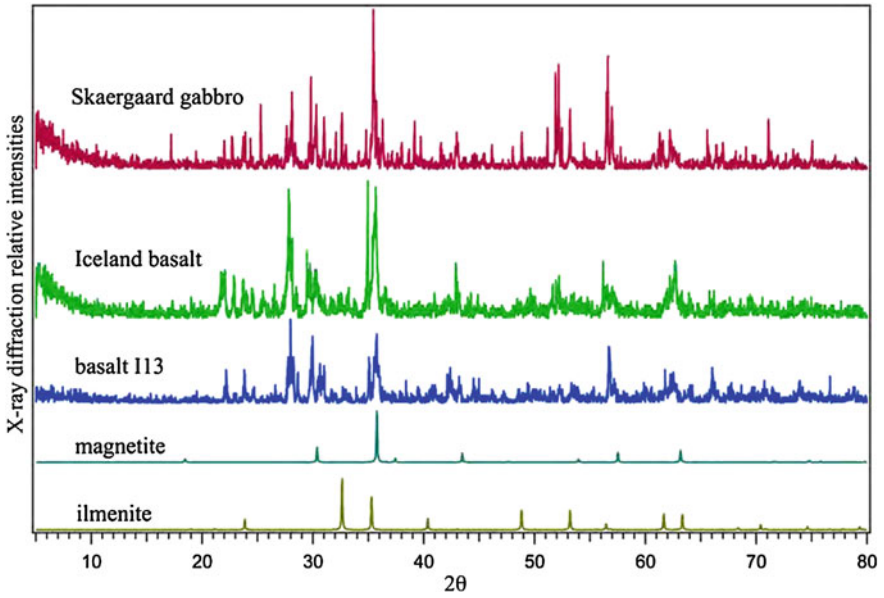

Fig. 3.7 X-ray powder diffractions of the Fe–Ti oxides in concentrates of the three igneous rocks. X-ray patterns of both magnetite and ilmenite are shown as reference patterns

Table 3.2 The chemical compositions[a] for olivine [Fo*xx*], clinopyroxene [Di*xx*$^{(c)}$], feldspar [Ab*xx*] and glass [Di*xx*$^{(g)}$] in Iceland basalt

Iceland basalt 'as received'	
Phenocrysts	
Ab18	$(Na_{0.13(3)}Ca_{0.86(3)}Mg_{0.02(0)}Fe_{0.02(0)})(Si_{2.16(3)}Al_{1.81(3)})O_8$
Groundmass	
Fo70	$(Mg_{1.38(26)}Fe_{0.59(26)})Si_{1.00(1)}O_4$
Di77$^{(c)}$	$(Ca_{0.75(9)}Mg_{0.87(19)}Fe_{0.31(27)}Ti_{0.02(1)})(Si_{1.93(2)}Al_{0.10(5)})O_6$
Ab35	$(Na_{0.28(11)}Ca_{0.70(12)}Mg_{0.04(8)}Fe_{0.05(7)})(Si_{2.32(13)}Al_{1.62(19)})O_8$
Glass	
Di54$^{(g)}$	$(Ca_{0.50}Na_{0.04}Mg_{0.81}Fe_{0.50}Ti_{0.04}Al_{0.09})(Si_{1.87}Al_{0.13})O_6$

Selected raw data are provided in Appendix A

[a] Chemical compositions are averaged from 18 points for phenocryst feldspar, 17 points for groundmass olivine, 17 points for groundmass pyroxene, 7 points for groundmass feldspar and 1 point for glass

roughly 48 wt% SiO_2 and 15–16 wt% total FeO (including 2 wt% ilmenite and 1 wt% magnetite) [6]. Olivine (1–2 mm) and plagioclase feldspars form large granular crystals with abundant interstitial augite and inverted pigeonite (Ca-poor pyroxene). The inverted pigeonite is a replacement product encasing corroded cores of augite and olivine. Small amounts of zoned plagioclase, biotite and apatite are observed as well. Some olivines and plagioclase feldspars are surrounded by poikilitic pyroxene in the

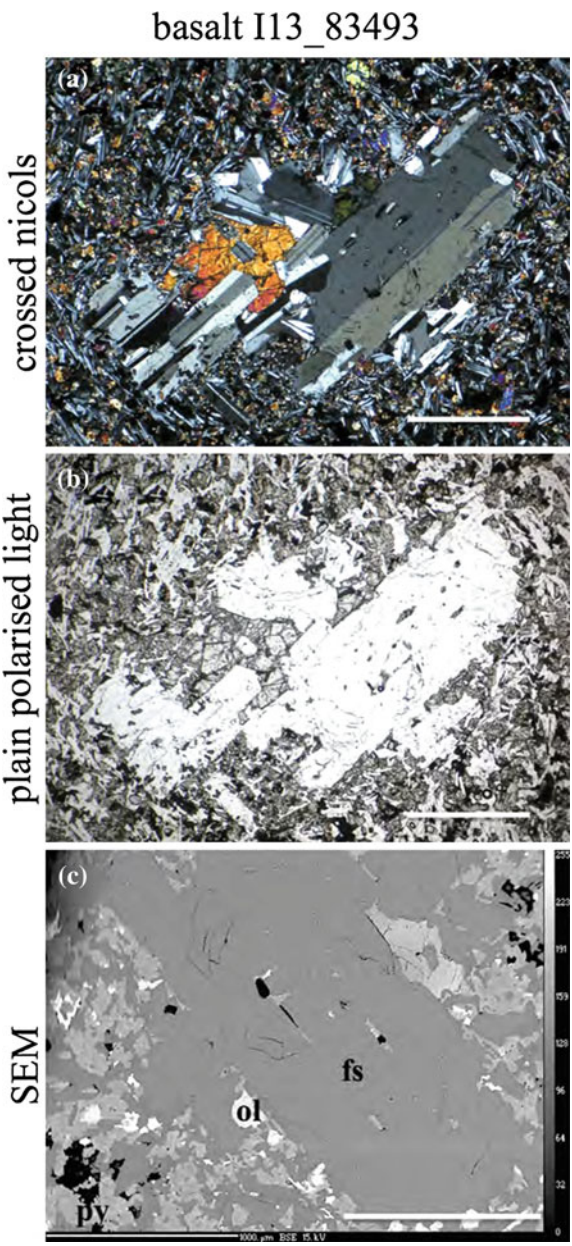

Fig. 3.8 Microstructures of basalt I13_83493 in **a** crossed nicols, **b** plain polarised light and **c** scanning electron microscopy (SEM). The images of crossed nicols and plain polarised light are taken at the same location. The *grey* levels in SEM image correspond to different mineral phases and *black areas* are voids (pores). The scale bar is 1 mm in all images. (*ol* olivine, *py* pyroxene, *fs* feldspar)

thin sections of the sample (Fig. 3.10). A symplectic intergrowth of Fe–Ti oxides (Fig. 3.11) occurs at the edges of olivines. The chemical composition determined by

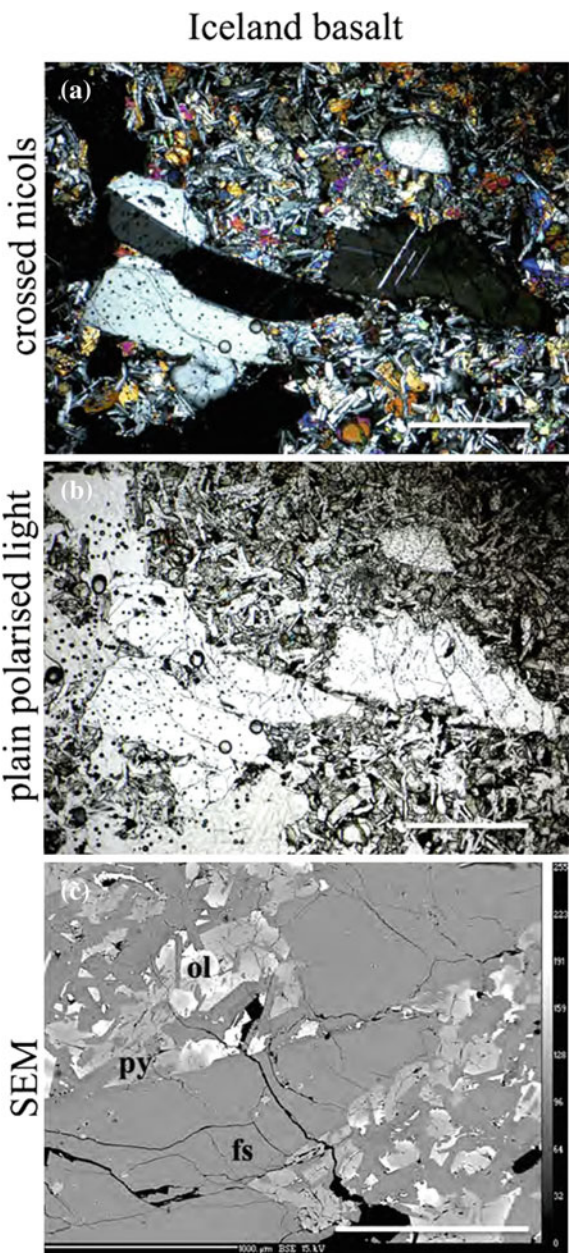

Fig. 3.9 Microstructures of Iceland basalt in **a** crossed nicols, **b** plain polarised light and **c** scanning electron microscopy (SEM). The images of crossed nicols and plain polarised light are taken at the same location. The *grey* levels in SEM image correspond to different mineral phases and *black areas* are voids (pores). The scale bar is 1 mm in all images. (*ol* olivine, *py* pyroxene, *fs* feldspar)

microprobe for olivines (Fo61), clinopyroxenes (Di84), orthopyroxenes (Di5) and plagioclase feldspars (Ab39) are shown in Table 3.3.

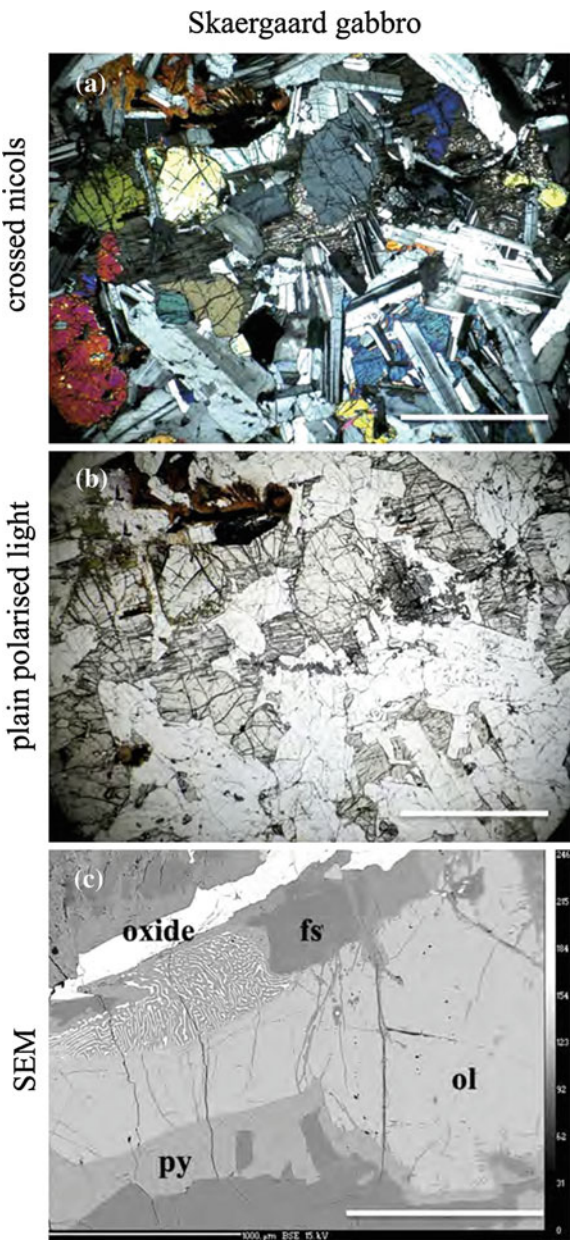

Fig. 3.10 Microstructures of Skaergaard gabbro in **a** crossed nicols, **b** plain polarised light and **c** scanning electron microscopy (SEM). The images of crossed nicols and plain polarised light are taken at the same location. The *grey* levels in SEM image correspond to different mineral phases and *black areas* are voids (pores). The scale bar is 1 mm in all images. (*ol* olivine, *py* pyroxene, *fs* feldspar)

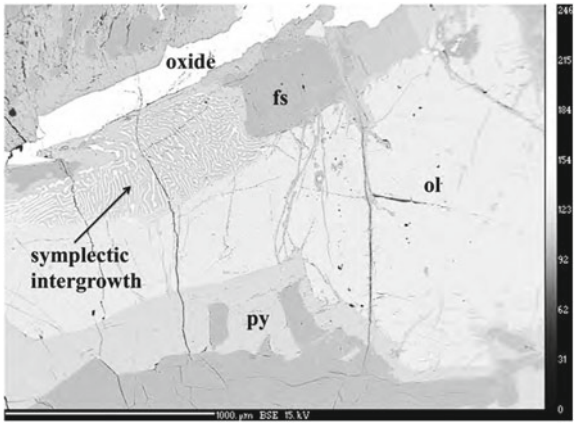

Fig. 3.11 The enlarged SEM image from Fig. 3.10c shown the symplectic structure of Fe–Ti oxides. The *grey* levels in SEM images correspond to different mineral phases and *black areas* are voids (pores). The scale bar is 1 mm. (*ol* olivine, *py* pyroxene, *fs* feldspar)

3.3 Heat-Treated Igneous Rocks

Two Skaergaard gabbros were heated separately to 900, 1,250 K and one was repeatedly heated to, and cooled from 1,400 K twice, under high vacuum (10^{-3} Pa) in the inverted forced torsion pendulum. The microstructures of the three heat-treated gabbros were characterised by transmitted light microscopy and SEM, and were probed by Cameca SX-100 electron microprobe. Two other gabbros (sample 'as received' and the sample heated repeatedly to 1,400 K seven times in the shear stress experiment by inverted torsion pendulum) were also characterised and are shown in Fig. 3.12. The groundmass pyroxenes were seen to grow gradually with temperature and with pyroxene predominantly developed at 1,400 K in the shear stress experiment. In the meanwhile, the olivines and plagioclase feldspars change from irregular shapes to more and more rounded shapes and also become relatively smaller, surrounded by the growing groundmass pyroxene.

The chemical composition determined by microprobe for the mineral phases in gabbro 'as received', heat-treated and stress-treated gabbros are shown in Table 3.4. The Mg-content increases as the Fe-content decreases in the olivines with increasing

Table 3.3 The chemical compositions[a] for olivine [Fo*xx*], clinopyroxene [Di*xx*$^{(c)}$], orthopyroxene [Di*xx*$^{(o)}$], and feldspar [Ab*xx*] in Skaergaard gabbro

Skaergaard gabbro 'as received'	
Fo61	$(Mg_{1.22(1)}Fe_{0.78(1)})Si_{0.99(0)}O_4$
Di84$^{(c)}$	$(Ca_{0.82(4)}Na_{0.02(1)}Mg_{0.82(3)}Fe_{0.28(1)}Ti_{0.03(0)})(Si_{1.93(1)}Al_{0.10(0)})O_6$
Di5$^{(o)}$	$(Ca_{0.06(2)}Mg_{1.29(2)}Fe_{0.64(2)})(Si_{1.95(1)}Al_{0.04(1)})O_6$
Ab39	$(Na_{0.36(7)}Ca_{0.62(7)})(Si_{2.38(7)}Al_{1.60(7)}Fe_{0.02(1)})O_8$

Selected raw data are provided in Appendix B

[a] Chemical compositions are averaged from 10 points for olivine, 2 points for clinopyroxene, 6 points for orthopyroxene and 9 points for feldspar

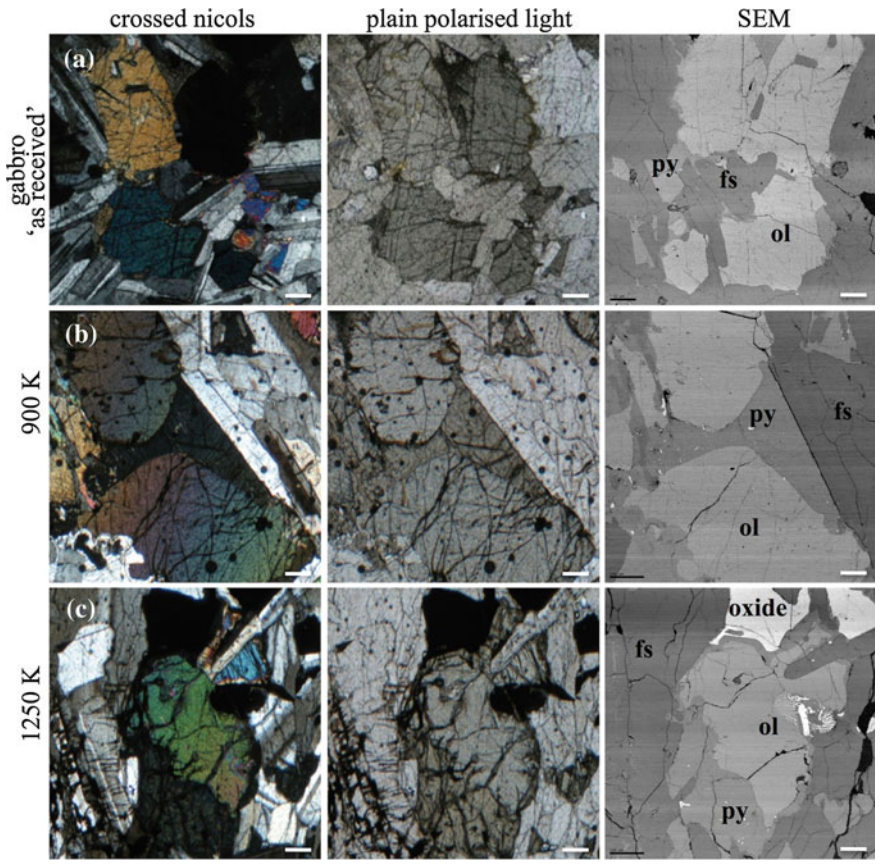

Fig. 3.12 Pyroxene growth (*dark-brownish* in the crossed nicols) in the Skaergaard gabbro under different heating histories are shown in crossed nicols, plain polarised light, and scanning electron microscopy (SEM) images. **a** sample 'as received', **b** sample annealed at 900 K, and **c** sample annealed at 1,250 K. The images under crossed nicols and plain polarised light are taken at the same location. The *grey* levels in SEM images correspond to different mineral phases and *black areas* are voids. The scale bar is 200 μm in all images. (*ol* olivine, *py* pyroxene, *fs* feldspar). Pyroxene growth (*yellowish* in the crossed nicols) in the Skaergaard gabbro under different heating histories are shown in crossed nicols, plain polarised light, and SEM images. **d** sample annealed twice at 1400 K and **e** sample heated repeatedly at 1400 K for seven times under shear stress. The images under crossed nicols and plain polarised light are taken at the same location. The *grey* levels in SEM images correspond to different mineral phases and *black areas* are voids. The scale bar is 200 μm in all images. (*ol* olivine, *py* pyroxene, *fs* feldspar)

temperature. The chemical composition of the plagioclase feldspars is stable for different heat-treated samples, although feldspars in the gabbro heated at 900 K show higher sodium and silicon content.The iron content is lower in orthopyroxene while it is higher in clinopyroxene from the sample heated to 1,400 K compared to the gabbro 'as received', but the variation is not as great as the changes of Mg and Fe

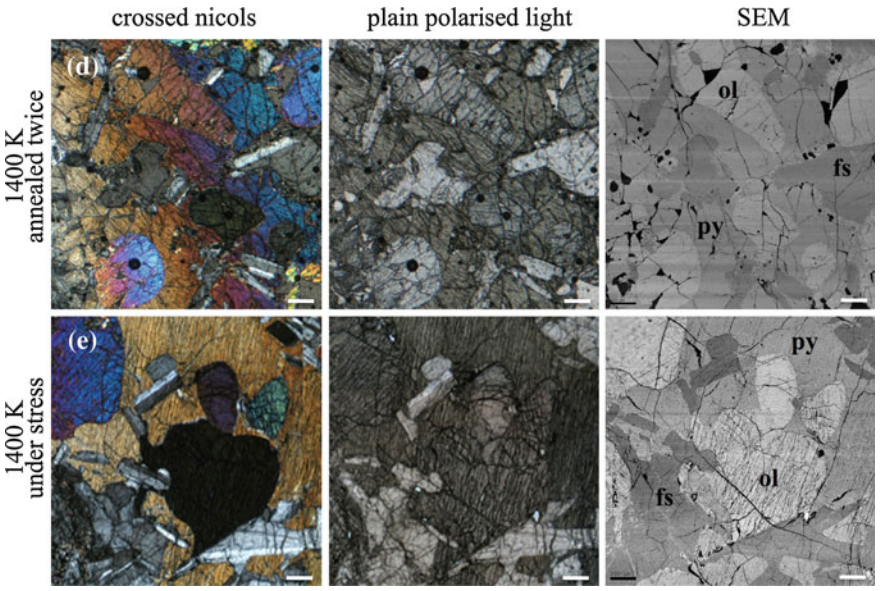

Fig. 3.12 (Continued)

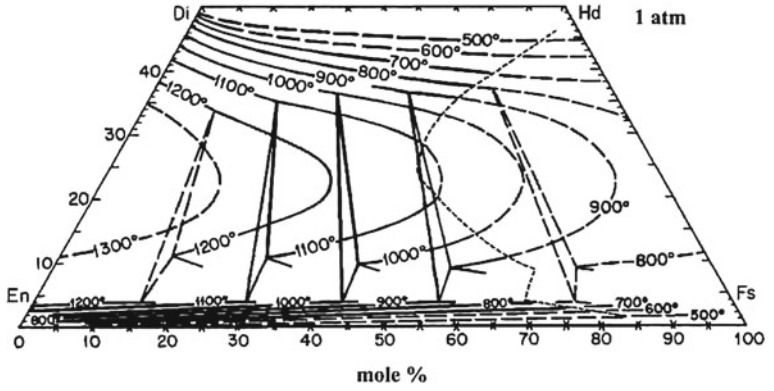

Fig. 3.13 Pyroxene relations, contoured at 100 °C, in the En-Di-Hd-Fs quadrilateral at low pressure. *Di* diopside ($CaMgSi_2O_6$), *Hd* hedenbergite ($CaFeSi_2O_6$), *En* enstatite ($Mg_2Si_2O_6$), *Fs* ferrosilite($Fe_2Si_2O_6$). After [7]

in olivine. The calcium content in clinopyroxene is lower while that in orthopyroxene tends to become higher at 1,400 K in the heat-treated samples than in the gabbro 'as received'. This result is in good agreement with Lindsley et al.'s study on the phase relations in pyroxene [7], as shown in Fig. 3.13. The Ca content decreases in high-Ca pyroxenes (augite) with increasing temperature while that in low-Ca pyroxenes (orthopyroxene or pigeonite) increases. No orthopyroxene was found in the thin section of the gabbro in the high-temperature shear stress experiment, implying that

Table 3.4 The chemical compositions[a] for olivine [Fo*xx*], clinopyroxene [Di*xx*$^{(c)}$], orthopyroxene [Di*xx*$^{(o)}$], and feldspar [Ab*xx*] in gabbros (sample 'as received' [I], at 900 K [II], at 1,250 K [III], annealed twice at 1,400 K [IV] and heated repeatedly up to 1,400 K for seven times under the stress [V])

Olivine		
I	Fo61	$(Mg_{1.22(1)}Fe_{0.78(1)})Si_{0.99(0)}O_4$
II	Fo60	$(Mg_{1.21(1)}Fe_{0.78(1)})Si_{1.00(0)}O_4$
III	Fo61	$(Mg_{1.23(0)}Fe_{0.77(1)})Si_{0.99(0)}O_4$
IV	Fo62	$(Mg_{1.24(1)}Fe_{0.76(2)})Si_{0.99(0)}O_4$
V	Fo64	$(Mg_{1.28(4)}Fe_{0.70(4)})Si_{1.00(0)}O_4$
Clinopyroxene		
I	Di84$^{(c)}$	$(Ca_{0.82(4)}Na_{0.02(1)}Mg_{0.82(3)}Fe_{0.28(1)}Ti_{0.03(0)})(Si_{1.93(1)}Al_{0.10(0)})O_6$
II	Di78$^{(c)}$	$(Ca_{0.76(14)}Na_{0.02(0)}Mg_{0.84(8)}Fe_{0.32(7)}Ti_{0.02(0)})(Si_{1.93(1)}Al_{0.08(1)})O_6$
III	Di73$^{(c)}$	$(Ca_{0.72(18)}Na_{0.02(1)}Mg_{0.89(13)}Fe_{0.34(7)}Ti_{0.02(1)})(Si_{1.92(2)}Al_{0.09(3)})O_6$
IV	Di74$^{(c)}$	$(Ca_{0.73(12)}Na_{0.02(0)}Mg_{0.87(8)}Fe_{0.34(6)}Ti_{0.03(2)})(Si_{1.91(3)}Al_{0.10(2)})O_6$
V	Di78$^{(c)}$	$(Ca_{0.76(12)}Na_{0.02(0)}Mg_{0.87(7)}Fe_{0.29(6)}Ti_{0.02(0)})(Si_{1.93(1)}Al_{0.10(2)})O_6$
Orthopyroxene		
I	Di5$^{(o)}$	$(Ca_{0.06(2)}Mg_{1.29(2)}Fe_{0.64(2)})(Si_{1.95(1)}Al_{0.04(1)})O_6$
II	Di6$^{(o)}$	$(Ca_{0.06(1)}Mg_{1.28(2)}Fe_{0.62(1)})(Si_{1.95(1)}Al_{0.05(0)})O_6$
III	Di4$^{(o)}$	$(Ca_{0.04(1)}Mg_{1.32(1)}Fe_{0.62(1)})(Si_{1.96(1)}Al_{0.04(0)})O_6$
IV	Di12$^{(o)}$	$(Ca_{0.12(11)}Mg_{1.30(1)}Fe_{0.58(8)})(Si_{1.97(1)}Al_{0.03(2)})O_6$
V	n/a	n/a
Feldspar		
I	Ab39	$(Na_{0.36(7)}Ca_{0.62(7)}Fe_{0.02(1)})(Si_{2.38(7)}Al_{1.60(7)})O_8$
II	Ab44	$(Na_{0.39(5)}K_{0.02(0)}Ca_{0.57(6)})(Si_{2.43(6)}Al_{1.56(5)})O_8$
III	Ab37	$(Na_{0.33(5)}Ca_{0.65(6)}Fe_{0.02(0)})(Si_{2.36(6)}Al_{1.63(6)})O_8$
IV	Ab38	$(Na_{0.33(3)}K_{0.02(0)}Ca_{0.64(3)}Fe_{0.02(0)})(Si_{2.37(3)}Al_{1.61(3)})O_8$
V	Ab38	$(Na_{0.33(5)}Ca_{0.64(6)})(Si_{2.37(6)}Al_{1.61(6)})O_8$

Selected raw data are provided in Appendix B

[a] Numbers of points analysed for I are described in Table 3.3. Chemical compositions for olivine are averaged from 12 points in II, 10 points in III, 8 points in IV, and 8 points in V; for clinopyroxene are 10 points in II, 4 points in III, 9 points in IV, and 14 points in V; for orthopyroxene are 4 points in II, 5 points in III and 2 points in IV; for feldspar are 5 points in II, 12 points in II, 7 points in IV and 12 points in V

most of the orthopyroxene has transformed to clinopyroxene at 1,400 K under shear stress.

Another significant change is the reaction of oxides in the high-temperature shear stress experiment (Fig. 3.14). The symplectic structure of Fe–Ti oxides as well as the bulk Fe-rich (hematite) or Ti-rich (ilmenite) oxides is abundant in the gabbro 'as received', in which Fe-rich oxides predominate over Ti-rich oxides. The bulk Fe–Ti oxides and the symplectic structure are still observed when temperature increase up to 1,250 K (as shown in Fig. 3.12) where the amount of bulk Fe-rich oxides observed approaches that of Ti-rich oxides, although the total ratio of Ti/(Fe + Ti) does not vary a lot compared to the sample 'as received'. Small amounts of bulk oxides are

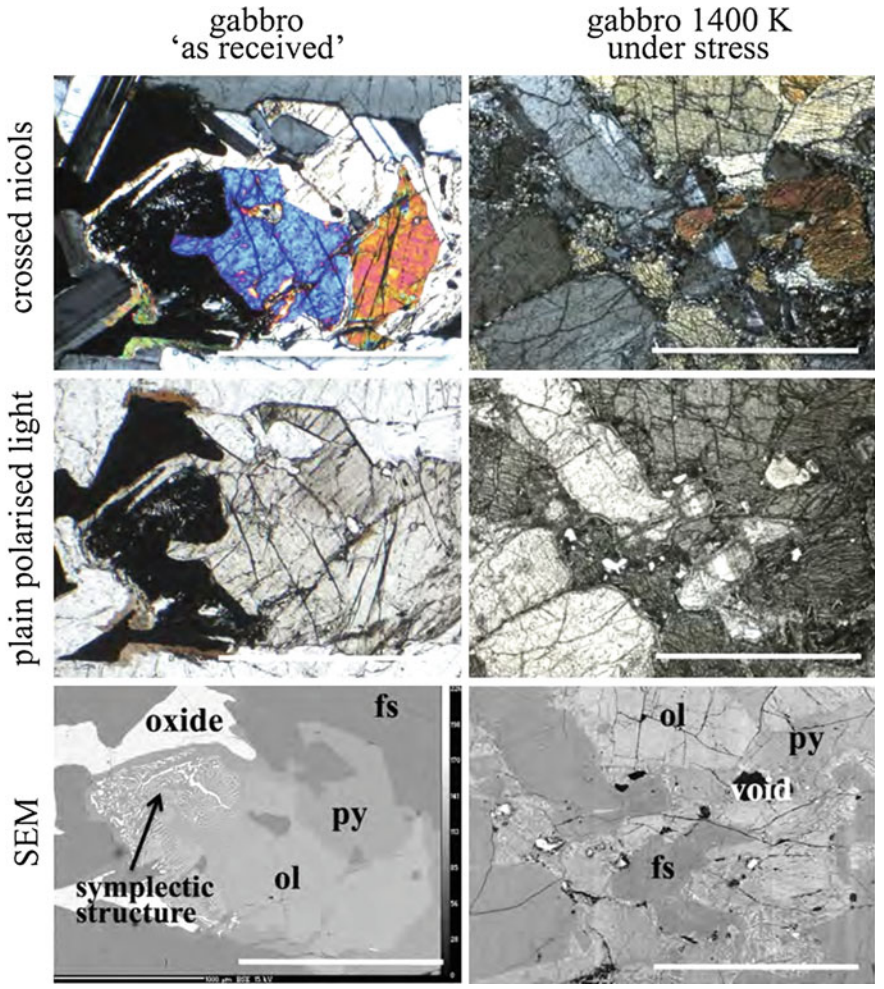

Fig. 3.14 Microstructures of oxides in Skaergaard gabbro 'as received' (*left*) and the gabbro in the high-temperature shear stress experiment (*right*) are shown in crossed nicols, in plain polarised light, and SEM images. The images of crossed nicols and plain polarised light are taken at the same location. The *grey* levels in SEM images correspond to different mineral phases and *black areas* are voids. The scale bar is 1 mm in all images. (*ol* olivine, *py* pyroxene, *fs* feldspar)

still found in the thin section of the gabbro heat-treated to 1,400 K. For the gabbro which has been heated repeatedly to 1,400 K for seven times under shear stress at a frequency of 1 Hz, neither bulk oxides nor symplectic structures are observed in the thin section or in the microprobe. Instead, tiny oxides (mostly Ti-rich oxides) are seen abundantly along the edges of feldspars and olivines in the microstructures.

Needle domains are seen in the feldspars of both Iceland basalt and Skaergaard gabbro that were conducted at high temperature (1,300 and 1,400 K, respectively)

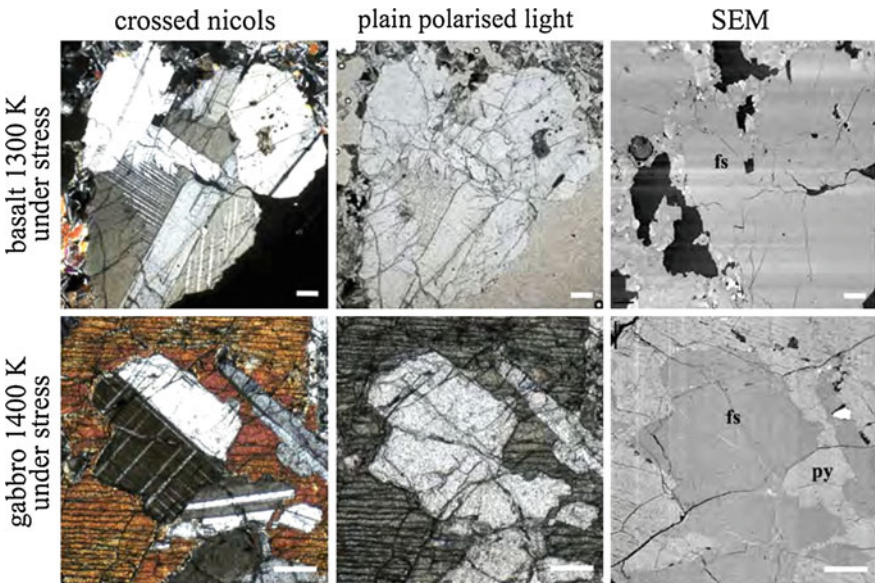

Fig. 3.15 Microstructures of needle domain developments in both Iceland basalt at 1,300 K (*top*) and Skaergaard gabbro at 1,400 K (*bottom*) under shear stress are shown in crossed nicols, in plain polarised light, and SEM images. The images of crossed nicols and plain polarised light are taken at the same location. The *grey* levels in SEM images correspond to different mineral phases and *black areas* are voids. The scale bar is 200 μm in all images. (*py* pyroxene, *fs* feldspar)

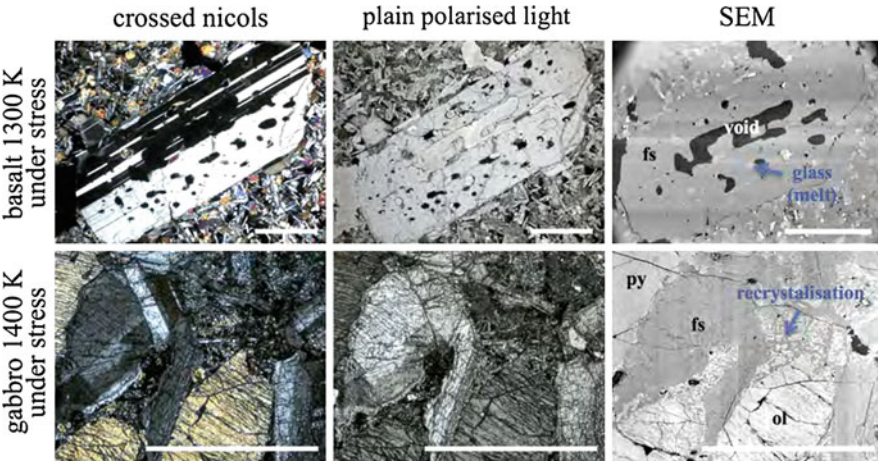

Fig. 3.16 Microstructures of partial melting in Iceland basalt at 1,300 K (*top*) and recrystallisation in Skaergaard gabbro at 1,400 K (*bottom*) under shear stress shown in crossed nicols, in plain polarised light, and SEM images. The images under crossed nicols, plain polarised light, and SEM images are taken at the same location. The *grey* levels in SEM images correspond to different mineral phases and *black areas* are voids. The scale bar is 1 mm in all images. (*ol* olivine, *py* pyroxene, *fs* feldspar)

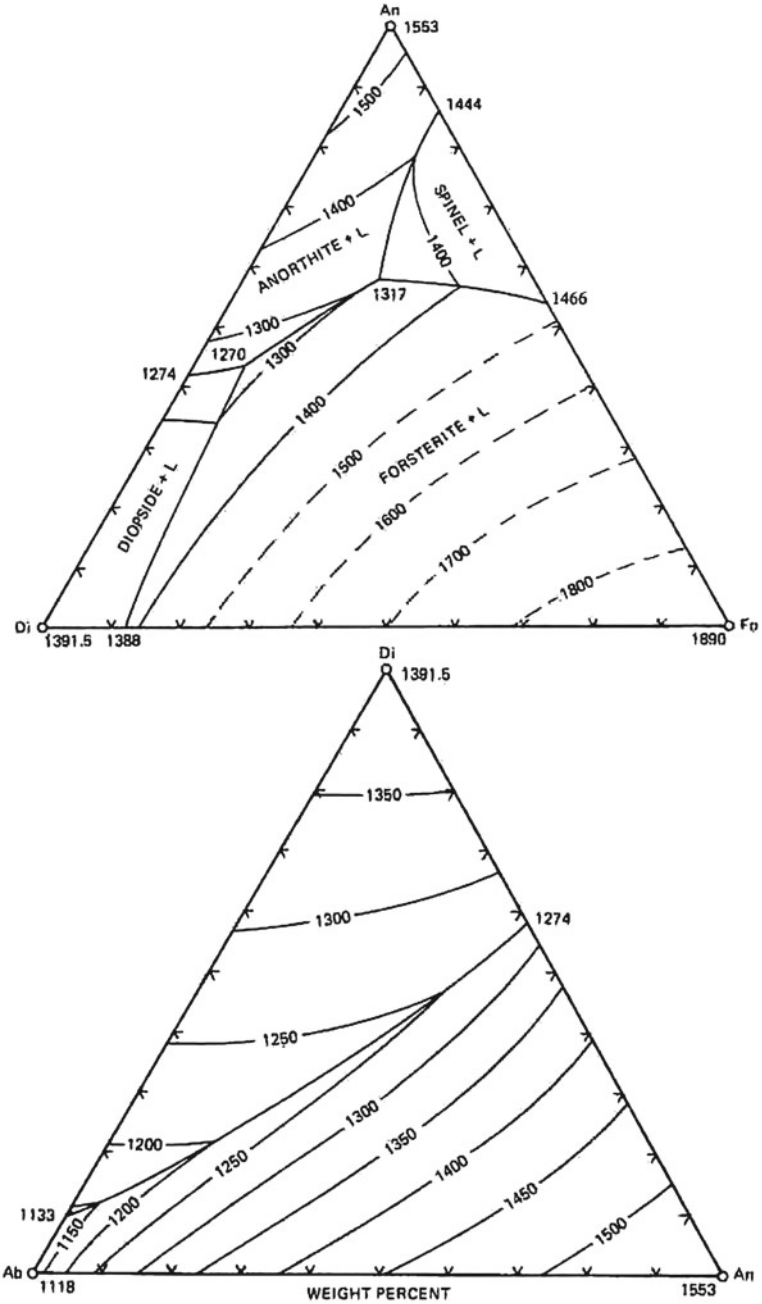

Fig. 3.17 Equilibrium diagram of the system albite-diopside-anorthite and the system forsterite-diopside-anorthite, contoured with temperature (°C), in the basalt. *L* liquid, *Ab* albite ($NaAlSi_3O_8$), *An* anorthite ($CaAl_2Si_2O_8$), *Di* diopside ($CaMgSi_2O_6$), *Fo* forsterite ($Mg_2Si_2O_4$). After [8]

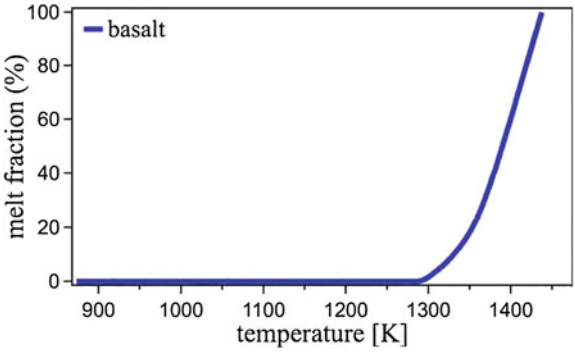

Fig. 3.18 Melt fraction generated in basalt as a function of temperature. After [9]

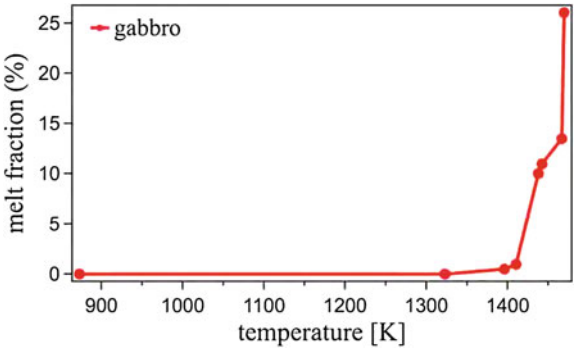

Fig. 3.19 Melt fraction generated in gabbro as a function of temperature (to 1,470 K). After [10]

under shear stress, as shown in the Fig. 3.15. Two different orientations of the needle domains, which are considered to be generated by shear stress, are developing in the lamellar twinning of feldspars of both samples. The SEM images from the microprobe analysis indicate that the chemical composition remains the same across the whole feldspar, in which the needle domain develops.

Numerous optically-isotropic regions are found in one large phenocryst plagioclase feldspar in the Iceland basalt from torsion experiments (as shown in Fig. 3.16), which indicates that partial melting has occurred at 1,300 K under seismic frequency stress of 1 Hz. According to the equilibrium diagram of the system albite-anorthite-dipside-forsterite in basalt (Fig. 3.17) [8], albite feldspars in the Iceland basalt may melt first at 1,300 K under stress. Petcovic and Dufek produced the melting curve for the basalt using the MELTS program [9]. Their study reveals that 1.5 % melt is generated in basalt at 1,300 K (Fig. 3.18).

When the partial melting occurs in the basalt, recrystallisation is also seen in the Skaergaard gabbro under high-temperature shear experiments at 1,400 K and at a frequency of 1 Hz. The feldspars and olivines are seen to re-crystallise at the boundaries of minerals, especially between feldspars and olivine. Relatively few reactions (recrystallisation) occur at the boundaries between feldspars and pyroxenes. Fontaine et al. have studied the melt fraction in gabbro to 1,470 K [10] (Fig. 3.19).

Table 3.5 The chemical compositions[a] for olivine [Fo*xx*], clinopyroxene [Di*xx*$^{(c)}$], orthopyroxene [Di*xx*$^{(o)}$], feldspar [Ab*xx*] and glass [Di*xx*(g)] in both Iceland basalt and Skaergaard gabbro before and after torsion experiments

Iceland basalt	
1. Basalt 'as received'	
Phenocrysts	
Ab18	$(Na_{0.13(3)}Ca_{0.86(3)}Mg_{0.02(0)}Fe_{0.02(0)})(Si_{2.16(3)}Al_{1.81(3)})O_8$
Groundmass	
Fo70	$(Mg_{1.38(26)}Fe_{0.59(26)})Si_{1.00(1)}O_4$
Di77$^{(c)}$	$(Ca_{0.75(9)}Mg_{0.87(19)}Fe_{0.31(27)}Ti_{0.02(1)})(Si_{1.93(2)}Al_{0.10(5)})O_6$
Ab35	$(Na_{0.28(11)}Ca_{0.70(12)}Mg_{0.04(8)}Fe_{0.05(7)})(Si_{2.32(13)}Al_{1.62(19)})O_8$
Glass	
Di54$^{(g)}$	$(Ca_{0.50}Na_{0.04}Mg_{0.81}Fe_{0.50}Ti_{0.04}Al_{0.09})(Si_{1.87}Al_{0.13})O_6$
2. Basalt heated repeatedly to 1300 K under shear stress	
Phenocrysts	
Ab17	$(Na_{0.13(2)}Ca_{0.86(3)}Fe_{0.02(0)})(Si_{2.16(3)}Al_{1.82(3)})O_8$
Groundmass	
Fo67	$(Mg_{1.31(19)}Fe_{0.65(20)})Si_{1.00(1)}O_4$
Di72$^{(c)}$	$(Ca_{0.70(14)}Mg_{0.86(10)}Fe_{0.37(21)}Ti_{0.02(1)})(Si_{1.93(2)}Al_{0.11(3)})O_6$
Ab40	$(Na_{0.28(8)}Ca_{0.69(11)}Mg_{0.06(8)}Fe_{0.04(4)})(Si_{2.36(13)}Al_{1.56(21)})O_8$
Glass	
Di57$^{(g)}$	$(Ca_{0.52(9)}Na_{0.04(3)}Mg_{0.80(10)}Fe_{0.47(6)}Ti_{0.04(1)})(Si_{1.87(2)}Al_{0.24(9)})O_6$
Skaergaard gabbro	
1. Gabbro 'as received'	
Fo61	$(Mg_{1.22(1)}Fe_{0.78(1)})Si_{0.99(0)}O_4$
Di84$^{(c)}$	$(Ca_{0.82(4)}Na_{0.02(1)}Mg_{0.82(3)}Fe_{0.28(1)}Ti_{0.03(0)})(Si_{1.93(1)}Al_{0.10(0)})O_6$
Di5$^{(o)}$	$(Ca_{0.06(2)}Mg_{1.29(2)}Fe_{0.64(2)})(Si_{1.95(1)}Al_{0.04(1)})O_6$
Ab39	$(Na_{0.36(7)}Ca_{0.62(7)})(Si_{2.38(7)}Al_{1.60(7)}Fe_{0.02(1)})O_8$
2. Gabbro heated repeatedly to 1400 K under shear stress	
Fo64	$(Mg_{1.28(4)}Fe_{0.70(4)})Si_{1.00(0)}O_4$
Di78$^{(c)}$	$(Ca_{0.76(12)}Na_{0.02(0)}Mg_{0.87(7)}Fe_{0.29(6)}Ti_{0.02(0)})(Si_{1.93(1)}Al_{0.10(2)})O_6$
Ab38	$(Na_{0.33(5)}Ca_{0.64(6)})(Si_{2.37(6)}Al_{1.61(6)})O_8$

Selected raw data are provided in Appendix A for basalt and Appendix B for gabbro

[a] Chemical compositions for Iceland basalt under shear stress are averaged from 32 points for phenocryst feldspar, 11 points for groundmass olivine, 15 points for groundmass pyroxene, 9 points for groundmass feldspar and 18 points for glass. Numbers of points analysed for the rest are described in Tables 3.2, 3.3 and 3.4

Comparison with their results indicates that approximately 1 % melt fraction is likely generated in the Skaergaard gabbro in this study and nearly 10 % melt fraction can be produced when gabbro is heated to 1,450 K.

Microprobe analysis shows the optically-isotropic phases in the feldspar phenocrysts of Iceland basalt are glasses with a pyroxene composition (Di57) in the high-temperature shear experiments, which is similar to the glass composition found in the original Iceland basalt 'as received' (Di54). The compositions of different mineral phases in both basalt and gabbro before and after experiments are shown in

Table 3.5. The chemical compositions of feldspars in Iceland basalt are similar before and after experiments, but the sodium content in the feldspar phenocrysts (Ab18 and Ab17) is much lower than that in the groundmass feldspars (Ab35 and Ab40). The compositions of groundmass feldspars in basalt are similar to the feldspars in gabbro (Ab39 and Ab38).

The Mg ratio in the olivines in the Iceland basalt decreases at 1,300 K (Fo70 → Fo67) while that of the olivine in gabbro increases (Fo61 → Fo64) at 1,400 K under the shear stress. On the other hand, the calcium content in the clinopyroxene may be lower in both basalt (Di77 → Di72) and gabbro (Di84 → Di78) after experiments, while the orthopyroxene (Di5) is only found in the thin section of gabbro 'as received'. It is likely that calcium diffusion occurs between clinopyroxenes and orthopyroxenes in the Skaergaard gabbro as the pyroxene grows pervasively with increasing temperature during the experiments.

References

1. Heap, M. J., Baud, P., Meredith, P. G., Bell, A. F., & Main, I. G. (2009). Time-dependent brittle creep in darley dale sandstone. *Journal of Geophysical Research*, *114*(B7), B07203.
2. Wu, X. Y., Baud, P., & Wong, T.-f., (2000). Micromechanics of compressive failure and spatial evolution of anisotropic damage in darley dale sandstone. *International Journal of Rock Mechanics and Mining Sciences*, *37*(1–2), 143–160.
3. van Panhuys-Sigler, M., & Trewin, N. H. (1990). Authigenic sphene cement in permian sandstones from arran. *Scottish Journal of Geology*, *26*(2), 139–144.
4. Slater, L., McKenzie, D., Grönvold, K., & Shimizu, N. (2001). Melt generation and movement beneath theistareykir, ne iceland. *Journal of Petrology*, *42*(2), 321–354.
5. McBirney, A. R. (1989). The skaergaard layered series: I. structure and average compositions. *Journal of Petrology*, *30*(2), 363–397.
6. Thy, P., Lesher, C., & Tegner, C. (2009). The skaergaard liquid line of descent revisited. *Contributions to Mineralogy and Petrology*, *157*(6), 735–747.
7. Lindsley, D. H., & Andersen, D. J. (1983). A two-pyroxene thermometer. *Journal of Geophysical Research*, *88*(S2), A887–A906.
8. Morse, S. A. (1980). *Basalts and phase diagrams: An introduction to the quantitative use of phase diagrams in igneous petrology*. New York: Springer-Verlag New York Inc.
9. Petcovic, H. L., & Dufek, J. D. (2005). Modeling magma flow and cooling in dikes: Implications for emplacement of columbia river flood basalts. *Journal of Geophysical Research*, *110*(B10), B10201.
10. Fontaine, F. R., Ildefonse, B., & Bagdassarov, N. S. (2005). Temperature dependence of shear wave attenuation in partially molten gabbronorite at seismic frequencies. *Geophysical Journal International*, *163*(3), 1025–1038.

Chapter 4
Thermal Relaxations in Gabbro and Basalt

4.1 Introduction

Since the Earth is not perfectly elastic and responds anelastically at seismic frequencies, seismic waves dissipate in time and space. Attenuation (Q^{-1}) potentially provides direct information on the anelastic properties of the Earth. Anomalously weak regions, with low shear velocities and high attenuation, have been observed in the asthenosphere [1, 2], in geothermal source regions (such as rift zones, subduction zones, mantle plumes and hotspots) [3] and at the core-mantle boundary [4]. These seismically anomalous zones of low velocity and high attenuation are often explained in terms of the presence of a small amount of melt or enhanced anelasticity due to high temperatures. Understanding the rheological properties of minerals and rocks remains important in order to interpret such seismological observations.

Early studies in the upper mantle and at the core-mantle boundary have indicated that partial melting accounts for seismic anomalies in the low-velocity zones. Karato and Jung [5] suggested a model for variations in seismic velocity based on details of the geotherm, partial melting and upwelling flow to the sub-oceanic upper mantle [5]. They proposed that anelastic relaxation will be enhanced by the presence of water and seismic velocities also decrease significantly through anelastic relaxation somehow enhanced by water content. However, Faul and Jackson [6] suggested that neither water nor partial melting are necessary in the model if other anelastic effects are taken into account [6]. They use a model which highlights the sensitivity of shear velocities and attenuation to temperature and grain size to fit the experimental data. The results show that solid state mechanisms may be sufficient to explain the low-velocity zones in the upper mantle, as temperature increases with depth even in the absence of water or melt.

The study of Tan et al. by torsional microcreep experiments on fine-grained olivine aggregates [7] also highlights the grain-size sensitivity associated with modulus dispersion and dissipation at seismic frequencies. In material sciences, the effects of grain boundaries and grain size on attenuation in metals have been widely studied. Stress relaxations across grain boundaries were measured in poly-crystalline and

S.-Y. Chien, *Rheological and Seismic Properties of Solid-Melt Systems*,
Springer Theses, DOI: 10.1007/978-3-319-03098-2_4,

single crystal aluminium wires to 723 K [8]. An additional high attenuation peak (near 523 K) occurs in poly-crystal aluminium while only the slowly increasing attenuation background, known as high temperature background, was found for the single crystal aluminium. The relaxation peak is, therefore, assumed to result from the presence of grain boundaries. Kê's experiments also show that the relaxation peak is grain size dependent. With larger grain size, the relaxation peak become broader and occurs at higher temperature.

Following the concept of Kê, Jackson et al. [9] suggested a power law relation to model grain size effects on inverse quality factor (Q^{-1}) as

$$Q^{-1} = Ad^{-m_d}[\omega^{-1}\exp(\frac{-E_{\text{act}}}{\text{R}T})]^{\alpha_d} \tag{4.1}$$

where d is the grain size, ω is the frequency of stress oscillation, T is the absolute temperature, E_{act} is the activation energy, R is the gas constant, m_d and α_d are empirical exponent and A is a pre-exponential constant.

Using the proposed power law, Jackson et al. [9] conducted the first measurements of strain energy dissipation in fine-grained polycrystalline olivine to examine the grain-size sensitivity of Q^{-1}. The internal friction was found to be greater with smaller grain size at a constant temperature and period. Their data fits well with this model for measurements at short periods (1–100 s) at temperatures between 1,273 and 1,473 K, although the model does not explain well the long period data (300–1,000 s) of Jackson et al. [9] and of Tan et al. [7]. Fontaine et al. [10] also used the same model to examine their data in partially-molten gabbros at high temperatures (873–1,443 K) and at low frequencies (0.002–20 Hz) [10]. However, their data failed to show a clear relationship between internal friction and grain size, which is also supported by the findings of Kampfmann and Berckhemer [11] on ultrabasic and basic magmatic rocks, at temperatures between 873 and 1,773 K and frequencies between 0.003 and 30 Hz. No clear dependence of internal friction on grain size is seen in their results. This throws into question whether Jackson and co-workers' hypothesis of grain size as the dominant mechanism of anelasticity is universally applicable in polymineralic rocks.

Transient creep may also occur in partially-molten rocks [12] when the interactions and processes at the grain surface cause strain-dependent frictional resistance and result in transient rheology of rocks with transient elastic moduli and transient viscosities. Depending on the relative amplitude of stresses applied to the rock and the degree of partial melting, the rock may behave as a Newtonian liquid at low stresses, or display power law creep at intermediate stresses ($\dot{\varepsilon} \propto \sigma^n$), or even exponential creep at high stresses ($\dot{\varepsilon} \propto \exp(\beta_n \sigma)$) [13]. Under low stress, the anelastic rheology of a Newtonian (linear) polycrystalline aggregate is often described by the Andrade creep model [14], which also includes a power law transient behaviour which is followed by a Newtonian steady state behaviour [15]:

$$\varepsilon = \sigma(\frac{1}{G} + \beta_n t^n + \frac{t}{\eta_{\text{ss}}}) \tag{4.2}$$

where ε is the anelastic shear strain, σ is the stress, G is the (unrelaxed) shear modulus, t is time and β_n and n ($0 \leqslant n \leqslant 1$) are constants, and η_{ss} is the steady state viscosity. The creep behaviour is known as Andrade creep when $n = 1/3$ for the transient creep.

Gribb and Cooper [15] demonstrated that shear attenuation in polycrystalline olivine may be explained by the Andrade model at high temperature (1,473 and 1,558 K) and at low frequencies (0.001–1 Hz). Under these conditions, materials are found to have constant strain rate, which Gribb and Cooper explain in terms of deformation due to chemical diffusion. In frequency space, the attenuation band is associated with a physical transient process in which the strain rate decreases initially (transient creep) and then progresses to a nominally constant steady state creep. Gribb and Cooper also suggest the "high-temperature background", which is highly structure-sensitive and generally smaller in single crystals than that in polycrystals, can be predicted from the creep response without knowing the distribution of grain size or of lattice defects. In the recent studies, Jackson et al. [16] have provided an Andrade-pesudoperiod model [16] by $Q^{-1} \propto \exp(-E_{HTB}/RT)]^n$ following the models of Kê and Andrade [8, 14]. The Andrade-pesudoperiod model shows similar form to the expression provided by Schoeck et al. [17] (as expressed in Eq. 1.26, Chap. 1), that describes high temperature damping generated by the diffusion-controlled relaxation processes in materials.

Three different steady-state diffusion-controlled transient deformation processes can occur in the polycrystals [18]: diffusional creep, diffusional-accommodated grain boundary sliding and inter-granular crack growth. In the steady state, the rate of matter transport by bulk (lattice) and grain boundary diffusion controls the rates of creep deformation, grain boundary sliding and crack growth. On application of stress to a polycrystalline solid, the initial response is homogeneous linear elastic strain. As time increases, shear stresses are relaxed at grain boundaries by sliding, resulting in inhomogenous deformation. If diffusion dominates in the system (for example, with increasing temperature), further time-dependent deformation can occur and the behaviour will change from elastically accommodated grain boundary sliding to steady state diffusion. As an example, in the study of Jackson et al. [9], microcreep measurements of fine-grained polycrystalline aggregates show a smooth transition from elastic (rigid body displacement) through anelastic (elastically-accommodated grain boundary sliding) to viscous (diffusionally-accommodated grain boundary sliding) deformation with the increasing temperature or with increasing relaxation time (Fig. 4.1).

The geometry of the grain boundaries also controls the relative extent of diffusion at the interfaces. Grain boundaries in minerals and rocks are not perfectly planar and contain defects. As a shear stress is applied in the system, the relative sliding of adjacent grains occurs to adjust the stress initially and then is impeded by triple junctions and steps between pairs of grains (Fig. 4.2). The shear stress, which accumulates at triple junctions and at the rough surface of grain boundaries, can be relaxed through faster diffusional transport along grain boundaries and by climb of grain boundary dislocations [19].

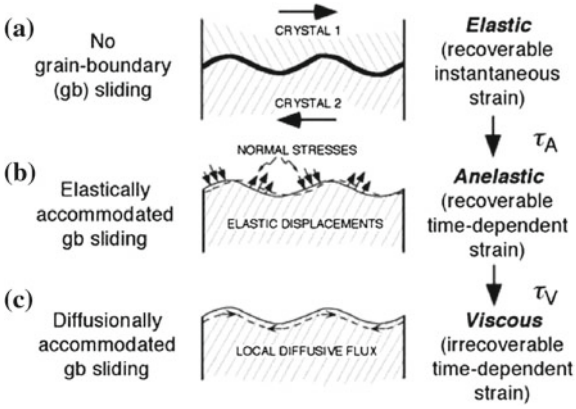

Fig. 4.1 The response to applied stress along a grain boundary with increasing temperature or increasing relaxation time: behaviours change from (**a**) elastic through (**b**) anelastic to (**c**) viscous. τ_A and τ_V are the timescales (relaxation times) for the transitions from **a** to **b** and from **b** to **c**, respectively. After [9]

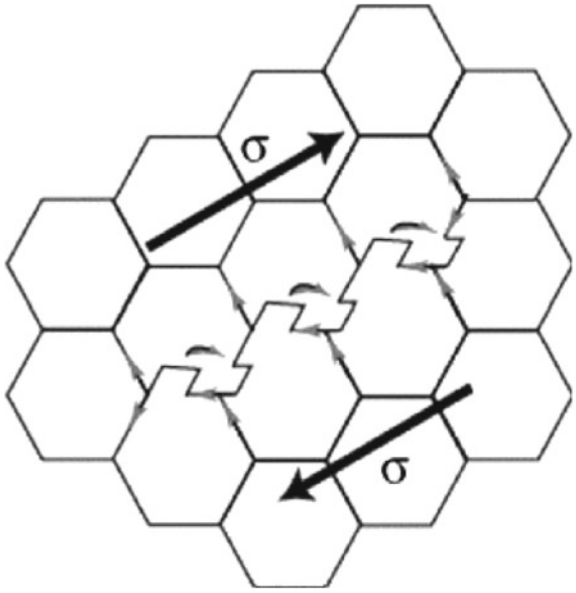

Fig. 4.2 A conceptual sketch of the sliding at grain boundaries under shear stress. When a shear stress applied to grains, the adjacent grains slide initially to adjust the stress and then the sliding is impeded by by triple junctions and steps between pairs of grains

Previous studies have focused on grain boundary processes in monomineralic systems. Two diffusional processes can occur at grain boundaries depending on microstructure [20]. In polycrystalline monomineralic materials with clean (or dry) grain boundaries (Fig. 4.3a), materials deform by diffusional creep, which can be modelled by a grain boundary dislocation. Deformation is generated by grain boundary sliding, but the rate of diffusion is controlled by dislocation climb. Grain boundary dislocations climb at boundaries through the diffusion of vacancies. When the vacancy reaches the boundary dislocation, the dislocation then moves along the boundary. For a partially-molten material, small amounts of melt go into voids or grain boundaries forming a wetted grain boundary, as may be simply modelled by

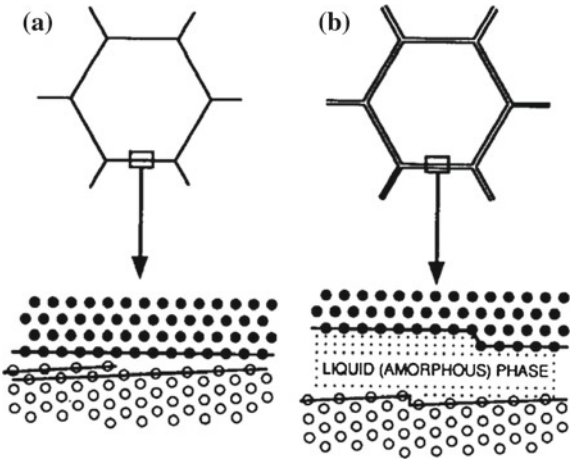

Fig. 4.3 Microstructures at a grain boundary. **a** A clean (or dry) grain boundary modelled by a *line* defect (dislocation) **b** a wetted grain boundary with a thin amorphous film as a step. From [20]

insertion of a liquid (or amorphous) film at grain boundaries in Fig. 4.3b. The deformation is controlled by the solution-precipitation creep, which occurs at line defects of grain boundaries, namely, at the step [20]. The concept behind this model is that the atoms from one grain surface dissolve into the liquid phase, diffuse into a direction of applied stress and then precipitate on the other boundary. In other words, the step moves along the grain surface when atoms reach a boundary step.

Grain sizes effects and grain boundary relaxation processes have been used to explain the mechanical response of polycrystalline monomineralic samples and rocks. The observations of relaxation processes in the natural rocks, however, are more complicated and the interpretation of measurements becomes difficult. Berckhemer et al. [21] have studied partially-molten natural dunite (to 1,673 K) and synthetic polycrystalline forsterite (to 1,773 K) by forced torsion oscillation at frequencies from 0.003 to 30 Hz [21]. Significant softening of the shear modulus occurs in natural dunite above 1,473 K, while the shear strength of forsterite at similar temperatures changes relatively little. In both, modulus softening is stronger at lower frequency (0.003 Hz) than that at higher frequency (30 Hz). No dissipation peak was seen, but rising internal friction is found with increasing temperature in both samples, with no significant changes in the region of partial melting. Berckhemer et al. conclude that the dissipation mechanism is dominated by some undefined solid state high-temperature background attenuation, even with a small amount of melt existing in the sample.

Similar modulus dispersion behaviours are shown in the viscoelastic study of James et al. [22] on basaltic lavas at frequencies between 0.002 and 20 Hz and at temperatures between 773 and 1,423 K [22]. Both shear modulus and internal friction show frequency-dependent dispersion, more evident at higher temperature. A clear dissipation peak occurs as a function of frequency in the samples which were annealed at 987 K, and this disappears in samples that have been annealed at temperatures above 1,085 K. James et al. attribute these time-varying characteristics of basaltic

lavas to the healing of the microcracks and pores. On the other hand, Weiner et al. [23] measured internal friction in theoleiitic basalts at 1.3 Hz and at temperatures between 773 and 1,173 K by inverted torsional pendulum [23]. Their measurements of mechanical dissipation as a function of temperature show two internal friction peaks occurring at temperatures near 893 and 1,103 K. They suggest grain boundary sliding as the possible mechanism behind these dissipation peaks and explain the double peaks in terms of a bimodal grain size distribution, such that the larger grain size (100–500 μm) contributes to the peak at 1,103 K and a smaller grain size (2 μm) is associated with the peak at 893 K.

Kampfmann and Berckhemer [11] measured the complex shear modulus and electrical resistivity of various ultrabasic and basic rocks (dunite, peridotite, gabbro and basalts) in the frequency range 0.003–30 Hz under forced torsional oscillations [11]. An absorption peak was found at $T > 0.5\ T_m$ in all the samples, which Kampfmann and Berckhemer suggest is due to the climb of dislocations. The dislocation mechanism is also suggested in Woirgard and Gueguen's study [24] of single crystal enstatite, polycrystalline forsterite and peridotite, all measured at high temperature at frequencies between 2 and 8 Hz by flexion pendulum. Dissipation peaks not only occur in peridotite (at 1,203 K) and in forsterite (at 823 and 1,023 K), but also in the single crystal enstatite (at 1,033 K), in which no grain boundary can be involved as a cause of internal friction.

Temperature-dependent attenuation in partially-molten gabbro has also been studied at temperatures to 1,443 K over a frequency range (0.002–20 Hz) using forced torsion oscillation by Fontaine et al. [10]. Their microstructural observations show the onset of melting occurring at 1,310 K, and 10 % melt fraction generated at 1,438 K. A dissipation peak, which is more obvious at lower frequency, occurs above 1,310 K, followed by a rapidly rising internal friction above 1,417 K. They attribute diffusionally-controlled grain boundary sliding as the mechanism of the attenuation peak. For the rapidly increasing attenuation background at high temperature, they suggest that melt squirt flow in the grain boundaries may be the major contribution and that elastic wave propagation could trigger melt flow from high-fluid-pressure cracks to adjacent low-fluid-pressure cracks [25].

In a very recent review paper, Karato [26] has pointed out that most of upper mantle, except for the lithosphere, contains very small amounts of melt (less than 0.1 %), in which case grain boundaries are not completely wetted. As a result, the effects of partial melting on mechanical properties will be small, according to Stocker and Gordon's dihedral angle study at partially-molten alloy [27]. Karato has suggested that the sub-solidus grain boundary sliding process and the influence of water on it are more profound and may be responsible for the lithosphere-asthenosphere boundary (LAB) at depths of about 200–250 km and in the mid-lithosphere at depths of about 100–150 km, where larger amounts of water are suggested [26]. As difficulties are found in both the partial melting model and the sub-solidus process model, Karato proposed a new model to explain the dominate characteristics of the LAB, such that, with an applied stress and a proper characteristic frequency of grain boundary relaxation, the attenuation is controlled by high-frequency elastically-accommodated grain boundary sliding (low temperature) and followed by low-frequency anelastic

diffusionally-accommodated mass transport (high temperature), which dominates in areas of high temperature and higher water content.

Many mechanisms have been involved to explain the relaxation processes in mantle minerals and rocks. Mechanical properties of partially-molten rocks show differing behaviour in the previous studies, depending on different experimental conditions and sample characteristics, such as the occurrence of thermal micro-cracking, or the progressive dehydration of hydrous-layered silicate minerals, partial melting and chemical complexity. In addition, most of the data collected on natural rocks in previous studies are too sparse to accurately define the relaxation processes, especially for basalts and gabbros, in which attenuation peaks associated with grain boundary sliding have been reported. It is, therefore, essential to augment previous investigations with detailed studies of their anelastic behaviour to temperatures approaching the melting point. In this study, two basalts and one gabbro have been subjected to detailed measurement in the inverted forced torsion pendulum (IFTP) to examine the effects of grain size and the effects of partial melting on the relaxation processes across the temperature range that grain boundary sliding is invoked.

4.2 Samples and Experimental Methods

Two basalts (I13_83493 basalt and Iceland basalt) and one Skaergaard gabbro were prepared for thermal relaxation experiments. The details of these samples 'as received' have been described in Sect. 3.2 and Figs. 3.8, 3.9 and 3.10. All samples were cut into rectangular bars to be clamped in the inverted forced torsion pendulum (detailed in Sect. 2.1 and Fig. 2.3). Sample dimensions were 10.7 mm in width, 2.3 mm in thickness and 16.3 mm in length for I13_83493 basalt (referred to as I13 basalt hereafter), 10.8 mm in width, 1.9 mm in thickness and 27.5 mm in length for Iceland basalt, and 14.4 mm in width, 2.1 mm in thickness and 34.2 mm in length for Skaergaard gabbro. At the preparation stage, I13 basalt was annealed below 800 K for 3 days (heated at 400, 500, 600, 700 and 800 K for half a day in turn), whereas no heat treatment on Iceland basalt and Skaergaard gabbro were conducted before experiments. All measurements were conducted at a temperature ramp rate of 1 K/min and under high vacuum (10^{-3}–10^{-6} Pa).

The temperature-dependent shear modulus and internal friction of I13 basalt were measured as a function of temperature at different frequencies of applied shear stress (1, 5 and 10 Hz) while the sample was heated to a maximum temperature of 900 K and subsequently cooled to 500 K. Following this, measurements were made under the same conditions, but heated to a maximum temperature of 1,100 K at frequencies of 1, 5 and 10 Hz. The sample was then measured at a frequency of 1 Hz when heated to and cooled from a maximum temperature of 1,250 K for three cycles and the experiment ended due to sample failure, which may have been caused by unbalanced vertical stresses that occur in the measurements (as discussed in Chap. 5). The stress was better balanced in the later measurements of Iceland basalt and gabbro.

Three different kinds of measurements were conducted on Iceland basalt as a function of frequency, temperature, and time. Initially, the shear modulus and internal friction of Iceland basalt were measured as a function of temperature as the sample was heated to 1,150 K. The temperature then was maintained at 1,150 K for microcreep and frequency-dependent measurements. The strain (of order of 10^{-6}–10^{-7}) was measured under applied shear stress for 20,000 s, which was then followed by isothermal dynamic shear modulus and internal friction measurements as a function of frequency (0.05–10 Hz). After three different measurements at 1,150 K, the temperature was lowered to 700 K before the next heating step. In the same method and order, temperature-dependent, frequency-dependent and microcreep measurements were then conducted at temperature on heating to 1,175, 1,200, 1,250 and 1,300 K (temperature was always lowered to 700 K before the next heating step). Temperature-dependent properties were also measured at frequencies of 0.1 and 0.05 Hz on heating to 1,300 K.

The shear modulus and internal friction of Skaergaard gabbro were measured as a function of temperature. The sample was initially heated to 1,200 K and cooled to room temperature at a stress frequency of 1 Hz during these measurements. Then, the sample was heated to 1,300 K and cooled to 500 K, followed by subsequent heating to 1,400 K. In the following measurements, the sample was repeatedly cooled to 500 K and heated to 1,400 K under stress of frequency 1 Hz. Five cycles of heating and cooling measurements were collected as a function of temperature to 1,400 K at a frequency of 1 Hz. Then, two cycles of heating and cooling curves at frequency of 0.1 Hz were measured as a function of temperature between 500 and 1,400 K.

4.3 Results and Analysis

The shear modulus and internal friction have been measured as a function of temperature in three igneous rocks (I13 basalt, Iceland basalt and Skaergaard gabbro) as well as a function of frequency in Iceland basalt, and the strain in Iceland basalt was also measured as a function of time, using the inverted torsion pendulum. In all cases, the shear modulus measured on heating does not follow the same path as that of cooling curves, whereas the internal friction in both heating and cooling curves have similar behaviours (further discussions in Chap. 5). The amplitude of the shear modulus varies in the different samples, but its variation with temperature or frequency of applied stress remains the focus of this study. In order to make comparison between datasets, all the shear modulus data have been normalised by dividing by the maximum value of modulus in the same heating run. Only heating curves are discussed further in this chapter to gain better understanding of the changes of mechanical properties as a function of temperature and frequency.

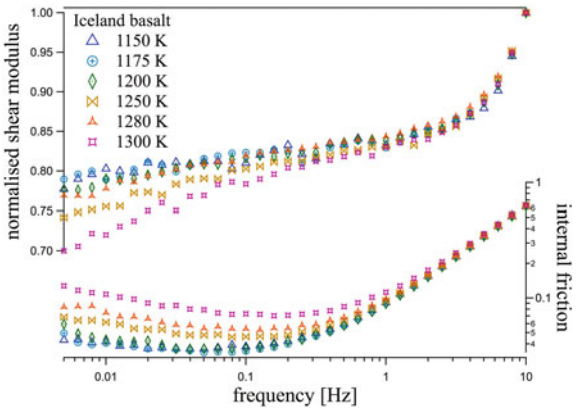

Fig. 4.4 Normalised shear modulus and internal friction of Iceland basalt as a function of frequency at different temperatures from 1,150 to 1,300 K. Internal friction and frequency are presented on a logarithmic scale

4.3.1 Frequency-Dependent Measurements

The normalised shear modulus and internal friction of Iceland basalt are plotted as a function of frequency (0.005–10 Hz) in Fig. 4.4, as measured isothermally at six different temperatures (1,150, 1,175, 1,200, 1,250, 1,280 and 1,300 K). The shear modulus increases with the increasing frequency, and rises rapidly above 1 Hz. The internal friction decreases initially with a decrease of frequency and then increases with further lowering of frequency (below 0.2 Hz). Both normalised shear modulus and internal friction show larger variations with temperature in the low-frequency region, below 2 Hz, but converge to the same trends at high frequency, above 2 Hz. The converging behaviour indicates that the data at high frequency are strongly affected by the resonance of pendulum device itself, which is at around 50 Hz. In the low-frequency region, below 1 Hz, the shear modulus decreases with increasing temperature. A tail of the relaxation peak shows at low frequency (10^{-2} Hz) and, with increasing temperature, the peak becomes stronger and broader, or shifts to higher frequency.

The normalised shear modulus and normalised internal friction of I13 basalt, Iceland basalt and Skaergaard gabbro on heating are also plotted as a function of temperature at different frequencies in Fig. 4.5. I13 basalt was heated to 1,100 K at 1, 5 and 10 Hz (Fig. 4.5 top). The normalised internal friction is used to compare the changes at different frequencies because the internal friction background increases significantly from 0.1 to 0.6 at 1,100 K at frequencies from 1 to 10 Hz. No relation is found between properties after normalised shear modulus and frequency over temperature range between 500 and 1,100 K. The shear modulus continuously increases from 500 to 1,000 K. An internal friction peak appears above 1,000 K while the internal friction remains low and constant at low temperature, although a peak-like increase shows below 600 K at high frequency (10 Hz). The increase of shear modulus in I13 basalt is about 100 % when it is about 40–70 % in Iceland basalt and gabbro.

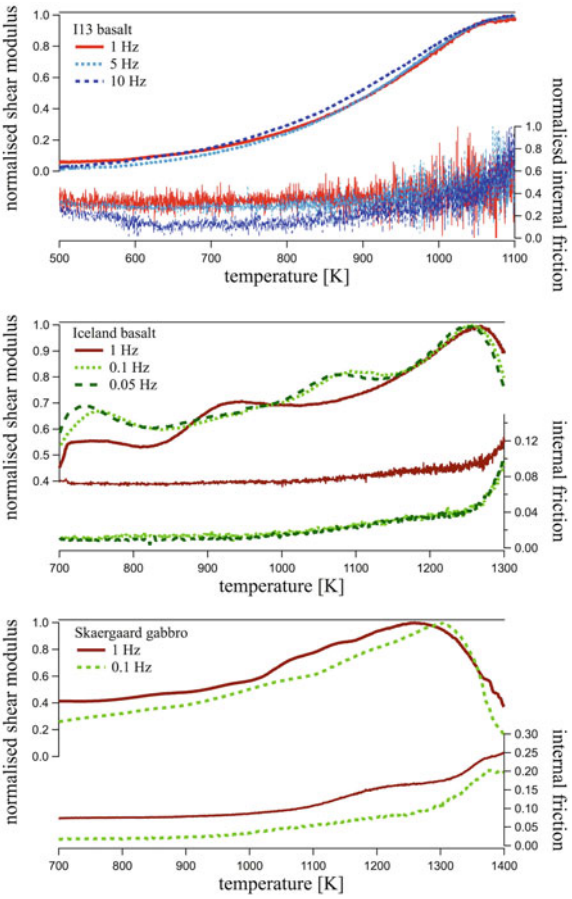

Fig. 4.5 Normalised shear modulus and internal friction of I13 basalt (*top*), Iceland basalt (*middle*) and Skaergaard gabbro (*bottom*) as a function of temperature at different frequencies

Iceland basalt was heated to temperatures above the glass transition temperature and normalised shear modulus and internal friction measured at frequencies of 0.05, 0.1 and 1 Hz as a function of temperature (Fig. 4.5 middle). The shear modulus increases in a non-uniform manner (40–55 %) and reaches its maximum at the glass transition temperature (between 1,250 and 1,290 K), followed by a decreasing shear modulus to 1,300 K on heating. The maximum of shear modulus is clearly frequency dependent, such that the modulus curves shift to lower temperature with decreasing frequency (1,249 K at 0.05 Hz, 1,257 K at 0.1 Hz and 1,269 K at 1 Hz). The softening of shear modulus at temperatures above the glass transition temperature is more pronounced at frequencies of 0.1 and 0.05 Hz than at 1 Hz. The behaviour of shear modulus is similar at stress frequencies of 0.1 and 0.05 Hz, but different from that measured at 1 Hz. The internal friction at frequencies of 0.1 and 0.05 Hz are identical, but the backgrounds at both frequences are lower than that measured for stress cycled

at 1 Hz. The internal friction data at these frequencies all remain low and constant in the low temperature regime, followed by a two stage increase from 1,000 to 1,300 K.

The normalised shear modulus and internal friction of Skaergaard gabbro are plotted as a function of temperature to 1,400 K at frequencies of 1 and 0.1 Hz (Fig. 4.5 bottom). The measured shear modulus of gabbro decreases more significantly from the maximum value for data measured at 0.1 Hz (70 %) compared to 1 Hz (60 %). The softening of shear modulus is larger at lower frequency at temperatures above the glass transition temperature. At least two rising internal friction peaks are seen above 1,100 K, where the internal friction background is higher at 1 Hz than that at 0.1 Hz.

4.3.2 Time-Dependent Measurements

Microcreep experiments have also been conducted on Iceland basalt as a function of time at different temperatures (Fig. 4.6). Stress, of the order of 10^{-1} MPa, was applied instantaneously at time $t = 0$ and strain measured as a function of time. Accumulated creep strains of the order of 10^{-3} were obtained at 1,150, 1,175, 1,200, 1,250, 1,280, and 1,300 K. Displacement measured at higher temperature has higher initial value at $t = 0$ because of the deformation of the sample during the creep experiments. Therefore, all the strain data at high temperatures are offset to the same initial value as that at 1,150 K to gain better understanding on the microcreep behaviours with increasing temperature. The strain initially increases following a power law behaviour, followed by a linear behaviour with time under the applied stress. After the removal of the stress, the strain drops immediately and this is followed by a non-linear decrease as a function of time. The initial increasing rate of strain is found to get bigger in the measurements conducted at higher temperatures and the recovery of the strain after removal of the stress becomes less efficient with increasing temperature.

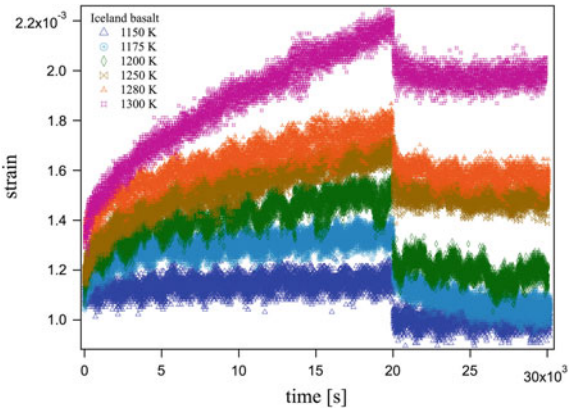

Fig. 4.6 Strain of Iceland basalt as a function of time over a temperature range at 1,150, 1,175, 1,200, 1,250, 1,280, and 1,300 K. Stress is removed after 20,000 s at each temperature. The instantaneous strain at $t = 0$ has been set to approximately 10^{-3} for all curves for clarity

4.3.3 Temperature-Dependent Measurements

The normalised shear modulus and internal friction of basalts and gabbro, all measured at 1 Hz, are shown as a function of temperature for different heating histories (Fig. 4.7). The normalised shear modulus and internal friction of I13 basalt (Fig. 4.7 top) are almost identical for both heating curves where the first heating run was restricted to temperatures just below the glass transition temperature (1,100 K) and the second heating experiment extended to temperatures above the glass transition temperature (at 1,250 K). Two maxima of shear modulus over the glass transition (detailed definition and discussions in Chap. 5) are seen in the heating curve to 1,250 K, with a corresponding increase of the internal friction above 1,100 K.

Further detailed heating histories of the normalised shear modulus and internal friction were conducted for Iceland basalt (Fig. 4.7 middle), which was heated to maximum temperatures of 1,150, 1,175, 1,200, 1,250, 1,280, and 1,300 K in turn

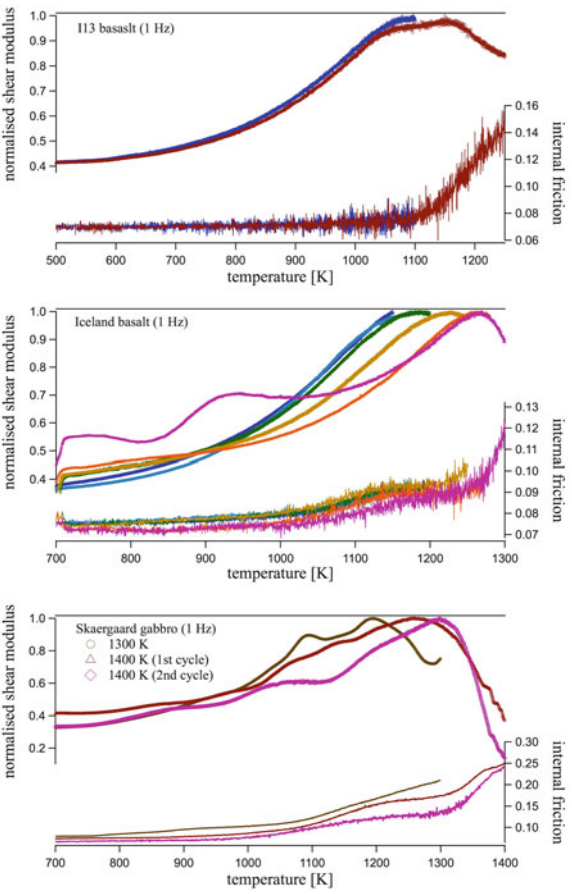

Fig. 4.7 Normalised shear modulus and internal friction of I13 basalt (*top*), Iceland basalt (*middle*) and Skaergaard gabbro (*bottom*) with different heating histories are shown as a function of temperature at cyclic stress frequency of 1 Hz

(the sample was cooled to 700 K before each heating cycle). The normalised shear modulus measurements are identical for the heating runs to 1,150, 1,175 and 1,200 K, which are temperatures below or near the glass transition temperature. The maximum point and the rising curves of the modulus shifts to higher temperature on heating to 1,250 and 1,280 K, where the previous heating run has reached the glass transition temperature in each case. The initial softening of Iceland basalt is seen near 1,280 K on heating and further softening is seen on heating to 1,300 K. The modulus of heating curve to 1,300 K shows a complex pattern (stepwise) and the maximum heating temperature is lower. The internal friction data are similar for different heating histories, expect the overall value is smaller for longer heating histories or higher maximum temperature. A broad peak occurs at temperatures between 1,000 and 1,250 K, which is followed by a rapid rising peak above 1,250 K, which coincides with the softening of the modulus.

The heating curves of gabbro show more complicated behaviour than data obtained for basalts. Data collected for the first heating run to 1,300 K, first heating to 1,400 K and second heating to 1,400 K are plotted in Fig. 4.7 (bottom). None of the normalised shear modulus patterns are similar to each others. In the first heating curve to 1,300 K, 30 % softening has found above 1,200 K, but the sample becomes stiffening again at 1,280 K. With further heating cycles to 1,400 K, the maximum of the shear modulus occurs near 1,270 K at first, and shifts to near 1,300 K in the next heating cycle. A strong softening of modulus is seen above 1,300 K and much more softening occurs when gabbro was repeatedly heated to 1,400 K. The overall internal friction amplitude decreases with repeated heating cycles. More than three broad peaks appear over the temperature range between 700 and 1,400 K on heating. It is difficult to tell whether these broad peaks in one curve are identical with those in anther run, even if they occur in the similar temperature range, because of the complexity of shear modulus behaviour in gabbro.

4.4 Mechanisms

The high values of internal friction seen in the background for I13 basalt at 5 and 10 Hz ($\tan\delta > 0.3$) are an artefact of the resonance of the pendulum, since the modulus and internal friction are primarily determined by pendulum oscillation above 2 Hz as seen in the frequency-dependent measurements (Fig. 4.4). The shear modulus data are also affected by the pendulum's natural resonance (at 50 Hz) which results in frequency-independent variations in the measurements of the sample at frequencies of 5 and 10 Hz. At lower frequencies, the internal friction background (e.g. at 1 Hz) is still higher than that seen at frequencies of 0.1 and 0.05 Hz, and data are also affected by the pendulum resonance, but less profoundly than that in higher frequency regime above 1 Hz.

The maximum shear modulus in Skaergaard gabbro shifts to higher temperature at lower frequency, which is opposite to what is expected for a simple material dominated by a thermally-activated process and opposite to the trends, shown for the

Iceland basalt data (Fig. 4.5). This is most likely due to changes in microstructure and mineralogy in the sample after repeatedly heated across the glass transition temperatures, a view which is supported by the observations at the microstructures of gabbro (Fig. 3.12), where pyroxene growth is pervasive and more evident in the samples after repeatedly heated to 1,400 K. Similarly, the complicated modulus behaviours show changes which depend on whether or not the sample is initially heated above the glass transition temperature at stress frequency of 1 Hz (Fig. 4.7).

4.4.1 Relaxation Time Distribution

The shear modulus and internal friction in the Iceland basalt show frequency-dependence (Fig. 4.4) at frequencies below 1 Hz, which implies the dominance of a thermal relaxation process at lower frequency or at higher temperature. The Cole–Cole relation (Fig. 1.7) can give the information of the relaxation time distribution for a thermal relaxation process. Hence, the storage compliance (J_1) and loss compliance (J_2) of I13 basalt (500–900 K), Iceland basalt (1,150–1,300 K) and Al_2O_3 (500–1,300 K, as a reference) have been obtained from the frequency-dependent shear modulus and internal friction data, by applying Eqs. 1.8 and 1.9. The loss compliance and storage compliance are presented as a Cole–Cole plot in Fig. 4.8 (top), where the fits for resonant peaks (1–10 Hz) of the three samples are also shown.

It is clear that the relaxation strength, the difference between relaxed and unrelaxed compliance (Δ), for Al_2O_3 is approximately constant between 500 and 1,300 K, but the relaxation strength for both basalts decreases linearly with increasing temperature (Fig. 4.8 middle). The change of relaxation strength is related to the stiffening of basalt with increasing temperature, which is interpreted here in terms of crack healing. The Cole–Cole fit results show that the distribution coefficients, c, in each sample does not change much and remains in the range 0.8–0.9, which shows that the relaxation distribution for this feature is independent of sample characteristics.

The Cole–Cole curves of Iceland basalt (Fig. 4.8 top) indicate two relaxation processes in the system. Two Cole–Cole circles are seen and the data at ,1300 K were analysed and fitted by the Cole–Cole distribution function (Eq. 1.20) in Fig. 4.8 (bottom). The relaxation process in the smaller storage compliance regime (corresponding to high frequencies between 1 and 10 Hz) is associated with a resonance with a distribution parameter $c = 0.84 \pm 0.02$, which is close to unity (nearly a perfect single relaxation time). The other relaxation process, seen at larger storage compliances (corresponding to low frequencies between 0.05 and 1 Hz) is associated with other relaxation processes in the basalt. The data are far from complete, and only a partial Cole–Cole semi-circle can be measured, but from this a distribution factor of $c = 0.37 \pm 0.04$ is obtained (a broad relaxation time distribution). The Cole–Cole circle of this relaxation process is more depressed than that of the main semicircle, and more than one relaxation process or relaxation time characterises the mechanical response of basalt as seen in these experiments.

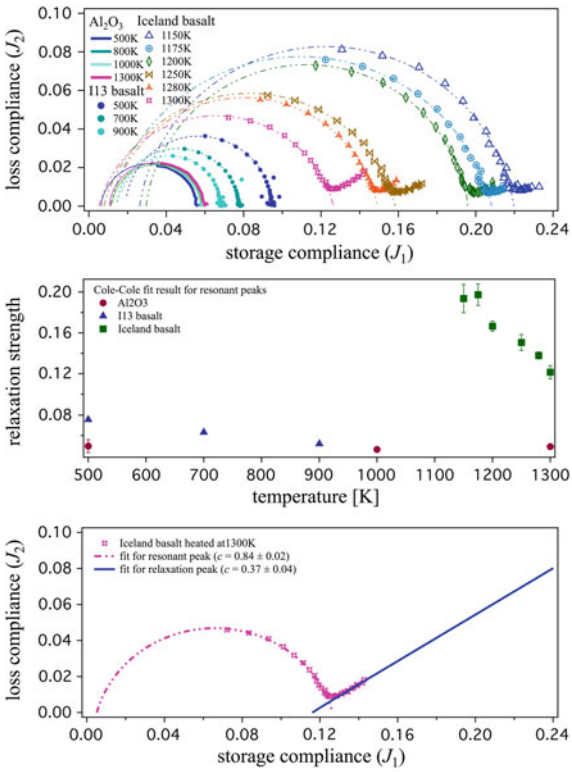

Fig. 4.8 (*top*) Cole–Cole plot of I13 basalt, Iceland basalt and Al_2O_3 for different frequency-dependent isothermal measurements and the fitting patterns for resonant peaks. (*middle*) The relaxation strength (radius of Cole–Cole fit circle) of resonant peaks against temperature. (*bottom*) Results for data obtained from Iceland basalt at 1,300 K, giving $c = 0.84 \pm 0.02$ for the pendulum resonance (data at 1–10 Hz) and $c = 0.37 \pm 0.04$ for the relaxation process (data at 0.05–1 Hz)

With increasing temperature, the curvature of the higher frequency semi-circle remains for all samples largely unchanged (c is close to 0.9 at all temperatures), although the radius (half the compliance strength) becomes smaller at high temperature. These findings indicate that the resonance is stable over the temperature and frequency domain of the measurements, although the difference between unrelaxed and relaxed compliance decreases at high temperature. The Cole–Cole plot corresponding to the basalt sample at low frequency and its relaxation processes become stronger and less depressed at high temperature, showing that the relaxation processes in the sample become simpler as the sample is annealed at higher temperatures.

4.4.2 Microcreep Flow

Since the strain behaviours under constant stress creep experiments in Iceland basalt are found to follow an initial power law pattern which then leads to a linear trend (Fig. 4.9 top), they may be described by the Andrade model (Eq. 4.2). The strain has thus been analysed with an Andrade form of expression, with

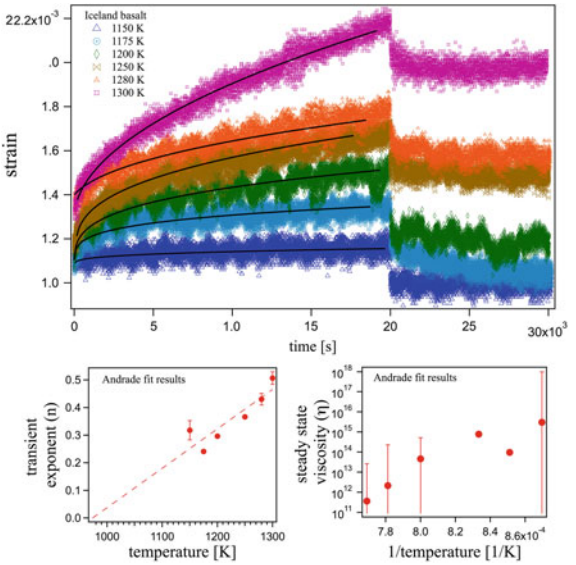

Fig. 4.9 The results of fitting the strain of Iceland basalt as a function of time (*top*) to the Andrade model, where the *black lines* are the Andrade model fitting results, and the resultant transient exponent against temperature (*bottom left*) and steady state viscosity with standard deviations (calculated from fit results) against inverse temperature (*bottom right*)

$\varepsilon = A_1 + A_2 t^n + A_3 t/\eta_{ss}$, where A_1, A_2, A_3 are material-dependent pre-factors. The resultant exponent n in the power law transient term is found to lie between 1/4 and 1/2 at temperatures between 1,150 and 1,300 K, and the exponent tends to increasing values with temperature (Fig. 4.9 bottom left). Gribb and Cooper also found their exponent for transient creep converges to $n = 1/2$ when $t \leq 0.2\tau_n$, that Gribb and Cooper define τ_n by $\tau_n \cong \frac{10\sigma_{xy}}{E\dot{\gamma}_{ss}} = \frac{10\eta_{ss}}{E} \cong \frac{4\eta_{ss}}{G}$ (where σ_{xy} is stress, $\dot{\gamma}_{ss}$ is the steady state strain rate, η_{ss} is the steady state shear viscosity, E is Young's modulus, and G is the shear modulus) [15] in polycrystalline olivine, measured by torsional apparatus at high temperatures (1,473–1,558 K) and low frequency (0.001–1 Hz) and attribute this to grain boundary diffusional creep, where stress concentrations at the triple junction of grain boundaries are relaxed by chemical diffusion along grain boundaries.

Gribb and Cooper suggest that the viscoelastic attenuation (Q^{-1}) is related to frequency (f), as expressed as $1/\tau_n$, following a power law behaviour ($Q^{-1} \propto f^{-m_n}$). This may be related to the Andrade transient exponent (n), as the attenuation of such viscoelastic materials is linked to the universal creep behaviour deformation through grain boundary diffusion. In this model, grain boundary diffusional creep is dominated by linear steady state behaviour at low frequency ($<0.3/\tau_n$) and hence attenuation responds linearly to frequency with $m_n = 1$. At intermediate frequencies (between $0.3/\tau_n$ and $1,000/\tau_n$), transient creep behaviour becomes important in addition to the steady state response, and this leads attenuation (which depends on frequency) with exponents $0.25 \leqslant m_n \leqslant 0.4$. At further higher frequency ($>1,000/\tau_n$), elastic behaviour dominates and is associated with transient creep

responses which results in $m_n = 0.5$ for the attenuation-frequency relation. The frequency exponent at intermediate frequency ($0.25 \leqslant m_n \leqslant 0.4$) may be related to the Andrade model following the empirical correlation observed by Gribb and Cooper, giving an Andrade transient exponent with $1/3 \leqslant n \leqslant 1/2$ [15], and corresponds to the transient strain of the diffusional transient creep. The values of n found in this study (Fig. 4.9 bottom left) appear to follow Gribb and Cooper's model, suggesting the transient creep behaviour in Iceland basalt (at 1,150–1,300 K) is controlled by the chemical diffusion. The extrapolation of the transient exponent indicates $n = 0$ at 974 K, which implies that creep behaviour is unlikely to occur below this temperature. Even though creep may not occur, thermal relaxation (Debye peaks) can still appear in the low temperature (discussed in the later section), since they may arise from different processes.

The viscosity of Iceland basalt may also be obtained from analysis of the creep data using the Andrade model for the high temperature data (Fig. 4.9 bottom right). The viscosity decreases with temperature and is close to a viscosity between 10^{11} and 10^{12} Pa.s at 1,300 K. The viscosity at which a material transforms from a viscous material (supercooled liquid) to an elastic solid (glass) is typically taken as 10^{13} poise (10^{12} Pa.s) [28], indicating the data for basalt are at the threshold of viscous behaviour. The trend to viscous flow at temperatures close to 1,300 K is supported by the observation of shear modulus softening in Iceland basalt, seen in this study above 1,270 K (Fig. 4.7 middle). Viscosity may be anticipated to follow an Arrhenius relation ($\eta = \eta_0 \exp(E_{act}/\mathrm{R}T)$), although some other studies have used the Vogel-Fulcher-Tamman relation to describe their data (where T is replaced by $T - T_0$ in the viscosity equation). The Vogel-Fulcher-Tamman relation is suitable to describe mechanical behaviour which contains low temperature glass viscosity (below the glass transition temperature) and high temperature melt viscosity (above the glass transition temperature) in one dataset. The creep data in this study are collected at temperatures below the glass transition of basalt, and hence it is sufficient to describe the viscosity behaviour with the Arrhenius relation to give an effective activation energy. Following this approach, the slope from viscosity against reciprocal temperature (Fig. 4.9 bottom right) gives an activation energy of 654 ± 140 kJ/mol for steady state creep in Iceland basalt.

The viscosity obtained from the Andrade model is plotted in Fig. 4.10 and compared with previous measurements of other basaltic rocks measured at low strain rates of $10^{-3} - 10^{-7}$ s^{-1} by creep apparatus [29], torsion oscillation [22], and the fibre-extension method [28], and at high strain rates of $\sim 10^{-2}$–10^{2} s^{-1} by rotational viscometer [30, 31], concentric cylinder viscometer [32] and rotating cup viscometer [33]. Despite the differences in chemistry and microstructures among samples (as well as experimental methods), the main difference of viscosity found in these measurements is from the effect of the magnitude of strain rates. The high strain-rate experiments result in relatively small viscosity while high viscosity is obtained in the low strain-rate experiments.

In low strain-rate experiments, the internal structure of the basalts is not destroyed and the resultant creep behaviours can be considered to be controlled by essentially anelastic relaxation processes. In high-strain experiments (by viscometer), high stress

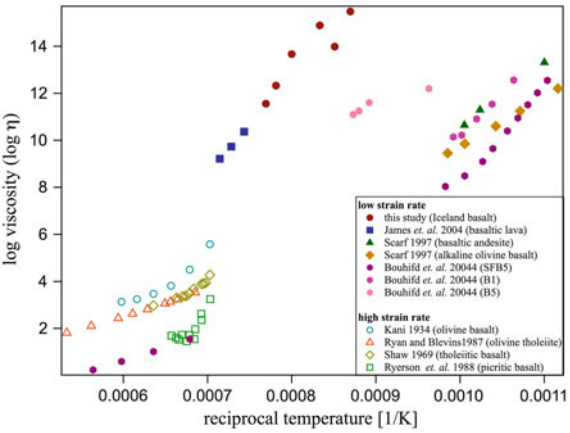

Fig. 4.10 The viscosity of Iceland basalt in this study are presented as a function of inverse temperature and compared with other studies in the literatures. *B1* Stein Frentz alkali basalt (SFB), *B5* SFB sample previously annealed in air at 973 K for 24 h, *SFB5* synthetic glass simulating the residual SFB melt phase during basalt crystallisation for 5 vol% crystal fraction. From [22, 28–33]

and strain disrupt the intrinsic microstructural nature of the sample (such as the deformation of gas bubbles or the rotation, interaction and small displacement of suspensions in the viscous melt matrix) with time and may result in two viscosities depending on stress-strain scale [22]. This results in a lower activation energy at high temperature and large activation energy in the low temperature. These findings are supported by the stress-strain rate study on a Hawaii tholeiitic basalt at 990 K (10^{-3} and 10^{-6} s^{-1}) [34]. The results show that the viscosity is constant at low strain rate (Newtonian behaviour) and decreases with increasing strain rate at strain rates greater than 5×10^{-5} s^{-1} (non-Newtonian behaviour).

The activation energy for the viscous flow in Iceland basalt (654 ± 140 kJ/mol) is lower than that previously measured in basaltic lavas (760 ± 26 kJ/mol from Arrhenius relation, but 950 ± 5 kJ/mol in James et al.'s paper which include data collected in dilatometer) and higher than that in basaltic andesite (589 ± 21 kJ/mol), but in each case lie within one standard deviation of these values. The activation energy in this study is, therefore, similar to the studies of James et al. [22] in basaltic lavas and Scarf [28] in basaltic andesite if taking one standard deviation into consideration. Scarf [28] suggested the compositional effects result in different temperature-dependent viscosity trends, based on experimental observations in four different basaltic rocks (basaltic andesite, tholeiite, alkaline olivine basalt, olivine melamephelinite). The higher content of the network-forming oxides SiO_2 and Al_2O_3 contributes to higher viscosity in basaltic andesite. However, this effect is uncertain in Iceland basalt, partly because these data are obtained from rather a different approach, and compositional variations have not been directly probed.

One of Bouhifd et al.'s data sets [29], from a sample that was previously annealed in air at 973 K for one day, is seen to fill in the gap between Scarfe's work and the data in James' and in this study. The alkali basalt (SFB) and synthetic basaltic glass in Bouhifd et al.'s studies show similar viscosity at 900–1,000 K as Scarfe's data in which both samples were powdered from basalt and fully melted before being cooled and solidifying. Bouhifd et al.'s data indicate that the thermal history of the samples

controls the viscosity of partially-crystallised basalt. In contrast, data from natural rocks (lava in James et al.' study and basalt in this study) in the similar viscosity range occur at temperatures between 1,100 and 1,400 K. The corresponding temperature for viscosity of basalt deformed at low strain rates may, therefore, depend on thermal history or degree of crystallinity in the sample.

Two viscosities are also obtained from Scarfe's studies for samples at temperatures below and above the glass transition temperature [28, 35], where bond breaking (or rupture) is suggested for low temperature flow mechanism and depolymerisation of melt structures is proposed as responsible for the high temperature flow mechanism [36]. The activation energies obtained in Scarfe's work show that the ratio of the activation energies from low temperature viscosity and high temperature viscosity is approximately 2:1 among four basaltic rocks. If this relation is applicable to this study, the activation energy of Iceland basalt is expected to be $\sim 327 \pm 70$ kJ/mol above 1,270 K.

4.4.3 Thermally-Activated Relaxation Processes

In the temperature-dependent dynamic pendulum experiments, the shear modulus is found to increase initially with increasing temperature in all experiments. This is rather unexpected and merits consideration. This effect may be attributed to the closure of the thermal cracks (Chap. 5). Initial samples are somewhat porous and contain vesicles and cracks. The largest changes (60–95 %) of shear modulus on heating are found in I13 basalt than those in Iceland basalt and in gabbro (Fig. 4.5), which may indicate that I13 basalt has more pre-existing micro-cracks and pores, which may even lead to crack percolation when the sample was cooled from above the glass transition temperature (examples and further discussions in Chap. 5). The suggestion of crack healing processes dominating is also supported by the findings from different heating histories for Iceland basalt (Fig. 4.4), since the shear modulus curve shifts to higher temperature with repeated annealed and increased thermal history of the sample.

Several thermally-activated relaxations processes, superimposed on the exponential high-temperature background, are also seen in basalts and gabbro. The universal exponentially increasing attenuation, generally referred to as "high-temperature background" in materials science [37] and sometimes referred to as an "attenuation band" in seismology [38], was also seen in early studies of metals [17, 39, 40] and concluded to be controlled by diffusion-controlled relaxations (involving dislocation motion, such as climb and glide of bowing dislocations), under conditions where relaxation can be maintained in the material. If the material becomes plastically viscous through a thermally-activated process at high temperature, the material will lose its anelastic character and show viscous behaviour such as Nabarro-Herring creep, in which atoms diffuse through the lattice and cause grains to elongate parallel to the stress axis [37]. Hence, the high-temperature background can be considered to be associated with the high temperature behaviour of dislocations. In addition

to the intrinsic effects of the high-temperature background, Woirgard and Gueguen [24] found that thermal cracks can also influence the high-temperature background by observing discrepancies in the background between annealed and non-annealed peridotite [24]. They suggest that crack volume was increased by the presence of thermal stresses during annealing and thus enhanced the contribution to the background.

To obtain the activation energies for relaxation processes associated with the high-temperature background, an expression obtained by combining Eqs. 1.24 and 1.26 has been used in this study:

$$\tan\delta = A_1 + \frac{\Delta}{2}\cosh^{-1}\left[\frac{E_{\text{act}}}{\text{R}}\left(\frac{1}{T}-\frac{1}{T_P}\right)\right] + \frac{A_2}{(\omega e^{E_{\text{HTB}}/\text{R}T})^{\text{n}}} \tag{4.3}$$

where A_1 and A_2 are pre-factors, for internal friction with a single relaxation peak. For more relaxation peaks, multiple terms of Eq. 1.24 are added into Eq. 4.3. Based on Jackson et al.'s model [16] of high-temperature background corresponding to the transient term in the Andrade model, n may be fixed at 0.5 for all the fittings for high-temperature background in this study, since n approaches 0.5 in the creep measurements of Iceland basalt above the glass transition temperature (Fig. 4.9). The fitting results are shown in Fig. 4.11 for basalts and in Fig. 4.12 for gabbro. Relaxation peaks are labelled as peak 1 to peak 4 from low to high temperature in each sample. The activation energy for each Debye relaxation peak and for the apparent high-temperature background (HTB $= n \times E_{\text{HTB}}$) are presented in Table 4.1 for I13 basalt, Iceland basalt and Skaergaard gabbro.

The apparent activation energies for high-temperature background (HTB) in the table give an average value of 140 ± 80 kJ/mol for basalts and of 180 ± 120 kJ/mol for gabbro. The higher activation energy in I13 basalt than that of Iceland basalt may be due to thermal cracks on the I13 basalt at low temperatures (400–900 K), which would fit with Woirgard and Gueguen [24]'s assumption. The results of apparent activation energy in this study are in a good agreement with Kampfmann and Berckhemer [11] and Fontaine et al. [10]. The apparent activation energies reported by Kampfmann and Berckhemer [11] for high-temperature background are between 100 and 200 kJ/mol at high temperatures ($T > 0.8\ T_{\text{m}}$), in magmatic rocks (dunite, peridotite, gabbro and basalts). They explain this apparent activation energy in terms of the relaxation of pinned dislocation lines, for which 92–168 kJ/mol was obtained for a diopside-bearing hornblende gabbro and 159–196 kJ/mol for a basalt from Eifel [11]. The HTB results of basalts and gabbro in this study are in a good agreement with the study of Kampfmann and Berckhemer.

On the other hand, a gabbro from the Oman ophiolite (to 1,441 K) studied by Fontaine et al. [10] showed a lower energy for the apparent high-temperature background (70 ± 1 kJ/mol). The activation energy for the high-temperature background in gabbro from Fontaine et al. (873 ± 13 kJ/mol with an exponent 0.08), using linear regression from Jackson et al. ([9]; Fig. 4.9), is still higher than that obtained by Kampfmann and Berckhemer (730 ± 290 kJ/mol with an exponent 0.19). Fontaine et al. attribute the discrepancy and their higher activation energy to a high melt

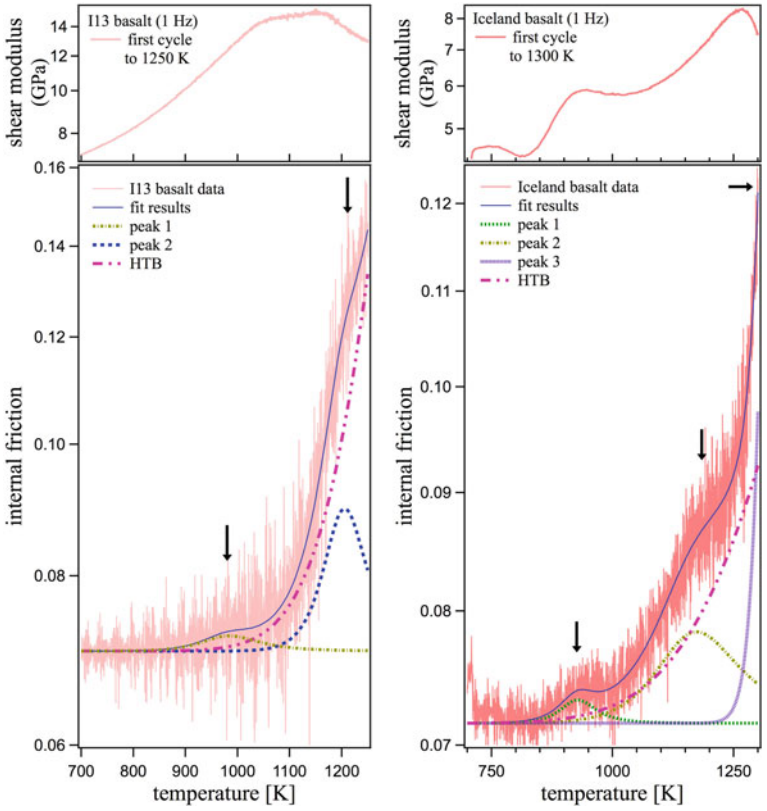

Fig. 4.11 The fit results of internal friction of I13 basalt (*left*) and Iceland basalt (*right*) with Deybe and high temperature models. Two relaxation peaks with high-temperature background is fitted for the I13 basalt data and three relaxation peaks with high-temperature background are fitted to internal friction for Iceland basalt. The corresponding shear modulus of the samples is presented above the internal friction graphs. The internal friction axis is plotted on a logarithmic scale to show the small internal friction peak more clearly

fraction in their samples. However, this explanation does not accord with observations from two heating curves at temperatures below and above the glass transition temperature in gabbro from this study, where no such change in activation energy from the high temperature background is found, despite the obvious change in melt (or glass) fraction.

Assuming each relaxation peak is due to a relaxation process with one single relaxation time, the apparent activation energies of relaxation peaks from fitting to the Debye expression can be grouped into at least three major categories of relaxation process, namely low energy 'below 300 kJ/mol', intermediate energy 'between 300 and 600 kJ/mol', and high energy 'above 600 kJ/mol' (Table 4.1). The large range of values in this study reflects the different mechanisms that have been proposed, with a variety of activation energies, to exist in similar materials. These include crack

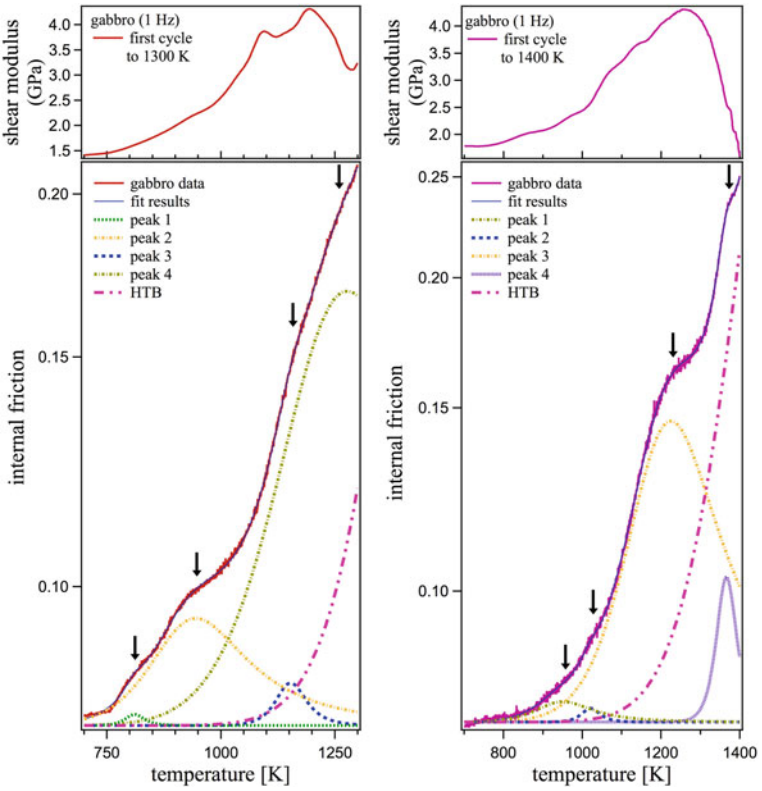

Fig. 4.12 The fit results of internal friction of gabbro with Deybe and high temperature models in the heating curves of first cycle to 1,300 K (*left*) and first cycle to 1,400 K (*right*). Four relaxation peaks are fitted together with a high-temperature background in both heating curves. The corresponding shear modulus is presented above the internal friction graphs. The internal friction axis is plotted on a logarithmic scale to show the small internal friction peak more clearly

healing, oxidation, crystallisation, self-diffusion, dislocation movement (creep), and partial melting.

Crack healing processes, which are thermal activated, have been studied extensively in quartz [41–43] and indicated the activation energy for crack healing in quartz at 873 K (or below) is between 35 and 80 kJ/mol with 200 MPa fluid pressure, where the activation energy for a diffusional aqueous solution is about 21 kJ/mol for comparison (discussions of crack propagation and fluid pressure can be found in Chap. 7). James et al. suggest that an activation energy of 150 ± 20 kJ/mol obtained in annealed Etna basaltic lava, using the Arrhenius relation between characteristic time and temperature, is attributed to a crack healing process. The activation process corresponds to the effective diffusion coefficient of elements associated with pinching at microcracks at grain boundaries [41]. The crack healing process (the closure of the crack) in a sample will enhance the strength of the material and, therefore,

Table 4.1 Activation energies (kJ/mole) for Debye relaxation peaks and the apparent high-temperature background (HTB $= n \times E_{\mathrm{HTB}}$, where $n = 0.5$) at temperatures where internal friction relaxation peaks (tanδ peaks) occur for heating curves in I13 basalt to 1,250 K, Iceland basalt to 1,300 K, gabbro firstly to 1,300 K (a), and gabbro firstly to 1,400 K (b)

Sample	I13 basalt	Iceland basalt	Gabbro (a)	Gabbro (b)
tanδ peak			290 ± 30	
(below 900 K)			at 811 ± 1 K	
tanδ peak	170 ± 70	220 ± 60	82 ± 2	118 ± 10
(900–1,000 K)	at 984 ± 15 K	at 928 ± 6 K	at 945 ± 2 K	at 950 ± 8 K
tanδ peak		152 ± 50	380 ± 30	420 ± 60
(1,000–1,200 K)		at $1{,}173 \pm 18$ K	at $1{,}153 \pm 1$ K	at $1{,}021 \pm 2$ K
tanδ peak	350 ± 40		109 ± 2	135 ± 1
(1,200–1,300 K)	at $1{,}206 \pm 4$ K		at $1{,}277 \pm 19$ K	at $1{,}225 \pm 1$ K
tanδ peak		840 ± 170		730 ± 20
(above 1,300 K)		at $1{,}340 \pm 230$ K		at $1{,}366.0 \pm 0.3$ K
E_{HTB}	365 ± 60	200 ± 80	380 ± 240	359 ± 6
HTB	180 ± 30	100 ± 40	190 ± 120	179 ± 3

for relaxation peaks with small energy, one anticipates a corresponding increasing shear modulus on heating due to crack healing.

In this study, hydrogen is continuously lost under high vacuum and hence the self-oxidation in the sample is possible to occur. Crystallisation and oxidation is commonly known to occur on cooling from a melt, whereas recrystallisation and grain growth can also happen on re-heating [44]. The crystallisation and oxidation of the crystals can also contribute to an increase of sample strength. Burkhard carried out re-heating experiments on Kilauea basalt glass at temperatures to 1,363 K, which show the formation of pyroxene dendrites and Fe–Ti oxides occur below 1,113 K, followed by the bulk crystallisation of basaltic glass and the growth of plagioclase above 1,150 K. Similarly, clinopyroxene growth with increasing temperature is found in this study (Fig. 3.12), leading to large areas of contiguous pyroxene in the matrix above 1,400 K; however, the amount of olivine, plagioclase, and bulk Fe–Ti oxides with symplectic structures reduces with temperature, as seen from thin section observations (Fig. 3.14).

The activation energy for Fe^{3+} formation (oxidisation) from Burkhard's study [44], which is caused by the removal of cations, is obtained as ~100 kJ/mol [45], and found to be associated with the diffusion of cations (Ca^{2+} and Mg^{2+}) and vacancy exchange (~210 kJ/mol) [46]. The nucleation and growth rates of pyroxene, plagioclase and Fe–Ti oxides in Kilauea basaltic glass have also been studied at temperatures to 1,263 K [45]. The nucleation and growth rates for these three minerals have a minimum at 1,203 K and show positive Arrhenius behaviour above 1,103 K. Activation energies of nucleation and growth (± 7 kJ/mol) are obtained for pyroxene (180 and 200 kJ/mol), for plagioclase (353 and 307 kJ/mol), and for Fe–Ti oxides (292 and 343 kJ/mol) [45]. At temperatures between 1,053 and 1,293 K (except 1,233–1,263 K), the growth rate of pyroxene is generally higher than that of both plagioclase

and Fe–Ti oxides. This may explain the pervasive growth of (and replacement by) pyroxene in the gabbro groundmass observed at 1,400 K at this study.

Self-diffusion spontaneously occurs as temperature increases. At high temperature, grain boundary diffusion can exceed crystal lattice diffusion. Diffusion experiments [47] show that activation energies for cation inter-diffusion in the relevant minerals for this study are 516 ± 19 kJ/mol for CaAl–NaSi in feldspar (1,373–1,673 K), ~233 kJ/mol for Fe–Mg in orthopyroxene (873–1,073 K), 361 ± 190 kJ/mol for Ca–(Mg, Fe) in clinopyroxene (1,423–1,523 K), and 214 ± 19 kJ/mol for Fe–Mg in olivine (1,173–1,373 K). In the same study, activation energies for O diffusion in Goose Island basalt melt were found to be 216 ± 13 kJ/mol (1,433–1,633 K). Generally, the activation energies of Si and O diffusion are between 180 and 400 kJ/mol and that for alkali species is lower (<170 kJ/mol) in basalt and rhyolite [48]. The activation energy for Si diffusion is greater than that for O diffusion and the activation energy decreases with the increasing pressure [49], whereas both activation energies can be similar if Si and O diffusion are associated with motions of high-coordinated species. For example, one non-bridging O of one $(SiO_4)^{4-}$ tetrahedron impinges on another $(SiO_4)^{4-}$ tetrahedron that leads to all bridging oxygen bonded with Si. This model has been used to explain Lesher et al.'s findings in synthesised basalt enriched in ^{30}Si and ^{18}O, that the activation energy is 170 ± 2 kJ/mol (1,593–1,873 K and 1 GPa) for both Si and O diffusion [50]. These activation energies for self-diffusion may be applicable to explain the relaxation peaks over the intermediate energy range in this study, where the shear modulus either increase or becomes flat, even though the effects of self-diffusion on the shear modulus are still unknown in basalts and gabbro.

Diffusional creep on the grain boundaries generally gives a larger activation energy (>300 kJ/mol), which often involves the movements of dislocations and defects. The activation energy for the dissipation at high temperature to 1,573 K in fine-grained polycrystalline olivine is found to be 410 ± 54 kJ/mol and is assumed to be due to diffusional processes, using torsional forced-oscillation and microcreep methods [7, 9]. Kampfmann and Berckhemer [11] explain the relaxation peak (400–600 kJ/mol) occurring in magmatic rocks (including basalt and gabbro), at temperatures between 873 and 1,773 K under forced torsional oscillations, as a dislocation controlled grain boundary relaxation peak [11]. Their observation and model are consistent with the activation energy for the dislocation climb and diffusion (585 ± 125 kJ/mol) in olivine determined in the Mt. Albert peridotite, at temperatures between 1,563 and 1,723 K, where the diffusion along dislocation cores activates the climb of dislocations into subboundaries [51]. Diffusional creep on grain boundary (grain boundary sliding) may be also responsible for the relaxation peaks with activation energy between 300 and 500 kJ/mol in basalts and gabbro in this study.

On the other hand, a relaxation process for natural dunite (to 1,673 K) with activation energy of 732 kJ/mol and for polycrystalline forsterite (to 1,773 K) with activation energy of 627 kJ/mole have been explained in terms of motions of thermally-activated lattice defects in forced-oscillation experiments carried out by Berckhemer et al. [21]. Berckhemer et al. suggest this high activation energy may be due to multiple contributions from Si and O self diffusion, jog and kink

pair-formation associated with bowing of dislocations, and temperature-dependence of the relaxation strength. Alternatively, shear creep and attenuation experiments on fine grain polycrystalline olivine, using subresonant torsion apparatus, shows the same activation energy for melt-free and melt-bearing samples (700 ± 30 kJ/mol) at temperatures from 1,323 to 1,573 K, while the presence of melt reduces the shear viscosity of the sample [52]. Gribb and Cooper [52] suggest that diffusion is enhanced by the melt network and the high activation energy for diffusional creep in olivine does not result from the melt, but is due to impurities on the grain boundary, including chemical segregation of Ca^{2+}, as an impurity, diffusing on to the grain boundary. This may explain the high activation energy (above 650 kJ/mol) in this study where a small amount of partial melting is found in the Iceland basalt and gabbro.

At very high temperature, the contribution of the steady state creep may influence measurements of anelastic deformation, which results in potential overestimation of internal friction. Kampfmann and Berckhemer [11] explored this effect in their study of the strain rate behaviour of forsterite (1,658–1,858 K), gabbro (1,188–1,336 K) and Eifel basalt (1,113–1,261 K) at constant torque between 75 and 300 kPa and analysed the remaining plastic deformation after relaxation. The largest influence to the total attenuation was found in forsterite at 1,858 K and 0.003 Hz with a effect of $<20\,\%$ and this effect decreases rapidly with decreasing temperature or increasing frequency. Hence, any effect from high temperature steady state creep on internal friction can be ignored in this study.

4.5 Conclusion

To a first approximation, basalt and gabbro may be considered as similar in composition but differing in grain size. It is expected that one might see differences in grain size effects between them, especially in the light of the studies of Kê [8] and Jackson et al. [9]. However, there seems to be no direct evidence to show that grain size has a significant effect on the internal friction in both basalt and gabbro in this study. Grain sizes effects are also not seen by Fontaine [10] and by Kampfmann and Berckhemer [11]. The relaxation peaks of basalt and gabbro at high temperature are strongly affected by the microstructure and diffusion in the lattice within grains or across grain boundaries, which may override the effects from grain size such that grain size effect can be neglected in the presence of highly complex mineral assemblies and associated microstructures in natural rocks. According to this study, different mechanisms appear to dominate the measured attenuation with two attenuation peaks seen in theoleiitic basalt at 893 and at 1,103 K as found by Weiner et al. [23] rather than the effects due to bimodal grain size distribution that are proposed by Weiner et al. in their paper.

Grain size effects may become important to some extent if grain boundaries are completely wetted by partial melting. If more than 10 % melt is generated, a thin layer of melt forms and fills grain boundaries, resulting in a completely wetted grain surface [53]. According to the coated sphere model, where each sphere (grain) is coated with

a rim (melt film), provided by Salje [54], the elastic moduli of the material begins to decrease (softening) due to soft interfaces when the rim proportion (the volume proportion of the melt film relative to the grain) is larger than 0.1 % [54]. The grain size effects, therefore, will be significant for materials of grain size on the μm scale with a ∼10 nm thick interface. This may explain the grain size sensitivity to shear attenuation in melt-bearing fine-grained polycrystalline olivine (3–23 μm [9]), where the grain boundary thickness (film thickness) is relatively large compared to the grain size. Based on the melt fraction observation at different temperatures in the study of Fontaine [10], less than 2 % of partial melting is likely generated in Skaergaard gabbro (to 1,400 K) and maybe much less in basalts (to 1,300 K), where melt may have accumulated at the triple junctions of grain boundaries [53]. In this case, there may be no melt film at grain boundaries (the soft interface in Salje's model) in the basalts and gabbro of this study. The lack of soft interface in the samples studied here may explain the weak influence of grain size on the shear modulus and internal friction in this study.

Pressure is also important when considering relaxation processes and attenuation in the deep Earth. As diffusion experiments carried out in synthetic dacite melt from 1 to 5.7 GPa and from 1,628 to 1,935 K demonstrate that increasing pressure suppresses the activation energy of both Si and O diffusion processes (293–380 kJ/mol at 1 GPa and 155–163 kJ/mol at 4 GPa) [49]. For a thermally-activated relaxation processes, the effects of pressure on amplitude of the attenuation can be ignored if the resultant activation energy is in the order of 10^2–10^3 kJ/mol, which can be demonstrated by Eq. 1.25. However, the decreasing activation energy contributes to broadened relaxation peaks, which makes the temperature range for the relaxation process larger. For example, the relaxation process activates over a temperature range of 200 K at activation energy 500 kJ/mol but extends over a range of 500 K at activation energies 100 kJ/mol. In other words, the relaxation peaks become broadened, but the amplitude of the peak remains the same with increasing pressure, which is similar to the effect of the broaden distribution factor function ($r(c)$).

Fontaine et al. [10] suggest a pressure dependence for the high-temperature background in terms of $\exp(-P\Delta V/\mathrm{R}T)$, where ΔV is the activation volume and P is pressure [10]. They demonstrate that attenuation is reduced by 7 % in a dry anorthite ($\Delta V = 24$ cm^3/mol) and results in a difference by 7 kJ/mol for activation energy at 973 K and at a depth of 10 km (∼0.3 GPa), where they assume the thermal conditions are dominated by high-temperature background. According to their calculations, the pressure effect is not significant for high temperature attenuation background in the lithosphere for temperature greater than 673 K and pressure less than 0.5 GPa.

The internal friction measurements in this study show that the microstructures and composition of basalts and gabbro changes when the samples are heated across or above the glass transition temperature and this then leads to a different attenuation pattern compared to those in the previous heating history. Different thermally-activated relaxation processes occur when sample is heated up and the mechanisms for the relaxation peaks are not the same for the different samples. More complicated relaxation processes occur in these natural and complicated microstructures with additional compositional complexity.

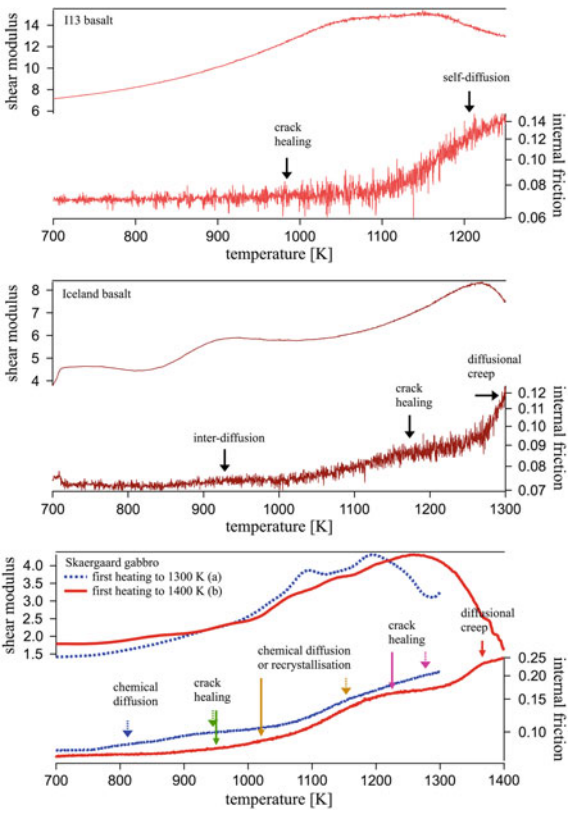

Fig. 4.13 The mechanisms for thermal activated relaxation processes on heating in I13 basalt (*top*), Iceland basalt (*middle*) and Skaergaard gabbro (*bottom*). *Arrows* point out the occurrence of mechanism at each temperature regime

In I13 basalt, two relaxation processes are found when the sample is heated from 700 to 1,250 K (Fig. 4.13 top). The data are consistent with a model in which, as the temperature increases, cracks start to close at 984 ± 15 K (170 ± 70 kJ/mol) and hence the shear modulus increases. With further heating, the shear modulus flattens across the glass transition temperature and then starts to decrease from 1,100 to 1,250 K, with corresponding large attenuation that may be attributed to nucleation and growth of crystals (plagioclase and Fe–Ti oxides), Si and O self diffusion or the climb of dislocations (350 ± 40 kJ/mol). At the onset of softening towards melting, Si-O bond exchange (Si and O diffusion) may dominate and be responsible for the attenuation peak at 1,206 ± 4 K.

Iceland basalt shows more complicated behaviour than I13 basalt. Three relaxation processes are found at temperatures between 700 and 1,300 K (Fig. 4.13 middle) after the sample had been repeatedly annealed between 700 and 1,100 K more than ten times. On heating, a low-temperature relaxation process at 928 ± 6 K occurs which, given the activation energy observed, may be due to Fe–Mg intracrystalline partitioning in orthopyroxene (220 ± 60 kJ/mol), as the shear modulus increases rapidly and reaches a temporary maximum. Then, the behaviour appears similar to I13 basalt and

is again consistent with closure of cracks starting at 1,173 ± 18 K (150 ± 50 kJ/mol), which generates a rising internal friction, with a gradual increase of shear modulus below the glass transition temperature, near 1,270 K. Above 1,270 K, the behaviour is consistent with a model in which melt-enhanced diffusional creep associated with dislocation climb (840 ± 170 kJ/mol) dominates and causes the attenuation peak at 1,340 ± 230 K. The high activation energy for this attenuation peak may be due to impurities (such as Ca^{2+} and Mg^{2+}) on the grain boundaries. Without detailed analysis of sample microstructures in situ under these conditions (which is difficult to say the least) it is difficult to be certain of the discrete processes involved.

Four relaxations processes are seen, separately, in two gabbro datasets from heated to 1,300 K (a) and 1,400 K (b) (Fig. 4.13 bottom). The last three high temperature peaks in curve (a) appear to have similar characteristics to the first three low-temperature peaks in curve (b). These three relaxations show larger activation energy and tend to occur at lower temperature in subsequent heating runs (curve (b)). Based on these findings, five relaxation processes appear to occur in the Skaergaard gabbro at temperatures between 700 and 1,400 K. When samples are heated from 700 K, a peak that can be attributed to chemical diffusion (Si and O) (290 ± 30 kJ/mol) occurs at 811 ± 1 K, but this relaxation disappears on reheating may be due to changes in microstructure and mineralogy (such as the growth of pyroxene) that likely occur on heating towards melting in the previous cycle. On further heating a peak occurs consistent with first stage crack healing at 945 ± 2 K for curve (a) (82 ± 2 kJ/mol). This effect becomes less pronounced on further reheating (curve (b)) (118 ± 10 kJ/mol) in the same temperature window (950 ± 8 K).

With further heating, chemical diffusion (Si and O) or recrystallisation and growth of plagioclase seem to dominate the anelastic behaviour at 1,153 ± 1 K (in the first heating curve (a)) (380 ± 30 kJ/mol) and this shifts to lower temperature (1,021 ± 2 K) in the reheating data (curve (b)) (420 ± 60 kJ/mol). The increase in activation energy suggests recrystallisation is likely the major controlling factor during additional heating runs. At temperatures near the glass transition temperature, a further peak occurs at 1,277 ± 19 K in curve (a) (109 ± 2 kJ/mol). It may be that oxidation occurs at this stage, and crack healing appears to occur at lower temperature (curve (b)) (135 ± 1 kJ/mol) at 1,225 ± 1 K. At temperatures above the glass transition temperature, melt-enhanced diffusional creep occurs, at 1,366.0 ± 0.3 K (730 ± 20 kJ/mol) when sample is heated to 1,400 K and cations (such as Ca^{2+} and Mg^{2+}) may segregate onto the grain boundary and hence a high activation energy is seen due to the presence of the impurities on the grain boundary.

4.5.1 Concluding Remarks

Overall, it is difficult to assign particular atomistic processes to each and every feature seen in the anelastic datasets obtained. What is certain is that mineralogical changes and the changes in melt/glass distributions are likely in these samples as they are heated under stress to temperatures beyond the solidus. These changes

manifest themselves as modified mechanical behaviour on repeated heating/cooling cycles. Here I have attempted to attribute particular anelastic relaxation processes seen in the data to particular processes, but such attribution is frustratingly speculative in many cases. What is certain is that, for real polymineralic natural igneous rocks, the ideal models of grain boundary sliding suggested by earlier models of anelasticity in polycrystalline olivine (even in the presence of melt) is inadequate for the description of anelastic character. It should be noted that grain growth of, for example, highly anisotropic clinopyroxene in same sample studied here is likely driven by stress-induced nucleation and growth during the experiment. The influence of phase interfaces between and within mineral grains will manifest itself as a diffusion-dominated anelastic peak in a mechanical spectrum. The results presented here point to the inherent complexity of anelasticity in igneous rocks at high homologous temperatures.

References

1. Mainprice, D. (1997). Modelling the anisotropic seismic properties of partially molten rocks found at mid-ocean ridges. *Tectonophysics, 279*(1–4), 161–179.
2. Yang, Y., Forsyth, D. W., & Weeraratne, D. S. (2007). Seismic attenuation near the east pacific rise and the origin of the low-velocity zone. *Earth and Planetary Science Letters, 258*(1–2), 260–268.
3. Butler, R., McCreery, C. S., Frazer, L. N., & Walker, D. A. (1987). High-frequency seismic attenuation of oceanic p and s waves in the western pacific. *Journal of Geophysical Research, 92*(B2), 1383–1396.
4. Revenaugh, J., & Meyer, R. (1997). Seismic evidence of partial melt within a possibly ubiquitous low-velocity layer at the base of the mantle. *Science, 277*(5326), 670–673.
5. Karato, S.-I., & Jung, H. (1998). Water, partial melting and the origin of the seismic low velocity and high attenuation zone in the upper mantle. *Earth and Planetary Science Letters, 157*(3–4), 193–207.
6. Faul, U. H., & Jackson, I. (2005). The seismological signature of temperature and grain size variations in the upper mantle. *Earth and Planetary Science Letters, 234*(1–2), 119–134.
7. Tan, B. H., Jackson, I., & Fitz Gerald, J. D. (2001). High-temperature viscoelasticity of fine-grained polycrystalline olivine. *Physics and Chemistry of Minerals, 28*(9), 641–664.
8. Kê, T.-S. (1947b). Stress relaxation across grain boundaries in metals. *Physical Review, 72*(1), 41–46.
9. Jackson, I., Fitz Gerald, J. D., Faul, U. H., & Tan, B. H. (2002). Grain-size-sensitive seismic wave attenuation in polycrystalline olivine. *Journal of Geophysical Research, 107*(B12), 2360.
10. Fontaine, F. R., Ildefonse, B., & Bagdassarov, N. S. (2005). Temperature dependence of shear wave attenuation in partially molten gabbronorite at seismic frequencies. *Geophysical Journal International, 163*(3), 1025–1038.
11. Kampfmann, W., & Berckhemer, H. (1985). High temperature experiments on the elastic and anelastic behaviour of magmatic rocks. *Physics of the Earth and Planetary Interiors, 40*(3), 223–247.
12. Smith, B. K., & Carpenter, F. O. (1987). Transient creep in orthosilicates. *Physics of the Earth and Planetary Interiors, 49*(3–4), 314–324.
13. Bagdassarov, N., & Dorfman, A. (1998). Viscoelastic behavior of partially molten granites. *Tectonophysics, 290*(1–2), 27–45.

14. Andrade, E. N. D. C. (1910). On the viscous flow in metals, and allied phenomena. *Proceedings of the Royal Society of London. Series A, Containing Papers of a Mathematical and Physical Character, 84*(567), 1–12.
15. Gribb, T. T., & Cooper, R. F. (1998). Low-frequency shear attenuation in polycrystalline olivine: Grain boundary diffusion and the physical significance of the andrade model for viscoelastic rheology. *Journal of Geophysical Research, 103*(B11), 27267–27279.
16. Jackson, I., Faul, U. H., Gerald, J. D. F., & Morris, S. J. S. (2006). Contrasting viscoelastic behavior of melt-free and melt-bearing olivine: Implications for the nature of grain-boundary sliding. *Materials Science and Engineering: A, 442*(1–2), 170–174.
17. Schoeck, G., Bisogni, E., & Shyne, J. (1964). The activation energy of high temperature internal friction. *Acta Metallurgica, 12*(12), 1466–1468.
18. Raj, R. (1975). Transient behavior of diffusion-induced creep and creep rupture. *Metallurgical and Materials Transactions A, 6*(8), 1499–1509.
19. Ashby, M. F. (1969). Boundary defects and the mechanism of particle movement through crystals. *Scripta Metallurgica, 3*(11), 843–848.
20. Wakai, F. (1994). Step model of solution-precipitation creep. *Acta Metallurgica et Materialia, 42*(4), 1163–1172.
21. Berckhemer, H., Kampfmann, W., Aulbach, E., & Schmeling, H. (1982). Shear modulus and q of forsterite and dunite near partial melting from forced-oscillation experiments. *Physics of the Earth and Planetary Interiors, 29*(1), 30–41.
22. James, M. R., Bagdassarov, N., Müller, K., & Pinkerton, H. (2004). Viscoelastic behaviour of basaltic lavas. *Journal of Volcanology and Geothermal Research, 132*(2–3), 99–113.
23. Weiner, A. T., Manghnani, M. H., & Raj, R. (1987). Internal friction in tholeiitic basalts. *Journal of Geophysical Research, 92*(B11), 11635–11643.
24. Woirgard, J., & Gueguen, Y. (1978). Elastic modulus and internal friction in enstatite, forsterite and peridotite at seismic frequencies and high temperatures. *Physics of the Earth and Planetary Interiors, 17*(2), 140–146.
25. Mavko, G., & Nur, A. (1975). Melt squirt in the asthenosphere. *Journal of Geophysical Research, 80*(11), 1444–1448.
26. Karato, S.-I. (2012). On the origin of the asthenosphere. *Earth and Planetary Science Letters, 321–322*, 95–103.
27. Stocker, R. L., & Gordon, R. B. (1975). Velocity and internal friction in partial melts. *Journal of Geophysical Research, 80*(35), 4828–4836.
28. Scarfe, C. M. (1997). Viscosity of some basaltic glasses at one atmosphere. *The Canadian Mineralogist, 15*, 190–194.
29. Bouhifd, M. A., Richet, P., Besson, P., Roskosz, M., & Ingrin, J. (2004). Redox state, microstructure and viscosity of a partially crystallized basalt melt. *Earth and Planetary Science Letters, 218*(1–2), 31–44.
30. Kani, K. (1934). The measurements of the viscosity of basalt glass at high temperature, i and ii. *Proceedings of the Imperial Academy (Tokyo), 10*(29–32), 79–82.
31. Ryan, M. P., & Blevins, J. Y. K. (1987). The Viscosity of synthetic and natural silicate melts and glasses at high temperatures and 1 bar (10^5 Pascals) pressure and at higher pressures. 1764. *U.S. Geological Survey Bulletin,* 84, 85
32. Shaw, H. R. (1969). Rheology of basalt in the melting range. *Journal of Petrology, 10*(3), 510–535.
33. Ryerson, F. J., Weed, H. C., & Piwinskii, A. J. (1988). Rheology of subliquidus magmas 1. picritic compositions. *Journal of Geophysical Research, 93*(B4), 3421–3436.
34. Webb, S. L., & Dingwell, D. B. (1990). Non-newtonian rheology of igneous melts at high stresses and strain rates: Experimental results for rhyolite, andesite, basalt, and nephelinite. *Journal of Geophysical Research, 95*(B10), 15695–15701.
35. Scarfe, C. M. (1973). Viscosity of basic magmas at varying pressure. *Nature Physical Science, 241*, 101–102.
36. Doremus, R. H. (1994). *Glass science*. New York: Wiley Interscience.

37. Nowick, A. S., & Berry, B. S. (1972). *Anelastic relaxation in crystalline solids*. New York and London: Academic Press.
38. Anderson, D. L., & Given, J. W. (1982). Absorption band q model for the earth. *Journal of Geophysical Research, 87*(B5), 3893–3904.
39. Kê, T.-S., & Zener, C. (1951). Structure of cold-worked metals as deduced from anelastic measurements. *Acta Physica Sinica, 8*(2), 131–142.
40. Kê, T.-S. (1950). Internal friction of metals at very high temperatures. *Journal of Applied Physics, 21*(5), 414–419.
41. Atkinson, B. K. (1984). Subcritical crack growth in geological materials. *Journal of Geophysical Research, 89*(B6), 4077–4114.
42. Brantley, S. L., Evans, B., Hickman, S. H., & Crerar, D. A. (1990). Healing of microcracks in quartz: Implications for fluid flow. *Geology, 18*(2), 136–139.
43. Smith, D. L., & Evans, B. (1984). Diffusional crack healing in quartz. *Journal of Geophysical Research, 89*(B6), 4125–4135.
44. Burkhard, D. J. M. (2001). Crystallization and oxidation of kilauea basalt glass: Processes during reheating experiments. *Journal of Petrology, 42*(3), 507–527.
45. Burkhard, D. J. M. (2005). Nucleation and growth rates of pyroxene, plagioclase, and fe-ti oxides in basalt under atmospheric conditions. *European Journal of Mineralogy, 17*(5), 675–685.
46. Cooper, R. F., Fanselow, J. B., & Poker, D. B. (1996). The mechanism of oxidation of a basaltic glass: Chemical diffusion of network-modifying cations. *Geochimica et Cosmochimica Acta, 60*(17), 3253–3265.
47. Brady, J. B. (1995). *Diffusion data for silicate minerals, glasses, and liquids* (Vol. 2, pp. 269–290). Washington, DC: AGU Reference Shelf.
48. Lesher, C. E. (2010). Self-diffusion in silicate melts: Theory, observations and applications to magmatic systems. *Reviews in Mineralogy and Geochemistry, 72*(1), 269–309.
49. Tinker, D., & Lesher, C. E. (2001). Self diffusion of si and o in dacitic liquid at high pressures. *American Mineralogist, 86*(1–2), 1–13.
50. Lesher, C. E., Hervig, R. L., & Tinker, D. (1996). Self diffusion of network formers (silicon and oxygen) in naturally occurring basaltic liquid. *Geochimica et Cosmochimica Acta, 60*(3), 405–413.
51. Goetze, C., & Kohlstedt, D. L. (1973). Laboratory sstudy of dislocation climb and diffusion in olivine. *Journal of Geophysical Research, 78*(26), 5961–5971.
52. Gribb, T. T., & Cooper, R. F. (2000). The effect of an equilibrated melt phase on the shear creep and attenuation behavior of polycrystalline olivine. *Geophysical Research Letters, 27*(15), 2341–2344.
53. Wakai, F., Kondo, N., Ogawa, H., Nagano, T., & Tsurekawa, S. (1996). Ceramics superplasticity: Deformation mechanisms and microstructures. *Materials Characterization, 37*(5), 331–341.
54. Salje, E. K. H. (2008). (An)elastic softening from static grain boundaries and possible effects on seismic wave propagation. *Physics and Chemistry of Minerals, 35*(6), 321–330.

Chapter 5
Glass Transition and Brittle Failure of Crystal-Glass Silicates

5.1 Introduction

Silicate glass-crystal mixtures form a large proportion of oceanic crust at spreading ridges. Total quantities are uncertain, but such mixtures are predominantly generated as intrusions in the crust. For example, in Iceland two-thirds of melt solidifies as intrusive rocks while one-third occurs as extrusive material [1, 2]. Rapid cooling of small-scale intrusions leads to glassy basaltic rocks. The presence of glass and glass transition on cooling influence the mechanical behaviour of such glassy basalts, especially its variability with temperature. For these reasons, the mechanical properties of silicate glass-crystal mixtures are of great potential importance in controlling microseismicity and the mechanical response of oceanic crust at spreading ridges.

Often, small (magnitude < 2.5) micro-earthquakes in the vicinity of dyke intrusions can be associated with magma migration [3, 4]. The brittle-ductile boundary within the lithosphere controls the distribution of earthquake foci with depth. At greater depths, long-period seismic events are commonly attributed to magma flow which can last over many years [3], while short-period earthquakes caused by brittle failure occur on timescales of a few weeks to several months. Beneath the rift zones at Kilauea, Hawaii, short-period seismic swarms accompany the emplacement of dykes while infrequent earthquakes observed below are considered to be a response to magma transport in aseismic area [4]. Compared to abundant observations of seismicity associated with magma movement and dyke propagation at shallow depths, earthquakes in the deeper aseismic crust, associated with prolonged presence of melt, are seldom recorded.

Recent volcanic activity in Iceland provides a good environment to study microseimicity in the mid-crust of intrusive dyke systems. Intense short-period earthquakes in the shallow and mid-crust (including aseismic depths) have been recorded in some studies [2, 5]. The spatial and temporal sequence of microearthquakes in these studies shows magma migration and continuously upward movement in dykes. Seismic clusters have been repeatedly and episodically recorded at different depths and separate times along the dyke plane (as shown in Fig. 5.1). The microearthquakes exhibit

S.-Y. Chien, *Rheological and Seismic Properties of Solid-Melt Systems*,
Springer Theses, DOI: 10.1007/978-3-319-03098-2_5,

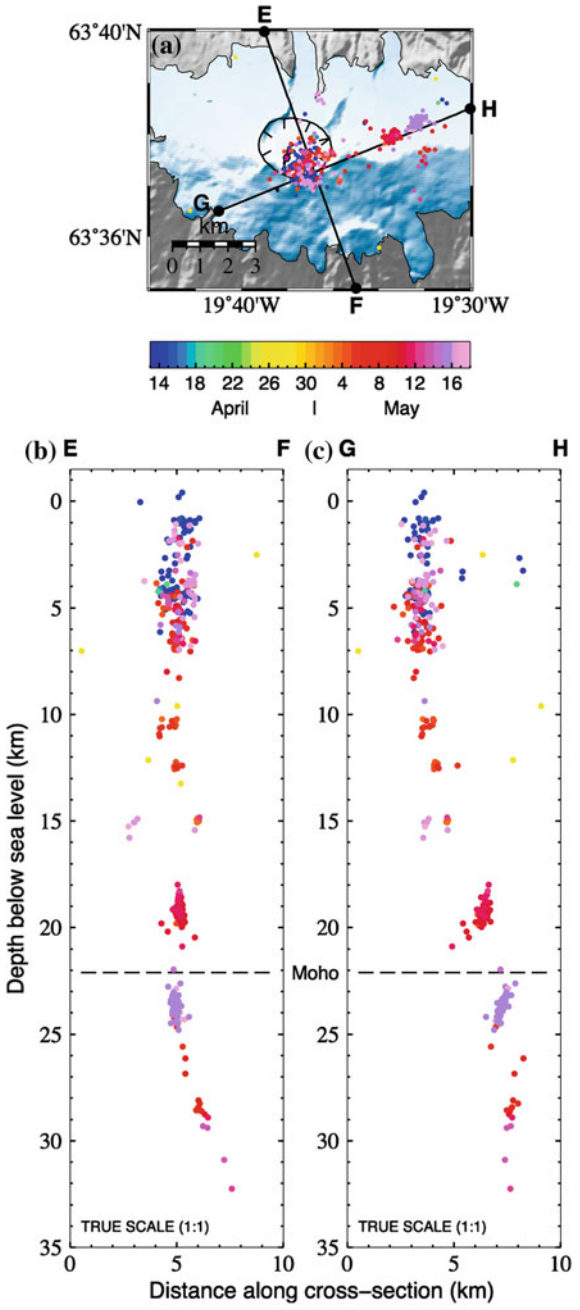

Fig. 5.1 An example of episodic seismic patterns reproduced from the study of Tarasewicz et al.: **a** earthquake locations associated with the Eyjafjallajkull stratovolcano in Iceland from 13 April to 17 May 2010. **b** and **c** Cross-sections along E–F and G–H shown in **a**, respectively, showing the depth distribution of the same hypocentres as in **a**. From [5]

the characteristics of brittle failure with similar waveforms and polarities within clusters, fault-like fractures along the plane of melt intrusion.

White et al. have proposed several mechanisms for faults along and parallel to dyke planes in Iceland [2]. One is fractures produced near the tip of a propagating dyke (due to the high stress field generated ahead of the dyke) or near constrictions in the dyke or on the contacted country rocks (due to large volumetric changes). Another possibility is that fractures are generated at plugs of solidified melt. When the melt moves upward along the dyke channel, it solidifies and forms a plug in the dyke. Pressure build-up beneath the plug is driven by continuous melt generation beneath, which moves upward against the plug. The plug will fail, causing earthquakes if the pressure from the melt is greater than the failure strength of the plug. Even though the suggested mechanisms can explain the brittle failure behaviours in a dyke system, the reason why earthquakes occur repeatedly and episodically in discrete time and space remains an open question. To untangle this question, it is necessary to understand the role of temperature on the mechanical properties of crystal-glass silicates.

Glass is an amorphous solid (non-crystalline) and is brittle. It has a topologically disordered distribution with elastic properties of an isotropic solid. Glass forms when the melt cools sufficiently quickly bypassing crystallisation through the liquid-glass transition (often known simply as the glass transition). Like a liquid, glass lacks a long-range periodic arrangement of atoms and molecules, but short-range order may exist. The glass transition typically occurs over a temperature range at a few tens of degrees. There are different ways to define glass transition temperature over the transition range. One conventional method is the temperature defined at which the shear viscosity reaches 10^{13} poise (or 10^{12} Pa.s) from viscosity measurements. Another one is the intersection of the liquid-like and glassy-like portions of the physical properties (volume or heat capacity) versus temperature curve, which usually occurs close to $2T_m/3$ under this definition (T_m = melting temperature of crystals) [6, 7]. Other features can be selected as the glass transition temperature in a physical property-temperature curve [8], such as the apex of the heat capacity.

The nature of the glass transition remains an area of intense scientific study. The heat capacity and coefficient of expansion (the temperature derivatives of enthalpy and volume) of amorphous materials display discontinuities when amorphous materials transform from a liquid state (melt) to a solid state (glass) at the glass transition temperature [9]. Although apparently similar to a second order phase transition in many respects, the glass transition is a kinetically-controlled transition, in which thermal history is important. In other words, glass is a non-equilibrium thermodynamic state and is metastable in nature. It is clear that the glass transition is not a thermodynamic phase transition due to its kinetic origin [10]. The glass transition temperature is always lower than melting temperature of materials, where melting is the first-order phase transition. The faster a material cools, the bigger difference between the glass transition temperature and melting temperature.

Glass can be treated as a viscoelastic material, and can exhibit rubber-like elasticity and has time- and temperature-dependent mechanical behaviour. Rubber is a nature polymer which forms glass more easily than a crystalline material on cooling.

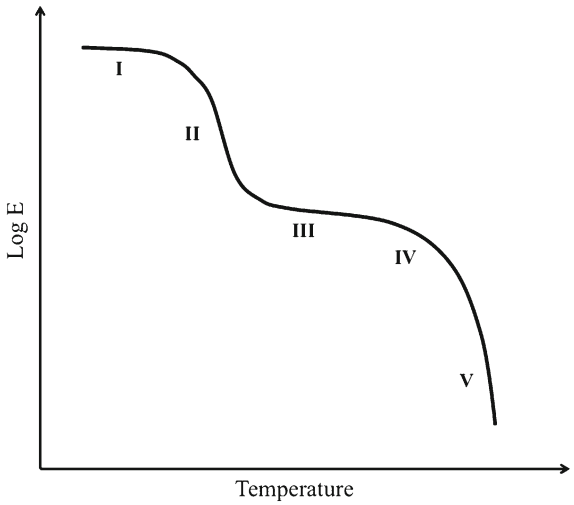

Fig. 5.2 Five regions of viscoelastic behaviour for a linear, amorphous polymer. After [9]

Amorphous polymers are often used (as analogues) to study the mechanical properties of glass and its brittle failure behaviour through the rubber-glass transition (also called the glass transition) in many industrial applications. Sperling [9] has briefly discussed that the amorphous polymers experience five different stages of viscoelastic behaviour in the logarithmic modulus versus temperature curve when they transform to a solid status (glassy) from a liquid status (molten) [9]. A simple sketch is shown in Fig. 5.2.

When the temperature increases from below the glass transition, the polymer transforms from a glassy solid to a liquid through five regions. The polymer is glassy and generally brittle in the region I. The Young's modulus is stiffer than other four regions and remains constant over a logarithmic scale in a wide range of polymers. In the glassy state, molecular motion is strongly limited to vibrations and short-range rotations. At high temperature, across the glass transition temperature, the polymer goes into the region II where the modulus typically drops by a factor of three on a logarithmic scale over a few tens of degrees. This region is interpreted as the onset of long-range, coordinated molecular motion. Ten times more chain atoms are involved in the coordinated motion than in region I. Region III is the rubbery plateau region at temperatures just above the glass transition temperature, where the modulus is almost constant (in a cross-linked polymer) or drops off slowly (in a linear polymer) on a logarithmic scale. Higher molecular weights of the polymer extend the width of the plateau further. The polymer, known as an elastomer in this stage, shows long-range rubber elasticity that it can be stretched to a large extent and returns to its original length after the stress is released. The polymer reaches the rubbery flow region in the region IV (which does not occur in cross-linked polymers), where the polymer exhibits both rubbery elasticity and flow properties. The polymer behaves as a rubber

on short time scales and flows over longer times. As the temperature is raised to reach the liquid flow region (region V), the material flows easily as a viscous liquid.

Silicate melts are viscous. More silica-rich melts are typically more polymerised (more links between silica tetrahedra) and more viscous. The mechanical behaviour of silicate melts as a function of temperature may be compared to that of amorphous polymers across the glass transition. Like them, the glass transition in silicate melts is associated with the breakage and reformation of chemical bonds. Chemical composition influences the glass transition temperature. Addition of low-valency elements (such as Na, K, or Ca) to a silicate glass decreases the numbers of bridging oxygens and results in a lower glass transition temperature. Similarly, the presence of high-valency elements (such as P) strengthens the network structure and leads to an increase in the glass transition temperature [10]. The glass transition in silicates occurs by Si-O bond exchange as silicon is exchanged among silicate species. This is the slowest structural relaxation, sometimes referred to as the 'alpha' structural relaxation, and is reflected as a relaxation of various physical properties [8]. Thus, the internal friction peak associated with Si-O exchange is found at the silicate vitrification. Other faster structural relaxations (denoted 'beta' and 'gamma' with decreasing temperature) occur at lower temperature if there are other elements involved. For example, the motion of alkalis is considered to be responsible for the fast relaxations in the $Na_2O-3SiO_2$ melt system [11].

Studies of silicate melts and their influence on the properties of basaltic rocks have mainly focused on the behaviours either close to or above the glass transition temperature. The mechanical behaviours of glassy rocks at temperatures far below the glass transition temperature are largely unexplored. It is intriguing to know how the brittle nature of glass influences the mechanical properties of glassy basalts at temperatures well below the glass transition temperature. Here, I focus on how crystal-glass silicates behave in this region and how fractures influence the mechanical properties below and through the glass transition. Two experiments have been conducted in this study of the glass transition and brittle failure on cooling under seismic frequencies: a basalt, measured in the inverted forced torsion pendulum (IFTP), and a crystalbond-saturated sandstone (as an analogue of a glass-crystal mixture), measured in the dynamic mechanical analyser (DMA-7e). The low-temperature experiments in DMA-7e have been carried out as an analogue to understand the general physical behaviour of crystal-glass systems and to elucidate the value of such analogues.

5.2 Samples and Experimental Methods

The I13_83493 basalt 'as received' and a crystalbond 509-saturated Darley Dale sandstone were prepared for two experiments. The details of these basalt and sandstone samples have described in Sect. 3.2, Fig. 3.8 and Sect. 3.1, Fig. 3.1, respectively. In the first experiment, I13_83493 basalt (referred to as I13 basalt hereafter) was cut into a rectangular bar 10.7 mm in width, 2.3 mm in thickness and 16.3 mm in length.

The I13 basalt was clamped in the inverted forced torsion pendulum (detailed in Sect. 2.1 and Fig. 2.3). Unlike the Iceland basalt and the Skaergaard gabbro, the vertical stress along the I13 basalt was not balanced, which means it was measured under a small bias stress. Before experiments, the sample has been initially annealed at lower temperatures (500–800 K) for three days, in the inverted forced torsion pendulum, under high vacuum (10^{-3} Pa) before high temperature experiments. The specimen was then repeatedly heated and cooled from 900–1100 K below the glass transition temperature under sinusoidal shear stress for at least twenty cycles (as discussed in Chap. 4). Finally, the I13 basalt was heated to, and cooled from, 1250 K (above the glass transition temperature) while stressed sinusoidally at 1 Hz for three cycles before the end of experiments. All experiments were conducted at a temperature ramp rate of 1 K/min. The shear modulus and internal friction of the I13 basalt were measured during the experiments.

In the second experiment, a crystalbond 509-saturated Darley Dale sandstone was prepared. Crystalbond 509 is a thermoplastic polymer, which includes phthalic anhydride and ethylene glycol (chemical information provided by Aremco Products, Inc. in USA). Crystalbond 509 was placed in a container on a hot plate and heated to 420 K (the melting point is close to 400 K) with a sliced section of Darley Dale sandstone submerged in the molten crystalbond 509 overnight. The crystalbond 509-saturated Darley Dale sandstone (referred to as x-DD sample hereafter) is obtained after the sample was cooled down in air. The x-DD sample was at first cut into a rectangular bar 5.7 mm in width, 2.5 mm in thickness and 15.0 mm in length. It was placed on the three point bending platform in the dynamic mechanical analyser (detailed in Sect. 2.2 and Fig. 2.6). Experiments are conducted with the sample under bias stress with additional modulated stress. The x-DD sample was heated to 350 K and cooled to 200 K at temperature ramp rates of 5–20 K/min under stresses applied at 1, 5 and 10 Hz. Two crystalbond samples and one Darley Dale sandstone of rectangular geometry were also prepared for comparison. The dimensions of the pure crystalbond 509 was 6.6 mm × 1.7 mm × 5.0 mm for measurements made at 1 Hz and 6.8 mm × 2.0 mm × 15.0 mm for the 10 Hz measurements. Sample were measured between 200 and 280 K at a temperature ramp rate of 5 K/min. The Darley Dale sandstone was cut to 6.6 mm × 2.0 mm × 15.0 mm for the 1 Hz measurements between 200 and 350 K with a temperature ramp rate of 10 K/min. All experiments are conducted at ambient pressure. The storage modulus and internal friction were measured by three bending system.

5.3 Results and Analysis

The modulus, internal friction and plastic strains of four different samples (I13 basalt, x-DD sample, crystalbond 509 and Darley Dale sandstone) have been measured using low-frequency spectroscopies (IFTP and DMA-7e) as a function of temperature. Despite the huge differences in the nature of the samples and the temperatures of the respective glass transitions, I13 basalt and x-DD sample are found to have similar

mechanical behaviours on cooling from temperatures above their glass transition temperatures. On cooling, the modulus initially increases across the glass transition and then decreases at temperatures below the glass transition. With further cooling, the modulus shows a sudden drop by variable extent in both samples. The mechanical properties of pure crystalbond 509 and Darley Dale sandstone themselves do not, however, show the same trends on cooling over the measured temperature range. All modulus and plastic strain data have been normalised (data divided by the maximum value in the dataset) to gain better understanding of the changes of properties between different samples. Data presented for x-DD sample, crystalbond and Darley Dale sandstone have been binned to smooth data and demonstrate variations in the mechanical behaviours of the samples more clearly.

The normalised shear modulus, internal friction and normalised plastic strain of I13 basalt are shown in Fig. 5.3. I13 basalt was at first heated to 1250 K. On heating from 500 to 1050 K, the shear modulus of I13 basalt increases by 55 % and then increases much more slowly from 1050 to 1175 K before finally decreasing at temperatures above 1175 K. The sample was then cooled down to 500 K and repeatedly heated and cooled between 500 and 1250 K for two more cycles. Unlike the heating curves, there are two distinct rising peaks seen in the cooling curves. On cooling, the shear modulus initially increases and then decreases below around 1175 K. It then increases again on further cooling from 1100 to 1000 K where the shear modulus begins to decrease more significantly, to about 60 % of its maximum value by 500 K. On the second and third cooling runs, a sudden drop (10 %) of shear modulus occurs at close to 825 K. This drop is smaller and the maximum in modulus occurs at lower temperatures on subsequent cooling runs. The observations of the changes of plastic strain also reflect these sudden changes in modulus. All internal friction curves of I13 basalt overlap with each other over the temperature range in this experiment. The internal friction of I13 basalt shows little change at low temperatures (below 1100 K), except for a very narrow large spike close to 825 K. At high temperatures (above 1100 K), the internal friction shows an increase exponential background on heating.

The mechanical properties (storage modulus, internal friction and plastic strain) of x-DD sample have been measured at 1, 5, and 10 Hz. Results are shown in Fig. 5.4. The sample was repeatedly heated and cooled for several cycles and shows reproducible behaviour at each frequency. Here, I show the results from one such heating or cooling run at each frequency for comparison of heating and cooling, respectively. Frequency does not appear to have a large influence on the general behaviour and data show similar behaviours at 1, 5 and 10 Hz. The modulus of x-DD sample increases by 30 % to its maximum on heating from 200 to 300–310 K and then on further heating deceases to 50–60 % (depending on frequency) lower over the next 40°. The peak of maximum modulus in the heating curves shifts slightly to higher temperature at higher frequency. On cooling, the curves initially follow similar trends to the heating curves (from 350 to 300 K). Subsequently, the modulus reaches a maximum plateau before a dramatic drop at temperatures between 230 and 260 K. The decrease in modulus occurs at lower temperature at lower frequency. For repeat measurements at a particular frequency features are located at similar temperatures within errors

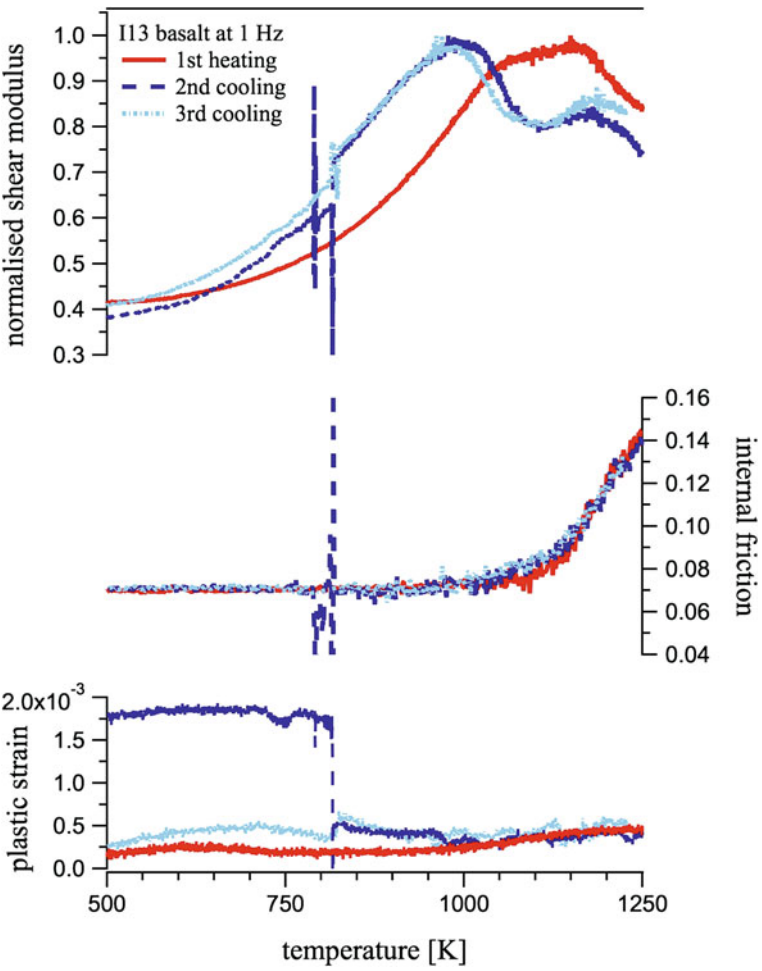

Fig. 5.3 The mechanical properties of I13 basalt at a stress frequency of 1 Hz and over a temperature range of 500–1250 K measured under high vacuum (10^{-3} Pa)

of 3–5 K. The behaviours of the plastic strain correspond to the changes of the storage modulus in the x-DD sample on cooling. The internal friction of x-DD sample remains constant below room temperature and rises quickly from 300 to 350 K. Two weak internal friction peaks are seen additional to the rising background. The overall value of internal friction is larger when measured at 1 Hz than the value at 10 Hz. Different temperature ramp rates (5–20 K/min) have been applied to the experiments conducted at 10 Hz. With increasing heating and cooling rates, the hysteresis between the heating and cooling rates becomes more evident. Otherwise, no obvious changes are related to the temperature rate during measurements.

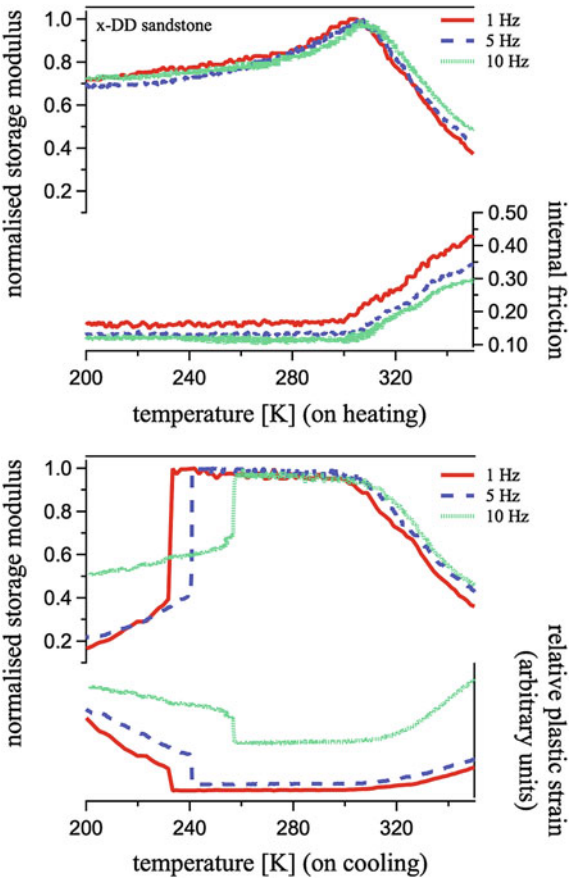

Fig. 5.4 The mechanical properties of crystalbond 509-saturated Darley Dale sandstone at stress frequencies of 1, 5, 10 Hz, respectively, as a function of temperature (200–350 K) in the ambient pressure on heating (*top*) and on cooling (*bottom*)

To understand which component (crystalbond 509 or Darley Dale sandstone) is responsible for the changes of x-DD sample, additional experiments on the individual components: bulk crystalbond 509 and Darley Dale sandstone, have been carried out at seismic frequencies. Each of bulk crystalbond 509 sample can only be used once for each temperature experiment, separately in stress frequencies of 1 and 10 Hz, because the sample flows and deforms significantly at high temperature. At 1 Hz, the bulk crystalbond 509 (as shown in Fig. 5.5) increases by 20 % from 220 to 273 K on heating followed by a rapid drop (50 %) over a few degrees. On cooling, the modulus increases less rapidly at temperatures between 280 and 260 K, where modulus reaches its maximum and starts to decrease slowly (20 %) with further cooling from 260 to 220 K. The plastic strain and internal friction curves are consistent with changes of the storage modulus at 1 Hz. Another bulk crystalbond 509 was measured at 10 Hz on heating from 225 to 275 K. It was not possible to run the sample at 10 Hz for temperatures above 250 K due to failure of the sample in every case, so it was not possible to approach as close to the melting temperature. On heating, the modulus of

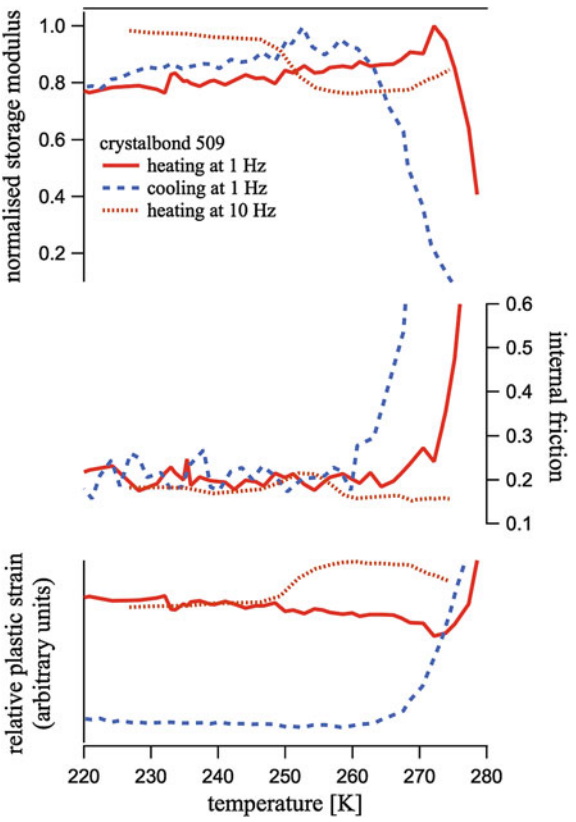

Fig. 5.5 The mechanical properties of a bulk crystalbond 509 at stress frequencies of 1 and 10 Hz, respectively, as a function of temperature (220–280 K) in the ambient pressure

crystalbond 509 at 10 Hz deceases very slightly at relative low temperature, followed by a more rapid decrease (15 %) at 250 K, and then increases more slowly in the relative high temperature (above 260 K). A weak internal friction peak occurs in the temperature range of 245–260 K at 10 Hz, when the rest of the internal friction curve stays almost constant as background. A sudden change in the plastic strain is also found close to 250 K at 10 Hz. The measurements of Darley Dale sandstone are shown in Fig. 5.6 at 200–340 K and at 1 Hz. The mechanical behaviours of the bulk sandstone on heating and on cooling are very much alike. Both storage modulus and plastic strain of the sandstone show little change over the entire temperature range, with only a very small decrease (less than 5 %) in modulus from 300 to 340 K. The internal friction is slightly higher on heating at temperature above 300 K. The internal friction on cooling is higher than that on heating between 240 and 300 K. In general, the variation of the internal friction curve is less than 8 %.

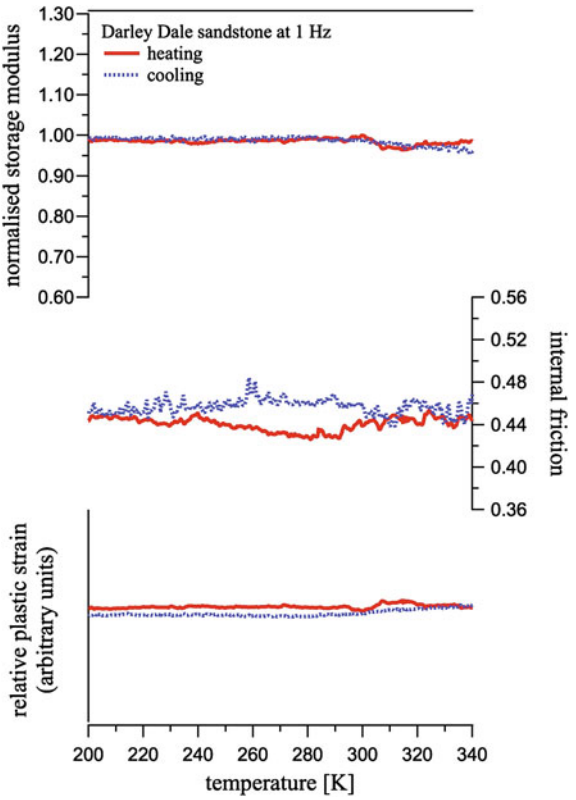

Fig. 5.6 The mechanical properties of a bulk Darely Dale sandstone (14 % porosity) at a stress frequency of 1 Hz as a function of temperature (200–340 K) at ambient pressure

5.4 Mechanisms

The x-DD composite (crystal-glass silicate) shows a mechanical response that contrasts strongly with both that of bulk crystalbond 509 (glass) and of bulk Darley Dale sandstone (crystalline solid). The sandstone shows monotonic behaviour from 200 to 350 K as its storage modulus shows little change. The glassy component (crystalbond) plays a major role on the mechanical properties of the crystal-glass silicate over the temperature range of interest. The crystalbond shows two different transitions at stress frequencies of 1 and 10 Hz. The rapid decrease in modulus at temperatures of 260–280 K at 1 Hz, where crystalbond 509 is very soft, indicates the onset of melting. This transition can be also considered in terms of region IV (rubbery flow) and V (liquid flow) of viscoelastic behaviours described by Sperling in Fig. 5.2 [9]. The small drop close to 250 K at 10 Hz appears to correspond to region II (glass transition).

Initially, before heating, the crystalbond part of x-DD sample is glassy and brittle and contains cooling-induced microcracks. As the temperature increases, the x-DD sample strengthens as cracks in the crystalbond start to close due to crack healing processes, which consists of cracks pinching off and healing to a pore-like shape

before subsequent decrease of the pore diameter [12]. When temperature continuously increases to above 250 K, the storage modulus of the x-DD sample might be expected to decrease in view of the observation of the glass transition for bulk crystalbond 509 at this temperature. However, the storage modulus of x-DD sample still increases through 250 K at both 1 and 10 Hz (Fig. 5.4) and does not start to decrease until the temperature reaches 300–310 K. This is interpreted as the glass transition temperature of x-DD composite mixture. Molecular dynamic computer simulations of super cooled liquid have demonstrated that the relaxation dynamics of particles close to the interface of a framework are slowed with respect to those in the bulk and the glass transition temperature increases with confinement of the supercooled liquid against non-smooth walls [13]. Following this concept, it is reasonable to expect the glass transition temperature of x-DD composite to be higher than that of crystalbond alone. Two weak internal friction peaks are seen above the exponential high temperature background at 300–350 K (Fig. 5.7). An Arrhenius plot gives two activations energies (407 ± 19 and 489 ± 26 kJ/mol) from the frequency dependence of selected peak positions. Previous studies of polymer-silicate interfaces have been conducted

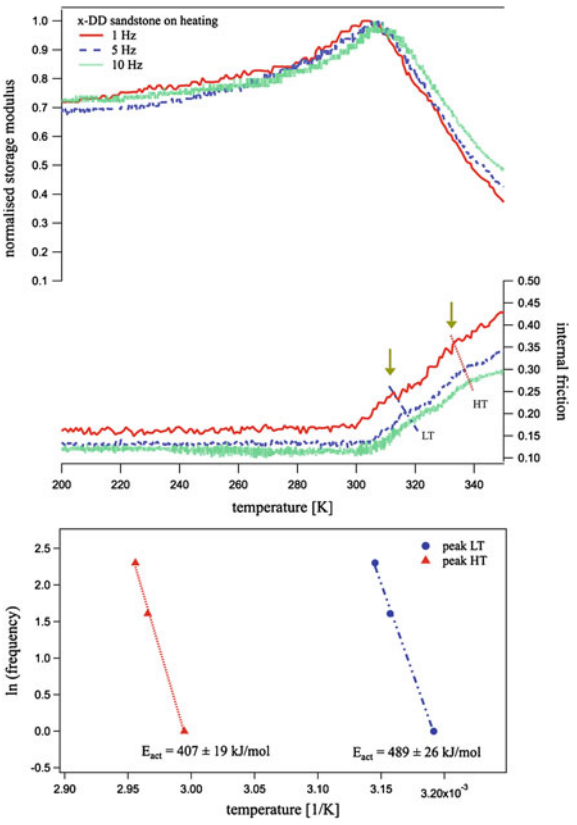

Fig. 5.7 The activation energies of two weak internal friction peaks are given in an Arrhenius plot for the x-DD sample at temperatures between 300 and 350 K at ambient pressure

in the context of understanding polydimethyl siloxane adhesive and its bonding to glass substrate (used in microchip fabrication). These investigations show that the fracture energy of glass-adhesive interfaces is of the order of 400 kJ/mol but also strongly dependent on viscoelastic processes near the interface [14]. The behaviour is dominated by dissociation of the siloxane bond and the breaking of Si-O-Si linkages at the glass surface. (445 kJ/mol [15] or 454 kJ/mol [14]). The mechanism for the internal friction peaks may, then, be due to the interaction between the polymer adhesive crystalbond within the sandstone pores and particularly the bond and de-bonding at the quartz surfaces within the pores.

On cooling from the highest temperatures, the storage modulus of x-DD increases initially due to the liquid-solid transition in the crystalbond 509. The modulus reaches its maximum when the crystalbond enters region III, "the rubbery plateau" of Sperling 2006 [9]. With further cooling, the modulus of the x-DD sample passes through its maximum, defined by the composite property of the crystalbond-sandstone mixture. On further cooling a light drop in modulus is seen and internal friction remains low. When temperature decreases to 260–230 K, a sudden 30–60 % drop in modulus is seen in the cooling curves. This is the same temperature range over which we see a stiffening in modulus of pure crystalbond, interpreted as the glass transition of crystalbond (Fig. 5.5, 10 Hz data). Consequently, the local stresses are generated when the crystalbond transforms to a glassy state and becomes stiffer but more brittle against the tough framework (sandstone). The brittle nature of glassy crystalbond results in the onset of fracture, with cracks that percolate in the crystalbond and subsequent failure, seen as a sudden drop in the modulus. The experiments are not conducted in a sealed environment, which means moisture in the air may also condense and freeze on the x-DD sample. Forssell et al. [16] demonstrate that the presence of water in thermoplastic polymers (glycerol-water-starch mixtures) results in dynamic mechanical relaxation at temperatures below 175–235 K, depending on water content. The greater the water content, the lower the temperature of the faster relaxation process. It is possible that water (even at low concentrations) in the sample may therefore contribute partly to the sudden drop.

The results from x-DD sample also show frequency-dependent characteristics at the glass transition and in the sudden drop of the storage modulus curves. The higher the frequency, the higher the temperature at which failure is seen. The observations in this study are in a good agreement with a system dominated by dynamic bond relaxations associated with glass formation. Different temperature ramp rates have been investigated in these experiments as well. There appears to be no relationship between the sudden modulus drop and the cooling rate, other than the expected hysteresis between heating and cooling curves seen in modulus data which becomes larger at higher temperature ramp rates. The relationship between the glass transition temperature of the crystalbond and the temperature ramp rate is not clear in this study. Even though there is no clear evidence from these data, the glass transition temperature is expected to move to higher temperature with the higher temperature ramp rate, as, for example, seen in the specific heat capacity data of a New Zealand obsidian [8].

The findings from the x-DD sample provide a few possible insights into the mechanisms of the mechanical behaviour of basalt (Fig. 5.3). On heating, the shear modulus of basalt increases rapidly above 500 K and then slowly at 1050–1175 K and then continuously decreases above 1175 K. The healing (closing) of microcracks contributes to the initial increase of the modulus; high aspect ratio (elongate shaped) cracks close first, followed by the closure of the low aspect ratio cracks (round shaped). At higher temperature, above 1050 K, the increase of the modulus may be explained in terms of continuous closure of the microcracks, although redox and recrystallisation processes in the basalt groundmass glass may also have a role to play [17]. For example, a contribution to shear modulus increase in Kilauea basalt glass has been related to the interface-controlled intergrowths of pyroxene dendrites and Fe-(Ti)-oxides between 1123 and 1213 K [18]. Balme et al. suggest other mechanisms, based on changes in fracture toughness found in experiments on basalts at temperatures upto 873 K [19]. In Balme et al.'s picture, basalt is initially tough and strengthens further as temperature increases, which leads to the crack tip to weaken, accompanied by an increase in plastic energy dissipation. More microcracks are expected on further heating if the fracture strength decreases, associated with surface energy decreasing with temperature [20]. This could lead to crack linkage, which results in a marked decrease in toughness up to the elastic-plastic transformation. If Balme's suggestions are applied to this study, crack leakages may be arrested by the populations of thermally-induced cracks, or indeed they may be overcome by redox and recrystallisation at temperatures between 1050 and 1175 K.

Alternatively, basalt may be dominated by the melt/glass component, and behave in the same way as amorphous polymers, with five characteristic regions. The crystalline component in basalt can result in similar effects as seen by the cross-link component of polymers, because both make the (polymer) network more resistant to breakage [9]. The presence of a crystalline component extends the width of the plateau (designated the rubber plateau in region III) up until melting [9]. Therefore, the plateau may be explained in terms of transforming from glassy solid to viscous melt at the glass transition temperature close to 1050 K, with a plateau before the viscous-liquid flow transition which occurs close to 1175 K. The decrease of modulus and the increase of the internal friction above 1050 K results from the slowest structural relaxation in the silicate melt, namely Si-O bond exchange, with mobility of silicon above the glass transition temperature.

On cooling, the shear modulus of basalt show a two step increase initially, which may result from the liquid-viscous-glass transition. The cooling rate of 1 K/min is fast enough for silicate melt to form silicate glass [10]. The redox of Fe-(Ti)-oxides and crystallisation of pyroxene become slow and their influence can be neglected below 1100 K. The maximum shear modulus on cooling appears at lower temperature than that on heating due to thermal hysteresis. On continuous cooling below the glass transition temperature (close to 1000 K), basalt becomes glassy and brittle. Microcracks may develop more easily in the presence of deviatoric stress [21]. The shear modulus thus begins to decrease rapidly below the glass transition temperature where the crack density increases on further cooling. Eventually, stress-induced microcracks percolate and failure occurs, resulting in the sudden drop on modulus

close to 825 K. Tuffen and his colleagues [22] find, from deformation experiments, that seismogenic fracture occurs close to 920 K in obsidian (crystal-free) and close to 1173 K in andsites (crystal-rich). Large changes in shear modulus are likely due to fractures generated in the glassy component of basalt.

It is interesting to note that the temperature at which the sudden drop of modulus is close to a homologous temperature of 0.6 in both x-DD sample and I13 basalt at 1 Hz. Creep in several polycrystalline alloys was found to change significantly at between 0.45 and 0.75 T_m, depending strain rate and material [23]. For example, a change in creep is seen in pure polycrystalline aluminium close to 0.5–0.75 T_m with strain rates of 10^{-5}–10^{-2} s^{-1}. In polycrystalline cadmium, the activation energy for creep and for self-diffusion become similar at homologous temperatures between 0.5–0.6 T_m. Brittle failure in both x-DD sample and I13 basalt occurs at a similar homologous temperature of 0.5–0.6 T_m. The underlying reasons cannot be identical to creep deformation of crystalline metals, and it may be purely coincidental but a link may exist through the generic dynamics of atomic diffusion in both metallic solids and silicate glass.

Pressure, viscosity and composition can modify the glass transition temperature. The viscosity of polymerised silica-rich melts (An composition) decreases with pressure, while less-polymerised melts (An-Di composition) show a positive pressure coefficient of viscosity [24]. The glass transition temperature shows negative correlation with pressure in anorthite-composition melts (less non-bridging oxygens) and positive pressure dependence in diopside melts(more non-bridging oxygens). The pressure dependence of melt viscosity is concluded to be more sensitive to the degree of melt polymerisation than to the specific melt composition. By applying the data of Del Gaudio and Behrens [24], the glass transition temperature for a feldspar-rich basaltic melt can decrease by approximately 30 K for each 1 GPa of increasing pressure in the deeper crust.

Mechanical properties can also be affected by strain rates. At low strain rates, a rock may deform in a ductile manner, as seen at high temperature, but the same rock may respond in a brittle manner under high strain rates, where fractures propagate and the response appears similar to that at low temperatures [25].

Several works have reported the role of pressure on the brittle behaviour of geomaterials. Ougier-Simonin et al. [21] carried out investigations of crack distributions of thermally-treated silicate glasses (upto 570 K) and Seljadur basalt under triaxial loading conditions. Under hydrostatic conditions (0–50 MPa), velocities of P-waves and S-waves increase initially and remain constant above 10 MPa, which is interpreted in terms of a crack density decrease with increasing hydrostatic pressure and cracks are closed above 10 MPa. With deviatoric stress (0–700 MPa), both velocities decreases non-linearly with increasing deviatoric stress and the crack density increases exponentially and rapidly above 100 MPa. The influence of temperature is, however, more significant than that of pressure, since they found that variations in thermal treatment of these glasses generated greater changes in crack density than variations of pressure.

Our data for basalts show that crack percolation and eventual fracture is only seen in I13 basalt under biased stress (deviatoric), but does not occur in Iceland basalt

(in Chap. 4), which is investigated under balanced stress. The observations in this study are in good agreement with the study of Ougier-Simonin et al. of Etna basalt at hydrostatic pressures upto 190 MPa and deviatoric pressures upto 420 MPa [21]. All these findings lead to the conclusion that cracks and fractures can be suppressed at higher hydrostatic pressures (closure of naturally occurring cracks) or at high temperature (suppression of crack linkage by thermal-induced microcracks) below the glass transition temperature [19]. In other words, cracks and fractures are favoured by higher deviatoric pressure, by decreasing hydrostatic pressure or by rapid cooling.

The resultant mechanical properties of crystal-glass silicates in this study provide a new insight to the mechanisms in dynamics of dyke intrusion in the mid-crust of Iceland. A dyke intruded in the mid-crust initially solidifies due to contact with the cooler country rock and forms a plug on the top of the intrusion. The strength of the plug increases when the temperature continuously cools down and is strong enough to stop the flow of melt from below. With further cooling below the glass transition temperature, the plug is weakened due to the presence of microcracks. At further

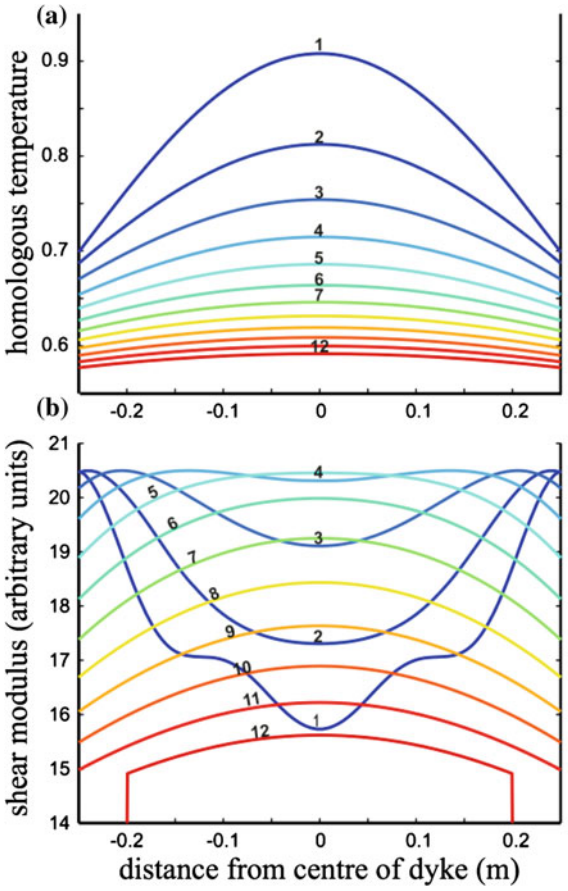

Fig. 5.8 Thermal modelling of a emplacing 0.5 m wide dyke in magma which cools from the melting point (i.e. homologous temperature of 1.0). After [26]. Numbers on the curves are the days of cooling. **a** Temperature distribution in the cross-section of the dyke from first day to the twelfth day. **b** Dynamic shear modulus distribution in the cross-section of the dyke, using the data from Fig. 5.3 in this study, with an initial country rock at 0.4 T_m

lower temperature (close to 0.6 T_m), mechanical failure (brittle failure) occurs when the fracture strength of the plug is slightly smaller than the stress associated with the driving force of the magma beneath the plug pushing upward. The re-intruded dyke cools and forms a plug again on cooling through the glass transition temperature. This gives an explanation for cyclicity in the seismicity seen in dykes in Iceland. An example, using the data of I13 basalt in this study is presented in Fig. 5.8 [26]. A 0.5 m thick dyke cooling from the melting temperature can form a plug and fail at the edge of the dyke after 12 days when it reaches a homologous temperature of 0.58, if there is an applied stress (such as pressure of melt from below). The duration of cooling is proportional to the square of the dyke thickness. Doubling the dyke thickness leads to a factor of four in the duration of fracture occurring on cooling. The data presented here for I13 basalt perfectly support a simple model for the seismic cyclicity studies in the Icelandic dyke intrusion. The data suggest that brittle failure of crystal-glass silicates, and their properties through the glass transition can give rise to the cyclic behaviour and should be expected as general characteristics of small-scale basaltic intrusive rocks in the upper and mid-crust.

References

1. White, R. S., Smith, L. K., Roberts, A. W., Christie, P. A. F., & Kusznir, N. J. (2008). Lower-crustal intrusion on the north atlantic continental margin. *Nature*, *452*(7186), 460–464.
2. White, R. S., Drew, J., Martens, H. R., Key, J., Soosalu, H., & Jakobsdóttir, S. S. (2011). Dynamics of dyke intrusion in the mid-crust of iceland. *Earth and Planetary Science Letters*, *304*(3–4), 300–312.
3. Pitt, A. M., Hill, D. P., Walter, S. W., & Johnson, M. J. S. (2002). Midcrustal, long-period earthquakes beneath northern california volcanic areas. *Seismological Research Letters*, *73*(2), 144–152.
4. Wright, T. L., & Klein, F. W. (2006). Deep magma transport at kilauea volcano, Hawaii. *Lithos*, *87*(1–2), 50–79.
5. Tarasewicz, J., Brandsdóttirs, B., White, R. S., Hensch, M., & Thorbjarnardóttir, B. (2012). Using microearthquakes to track repeated magma intrusions beneath the eyjafjallajökull stratovolcano, iceland. *Journal of Geophysical Research*, *117*(B00C06), 13.
6. Sakka, S., & Mackenzie, J. D. (1971). Relation between apparent glass transition temperature and liquids temperature for inorganic glasses. *Journal of Non-Crystalline Solids*, *6*(2), 145–162.
7. Debenedetti, P. G., & Stillinger, F. H. (2001). Supercooled liquids and the glass transition. *Nature*, *410*(6825), 259–267.
8. Webb, S., & Knoche, R. (1996). The glass-transition, structural relaxation and shear viscosity of silicate melts. *Chemical Geology*, *128*(1–4), 165–183.
9. Sperling, L. H. (2006). *Introduction to physical polymer science* (4th ed.). New Jersey: Wiley.
10. Ojovan, M. I. (2008). Configurons: Thermodynamic parameters and symmetry changes at glass transition. *Entropy*, *10*(3), 334–364.
11. Dingwell, D. B. (1990). Effects of structural relaxation on cationic tracer diffusion in silicate melts. *Chemical Geology*, *82*, 209–216.
12. Atkinson, B. K. (1984). Subcritical crack growth in geological materials. *Journal of Geophysical Research*, *89*(B6), 4077–4114.
13. Scheidler, P., Kob, W., & Binder, K. (2004). The relaxation dynamics of a supercooled liquid confined by rough walls. *The Journal of Physical Chemistry B*, *108*(21), 6673–6686.

14. Chaudhury, M. K. (1999). Rate-dependent fracture at adhesive interface. *The Journal of Physical Chemistry B*, *103*(31), 6562–6566.
15. Bhattacharya, Shantanu, Arindom Datta, J. M. B., & Gangopadhyay, S. (2005). Studies on surface wettability of poly(dimethyl) siloxane (pdms) and glass under oxygen-plasma treatment and correlation with bond strength. *Journal of Microelectromechanical System*, *14*(3), 590–597.
16. Forssell, P. M., Mikkilä, J. M., Moates, G. K., & Parker, R. (1997). Phase and glass transition behaviour of concentrated barley starch-glycerol-water mixtures, a model for thermoplastic starch. *Carbohydrate Polymers*, *34*(4), 275–282.
17. James, M. R., Bagdassarov, N., Müller, K., & Pinkerton, H. (2004). Viscoelastic behaviour of basaltic lavas. *Journal of Volcanology and Geothermal Research*, *132*(2–3), 99–113.
18. Burkhard, D. J. M. (2001). Crystallization and oxidation of kilauea basalt glass: Processes during reheating experiments. *Journal of Petrology*, *42*(3), 507–527.
19. Balme, M. R., Rocchi, V., Jones, C., Sammonds, P. R., Meredith, P. G., & Boon, S. (2004). Fracture toughness measurements on igneous rocks using a high-pressure, high-temperature rock fracture mechanics cell. *Journal of Volcanology and Geothermal Research*, *132*(2–3), 159–172.
20. Darot, M., Gueguen, Y., Benchemam, Z., & Gaboriaud, R. (1985). Ductile-brittle transition investigated by micro-indentation: Results for quartz and olivine. *Physics of the Earth and Planetary Interiors*, *40*(3), 180–186.
21. Ougier-Simonin, A., Fortin, J., Guéguen, Y., Schubnel, A., & Bouyer, F. (2011). Cracks in glass under triaxial conditions. *International Journal of Engineering Science*, *49*(1), 105–121.
22. Tuffen, H., Smith, R., & Sammonds, P. R. (2008). Evidence for seismogenic fracture of silicic magma. *Nature*, *453*(7194), 511–514.
23. Sherby, O. D., & Burke, P. M. (1968). *Mechanical Behavior of Crystalline Solids at Elevated Temperature*. Progress in materials science. Oxford: Pergamon Press.
24. Del Gaudio, P., & Behrens, H. (2009). An experimental study on the pressure dependence of viscosity in silicate melts. *The Journal of Chemical Physics*, *131*(4), 044504.
25. Rocchi, V., Sammonds, P. R., & Kilburn, C. R. J. (2003). Flow and fracture maps for basaltic rock deformation at high temperatures. *Journal of Volcanology and Geothermal Research*, *120*(1–2), 25–42.
26. White, R. S., Redfern, S. A. T., & Chien, S.-Y. (2012). Episodicity of seismicity accompanying melt intrusion into the crust. *Geophysical Research Letter*, *39*(8), L08306.

Chapter 6
Crackling Noise in Basalt and Gabbro

6.1 Introduction

A variety of systems ranging in size from as small as a crumpling piece of paper to as large as earthquakes on fault planes can produce crackling noise. A piece of paper crumples when it is squeezed into a ball. Small parts of the paper bend and jump into the new configurations to emit crackle sounds during the process. The Earth responds through earthquakes when tectonic plates interact with each other. Crackling noises are produced when earthquakes occur in the Earth, although on timescales so great that they may not be perceived as noise to the casual observer. An earthquake which simply represents a single crack (such as faulting) in the Earth is a crackling process. This crackling noise results from the response of a system to changing external conditions, by discrete events which occur with a wide range of sizes and waiting times.

Bak et al. connected crackling noise to dynamical critical phenomena through the concept of "self-organised criticality" [1, 2], which has inspired many subsequent studies on crackling noise. They suggest that self-organised criticality is an underlying mechanism for phenomena such as the widespread occurrence of $1/f$ noise (or flicker noise) for transport in systems (like resistors, hour glass, and luminosity of stars) and turbulence behaviour in spatially extended objects (like mountain landscapes and cosmic strings), in which the universal behaviour of power-law temporal or spatial correlations is observed.

Traditionally, the most important expression of this phenomenological law in Earth sciences has been proposed by Gutenberg and Richter in 1949 [3] for earthquakes. A broad range of earthquake magnitudes (sizes) are generated, from undetectable trembles to catastrophic quakes. Gutenberg and Richter reviewed shallow earthquakes in the Earth [3] and established a frequency-magnitude relationship for earthquakes, the well-known Gutenberg-Richter law. The Gutenberg-Richter relation reflects the observation that small earthquakes are common whilst it is very rare for huge earthquakes to occur. The number of earthquakes, $P(M_{th})$, forms a power law relation with the magnitude of corresponding earthquakes, M_{th},

S.-Y. Chien, *Rheological and Seismic Properties of Solid-Melt Systems*,
Springer Theses, DOI: 10.1007/978-3-319-03098-2_6,

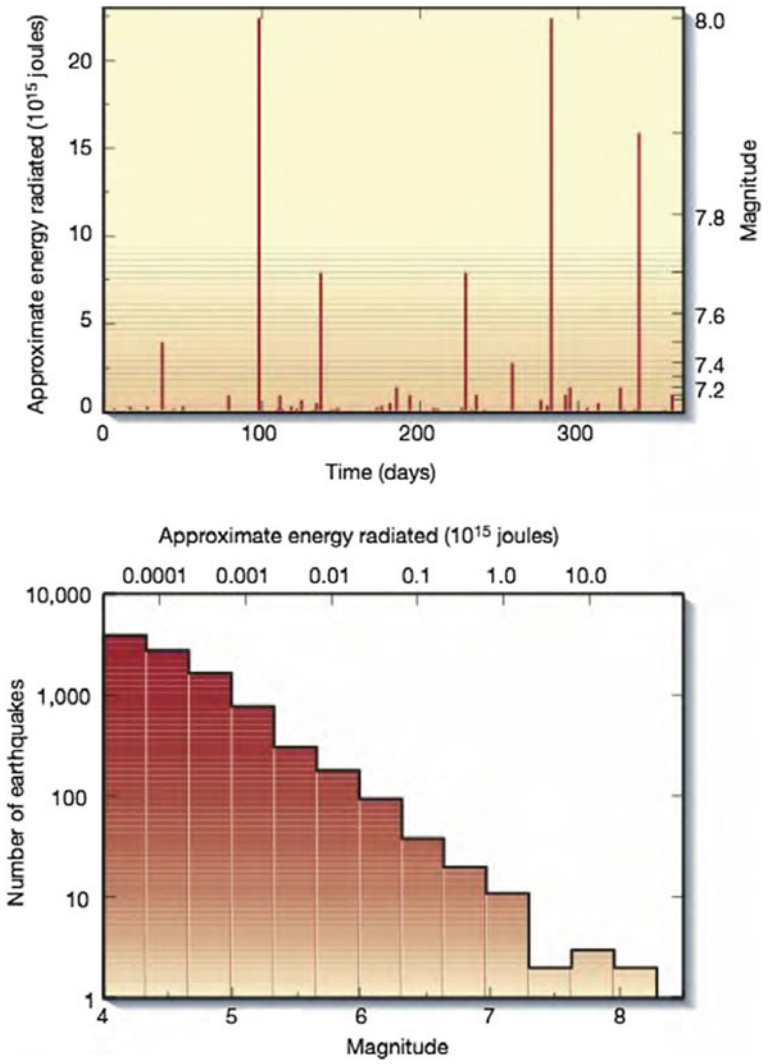

Fig. 6.1 An example for the magnitudes of earthquakes that occurred in 1995 (*top*) and the number of earthquakes (*frequency*) in 1995 as a function of corresponding magnitude in the log-log scale, which follows Gutenberg-Richter law. From Sethna et al. [4]

by $P(M_{th}) \propto 10^{-b_{th}M_{th}}$, where b_{th} is an exponent constant and the magnitude M_{th} is measured as a logarithmic scale. It thus shows a straight line on a log-log scale, that reveals a scale-invariant behaviour for the occurrence of earthquakes (Fig. 6.1).

As the constant b_{th} from the Gutenberg-Richter law reflects self-similarity for all magnitudes, earthquakes are expected to follow the same distribution for small and large earthquakes. However, the b_{th} value has been observed to vary slightly with

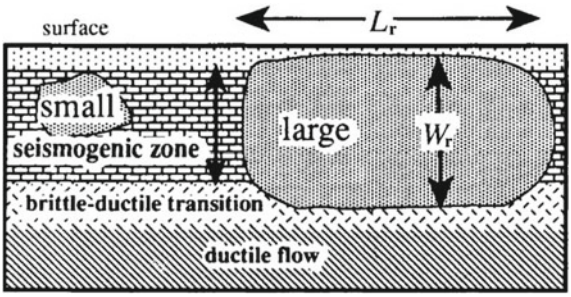

Fig. 6.2 The geometry constrains for small earthquakes scale (marked as '*small*') and for large earthquakes scale (marked as '*large*'). L_r and W_r are the length, along the strike of fault, and down-dip width of the rupture. From Pacheco et al. [6]

M_{th}. It is generally smaller for small earthquakes ($b_{th} \sim 0.80 - 1.06$) and larger for big earthquakes ($b_{th} \sim 1.23 - 1.54$) [5]. Pacheco et al. explain this variation in terms of differences in the constraints of geometries between small earthquakes and large earthquakes [6]. As illustrated in Fig. 6.2 by Pacheco et al. large earthquakes, in principle, have no limitations in lateral dimension (the length of rupture, L_r), but are limited in the down-dip direction (rupture width, W_r) based on the thickness of seismogenic layer, where earthquakes are able to occur. In contrast, small earthquakes have no bounds in either direction (L_r and W_r). These features lead to a break down in self-similarity seen as a slope change from small earthquakes to large earthquakes in the frequency-magnitude diagram. To support the model, Pacheco et al. have demonstrated a break in self-similarity occurs at the point in the data where the event scale is identical to the down-dip width of seismogenic layer (from earthquakes of magnitude between 5 and 9 and shallower than 350 km, covering the years from 1900 to 1990).

Given the general self-similarity of earthquakes, it is intriguing to know whether or not the ubiquitous noise observed in the far smaller scales in the laboratory, such as that resulting from crack movement in the materials, show similar behaviour. The fracture of materials can be defined broadly in terms of two scenarios [7]. For a perfect crystalline solid on loading, a homogeneous material may break in a perfect brittle manner through 'one crack' (a fracture propagates suddenly). On the other hand, for heterogenous materials subjected to loading, the intrinsic heterogeneities (dislocations and flaws) or disorder progressively adapt and generate microcracks. As the microcracks interact and correlate this may lead to coalescence to form progressive damage in the material. The process of nucleation and propagation of cracks then produces the crackling noise, seen before the ultimate failure of the solid [7, 8].

Niccolini et al. have analysed and compared the crackling noise generated from Italian earthquakes in the years 1984–2002 and from laboratory acoustic emission (AE) measurements of concrete [7]. The probability densities of waiting-times, i.e. the time intervals between consecutive events, shows similar power-law relations for different magnitudes in Italian earthquakes and for different amplitudes in the concrete specimen. In order to describe the waiting-time probability densities with different magnitudes in earthquakes and amplitudes in the concrete specimen, Niccolini et al. provided a rescaled model with waiting-time. The scaling law for waiting-time

distributions for both cases is:

$$f(t_\theta) \propto t_\theta^{-(1-\gamma_\theta)} \exp[(-t_\theta/\mathrm{A})^{b_\theta}] \tag{6.1}$$

where $t_\theta \equiv R_0 10^{-a_\theta M_{th}} t$ is the rescaled waiting-time, R_0 is the hypothetical mean rate for $M_{th} = 0$, M_{th} is the magnitude of earthquake, t is the waiting-time, a_θ, γ_θ, and b_θ are exponents, A is the constant. In both cases, scaling collapse onto a single scaling function is seen for different waiting-time distributions, implying scale invariance for waiting-times over a wide range of space and time scales. However, a broad range of power-law exponents for the waiting-time distributions is found among different studies, from 0.6 for Italian seismicity [7] upto 4.5 in laboratory acoustic emission (AE) time series data on rock fracture [9]. This large variance shows that problems remain in providing a unique scaling function for all fracture processes, irrespective of time, length, and magnitude scales.

Halász et al. simulated the effects of disorder on crackling noise for a single crack propagating in a bar-shaped specimen [8]. The model specimen was loaded at constant stress rate, in three-point bending, to ensure either no beam breaking occurs or only a single 'beam' breaks. Here, their 'beams' refer to components of a network of tessellated elements that make up the 'specimen', and give the object a granular nature. The distribution of burst size (the number of beams broken) varies with the extent of disorder. They found, with decreasing disorder, the size of a burst becomes larger, but the functional form remains similar. Hence, they provided a scaling structure for the data by

$$P(\Delta_z) = \bar{\Delta_z}^{\beta_z} g(\Delta_z/\bar{\Delta_z}^{\alpha_z}) \tag{6.2}$$

where $P(\Delta_z)$ is the size distribution, $\bar{\Delta_z}$ is the average burst size, α_z and β_z are numerical constants. The data are then seen to collapse into a master curve by $P(\Delta_z) \sim \Delta_z^{-\tau_z}$, which gives $\tau_z = 1.31 \pm 0.04$. This indicates that bursts from jerky propagation of a crack have a power law size distribution irrespective of the amount of disorder.

Large noise spikes, sometimes referred to as jerky elasticity [10], are also observed in the elastic responses of materials during transformation between austenite and martensite phase, using acoustic emission (AE) or equivalent measurements when the stress is the driving force for the interfacial movement in the material [10, 11]. Both jerky elasticity and acoustic noise reveal a power-law behaviour through a frequency-size (or frequency-energy) relation. Based on the acoustic emission, calorimetric and magnetic-susceptibility measurements of martensitic transitions in Fe–Pd material, Bonnot et al. [11] have shown that the probability of AE activities and energy distributions give power-law behaviours to both its AE activities (size, A_s) and to its energy (E_s). They have proposed models with a unique exponent (τ_s or ε_s) to represent these power-law distributions, which are defined as

$$P(A_s)dA_s = \frac{A_s^{-\tau_s}}{Z_A(\tau_s)}dA_s \tag{6.3}$$

$$P(E_s)dA_s = \frac{E_s^{-\varepsilon_s}}{Z_E(\varepsilon_s)}dE_s \tag{6.4}$$

where Z_A and Z_E are the functions of the exponents that act as normalisation factors, but are fixed in the fit. $P(A_s)$ and $P(E_s)$ are the size and energy distributions. Bonnot et al. then suggest a generic statistical dependence between size and energy ($E_s \sim A_s^{z_s}$) based on the exponents τ_s (2.14–2.95) and ε_s (1.59–2.00) obtained from experiments. They proposed the power-law exponents for the size distribution (τ_s) and energy distribution (ε_s) can be related by

$$z_s = \frac{\tau_s - 1}{\varepsilon_s - 1} \tag{6.5}$$

where $z_s \sim 2$ for all measurements on both heating and cooling, which gives $E_s \sim A_s^2$.

Jerky elasticity has also been observed in Cu–Al–Be shape-memory alloy, using dynamical mechanical analyser (DMA) [10]. Massive spikes (avalanches) occur in the dissipation of elastic response function during the martensitic transition (between a paraelastic and a ferroelastic phase). Avalanches can occur (athermal behaviour) if the stress in the system is driven slowly enough across the transition, where thermal fluctuations are less significant to the process. A total of 314 internal friction noise peaks were then used to characterise the probability distribution of internal friction noise peaks ($P(E_s)$) as a function of peak height (the amplitude of the peak). The distribution of $P(E_s)$ was seen to have a power-law behaviour with an exponent $\varepsilon_s = 1.3$ in Salje et al.'s study.

It is, therefore, interesting to see whether this universal power law behaviour also embedded in the noise spikes, that occur in the shear modulus and internal friction data by using inverted forced torsion pendulum (as equivalent measurement to DMA) for heterogeneous materials such as basaltic rocks. Here, I will discuss the method for determining noise peak size (A_s and E_s) from these studies to analyse the noise distributions observed in this study.

6.2 Samples and Noise Data Process Methods

Noise data have been collected from the heating patterns of shear modulus and internal friction in I13_83493 basalt (referred to as I13 basalt hereafter), Iceland basalt and Skaergaard gabbro. The sample descriptions are provided in Sect. 3.2 and Figs. 3.8, 3.9, 3.10 and their heating histories are described fully in Chap. 4. For consistency, only noise spikes from heating curves at a stress frequency of 1 Hz and

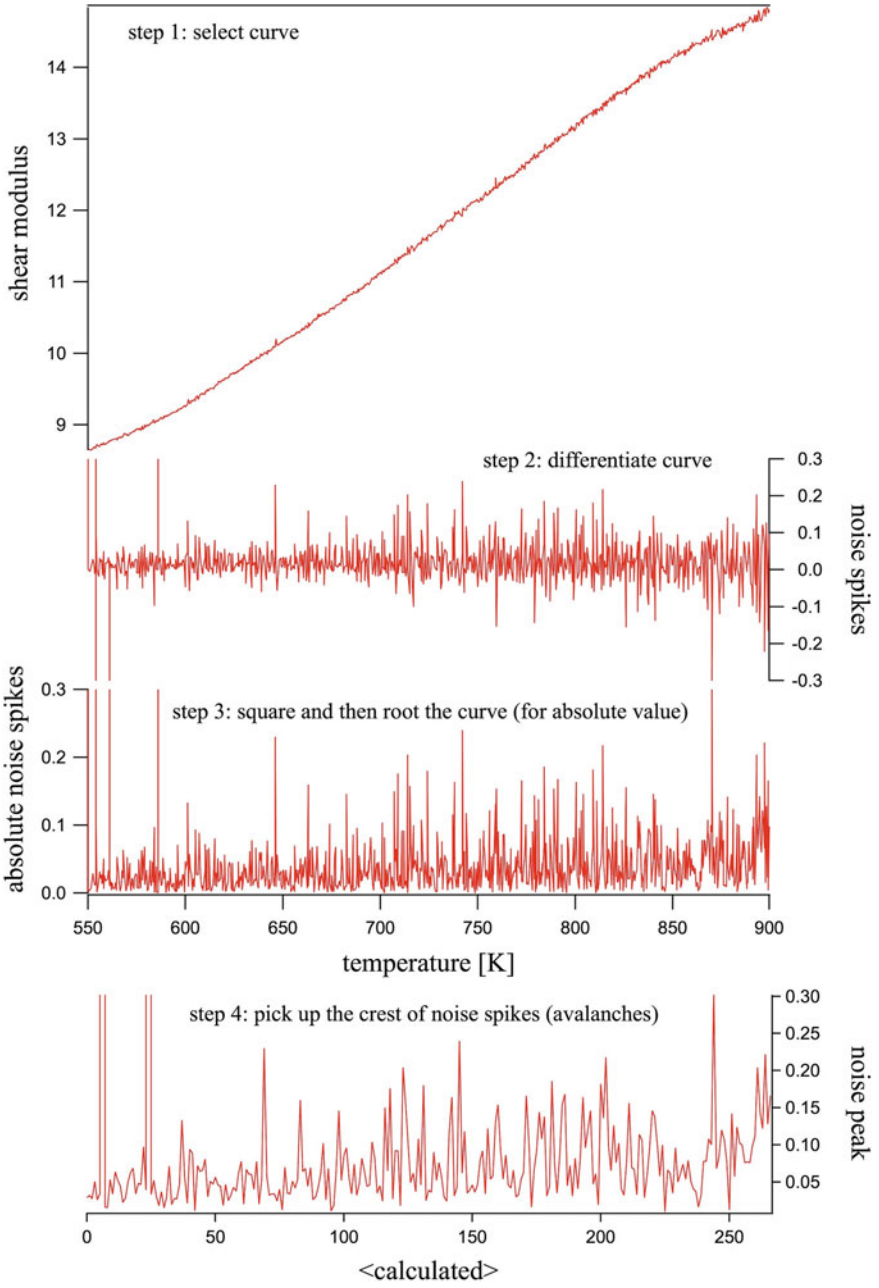

Fig. 6.3 Noise data processing from selection of a shear modulus heating run in I13 basalt, as an example, to finally producing the noise spike avalanches

at a temperature ramp rate of 1 K/min have been selected for comparison in this chapter. Figure 6.3 illustrates the process used to quantify noise peaks from a heating dataset. Firstly, the noise spikes themselves are obtained by differentiating the heating curves, using the Igor software suite. Then the noise spike data are squared and rooted to obtain absolute values of noise data. The noise spikes thus far represent groups of noise avalanches occurring on heating. Each crest of a local noise spike group represents one noise avalanche and hence they are selected as the noise peak data (Fig. 6.4).

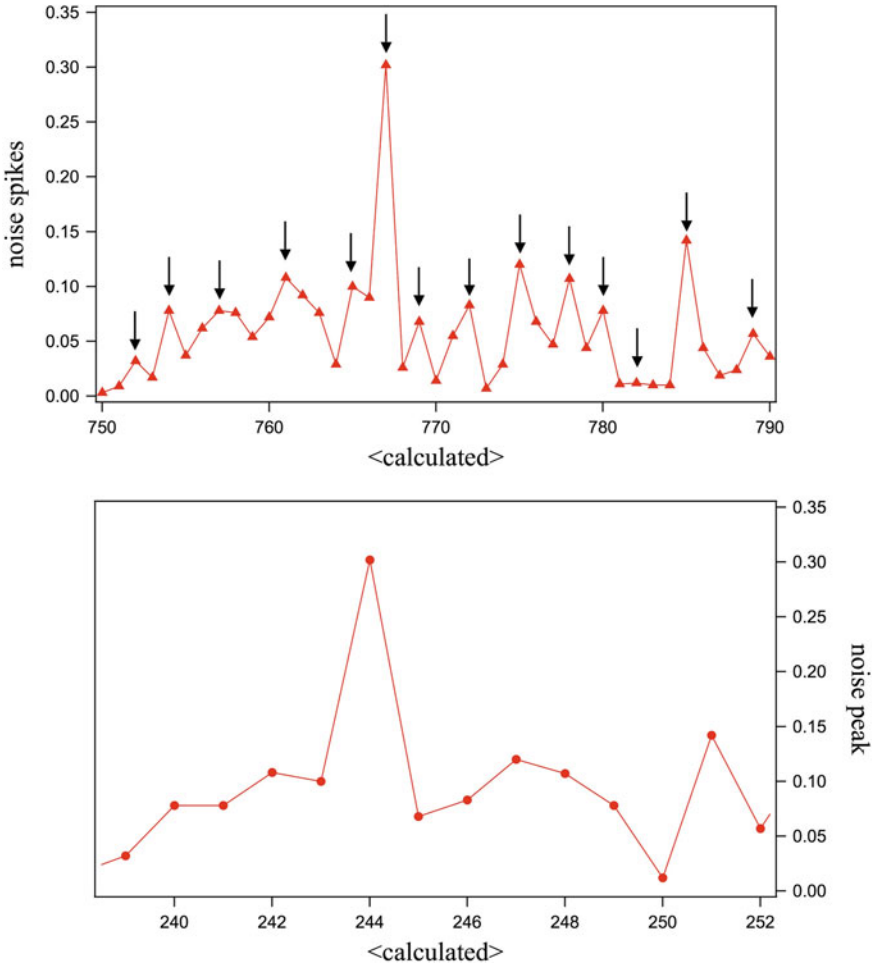

Fig. 6.4 The noise peak (*bottom*) is selected from the crests of noise spikes groups of noise avalanches (*top*)

To determine the relation between the probability of noise events and their magnitude on a logarithmic scale, a 'bin density' method has been used to group noise peaks. In other words, the number density of noise peaks (probability) are determined based on the logarithmic noise size, rather than noise size (i.e. the amplitudes of noise peaks). The resultant probabilities of noise size against noise size from this 'bin density' method are plotted and discussed in the following sections.

6.3 Results and Analysis

6.3.1 Noise from Shear Modulus

Noise spikes appear in all measured shear modulus curves as a function of temperature (Fig. 6.5). The noise spikes become larger in amplitude at higher temperatures of each heating curve and are also more evident in data from samples that have previously cooled from temperatures above the glass transition temperature. For example, the heating run in I13 basalt previously cooled from 1100 K (Fig. 6.5 top), the heating run in Iceland basalt previously cooled from 1290 K (Fig. 6.5 middle) and the heating run in Skaergaard gabbro previously cooled from 1400 K (Fig. 6.5 bottom) all show significant measurable noise. The larger noise spikes are particularly enhanced in the plateau (maximum) of the shear modulus curves, especially around the glass transition temperature and the beginning of the softening.

Noise peaks on shear modulus data obtained from the 'bin density' method are plotted as the distribution of noise peak size (probability, $P(A_s)$) against the magnitude of noise peak (noise peak size, A_s) in Fig. 6.6. The relationship between probability and magnitudes of noise peak in all heating curves reveals a power law behaviour such that small noise peaks show abundantly while only a few large noise peaks occur during the measurements. The noise distribution (probability against peak size) of heating runs, that previously cooled from the temperatures below the glass transition temperature, are seen to plot reproducibly on top of each other for Iceland basalt and gabbro. Also, the noise distribution of two heating runs in Iceland basalt (Fig. 6.6 middle), that previously cooled from the temperatures above the glass transition temperature (from 1270 K and from 1290 K), give similar patterns and both shift to the right, towards the larger noise peak size region. This shift is also seen in I13 basalt which previously cooled from 1100 K (Fig. 6.6 top) and in gabbro previously cooled from 1400 K (Fig. 6.6 bottom), both temperatures above their glass transition temperatures. The size of this shift is similar for I13 basalt and Iceland basalt while the shift is much larger and more significant in gabbro.

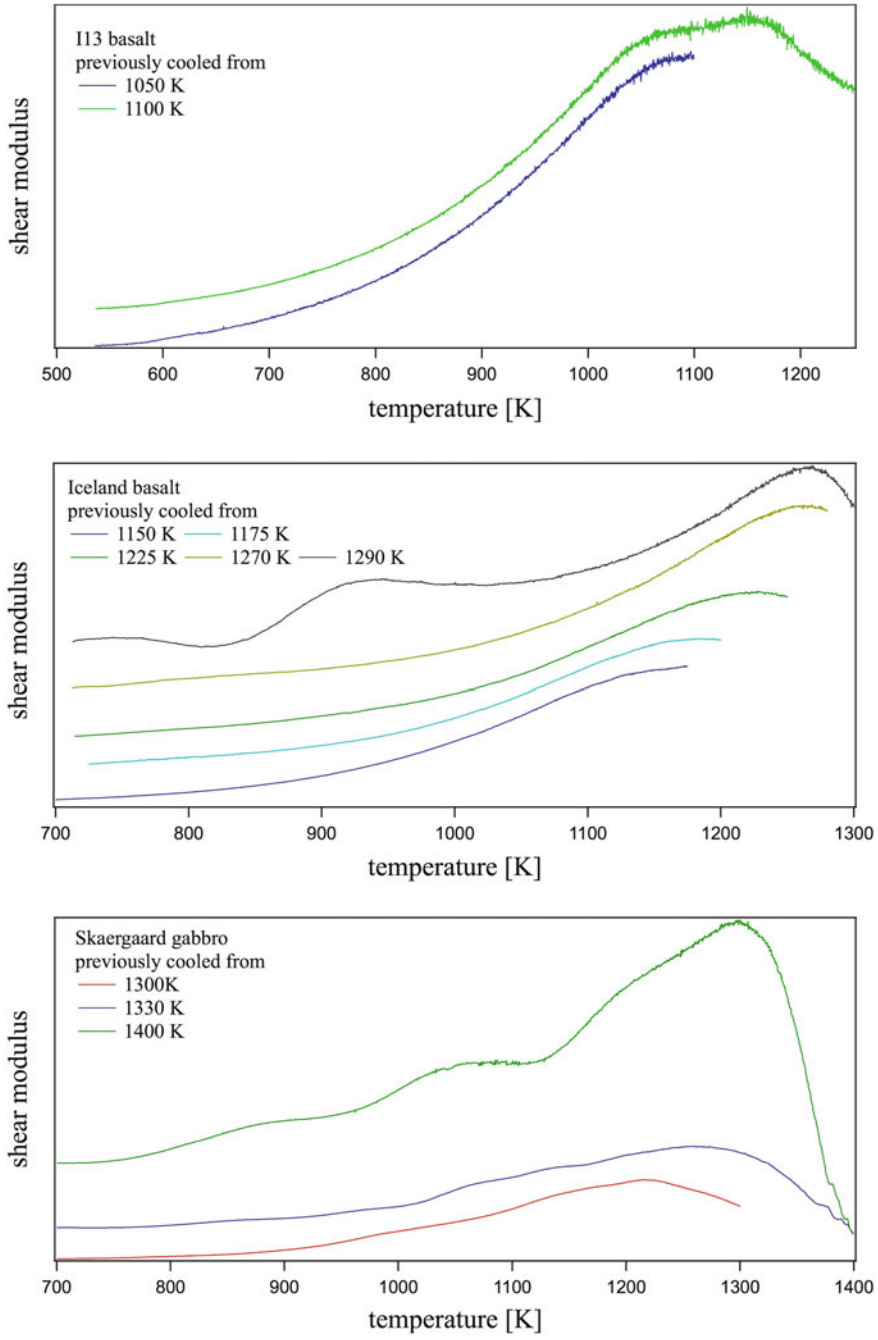

Fig. 6.5 The shear modulus of I13 basalt (*top*), Iceland basalt (*middle*) and Skaergaard gabbro (*bottom*) on heating. Temperature ramp is 1 K/min on heating as well as on cooling

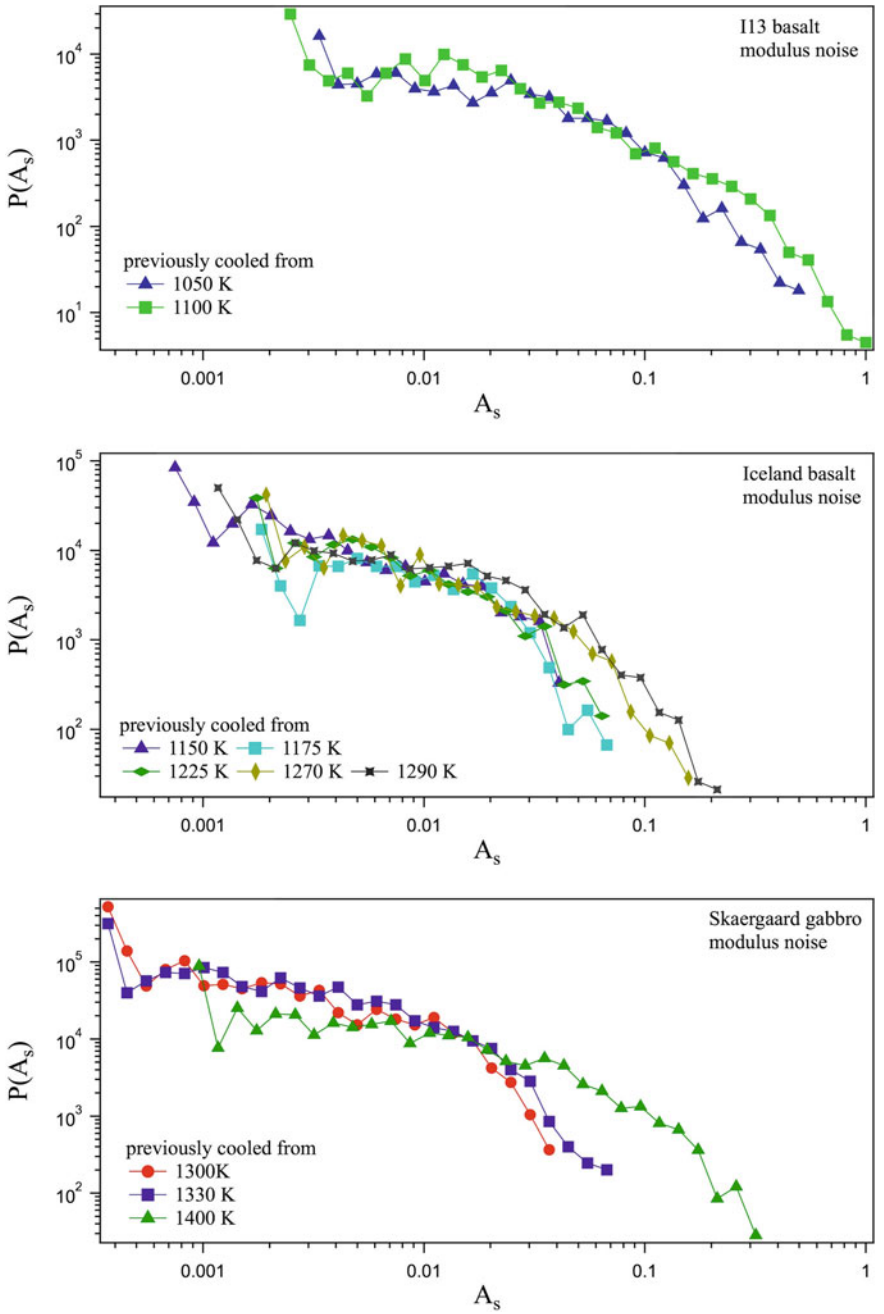

Fig. 6.6 The probability of noise peak size ($P(A_s)$) against noise peak size (A_s) for shear modulus data of I13 basalt (*top*), Iceland basalt (*middle*) and Saergaard gabbro (*bottom*) on heating. Temperature ramp is 1 /min on heating as well as on cooling

6.3.2 Noise from Internal Friction

Noise spikes in internal friction on heating occur abundantly in basalt and less so in gabbro (Fig. 6.7). The magnitudes of noise spikes increase with increasing temperature. The noise spikes are most significant in I13 basalt (Fig. 6.7 top) and less profound in Iceland basalt (Fig. 6.7 middle), for all heating runs. In addition, small discrete bursts of noise spikes are seen in the internal friction curves of Iceland basalt in the low-temperature regions and these become continuous avalanches toward to high-temperature regions in the vicinity of the thermally-activated internal friction relaxation peak. These discrete busts also occur in the low-temperature data of I13 basalt previously cooled from 1100 K. In contrast, no clear discrete bursts of noise spikes are seen in the heating runs of I13 basalt cooled from 800 K and from 1050 K or in any of the heating runs of gabbro (Fig. 6.7 bottom). The noise spikes in gabbro are relatively small compared with those in basalts, especially in the heating runs which were run after the samples was cooled from 1300 K and 1330 K (below the glass transition temperature). The noise spikes in gabbro previously cooled from 1400 K (above onset of partial melting) are larger and enhanced in the area between two thermally-activated relaxation peaks.

Noise peaks in the internal friction data obtained from the 'bin density' method are plotted as probability ($P(E_s)$) against magnitude of noise peak size (E_s) in Fig. 6.8. The distribution of probability and magnitudes of noise peaks in all internal friction heating curves also reveals a power law behaviour in all three samples. No obvious differences of the distributions of internal friction noise peaks are seen between I13 basalt and Iceland basalt (Fig. 6.8 top and middle) among the heating runs, but the noise distributions show a trend shifting to the region of larger noise peak sizes in the later heating runs. The internal friction noise distributions of gabbro previously cooled from 1300 K and from 1330 K lie on the top of each other and the heating run for the sample previously cooled from 1400 K shifts significantly to the right (larger noise peaks are more abundant).

6.4 Discussions

Data for both shear modulus and internal friction of basalts and gabbro show noise behaviour with peak distributions that have a power-law relation between probability and noise amplitude (Figs. 6.6 and 6.8). The noise size distribution for the shear modulus has a lower power law exponent (generally less than one) in the region of small noise amplitude for all samples. The noise information at small amplitudes is associated mainly with the instrument and electronics, and noise from the specimen is of the same orders, or smaller, so that it is not detected during the measurements. Similarly, these phenomena (due to the limitation of measurements) are seen in noise size distribution of internal friction in I13 basalt and gabbro.

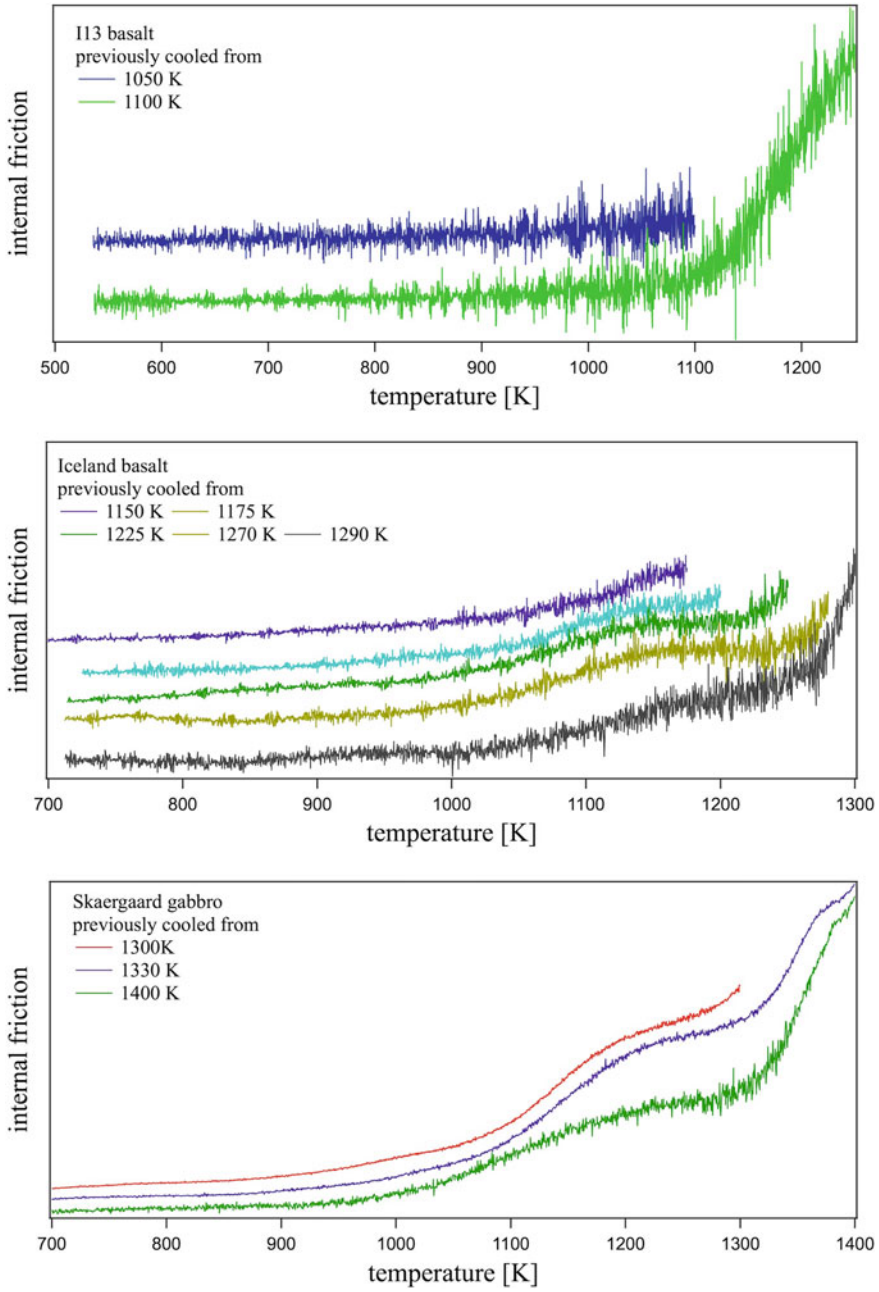

Fig. 6.7 The internal friction of I13 basalt (*top*), Iceland basalt (*middle*) and Skaergaard gabbro (*bottom*) on heating. Temperature ramp is 1 K/min on heating as well as on cooling

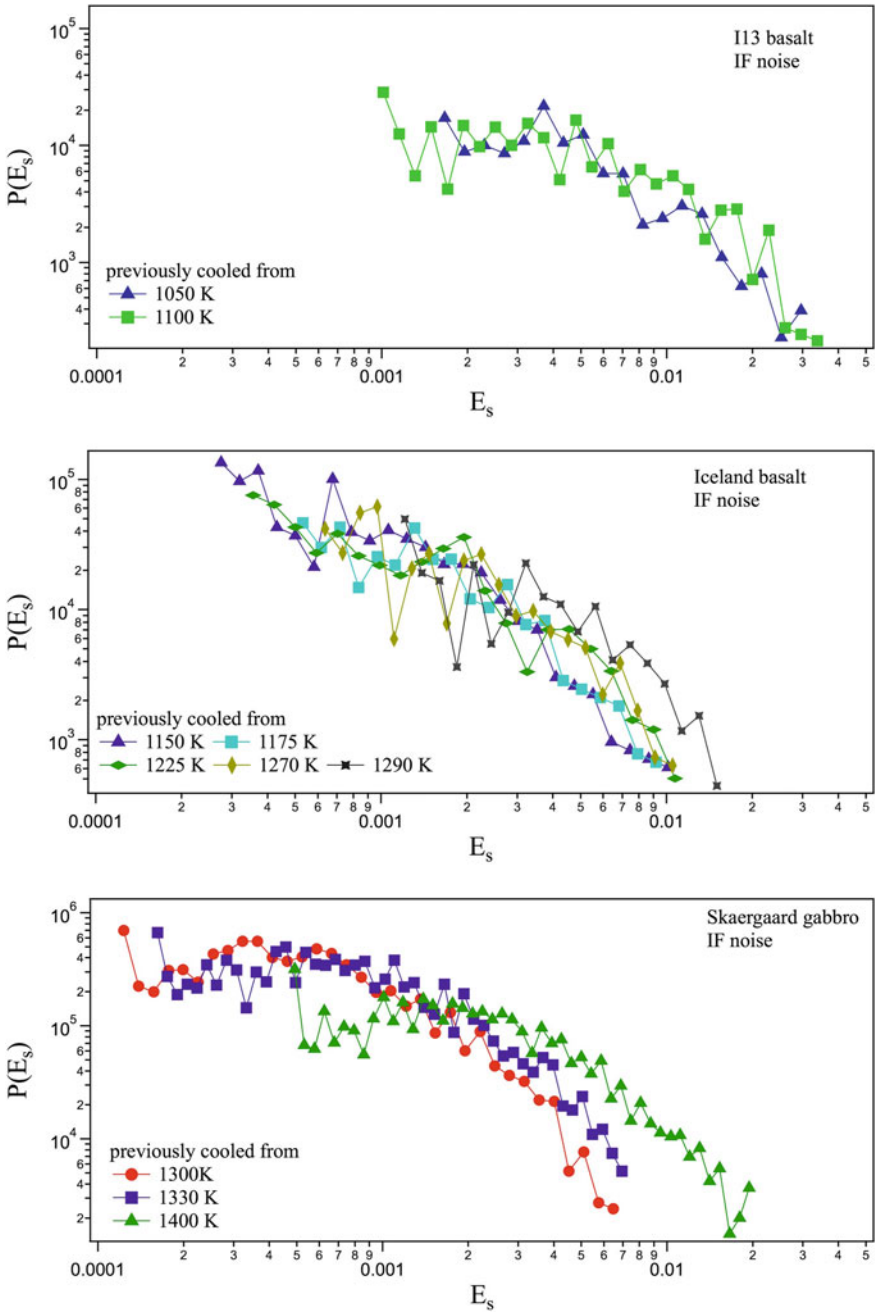

Fig. 6.8 The probability of noise peak size ($P(E_s)$) against noise peak size (E_s) for internal friction of I13 basalt (*top*), Iceland basalt (*middle*) and Skaergaard gabbro (*bottom*) on heating. Temperature ramp is 1 K/min on heating as well as on cooling

The samples' thermal history is seen to influence the noise distributions (Fig. 6.9). The noise distributions can be distinguished depending on whether or not the samples have been heated to a temperature above the glass transition temperature before the measurements. The noise distributions shift to the region of larger noise amplitudes for data from samples which have previously been heated above the glass transition temperature. This influence is more clear to see in the noise of the shear modulus data, compared to the internal friction data, and also more evident in gabbro than in basalt. It seems that samples that are more crystalline (i.e. before heating to the glass transition temperature) show smaller noise spikes. On the other hand, partial melting may be generated when samples are heated above the glass transition temperature, and this results in larger noise spikes during the subsequent measurements. This distribution shift suggests that the noise distribution in both shear modulus and internal friction data is likely generated due to processes associated with microstructural and mineralogy of the sample.

The noise power law distribution in both shear modulus and internal friction does not have a single straight line on a log–log scale. Instead, two breaks in slope of the distributions are found in shear modulus data while only one break in slope occurs in the internal friction noise distributions. The power law exponents for shear modulus noise (τ_s) and internal friction noise (ε_s) have been obtained from linear fits of the log–log frequency-size relation. The fit results for τ_s are ∼1.2 and ∼1.6 for small noise peaks in basalt and gabbro and ∼3 for large noise peaks in all samples (Fig. 6.10), while ε_s shows one exponent of 1.6–1.7 for basalt and 2.2 for gabbro (Fig. 6.11). Small exponents (<1) at very small noise peak sizes for both shear modulus and internal friction datasets are associated with the instrument. Exponents (ε_s and τ_s ∼1–2) obtained in gabbro are larger than those in basalts, which may be a result of the cut-off effect, due to the grain size. Grain size in basalt is much smaller than the sample size (thickness) while grain size in gabbro is close to or bigger than the sample size (thickness). The larger grain size results in a higher exponent.

The fit results of exponents for τ_s and ε_s have then been used for further calculations to obtain z_s values, based on Bonnot et al.'s relation (Eq. 6.5 above). Results of fits and calculations are presented in the Table 6.1. The z_s values in this study are consistent with Bonnot et al.'s results, within error, confirming that the relation between size and energy distribution (as real part and imaginary part of noise distribution) is $E_s \sim A_s^2$ [11]. Generally, the modulus data are easily influenced by instrumental noise, but the internal friction data are independent of instrumental interference. Therefore, the small exponent τ (1.20–1.55) may be the results from the interactions between the modulus noise and the instrumental noise. This may explain the absence of the corresponding small exponent ε_s, considering z values.

The energy distribution exponents for noise have been extensively investigated previously for martensitic transitions in alloys due to their technical demands. Noise associated with martensitic transition in Fe–Pd polycrystalline material and Cu-based shape-memory alloys gives ε_s values between 2 and 3 in acoustic emission measurements [11, 12] while the energy exponent related to the martensitic transition in another Cu-based shape memory alloy was found to be about 1.3, measured by dynamic mechanical analyser [10]. Noise distributions have also been analysed

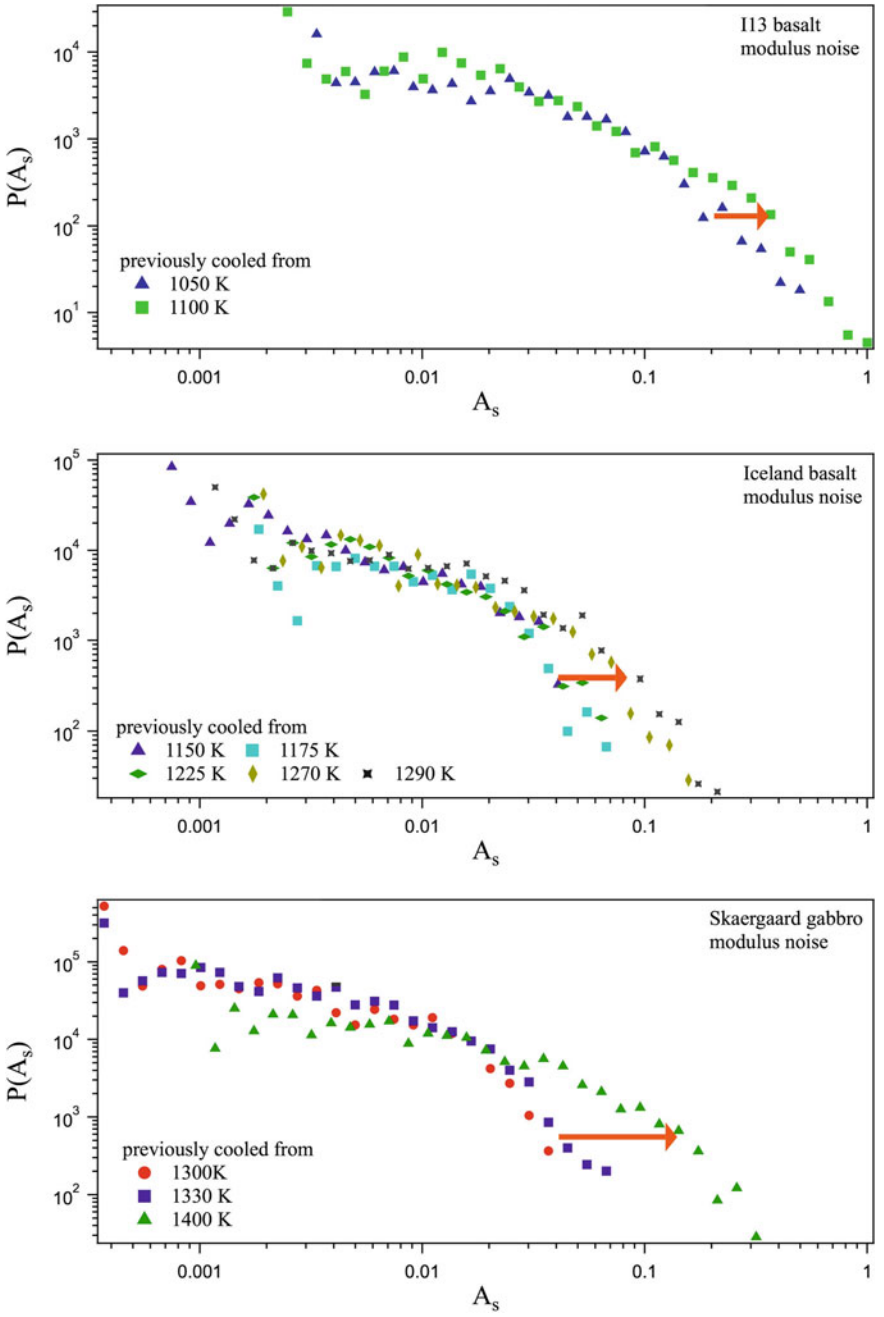

Fig. 6.9 Noise distribution shifts (*orange arrow*) to the higher noise peak size region for heating runs, which previously cooled from temperatures above the glass transition temperatures, seen in I13 basalt (*top*), Iceland basalt (*middle*) and Skaergaard gabbro (*bottom*). Temperature ramp is 1 K/min on heating as well as on cooling

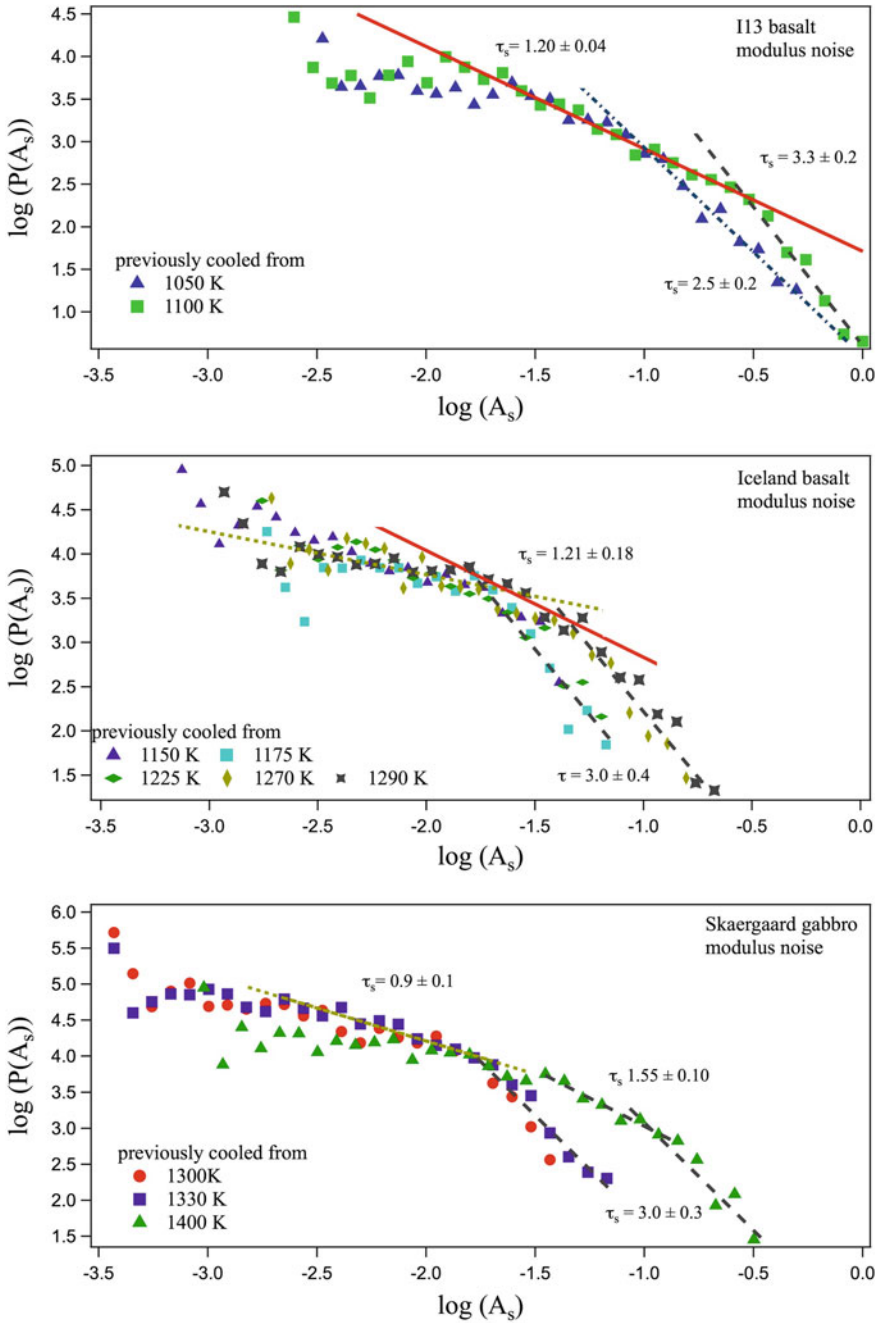

Fig. 6.10 The power law exponents (τ_s) from the shear modulus noise distributions in I13 basalt (*top*), Iceland basalt (*middle*) and Skaergaard gabbro (*bottom*). Temperature ramp is 1 K/min on heating as well as on cooling

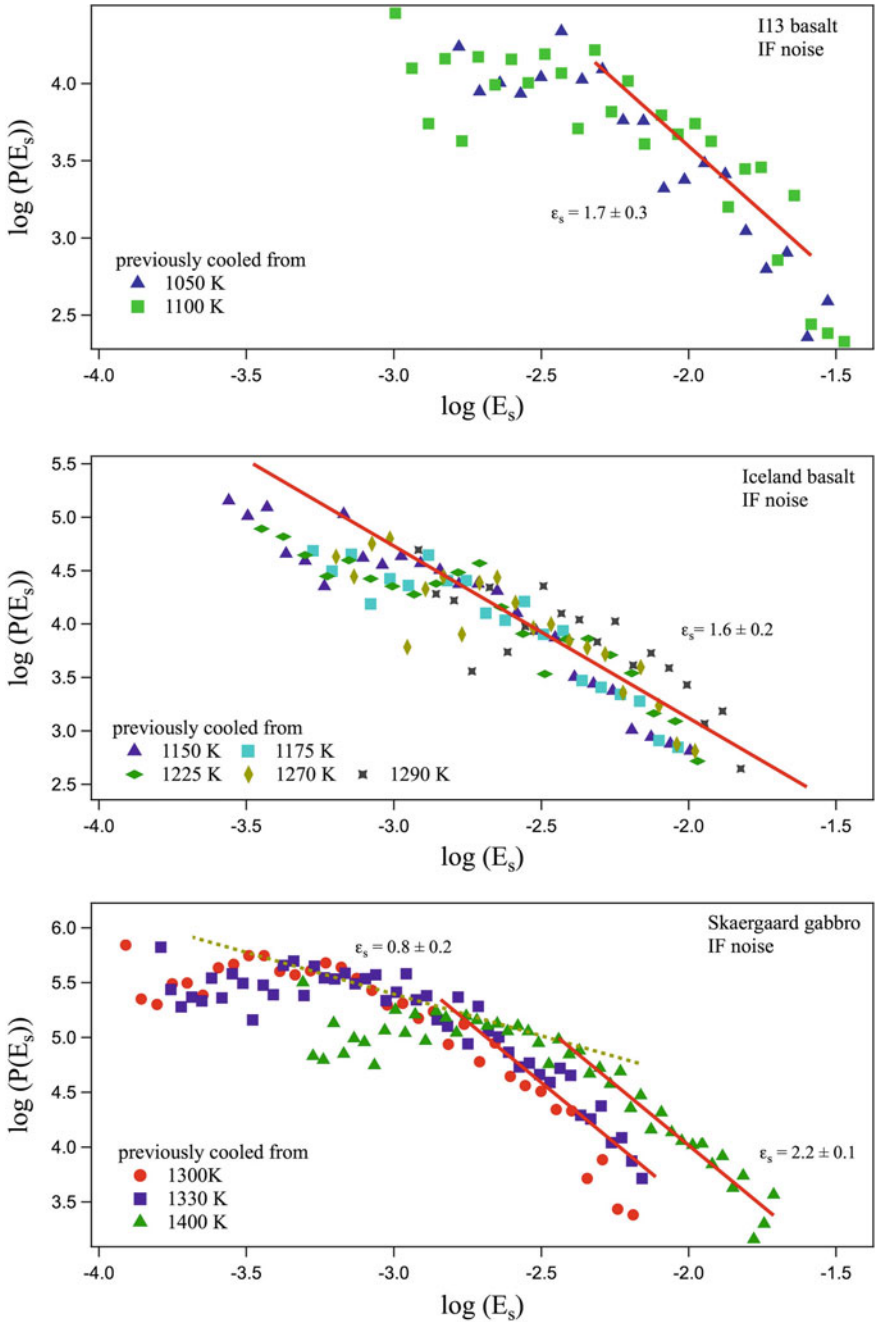

Fig. 6.11 The power law exponents (ε_s) from the internal friction noise distributions in I13 basalt (*top*), Iceland basalt (*middle*) and Skaergaard gabbro (*bottom*). Temperature ramp is 1 K/min on heating as well as on cooling

Table 6.1 Exponents of noise distribution for shear modulus data (τ_s) and internal friction data (ε_s) and the z_s values obtained from Eq. 6.5

sample	τ_s	ε_s	z_s
I13 basalt	1.20±0.04	n/a	n/a
	2.5±0.2	1.7±0.3	2.0±0.8
	3.3±0.2		3.2±1.1
Iceland basalt	1.21±0.18	n/a	n/a
	3.0±0.4	1.6±0.2	3.2±1.3
Skaergaard gabbro	1.55±0.10	n/a	n/a
	3.0±0.3	2.2±0.1	1.6±0.4

by acoustic emission experiments on sheets of paper and silica ceramics, with higher applied stress in the system. The acoustic activities were measured as a tear line develops in a sheet of paper, which eventually lead to paper peeling, under constant loading (in creep) by Koivisto et al. and this process gives an energy exponent 1.8 ± 0.1 from acoustic noise [13]. In addition, a compression test was carried out on the mesoporous silica ceramic (Vycor) by slowing increasing uniaxial stress during compression [10]. The acoustic activities were found to correlate with discontinuous strain changes in the sample upon increasing stress and follow a power law distribution with an energy exponent of 1.39 ± 0.02. Although the internal friction noise in this study has ε_s values that lie inbetween these previous investigations, it is difficult to define what is the precise process associated with internal friction noise behaviour at this stage.

The small size distribution exponents in shear modulus noise (τ_s =1.20–1.55) in basalt and gabbro are found to have similar values to those quoted in previous theoretical studies, which focused on crack propagation in solids. Laurson et al. use the crack line model to simulate a planar crack front propagating in a disordered medium and obtain a power-law size distribution with an exponent 1.25 ± 0.05 [14]. Halász et al. model a crack propagating in a three point bending test for heterogeneous materials, by changing the amount of disorder in the system, and then provide a rescaled size distribution exponent of 1.31 ± 0.04, regardless of the amount of disorder [8]. It may be worth mentioning that the size distribution exponent from three dimensional self-organised criticality simulations by Bak et al. is about 1.35 [1] and the experimental Barkhausen noise distributions, due to discontinuous magnetic domain movements, have exponents between 1.3 and 1.5 for short-range soft magnets [15].

Larger exponents are seen in noise distributions associated with the martensitic transition of Fe–Pd alloys from acoustic emission measurements, giving 1.59–2.00 for single crystals and polycrystals (on heating and cooling) [11]. Much larger exponents were also found in simulation studies of external loading for samples approaching to the limits of their tensile strength [16]. Kun et al. used a fibre bundle model to test two kinds of stress environment (homogeneous and inhomogeneous) for the subcritical fracture of heterogeneous materials under different loadings. In

an equal load sharing case (stress homogeneous), the size distribution exponents decrease from 2.5 to 1.5 with increasing loading close to tensile strength of fibre bundle. However, different behaviour is seen in the local load sharing case (stress inhomogeneous). The size exponents were found to increase from 1.8 to 4.5 upon increasing external stress close to the tensile strength of the bundle and finally lead to fracture growth.

It is unclear whether or not the varying size distribution exponents (τ_s) in this study are associated with fracture propagation, although the values are in the same range as those in previous studies. However, the exponent τ_s for small noise amplitudes in this study may be related to overall microstructural interactions while the exponents for large amplitude noise may be related to the interactions with the local environment, following Kun et al.'s model, or they may be due to the cut-off resulting from the larger grain size of the sample.

In Chap. 5, the 'episodic noise' associated with magmatic systems in Earth's brittle crust was associated with the overall mechanical response of basalt. Here we see that on a microscopic scale basalt follows similar general behaviours, in terms of the statistical nature of random events, as the Earth. The underlying physics of self-organised criticality provides the link between these disparate processes, that reveals a universal property. Here, I have shown that the nature of noise itself, in the way that its probability distribution scales, is linked to microstructural changes in complex heterogeneous solids, such as igneous rocks. As the nature of the samples change, either by crack percolation, glass formation (partial melting) or recrystallisation, the details of exponents may change. Torsion pendulum mechanical experiments appear to give a route to obtain both exponent τ_s and ε_s for noise distributions.

References

1. Bak, P., Tang, C., & Wiesenfeld, K. (1987). Self-organized criticality: An explanation of the 1/f noise. *Physical Review Letters*, *59*(4), 381–384.
2. Bak, P., Tang, C., & Wiesenfeld, K. (1988). Self-organized criticality. *Physical Review A*, *38*(1), 364–374.
3. Gutenberg, B., & Richter, C. (1954). *Seismicity of the earth and associated phenomena* (2nd ed.). Princeton: Princeton University Press. (1st ed. 1949).
4. Sethna, J. P., Dahmen, K. A., & Myers, C. R. (2001). Crackling noise. *Nature*, *410*(6825), 242–250.
5. Olami, Z., Feder, H. J. S., & Christensen, K. (1992). Self-organized criticality in a continuous, nonconservative cellular automaton modeling earthquakes. *Physical Review Letters*, *68*(8), 1244–1247.
6. Pacheco, J. F., Scholz, C. H., & Sykes, L. R. (1992). Changes in frequency-size relationship from small to large earthquakes. *Nature*, *355*(6355), 71–73.
7. Niccolini, G., Durin, G., Carpinteri, A., Lacidogna, G., & Manuello, A. (2009). Crackling noise and universality in fracture systems. *Journal of Statistical Mechanics: Theory and Experiment*, *2009*(1), P010203.
8. Halász, Z., Timár, G., & Kun, F. (2010). The effect of disorder on crackling noise in fracture phenomena. *Progress of Theoretical Physics Supplement*, *184*, 385–399.
9. Chmel, A., Kuksenko, V. S., Smirnov, V. S., & Tomilin, N. G. (2007). Anomalies of critical state in fracturing geophysical objects. *Nonlinear Processes in Geophysics*, *14*(2), 103–108.

10. Salje, E. K. H., Koppensteiner, J., Reinecker, M., Schranz, W., & Planes, A. (2009). Jerky elasticity: Avalanches and the martensitic transition in $cu_{74.08}al_{23.13}be_{2.79}$ shape-memory alloy. *Applied Physics Letters*, *95*(23), 231908.
11. Bonnot, E., Mańosa, L., Soto-Parra, A., Vives, D., Ludwig, E., & Strothkaemper, C. (2008). Acoustic emission in the fcc-fct martensitic transition of fe_68.8pd_31.2. *Physical Review B*, *78*(18), 184103.
12. Gallardo, M. C., Manchado, J., Romero, F. J., Salje, E. K. H., Planes, A., Vives, E., et al. (2010). Avalanche criticality in the martensitic transition of $cu_{67.64}zn_{16.71}al_{15.65}shape - memoryalloy : Acalorimetricandacousticemissionstudy$. *Physical Review B*, 81(17), 174102.
13. Koivisto, J., Rosti, J., & Alava, M. J. (2007). Creep of a fracture line in paper peeling. *Physical Review Letters*, *99*(14), 145504.
14. Laurson, L., Santucci, S., & Zapperi, S. (2010). Avalanches and clusters in planar crack front propagation. *Physical Review E*, *81*(4), 046116.
15. Colaiori, F. (2008). Exactly solvable model of avalanches dynamics for barkhausen crackling noise. *Advances in Physics*, *57*(4), 287–359.
16. Kun, F., & Halász, Z, Jr. (2009). Crackling noise in sub-critical fracture of heterogeneous materials. *Journal of Statistical Mechanics: Theory and Experiment*, *2009*(01), P01021.

Chapter 7
Fluid Pressure and Failure Modes of Sandstones

7.1 Introduction

The existence of the fractures and fluids in the rocks, together with the associated pore pressures can cause significant changes of rock properties. The role of fluids, their interaction with microstructure, and their influence on the internal stresses and pressures in a rock are all important when considering partially molten rocks, as well as when understanding porous rocks (e.g. sediments) in reservoir settings. For example, in a dyke system (such as discussed in Chap. 5), a moving "process zone" (a zone of inelastic deformation) is associated with microseismicity ahead of the tip of a propagating dyke [1, 2]. The near-tip stress field accumulates at high confining pressure (greater depth) and results in inelastic deformation at the tip of a propagating dyke. Such inelastic deformation can also be caused by changes in pore pressure associated with melts in the dyke cavity as the dyke progresses. Fractures may also be generated by the exsolution of magmatic volatiles or by influx of host rock pore fluids (including melts). The presence of fluids in such heterogeneous systems modifies the bulk rock properties. For example, predicted seismic velocities often poorly estimated at depth due to the presence of fractures, fluids (melts) and the associated effects of pore fluid pressures [3–5]. It is clear that for real geologic systems undergoing melting pore fluid pressure must be considered, especially if seismic velocities are to be accurately interpreted. Here, the influence of pore fluid pressure is investigated for a model sandstone system, saturated with water. The use of these sandstones as an analogue of partially-molten igneous rocks was discussed previously in Chap. 5.

For a dry system, fractures can lower the strength of a rock. The compressional velocity, V_P, of fractured porous rocks is lower than that of unfractured ones in the low pressure regime. Hysteresis of measured V_P on increasing and decreasing pressure is greater in the presence of microcracks, which increase the sensitivity of velocity to pore pressure [6]. During compression, damage can be generated, to modify pre-existing cracks, inducing fracture which is neither parallel nor perpendicular to the principal stress direction. A sliding wing crack model (as shown in Fig. 7.1), in

S.-Y. Chien, *Rheological and Seismic Properties of Solid-Melt Systems*,
Springer Theses, DOI: 10.1007/978-3-319-03098-2_7,

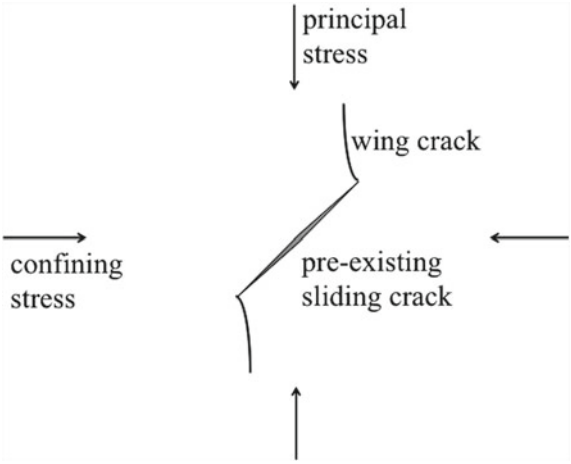

Fig. 7.1 Schematic sliding wing crack model for the new crack growth at the pre-existing crack in the brittle faulting regime. After [8]

which tension cracks occur (at the pre-existing crack tips) and grow in the direction of maximum compression [7, 8], has been used to describe the deformation and brittle faulting in rocks under low confining pressure. With the increasing deviatoric stress, the sliding wing cracks develop along a curved path and reach a stable state when the crack becomes parallel to the principal stress. Eventually, multiple cracks coalesce, resulting in a shear band (shear localisation) with accumulation of wing cracks throughout the rock. The principal stress (σ_1) at the onset of dilatancy is related to the confining stress (σ_3), critical fracture toughness (K_{IC}), crack length (l_c) according to:

$$\sigma_1 = H_1\sigma_3 + \frac{H_2 K_{IC}}{\sqrt{\pi \frac{l_c}{2}}} \tag{7.1}$$

where both H_1 and H_2 are functions which contain sliding crack orientation angle, number of sliding cracks and wing crack length [8].

With increasing confining pressure, the velocities of fractured and unfractured rocks tend to approach similar values due to the initial closure of ellipsoidal cracks at lower confining pressure and pore collapse at very high confining pressure. When the confining pressure is high enough to reach the critical grain crushing pressure, pore collapse, grain rotation and grain crushing may occur, resulting in compactive cataclastic flow [8, 9]. Zhang et al. [9] have used the Hertzian fracture model (Fig. 7.2), which involves pre-existing microcracks at non-adhesive elastic grain contacts, to describe the grain crushing pressures of several sandstones. The critical pressure (P_{cr}) for the onset of grain crushing depends on the Poisson's ratio (ν), Young's modulus (E), critical stress intensity factor (or critical fracture toughness, K_{IC}), porosity (ϕ) and the initial crack length (l_c).

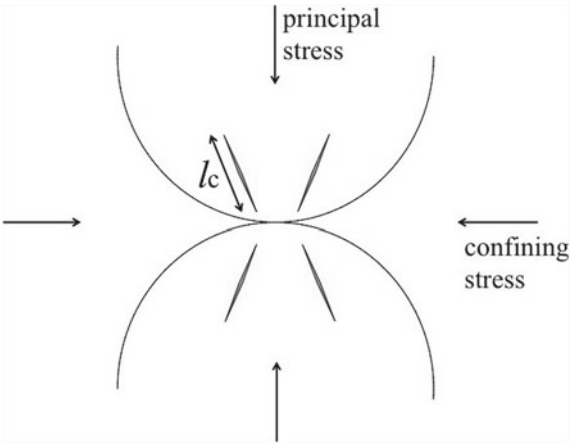

Fig. 7.2 Schematic Herztian fracture model for the onset of grain crushing with the initial crack length (l_c) in the compactive cataclastic flow regime. After [8]

$$P_{cr} = 2.2\frac{(1-\nu^2)^2}{E^2(1-2\nu)^3}\frac{K_{IC}^3}{(\phi l_c)^{3/2}} \tag{7.2}$$

The velocities of porous rocks do not show the same behaviour when fluid saturates the pores or cracks. For example, Tompkins and Christensen [10] found that the compressional wave velocity of a variety of basalts when fully-saturated with water was lower than that of the dry counterpart below 200 MPa, whereas, the shear wave velocity of water-saturated basalts was higher than that of dry samples [10]. Velocity variations with fluid saturation have also been measured in sandstones. Fluids- (water, NaCl and kerosene) saturated sandstones do not always have lower compressional wave velocities than dry ones, as shown in study of King [11]. Differences in the effect of water on the velocities of rocks may be due to differences in microstructures (such as ellipsoidal fractures and equant pores) and the interaction between the fluid and the rock frame [12, 13]. The presence of water may lower the fracture toughness in pre-existing cracks and hence gives rise to lower critical pressures for the damage (brittle faulting and shear localisation) and grain crushing in water-saturated rocks.

Even though the velocities of fluid-saturated rocks show different variations to those of dry rocks, the velocities of fluid-saturated rocks always decrease with increasing pore pressure upon compression. The pore fluid pressure influences the rock properties in the opposite way to the way confining pressure does. It is commonly assumed that the differential pressure (P_d, described in Chap. 1), also known as Terzaghi effective pressure [14], is a controlling factor for the rock properties and that differential pressure governs the pressure-dependent mechanical properties of soils and unconsolidated rocks. Several theoretical [15, 16] and experimental studies [6, 17, 18] have shown that the mechanical properties of reservoir rocks can generally be assumed to be a function of the difference between the rock overburden pressure (the confining pressure, P_c) and the pore fluid pressure (P_p) such that $P_d = P_c - P_p$.

The rock stiffness and rigidity both increase exponentially with differential pressure, as a result of decreasing porosity and an increase in the contact area between grains.

The differential pressure does not adequately represent the true stress state of the materials [11, 16]. Instead, the effective pressure P_e and an effective pressure coefficient (n_{Pe}), sometimes referred to as the pore pressure coefficient, are introduced to represent the modifying effect of the pore pressure, $P_e = P_c - n_{Pe}P_p$ [15]. Biot and Willis [15] first showed that the pressure-induced volume change of a linear poroelastic medium depends on the effective pressure. They introduced the pore pressure coefficient, also referred to as the Biot-Willis coefficient in later studies, and suggested that it can be obtained from the dry rock modulus (K_{dry}) and its constitutive mineral modulus (K_m) according to $n_{Pe} = 1 - \frac{K_{dry}}{K_m}$. The modulus of the dry rock is usually less than the modulus of the constitutive minerals due to the presence of porosity. As the upper bound for the relation, the critical porosity model by Nur et al. [19] can be used to obtain the effective pressure coefficient as $n_{Pe} = \frac{\phi}{\phi_c}$, where ϕ is the porosity and the critical porosity (ϕ_c) is typically observed to be 0.4–0.5 for clastic rocks [19, 20]. From this it can be seen that the effective pressure is close to the differential pressure at very high porosity ($n_{Pe} \to 1$) while the effective pressure is close to the confining pressure at very low porosity ($n_{Pe} \to 0$).

The Biot-Willis coefficient was derived in the context of static deformation and therefore its extrapolation to dynamic stress dependence of the rock properties demands further consideration. Todd and Simmons [16] derived an empirical relation to determine the effective pressure coefficient from pressure-dependent compressional-wave velocity measurements of low-porosity granites and limestones [16]. Their empirical effective pressure coefficient is obtained from the plot of compressional wave velocity (V_P) against confining pressure (Fig. 7.3) by taking the ratio of the partial derivatives of velocity with respect to the pore pressure at constant differential pressure ($\partial V_P/\partial P_P \mid_{P_d}$) and the partial derivatives of velocity with respect to the differential pressure for constant pore pressure ($\partial V_P/\partial P_d \mid_{P_p}$). The effective pressure coefficient can be expressed as

$$n_{Pe} = 1 - \frac{\partial V_P/\partial P_p \mid_{P_d}}{\partial V_P/\partial P_d \mid_{P_p}}. \tag{7.3}$$

It has been proposed that this empirical pore pressure coefficient relation may be applied to any other physical property (X), such as shear wave velocity or modulus, with the replacement of V_P by Xu [6, 17, 18] as

$$n_{Pe} = 1 - \frac{\partial X/\partial P_p \mid_{P_d}}{\partial X/\partial P_d \mid_{P_p}}. \tag{7.4}$$

Several experimental datasets have been analysed using the empirical relation of Todd and Simmons [16]. As the pore pressure coefficient indicates the influence of the pore pressure, the pore pressure can exactly compensate the effect of confining

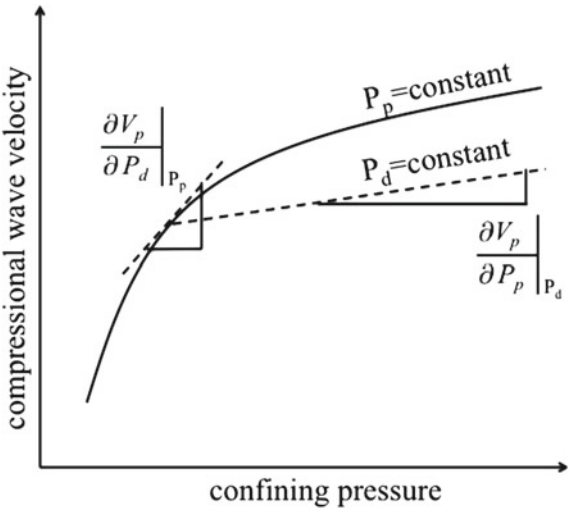

Fig. 7.3 Schematic behaviour of compressional wave velocity (V_P) against confining pressure. The two derivative quantities for the effective pressure coefficient are indicated. After [16]

pressure at $n_{Pe} = 1$, which is often the case in soils and unconsolidated rocks. The effect of confining pressure is greater than that of pore pressure when $n_{Pe} < 1$, as found in many studies of compressional wave velocities in low porosity rocks including sandstones [6, 18, 21]. The assumptions within the deviation of the effective pressure coefficient by Todd and Simmons [16] suggest $n_{Pe} \leqslant 1$. However, examples when $n_{Pe} > 1$ (the effect of pore pressure is greater than that of confining pressure) have been reported in some studies. King [11] shows that n_{Pe} is greater than the unity in both compressional and shear wave velocities of Berea and other sandstones [11]. On the other hand, Christensen and Wang [22] found n_{Pe} is less than the unity for P-wave velocity and modulus, but n_{Pe} is bigger than the unity for the shear wave velocities and Poisson's ratio of Berea sandstone [22]. The discrepancies between these studies indicate that the behaviour of the effective pressure coefficient (n_{Pe}) requires further investigation when considering the mechanical properties of fluid-saturated porous rocks.

Water-saturated sandstones provide a model system for the study of the effects of fluids, microstructures and pore pressures (and hence effective pressure) on both compressional and shear wave velocities of the fluid-saturated porous rocks. As discussed in Chap. 5, porous sandstones also provide a potential analogue of the behaviour of partially-molten igneous rock. Here, two water-saturated sandstones (Darley Dale sandstone and New Red Sandstone) have been studied to explore the influence of different pore fluid pressures on sound velocities under increasing confining pressure, using the 400 MPa ultrasonic piezoelectric oscillator (the 400 MPa UPO). The effective pressure coefficients for different pore pressures have been obtained from Todd and Simmon's relation and hence the resultant effective pressure has been determined.

7.2 Samples and Experimental Methods

Darley Dale sandstone and New Red Sandstone 'as received' were prepared for the ultrasonic velocity measurements. The microstructures and further characteristics of both sandstones have described in Sect. 3.1 and in Fig. 3.2. Cylindrical shaped samples were drilled for specimen loading in the 400 MPa UPO (detailed in Sect. 2.3 and in Fig. 2.10). The dimensions of the Darley Dale sandstone sample (14 % porosity and 6 % clay content) are 14.29 mm in length and 24.46 mm in diameter and the dimensions of the New Red Sandstone sample (17 % porosity and 12 % clay content) were 25.15 mm in length and 24.60 mm in diameter. Deionised water was used as the saturating fluid and pumped into the sample assembly after measurements on the dry sandstones.

The travel time (t_P, t_{S1} and t_{S2}) of the compressional waves (P-wave) and two perpendicularly polarised shear waves (S_1- and S_2-waves) were measured from the experiments. The travel time (t_0) of the three different waves between the ultrasonic transducers and buffer assembly (without a sample) was also measured after measurements of each sample separately. The travel times of P-wave, S_1-wave and S_2-wave through each sample were obtained from the difference between two measurements ($\Delta t_i = t_i - t_0$, where i = P, S_1 or S_2).

The travel time of both samples were separately measured as a function of confining pressure upto 150 MPa at intervals of 10 MPa for each of the different pore pressures. Each sample was firstly measured dry during compression. The measurements of the dry Darley Dale sandstone were recorded above 100 MPa while the measurements of the dry New Red Sandstone were recorded over the entire pressure range. Deionised water was then pumped into the sample assembly at a confining pressure of 150 MPa. The travel times for water-saturated samples were also measured during decompression.

The pore pressure was increased to 10 MPa for Darley Dale sandstone immediately and for New Red sandstone overnight. The travel time of samples at 10 MPa pore pressure was also recorded during compression. The samples then measured at 20 MPa pore pressure during decompression, followed by measurements at 30 MPa pore pressure during compression. Finally, the pore pressure was increased to 37 MPa for Darley Dale sandstone and to 40 MPa for New Red Sandstone during decompression. During the measurements of New Red Sandstone, the electronic cables for the detectors of S_1- and S_2-waves failed to work well at higher pore pressures. Therefore, the S_1 travel time was difficult to measure at 40 MPa pore pressure as was the travel time of the S_2-wave at 30 and 40 MPa pore pressures.

7.3 Results and Analysis

The compressional wave velocity (V_P) and two shear wave velocities (V_{S1} and V_{S2}) have been obtained from the travel time measurements on the Darley Dale sandstone and New Red Sandstone under both dry and water-saturated conditions. The results

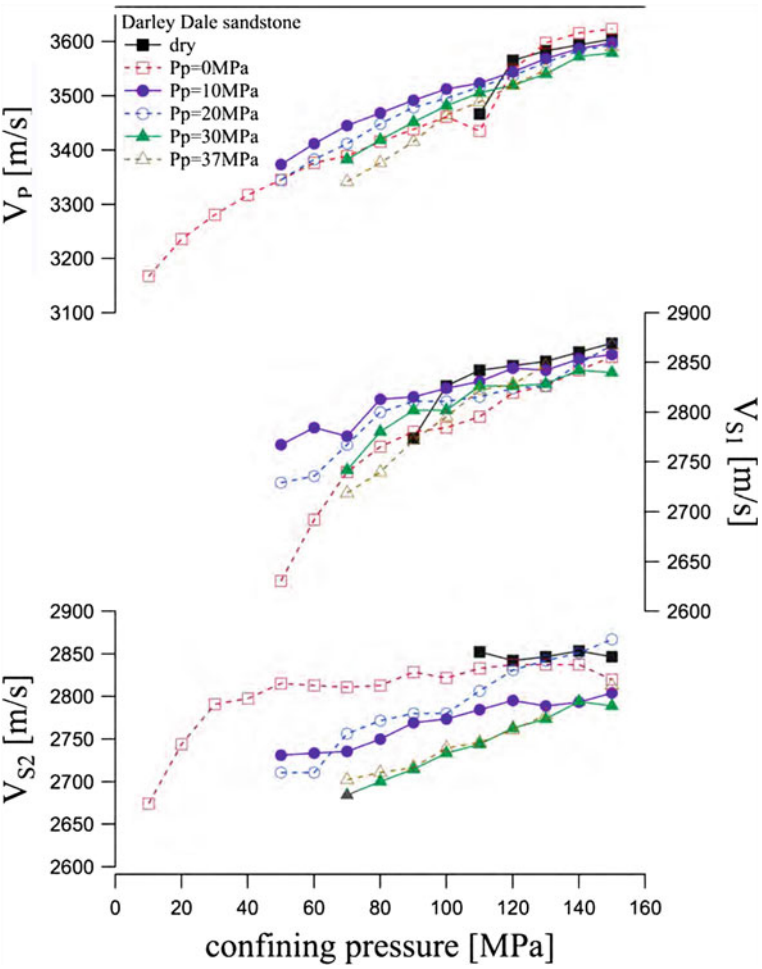

Fig. 7.4 The compressional wave velocity (V_P) and two shear wave velocities (V_{S1} and V_{S2}) of dry and water-saturated Darley Dale sandstone as a function of confining pressure. *Solid symbols* are data measured under compression and *open symbols* are data measured under decompression. P_P is the fluid pressure in water-saturated samples

are shown in Figs. 7.4 and 7.5, respectively. All velocities increase with increasing confining pressure. The V_P of Darley Dale sandstone (3,167–3,623 m/s) is found to be slower than that of New Red Sandstone (3,313–3,699 m/s), but both V_{S1} and V_{S2} for Darley Dale sandstone (2,630–2,870 and 2,674–2,867 m/s) are faster than those of New Red Sandstone (2,346–2,625 and 2,422–2,620 m/s) over the confining pressure range (20–150 MPa) of this study. The velocity errors are 7–8 m/s, which are equal to or smaller than the size of markers in the velocity-pressure plots, throughout the confining pressure range upto 150 MPa.

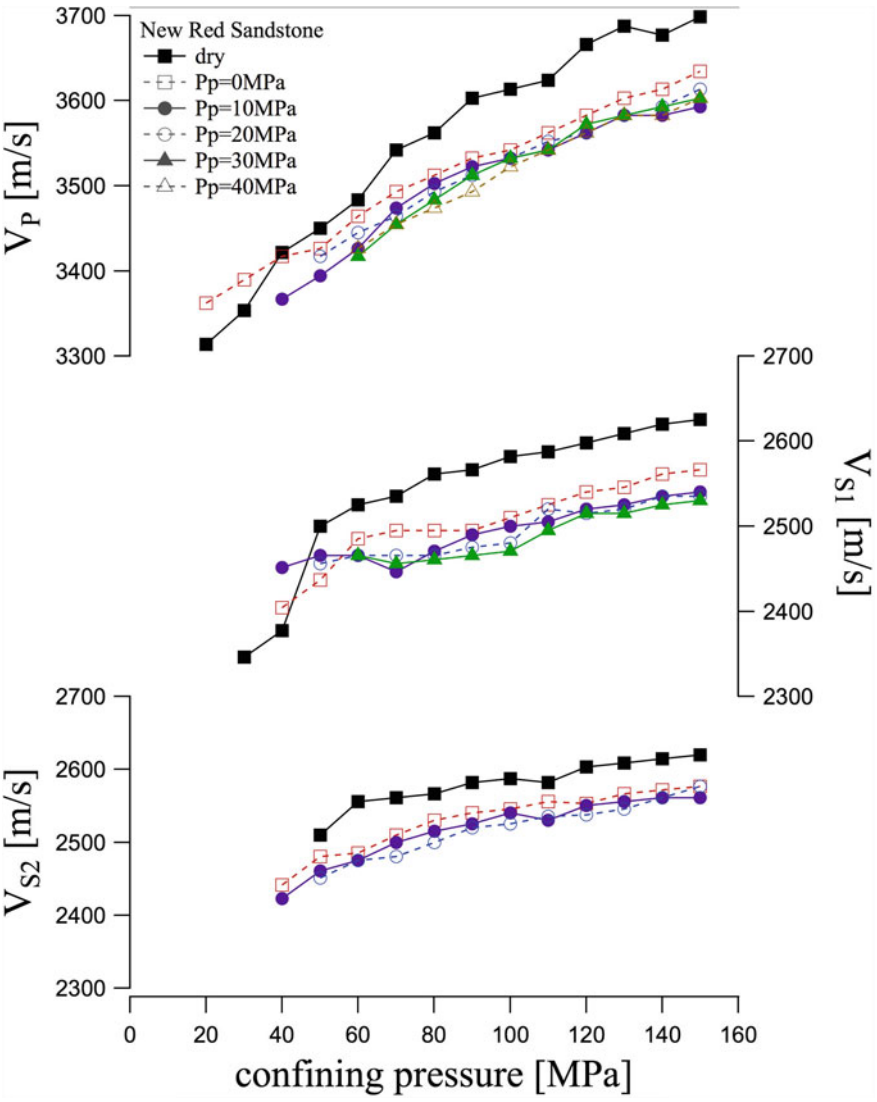

Fig. 7.5 The compressional wave velocity (V_P) and two shear wave velocities (V_{S1} and V_{S2}) of dry and water-saturated New Red Sandstone as a function of confining pressure. *Solid symbols* are data measured under compression and *open symbols* are data measured under decompression. P_P is the fluid pressure in water-saturated samples

The velocities of dry Darley Dale sandstone (Fig. 7.4) were only measured at high confining pressure above 90 MPa. In the absence of pore pressure, V_P in water-saturated samples is slower than that for dry samples, whereas both V_{S1} and V_{S2} of dry samples are faster than those for water-saturated samples. There is a small

drop of V_P in both dry and water-saturated rocks for 0 MPa pore pressure samples during decompression at confining pressure of 110 MPa. The velocities decrease with increasing pore pressure in both compression and decompression runs, although there is no clear trend between velocities with increasing pore pressures from 10 to 37 MPa. Generally, V_P and V_{S1} increase quasi-asymptotically (by 14 and 9 %, respectively) with the increasing confining pressure. The results show that V_{S2} is more sensitive to water pore pressure than V_P and V_{S1} in the lower confining pressure. For water-saturated samples with 0 MPa pore pressure, V_{S2} increases dramatically (by 5 %) on increase of P_c from 20 to 40 MPa and then increases more slowly by about 2 % from 40 to 150 MPa. At higher pore pressures, V_{S2} changes linearly between 50 and 150 MPa.

The values of V_P measured for dry New Red Sandstones increase by 12 % on increase of confining pressure to 150 MPa, and both V_{S1} and V_{S2} for dry samples increases by 6 % as P_c increases from 50 to 150 MPa, and V_{S1} is also found to increase strongly by 6 % from 30 to 50 MPa. All velocities of water-saturated New Red Sandstone samples are seen to increase by 7 % over the same pressure range below 150 MPa. The velocities of dry New Red Sandstone (Fig. 7.5) are higher than those of water-saturated samples with confining pressure between 50 and 150 MPa, but the velocities of dry samples are lower than the data obtained from water-saturated samples below 50 MPa confining pressure. Most velocities under high pore pressure are slower than those measured for dry or water-saturated samples at 0 MPa pore pressure, with the exception that V_{S1} tends to be faster in high-pore pressure samples in which P_c is below 50 MPa. For pore pressures upto 40 MPa and confining pressures upto 150 MPa, the observations on New Red Sandstone show that velocities are not sensitive to pore pressure, under either compression or decompression.

The velocity ratios between compressional wave velocity and shear wave velocities for Darley Dale sandstone are plotted in Fig. 7.6, as a function of confining pressure and differential pressure. The velocity ratio increases with confining pressure and the variation of this ratio in water-saturated samples for V_P/V_{S1} and for V_P/V_{S2} is about 4 %, with the exception that the velocity ratio of V_P/V_{S2} for 0 MPa water pore pressure increases by 8.5 %). No systematic variation is found for V_P/V_{S1} with the increasing confining pressure, but the velocity ratio of V_P/V_{S2} shows a positive correlation with increasing water pressure. The higher the pore pressure, the higher V_P/V_{S2}. The behaviour becomes more evident when the velocity ratios of both V_P/V_{S1} and V_P/V_{S2} are plotted against differential pressure.

Velocity ratios for New Red Sandstone samples are generally higher than those found for Darley Dale sandstone samples. The velocity ratios of dry and water-saturated New Red Sandstone are also shown separately in Fig. 7.7 as a function of confining pressure and differential pressure. The velocity ratios generally increase by around 3.7 % for both V_P/V_{S1} and V_P/V_{S2} with the increasing confining pressure. The velocity ratio V_P/V_{S1} is higher at higher pore pressures than under dry conditions above 60 MPa confining pressure. However, the relationship between velocity with confining pressure is not clear for V_P/V_{S2}. The velocity ratio V_P/V_{S2} in dry samples is lower below and higher above 90 MPa confining pressure than that for wet samples. The velocities plotted against differential pressure reflect those plotted against confining pressure.

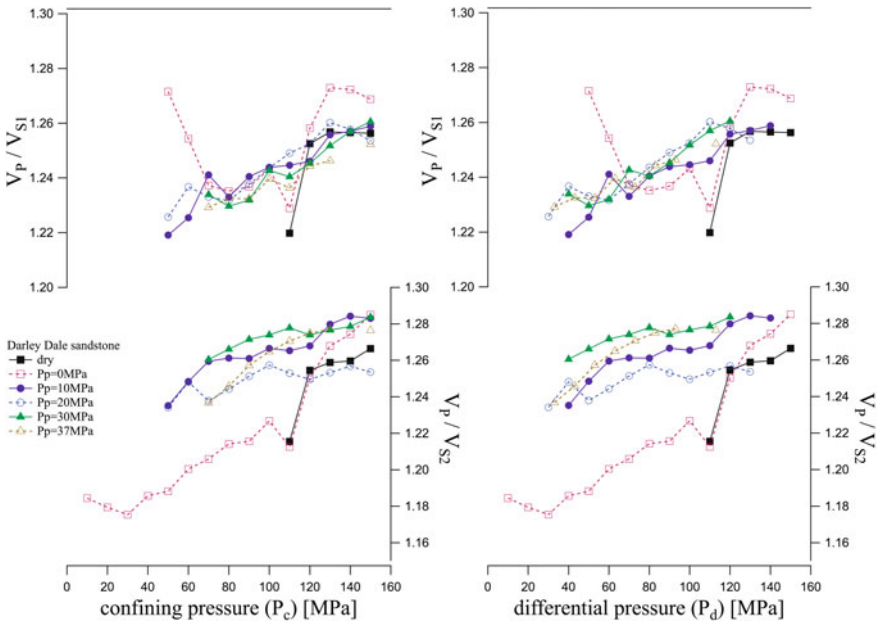

Fig. 7.6 The velocity ratio of V_P/V_{S1} and V_P/V_{S2} of dry and water-saturated Darley Dale sandstone are plotted against confining pressure and differential pressure, separately. *Solid symbols* are data measured under compression and *open symbols* are data measured under decompression. P_P is the fluid pressure in water-saturated samples

The effective pressure coefficients for these samples may be obtained using the empirical Todd-Simmons' relation (Eqs. 7.3 and 7.4) from the plots of velocity against confining pressure (P_c) (as shown in Fig. 7.8). The errors are about 0.003 for the resultant coefficients, which are smaller than the size of the symbols in the coefficient-pressure plots. The coefficients obtained from data obtained at different pore pressures are more sensitive to pressure history than the pore pressure itself. The coefficients under compression at 10 MPa pore pressure are similar to those at 30 MPa fluid pressure while the coefficients corresponding to decompression at 20 MPa and at 37 MPa pore pressure show similar trends. With increasing confining pressure, the coefficients for V_P data decrease initially (with a small increase at 80–100 MPa) before a rapid increase at 110 MPa. The coefficients from V_{S1} data decrease rapidly upto 60–80 MPa and start to increase under further compression (with a sudden peak at 70 MPa), but then decrease again under decompression (with a broader peak at 80 MPa) of the confining pressure. The effective pressure coefficients for V_{S2} data generally decrease with the increasing confining pressure, with a small peak at 80 MPa on compression and at 100 MPa on decompression. Only one value of the effective pressure coefficient for V_P at 130 MPa on decompression is greater than one, but nearly half of the coefficients for V_{S1} and V_{S2} data are found to be greater than unity. Negative coefficients are also obtained from the compression data for

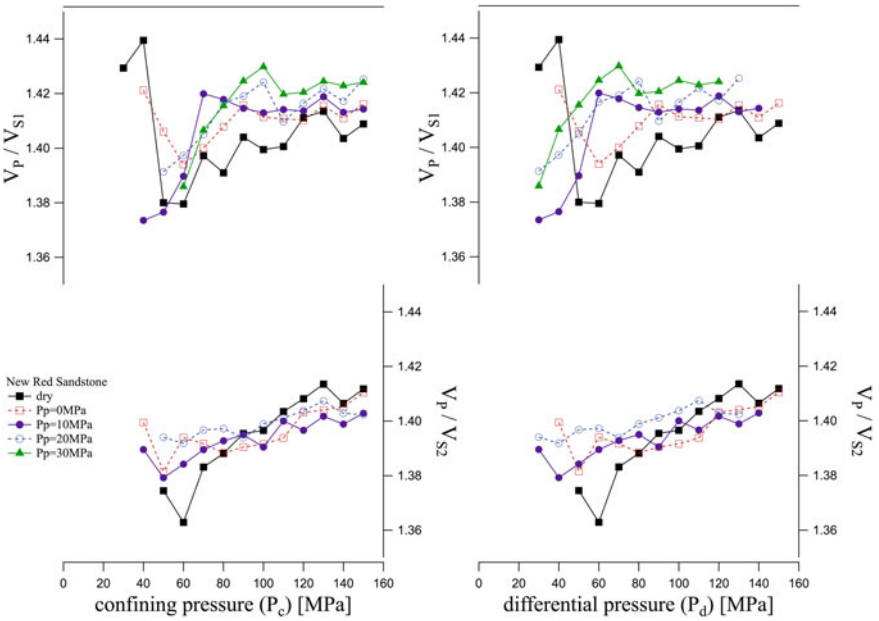

Fig. 7.7 The velocity ratio V_P/V_{S1} and V_P/V_{S2} of dry and water-saturated New Red Sandstone plotted against confining pressure and differential pressure, separately. *Solid symbols* are data measured under compression and *open symbols* are data measured under decompression. P_P is the fluid pressure in water-saturated samples

V_P, V_{S1} and V_{S2}. The effective pressures can then be calculated from the effective pressure coefficients (P_e), as shown in Fig. 7.8. The velocities plotted against the differential pressure (P_d) are also presented in Fig. 7.8 for comparison.

The effective pressure coefficients for V_P of New Red Sandstone decrease initially on increasing confining pressure up to 50 MPa and then increase again with a second drop at 80 MPa (Fig. 7.9), and once more increase down to 100 MPa, during compression. On decreasing pressure, the V_P effective pressure coefficients decrease initially and then converge to a stable value below 110 MPa. A negative coefficient is found for V_P at 10 MPa pore pressure and 100 MPa confining pressure during compression, otherwise values lie between 0 and 1. The coefficients for V_{S1} at 20 MPa pore pressure decease continuously (with a peak at 50–90 MPa) with the decreasing confining pressure. On compression, the coefficients for V_{S1} increase from 30 to 120 MPa with two peaks (at 40–50 and 70–80 MPa). Negative V_{S1} coefficients are found on compression below 50 MPa and coefficients bigger than unity are found under both compression and decompression. On decompression, the coefficients for V_{S2} increase initially and then start to decrease below 110 MPa. The effective pressure coefficients for V_{S2} between 80 and 110 MPa are greater than one, while some value below 60 MPa are negative. The effective pressures have subsequently been obtained from the effective pressure coefficients for V_P, V_{S1} and V_{S2}. The velocities are

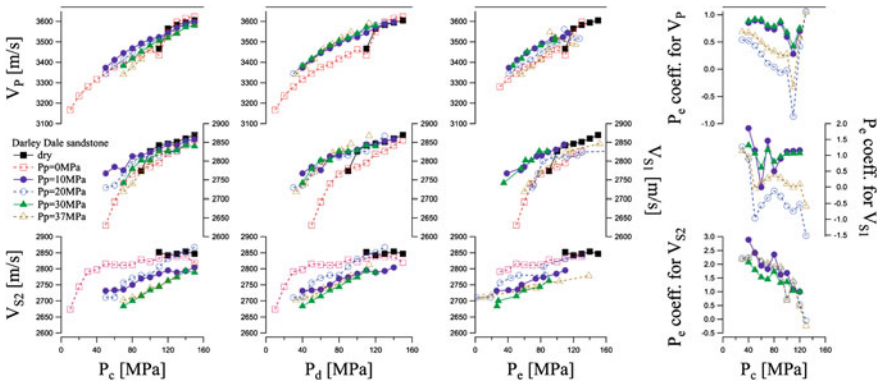

Fig. 7.8 The V_P, V_{S1} and V_{S2} of Darley Dale sandstone shown as a function of confining pressure (P_c), differential pressure (P_d) and effective pressure (P_e), separately. The effective pressure coefficients for the three different velocities are also presented as a function of confining pressure (P_c). *Solid symbols* are data measured under compression and *open symbols* are data measured upon decompression. P_P is the fluid pressure in water-saturated samples

also plotted against confining pressure (P_c), differential pressure (P_d) and effective pressure (P_e) in Fig. 7.9 for comparison.

If the effective pressure is calculated correctly, all velocity data should fold down onto a single curve. The data for New Red Sandstone demonstrate that the effective pressures for V_P do indeed provide a better description of the pressure dependence than differential pressure (Fig. 7.9). The same cannot be said for V_S, however, where differential pressure appears to be an adequate parameter. For Darley Dale sandstone

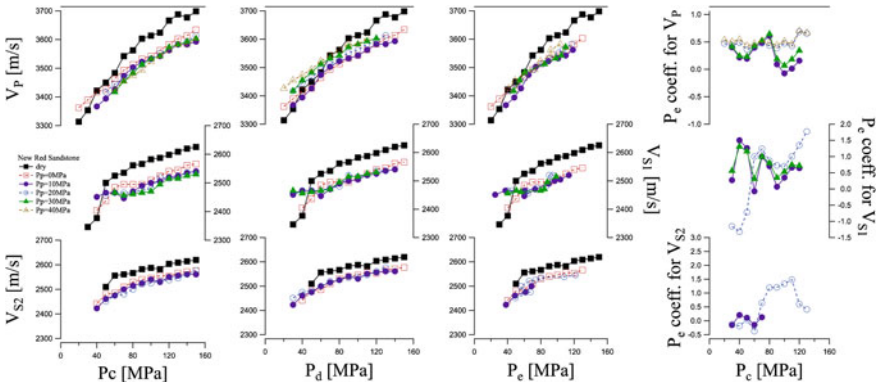

Fig. 7.9 The V_P, V_{S1} and V_{S2} of New Red Sandstone shown as a function of confining pressure (P_c), differential pressure (P_d) and effective pressure (P_e), separately. The effective pressure coefficients for the three different velocities are also presented as a function of confining pressure (P_c). *Solid symbols* are data measured under compression and *open symbols* are data measured upon decompression. P_P is the fluid pressure in water-saturated samples

the effective pressure provides a good description for V_P at high pore pressures and low confining pressure (Fig. 7.8). Again, V_S is not well-described against P_e for Darley Dale sandstone although data are reproducible under compressions and decompressions.

7.4 Mechanisms

7.4.1 General Trends

The velocity increases and the porosity decreases upon loading. Excess pore pressure may be generated upon rapid loading, and this acts against the confining pressure. During decompression, the velocities take a different path as a function of pressure compared to the pressurisation pathway (pressure hysteresis). This hysteresis, affecting the velocity during decompression, gives higher velocities on decompression than the velocity measured under compression [16, 23]. Gardner et al. [23] show that the compressional wave velocity depends on both pore pressure and confining pressure and also depends on the past pressure history of the sample [23]. The velocities are simply described by the differential pressure when the hysteresis is eliminated, but the velocity becomes more dependent on the effective pressure as the pore pressure coefficient (n_{Pe}) becomes non-zero. The velocities measured in this study decrease with higher pore pressures both on compression and decompression, which indicates the effects of pore fluid and fluid pressure override the effects of hysteresis. Hence, the influence of hysteresis is not considered in the discussion.

Generally, the velocity increases due to the decrease of the porosity during compression. Porosity has previously been found to follow a two-stage compaction curve and reaches a point beyond which no further compaction occurs for shales upto 50 MPa confining pressure (or 25 MPa differential pressure with the presence of pore pressure) [24]. The water-saturated Darley Dale sandstone shows a non-linear compaction behaviour with increasing mean effective pressure in the hydrostatic deformation experiments (about 1.5 % porosity reduction from 0 to 150 MPa mean effective pressure) [25]. Two-stage (or non-linear) compaction occurs because the total porosity is composed of spherical pores and the cracks with small aspect ratio. With the increasing confining pressure, the ellipsoidal fractures (perpendicular to the stress direction) will close first, followed by the closure of pores. In addition, the porosity also depends on the clay content. Porosity has found to be non-linear as a function of clay content in both lab and theoretical experiments [3]. They found that the porosity decreases as clay content increases from 0 to 25 wt%, and then increases between 25 to 100 wt% clay content. The minimum point of porosity is lower and shifts to higher clay fraction with increasing differential pressure or decreasing pore pressure. The porosity of New Red Sandstone with 12 % clay (17 % porosity) is higher than that of Darley Dale sandstone with 6 % clay (14 % porosity) in this study, which indicates porosity is expected to decrease (and velocity is expected to increase) with increasing differential pressure (as the clay contents of both samples are less than 25 %).

The measured compressional wave velocities of Darley Dale sandstone in this study are slower than those in the New Red Sandstone while the shear wave velocities of Darley Dale sandstone are faster, which is not expected. The cylinder of the Darley Dale sandstone used in these experiments were drilled perpendicular to the bedding direction. The low V_P may be caused by the anisotropy of the bedding or cracks. King [11] shows that velocities parallel to bedding are faster than that perpendicular to bedding in Berea and Bandera sandstones [11]. The variation of V_P is more sensitive to bedding than that of V_S. Therefore, the bedding direction in this study likely accounts for the lower V_P in Darley Dale sandstone. On the other hand, the velocities also depend on the crack directions if there are pre-existing cracks with small aspect ratio. The compressional wave velocities are faster parallel to the ellipsoidal cracks than that perpendicular to the ellipsoidal cracks and the variation is bigger with higher crack density [26]. Therefore, the ellipsoidal cracks in Darley Dale sandstone may orientate along the bedding direction.

The rate of change of V_P with pressure is higher than that of V_S in the water-saturated Darley Dale sandstone which may be due to higher pore fluid attenuation for shear waves. Chapman et al. [27] propose a squirt flow model for small aspect ratio cracks and spherical pores and show shear dispersion is more sensitive to crack fraction than the bulk dispersion. Other studies also provide the squirt flow model as the mechanisms for pore fluid attenuation [28, 29]. Squirt flow between cracks of different aspect ratio undergoes differential compression due to the propagating waves, which results in the much larger shear attenuation than the compressional attenuation. On the other hand, the rates of change of compressional waves and shear waves with pressure are similar in the New Red Sandstone, which may indicate fewer small aspect ratio cracks in this sample. The shear velocity variation between $S1$- and $S2$-waves in New Red Sandstone is small while that in Darley Dale sandstone is large (as shown in Fig. 7.10), which implies Darley Dale sandstone is more anisotropic than New Red Sandstone, which is very likely due to the presence of bedding. The difference between two samples may be likely due to the presence of bedding or orientated small aspect ratio cracks in Darley Dale sandstone.

Water is more incompressible than the air as the fluid in the porous rock under ultrasonic frequency measurements. The presence of water causes an increase in the compressional wave velocity, but not in the shear wave velocity (water has no shear wave velocity). Similar results are also observed in other studies [11, 30]. The different influences result in a higher V_P/V_S for water-saturated sandstone than that of dry sandstone (Figs. 7.8 and 7.9). The higher velocity ratio with higher pore pressure is well explained by Gassmann's [31] fluid substitution equation, that the rock frame is softer with high pore pressure and therefore the V_P/V_S ratio is higher [31, 32]. The empirical relation in the study of Eberhart-Phillips et al. [33] also demonstrated that a decrease in differential pressure, a decrease in porosity or an increase in clay content gives rise to an increase in V_P/V_S [33]. The observations in this study are in good agreement with this empirical model. The higher clay content of New Red Sandstone results in higher velocity ratios than those in Darley Dale sandstone with lower clay content.

7.4.2 Effective Pressures

The degree of fluid saturation influences compressional wave velocity and shear wave velocity differently. Experimental observations in dry, partially and fully saturated Massilon sandstones show that V_P is highest in the fully saturated sample and lowest for partial saturation, while V_S is higher in dry samples than water-saturated ones (the degree of saturation has the same effect on shear wave velocity) for effective stress upto 34.5 MPa in Winkler and Nur's study [30] and some measurements on sandstones in King's study upto 70 MPa [11]. The present data for Darley Dale sandstone (Fig. 7.10) are in agreement with previous studies. However, the compressional velocity of dry New Red Sandstone at high confining pressure shows lower velocity than the water-saturated sample. One possible explanation is that the water is only partially saturated at the beginning of decompression. The other possible reason may be linked to the fraction of clay content. The free surface energy is reduced due to the presence of a polar liquid (water) in the appreciable interstitial clay mineral content of Bandera sandstone [11]. New Red Sandstone has twice the clay content of Darley Dale sandstone, which may induce more influence on the velocity reduction in the water-saturated New Red Sandstone.

At low confining pressure, velocities in water-saturated New Red Sandstone are higher than that in dry New Red Sandstone (Fig. 7.10). Whereas, the opposite behaviour is found at high confining pressure. These observations are also seen in other studies [11, 16], in which liquid relaxation is assumed to be responsible for the response at lower confining pressure. The stress relaxation behaviour of the liquid (water) in small aspect ratio cracks affects the strength of the rock and results in water hardening effects on the rock. At higher confining pressure, the cracks are closed and only larger spherical pores remains. Consequently, the velocity of water-saturated sandstones becomes lower than that of dry samples due to the absence of the interaction between water and small cracks. In this sense, the S1-wave velocities in water-saturated Darley Dale sandstone below 100 MPa decrease faster than those in dry samples and then eventually become lower as indicated by the extrapolation of data for dry Darley Dale sandstone. Data for S2-wave velocities of dry samples are insufficient to prove this trend. However, the higher compressional velocity of water-saturated Darley Dale sandstone measured in this study (above 110 MPa) do not follow these trends.

The effective pressure coefficients (n_{Pe}) obtained for Darley Dale sandstone (Fig. 7.11 left) decrease generally with increasing confining pressure. This can be explained by the closure of cracks or pores. The increasing confining pressure flattens the contact area between spherical grains and also decreases the influence of the pore pressure on velocities. The observations of Xu et al. [6] support this view: they show that fractured samples have higher n_{Pe} values than the original samples, since the fractured sample is more sensitive to pore pressure. The decreasing trend of n_{Pe} can also be seen in the compression data for New Red Sandstone (Fig. 7.11 right), but not in the decompression data. The decreasing n_{Pe} in New Red Sandstone under decompression indicates the sample becomes less sensitive to pore pressure when

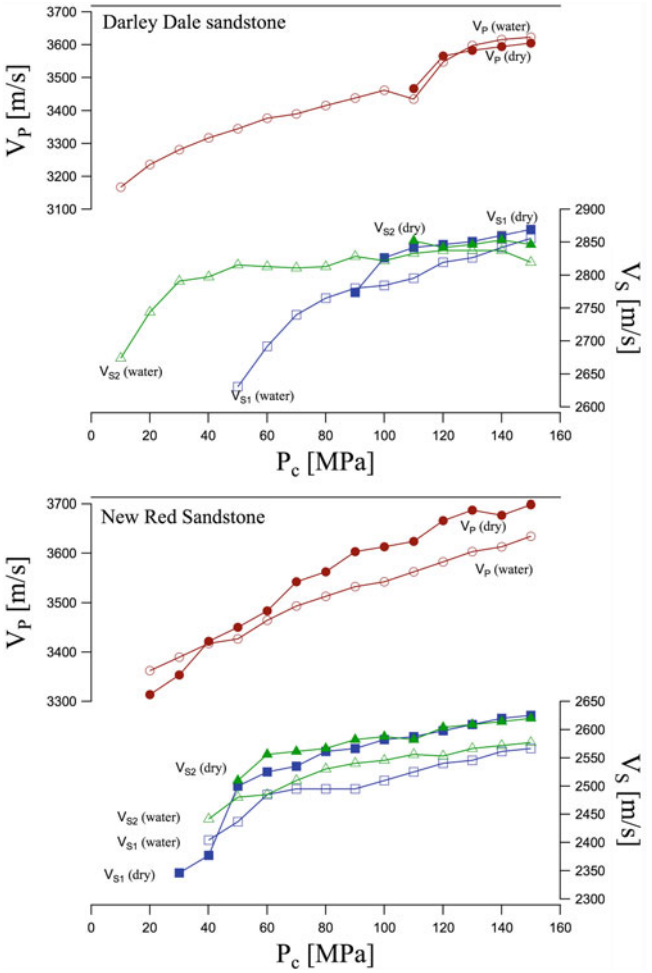

Fig. 7.10 The velocities (V_P, V_{S1} and V_{S2}) of dry and water-saturated Darley Dale sandstone (*top*) and New Red Sandstone (*bottom*) ($P_p = 0$ MPa). V_P is marked as *circles*, V_{S1} is marked as *squares* and V_{S2} is marked as *triangles*. *Solid symbols* represent dry samples and *open symbols* represent water-saturated samples

the confining pressure decreases. The observations show that effective pressure coefficients in both sandstones are sensitive to pressure. Compression data show smaller variations in n_{Pe} than decompression data in most of cases. This may indicate that the volumes of cracks and pores in the rocks appear to change more or faster under decompression than under compression.

Values of $n_{Pe} > 1$ are found for shear waves, while n_{Pe} is always less than unity for compressional waves in this study. This appears to conflict with the underlying concept of the Biot-Willis coefficient and the Todd-Simmons empirical coefficient,

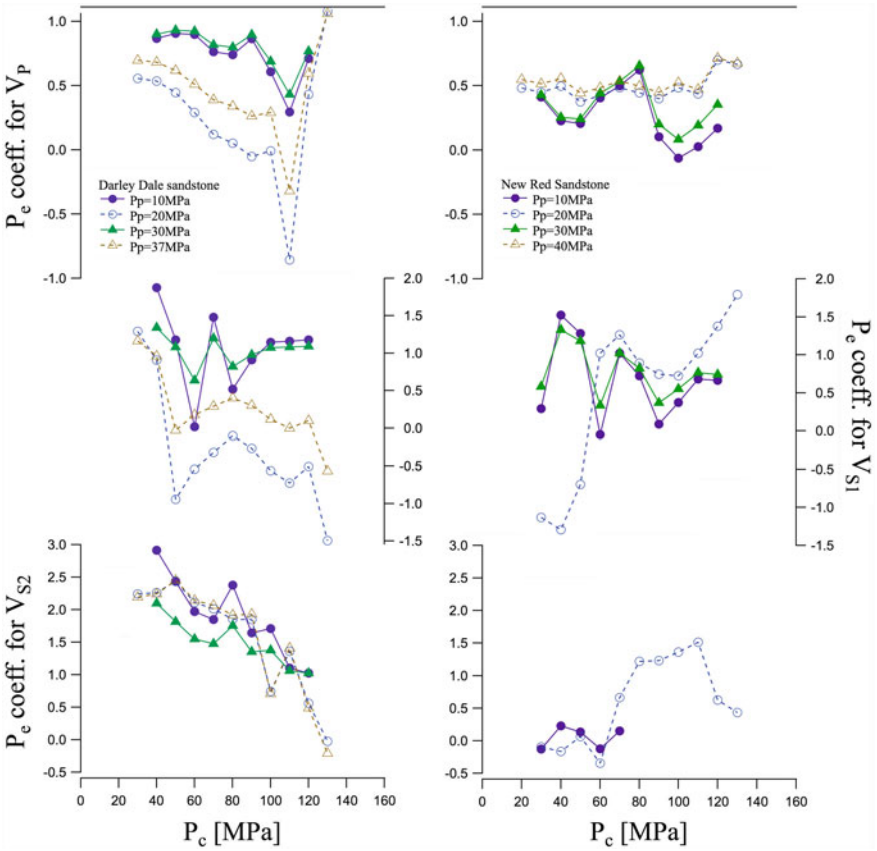

Fig. 7.11 The effective pressure coefficients of Darley Dale sandstone (*left*) and New Red Sandstone (*right*) for the compressional wave velocity (V_P), shear wave velocities (V_{S1} and V_{S2}) are plotted against confining pressure (P_c)

which both imply n_{Pe} is equal to or less than unity [15, 16]. The results of this study are, however, consistent with the the studies of Christensen and Wang (1985) on water-saturated Berea sandstone [22]. The coefficients in the water-saturated sandstone shows $n_{Pe} < 1$ for V_P while $n_{Pe} > 1$ for V_S at confining pressures upto 200 MPa. They proposed a conceptual model to explain this discrepancy, in which n_{Pe} can be bigger than unity if a high compressibility layer exists on the surface of the spherical grains, such as a layer of oxide or clay on the quartz spherical grains, as seen in the sandstones studied here (Fig. 7.12). The compressible mineral linings (clay) in the pore spaces are more influenced by the presence of pore pressure than the equivalent pure grain structure. The model indicates that $n_{Pe} < 1$ for both V_P and V_S for a non-clay sandstone, and $n_{Pe} < 1$ for V_P and $n_{Pe} > 1$ for V_S, with $n_{Pe} \to 1$ for V_S at high differential pressure for a clay-bearing sandstone.

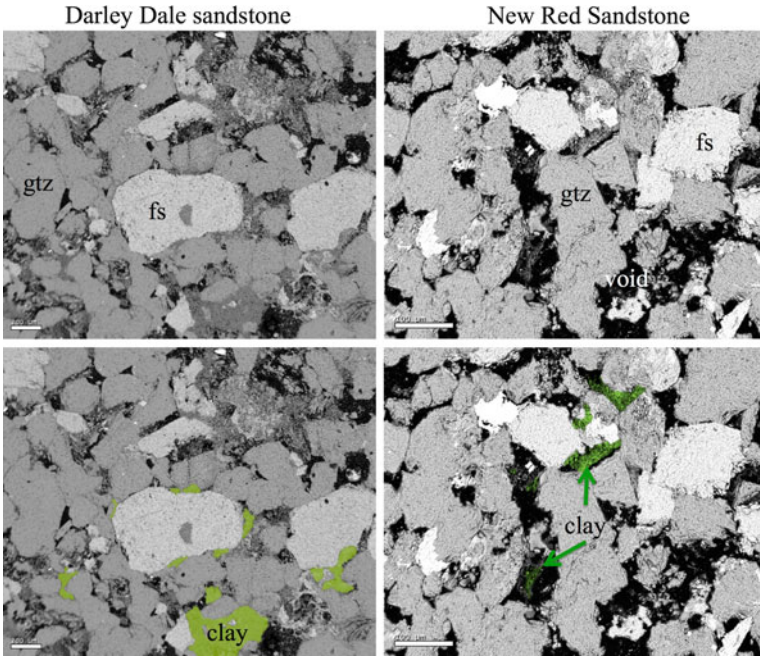

Fig. 7.12 The SEM images of Darley Dale sandstone (*left*) and New Red Sandstone (*right*). Clay minerals are marked in *green* (*bottom row*). The *grey* levels in SEM images correspond to different mineral phases and *black* areas are voids. The scale bar is 0.2 mm in Darley Dale sandstone images and 0.1 mm in New Red Sandstone images

Darley Dale sandstone and New Red Sandstone have a similar clay content (6 and 12 %) and porosity (14 and 17 %) to Berea sandstone (10 % clay and 20 % porosity). The n_{Pe} values for shear wave velocities in this study are close to unity at high confining pressure (equal to high differential pressure in the constant pore pressure curves). It is likely that clay covers the surface of the pores or cracks when water is injected into the sandstone and that this results in the high n_{Pe} values for shear wave velocity.

Negative n_{Pe} values are obtained in this study under conditions not discussed in previous studies. Most of the negative values are found for the shear wave velocities and especially on the decompression curves. The effective pressure coefficients are shown to be sensitive to pressure history and therefore the negative values may be associated with the pressure hysteresis in the sample since all the measurements were conducted in 24 h for Darley Dale sandstone and 48 h for New Red Sandstone, so that the pressure hysteresis is generated in both cases. On the other hand, the coefficients are calculated based on the Todd-Simmons's empirical relation from compressional wave velocities, which is weakly affected by n_{Pe} when high compressible clay linings are present in the sandstone. It seems likely that the current empirical relation for n_{Pe} for shear wave velocity is not suitable for clay-bearing sandstones.

The V_P of both water-saturated sandstones are better described by effective pressure obtained from n_{Pe} at different pore pressures, compared to differential pressure (Fig. 7.13). The effective pressures fail to describe V_S, which may be due to the most high positive n_{Pe} values (>1) for V_{S2} and negative n_{Pe} values for V_{S1} (Fig. 7.11), which are believed likely due to the presence of a clay. Indeed, V_S seems to be better presented against differential pressure ($n_{Pe} = 1$) than effective pressure (which show a large variation in decompression data) in New Red Sandstone. The discrepancy shows that the high n_{Pe} values may not be affected simply by the total clay content. The relation between the clay and the rock frame may also result in differences, considering that clays are about 20 times more compliant than quartz.

Al-Wardy and Zimmerman [34] have provided two pore-clay models (pore-lining clays and discrete particles of clay in pore space) to explain high effective stress coefficients (n_k), and they use different but conceptually similar empirical definitions for n_{Pe}, from the differential ratio of curves at constant confining pressure and constant pore pressure [34]. The clay particle model (discrete particles) gives a higher n_k than the clay shell model (linings). Therefore, the microstructural relation between the clay and the rock frame may well contribute differently to the effective pressure coefficients for Darley Dale sandstone and New Red Sandstone.

7.4.3 Interpretations of 'n_{Pe}' in Terms of Microstructural Changes

Similar behaviours for effective pressure coefficients with confining pressure are found in both compression and decompression data, with higher n_{Pe} values occurring at higher pore pressures over the same pressure history. To gain a better idea of how the coefficient changes with pressure, the average of velocities and coefficients (n_{Pe}) from all water-saturated data have been plotted against confining pressure (Fig. 7.14). Several consistent increasing and decreasing trends are found in both sandstones, even though the overall trend is for n_{Pe} to decrease for Darley Dale sandstone and remain constant for New Red Sandstones with the increasing pressure. Generally, increasing n_{Pe} indicates the opening of cracks or pores while decreasing n_{Pe} indicates the closure of cracks.

The coefficients (n_{Pe}) in Darley Dale sandstone initially increase with the increasing confining pressure, followed by two decreases and increases in turn. It is likely from the data that the velocities stop increasing (for V_P) or start decreasing (for V_S) when the effective pressure coefficients decrease. The coefficient behaviours for V_{S2} show different paths from V_{S1} at high confining pressure above 110 MPa. The transition pressures of these cracks and volume changes are generally found at 40–50, 70–80, 80–90, and 110 MPa. On the other hand, the coefficients (n_{Pe}) in New Red Sandstone initially decrease followed by an increase, a decrease and then an increase in turn for V_P and V_{S1}. The data for V_{S2} are most from decompression data at 20 MPa pore pressure, and may not properly represent the behaviours at other velocities. The transition pressures for New Red Sandstone, according to V_P and V_{S1}, are found at 50, 80 and 90–110 MPa.

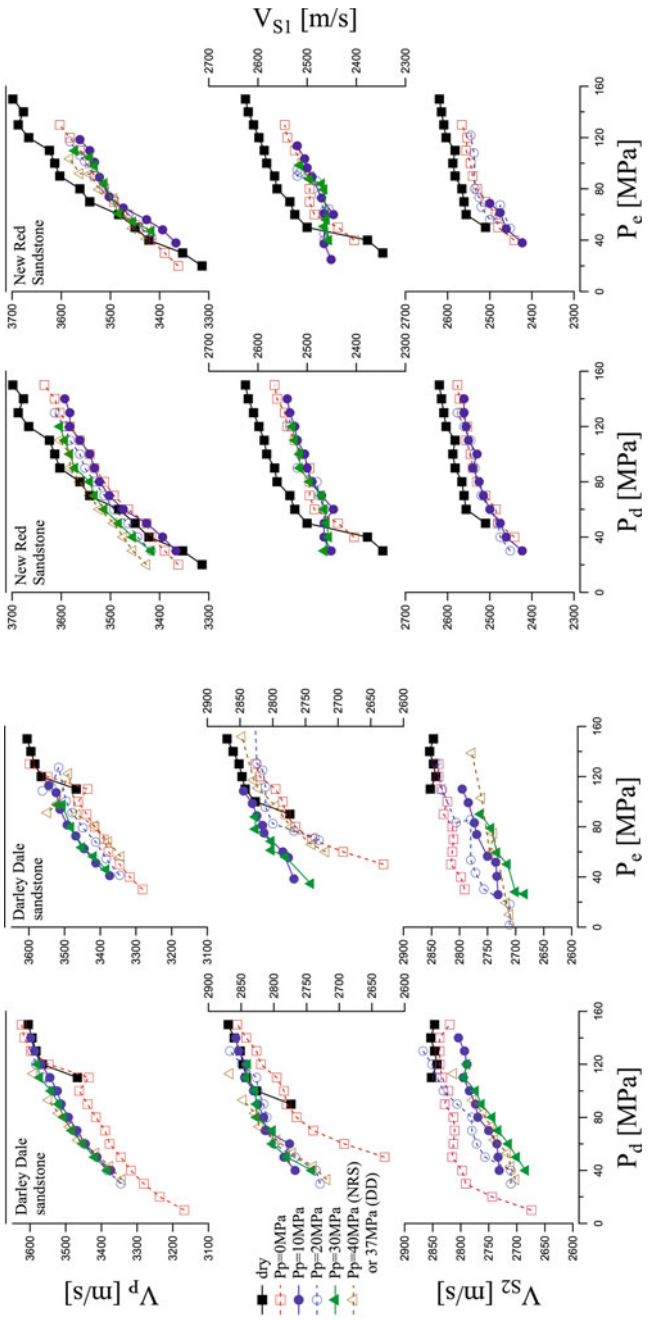

Fig. 7.13 The V_P, V_{S1} and V_{S2} of the Darley Dale sandstone and New Red Sandstone shown as a function of differential pressure (P_d) and effective pressure (P_e), separately. *Solid symbols* are data measured under compression and *open symbols* are data measured upon decompression. P_P is the fluid pressure in water-saturated samples

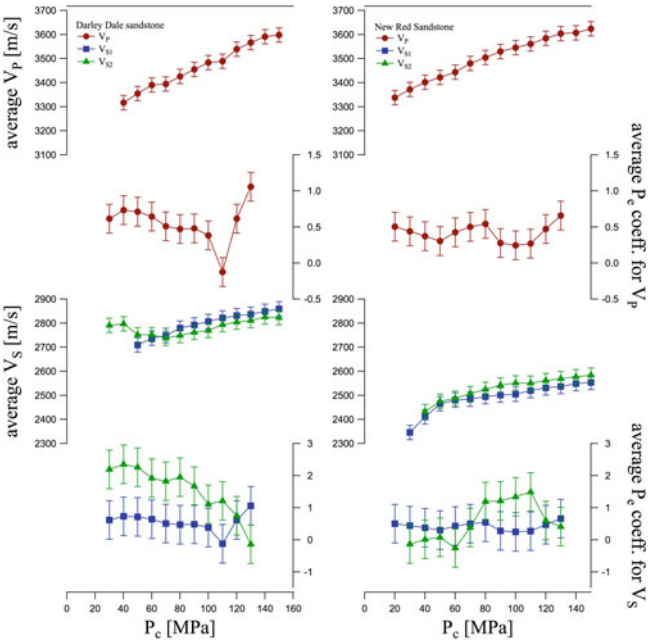

Fig. 7.14 The average V_P (*circle*), V_{S1} (*square*) and V_{S2} (*triangle*) and their corresponding average effective pressure coefficients n_{Pe} as a function of confining pressure P_c. Velocity errors are 8 m/s and n_{Pe} errors are estimated as 0.2 for V_P and 0.6 for V_S

Several failure modes (brittle faulting, cataclastic flow and grain crushing) with pressures have been observed for Darley Dale sandstone. Wong et al. [35] show that the transition pressure from shear localisation (brittle) to cataclastic flow (quasi-ductile) in Darley Dale sandstone occurs at a critical differential pressure of 50–100 MPa [35]. Additionally, Cuss et al. [25] mentioned that the critical effective mean pressure (P^*) for grain crushing occurs at 400 and 360 MPa for dry and wet Darley Dale sandstone under hydrostatic loading [25], based on the Fertzian fracture model as shown in Eq. 7.2 [9]. They suggest that shear localisation is dominate at low effective mean pressures ($P/P^* < 0.5$) while the pervasive cataclastic flow (with collapse of porosity) is dominant at high effective mean pressures ($P/P^* > 0.5$).

According to previous studies, the effective pressure coefficients in Darley Dale sandstone in this study are consistent with a model in which many cracks or wing cracks initially occur and form shear localisation zones at 40–50 MPa, with closure of cracks occurring due to increasing confining pressure. With further increase of confining pressure, the data suggest a few new cracks are generated at 80–90 MPa, followed by the collapse of pores at 110 MPa and finally pervasive cataclastic flow dominates in Darley Dale sandstone above 120 MPa. The transition pressures found in this study are in a good agreement with the study of Wong *et al.*, but the pervasive cataclastic flow seems to occur at pressures lower than seen by Cuss et al., who

predict a critical pressure for cataclastic flow at about 180 MPa in water-saturated Darley Dale sandstone.

The much lower transition pressure between this study and the study of Cuss et al. may be due to water weakening effects on the brittle failure modes. Baud et al. (2000) have demonstrated water weakening effects on failure modes in Darley Dale sandstone [8]. The critical pressure for failure modes can be reduced in the presence of water due to reductions in both fracture energy and the friction coefficient. However, the critical differential pressures required for shear localisation and cataclastic flow are higher at high confining pressure. Their data show that the differential stress reduction for the shear localisation and for cataclastic flow, due to the presence of water, is about 22 % at 50 MPa and about 20 % at 100 MPa confining pressure.

Similarly, shear localisation and cataclastic flow also occurs in New Red Sandstone. The data for n_{Pe} are consistent with a model in which pre-existing fractures and pores close initially with the increasing confining pressure and then the onset of sliding wing cracks start to occur at 50 MPa confining pressure. With further increasing confining pressure, more wing cracks are generated and eventually percolate and then form zones of shear localisation at about 80 MPa. As the confining pressure continuously increases, the cracks start to close again and then pores collapse at confining pressures of about 90–110 MPa. Consequently, the ductile cataclastic flow occurs and appears to become pervasive in the New Red Sandstone above 120 MPa confining pressure.

7.5 Conclusions

The observations in this study show that the effective pressure coefficient (n_{Pe}) is not simply a total porosity or pressure dependent parameter. Many factors can cause the changes of the effective pressure coefficient. Pre-existing cracks with different aspect ratio and the generation of wing cracks (shear cracks) may modify porosity with pressure. The presence of clay and its relation to the rock frame cause extremely high values of n_{Pe} and result in the failure of the predictions for effective pressure, based on the Todd-Simmons empirical relation. Different fluids (such as air and water) and their chemical reactions with the rock frame change the strength of the pores and rock frame and result in changes in n_{Pe}. For example, strong Si-O bonds are replaced by weaker hydrogen bonds when water exists in cracks in silicates[13], which results in a weakening effect on the fracture surface energy.

Fluid viscosity, which has a positive relation to pressure and negative relation to temperature, is found to have more influence on the shear wave modulus, while the bulk modulus is almost independent of the viscosity of the saturated rock [36]. Lu and Jackson [37] studied argon-saturated granite over a differential pressure range of 120–160 MPa at different temperatures from 573 to 873 K, using a torsional forced-oscillation technique at low frequency (mHz–Hz) [37]. The effective pressure coefficient increases with increasing temperature as well as with increasing pore pressure. They found that changes in the effective pressure coefficient are more

significant with changes from low to high temperature at constant pore pressure than that with changes from low to high pore pressure at constant high temperature.

Mavko and Vanorio [38] have modelled the influence of fluid and wave frequency (with $n_{Pe} \leq 1$) on the ultrasonic velocities of Berea sandstone [38], using the squirt model that involves the concept of a penny-shaped crack, to compare with the Gassmann's [31] fluid substitution formulation at low frequency [31]. For a thin crack, velocity with soft fluid (such as helium) saturation at constant pore pressure increases non-linearly, especially at low differential pressure, while with a stiff fluid (such as water at high frequency) velocities follow a more linear path as a function of confining pressure. However, Gassmann's theory only predicts linear pressure behaviour for velocity at constant pore pressure, as he assumed any wave-induced pore pressure remains equilibrated throughout the pore space at low frequency. The ultrasonic effective pressure coefficient shows a large pressure dispersion when the low frequency Gassmann's coefficient is essentially unity across the entire range of confining pressure (upto 50 MPa).

It is interesting to apply these concepts to the scenario of the mechanical properties of partially-molten igneous rocks, since fluid-filled sedimentary rocks may in some respects be considered analogous. As a dyke propagates and intrudes, the pore pressure may not equilibrate according to Gassmann's assumption in a dynamic propagating system. Therefore, the effective pressure coefficient (n_{Pe}) is expected to become pressure- and temperature-dependent. When viscous melts fill the crack tips a pore pressure is provided at the fracture tip against the confining pressure from the country rock and overburden. The velocities will decrease as more fractures occur and pore pressure pervades as the dyke propagates. The shapes and orientation of small aspect ratio cracks can affect the influence of the pore pressure on the rock properties (changes in effective pressure coefficient). The melt chemistry and its reactions with rock frame can also modify the rock properties, including the crack growth rate. Modification of the surfaces of minerals in the rock have an important influence on effective pressure coefficients as well. Therefore, it is important to take these factors (fracture shape, fracture orientation, grain shape, and fluid chemistry) into account when predicting the pore pressure and the confining pressure (corresponding to depth) in a fractured partially-molten rock. One anticipates that detailed studies of V_P and V_S in real partially-molten rocks, such as the Icelandic basalts studied here would yield insights into changes in microstructure through variations in n_{Pe} in the same way as for sandstones. The challenge, of course, is to control pore pressure and confining pressure while measuring velocities in a system where the relevant homologous temperature may correspond to 1,000 K or more.

References

1. Rubin, A. M. (1993). Tensile fracture of rock at high confining pressure: Implications for dike propagation. *Journal of Geophysical Research*, *98*(B9), 15919–15935.

2. White, R. S., Drew, J., Martens, H. R., Key, J., Soosalu, H., & Jakobsdóttir, S. S. (2011). Dynamics of dyke intrusion in the mid-crust of iceland. *Earth and Planetary Science Letters*, *304*(3–4), 300–312.
3. Mukerji, T., Dutta, N., Prasad, M., & Dvorkin, J. (2002). Seismic detection and estimation of overpressures part I: The rock physics basis. *Canadian Society of Exploration Geophysicists Recorder*, *27*, 36–57.
4. Dutta, N., Mukerji, T., Prasad, M., & Dvorkin, J. (2002). Seismic detection and estimation of overpressures part II: Field applications. *Canadian Society of Exploration Geophysicists Recorder*, *27* 59–73.
5. Rubin, A. M. (1995). Propagation of magma-filled cracks. *Annual Review Of Earth And Planetary Sciences*, *23*, 287–336.
6. Xu, X., Hofmann, R., Batzle, M., & Tshering, T. (2006). Influence of pore pressure on velocity in low-porosity sandstone: Implications for time-lapse feasibility and pore-pressure study. *Geophysical Prospecting*, *54*(5), 565–573.
7. Horii, H., & Nemat-Nasser, S. (1986). Brittle failure in compression: Splitting, faulting and brittle-ductile transition. *Philosophical Transactions of the Royal Society of London. Series A, Mathematical and Physical Sciences*, *319*(1549), 337–374.
8. Baud, P., Zhu, W., & Wong, T. -f. (2000). Failure mode and weakening effect of water on sandstone. *Journal of Geophysical Research*, *105*(B7), 16371–16389.
9. Zhang, J., Wong, T. -F., & Davis, D. M. (1990). Micromechanics of pressure-induced grain crushing in porous rocks. *Journal of Geophysical Research*, *95*(B1), 341–352.
10. Tompkins, M. J., & Christensen, N. I. (2001). Ultrasonic p- and s-wave attenuation in oceanic basalt. *Geophysical Journal International*, *145*(1), 172–186.
11. King, M. S. (1966). Wave velocities in rocks as a function of changes in overburden pressure and pore fluid saturants. *Geophysics*, *31*(1), 50–73.
12. Gist, G. A. (1994). Fluid effects on velocity and attenuation in sandstones. *The Journal of the Acoustical Society of America*, *96*(2), 1158–1173.
13. Waza, T., Kurita, K., & Mizutani, H. (1980). The effect of water on the subcritical crack growth in silicate rocks. *Tectonophysics*, *67*(1–2), 25–34.
14. Terzaghi, K. (1923). Die berechnung der durchlassigkeitsziffer des tones aus dem verlauf der hydrodynamischen spannungserscheinungen. *Sitzungsberichte Der Mathematisch-Naturwissenschaftlichen Classe Der Kaiserlichen Akademie*, *132*, 105–124.
15. Biot, M., & Willis, D. (1957). The elastic coefficients of the theory of consolidation. *Journal of Applied Mechanics*, *24*, 594–601.
16. Todd, T., & Simmons, G. (1972). Effect of pore pressure on the velocity of compressional waves in low-porosity rrocks. *Journal of Geophysical Research*, *77*(20), 3731–3743.
17. Hofmann, R., Xu, X., Batzle, M., Prasad, M., Furre, A.-K., & Pillitteri, A. (2005). Effective pressure or what is the effect of pressure? *The Leading Edge*, *24*(12), 1256–1260.
18. Vasquez, G. F., Vargas Junior, Ed A, Ribeiro, C. J. B., Leão, M., & Justen, J. C. R. (2009). Experimental determination of the effective pressure coefficients for brazilian limestones and sandstones. *Revista Brasileira de Geofísica*, *27*(1), 43–53.
19. Nur, A. M., Mavko, G., Dvorkin, J., & Gal, D. (1995). Critical porosity: The key to relating physical properties to porosity in rocks. *SEG Technical Program Expanded Abstracts*, *14*(1), 878–881.
20. Salje, E. K. H., Koppensteiner, J., Schranz, W., & Fritsch, E. (2010). Elastic instabilities in dry, mesoporous minerals and their relevance to geological applications. *Mineralogical Magazine*, *74*(2), 341–350.
21. Prasad, M., & Manghnani, M. H. (1997). Effects of pore and differential pressure on compressional wave velocity and quality factor in berea and michigan sandstones. *Geophysics*, *62*(4), 1163–1176.
22. Christensen, N. I., & Wang, H. F. (1985). The influence of pore pressure and confining pressure on dynamic elastic properties of berea sandstone. *Geophysics*, *50*(2), 207–213.
23. Gardner, G. H. F., Wyllie, M. R. J., & Droschak, D. M. (1965). Hysteresis in the velocity-pressure characteristics of rocks. *Geophysics*, *30*(1), 111–116.

24. Hart, B. S., Flemings, P. B., & Deshpande, A. (1995). Porosity and pressure: Role of compaction disequilibrium in the development of geopressures in a gulf coast pleistocene basin. *Geology*, *23*(1), 45–48.
25. Cuss, R. J., Rutter, E. H., & Holloway, R. F. (2003). The application of critical state soil mechanics to the mechanical behaviour of porous sandstones. *International Journal of Rock Mechanics and Mining Sciences*, *40*(6), 847–862.
26. Hatchell, P., & Bourne, S. (2005). Rocks under strain. *The Leading Edge*, *24*(12), 1222–1225.
27. Chapman, M., Zatsepin, S. V., & Crampin, S. (2002). Derivation of a microstructural poroelastic model. *Geophysical Journal International*, *151*(2), 427–451.
28. Mavko, G., & Nur, A. (1975). Melt squirt in the asthenosphere. *Journal of Geophysical Research*, *80*(11), 1444–1448.
29. O'Connell, R. J., & Budiansky, B. (1977). Viscoelastic properties of fluid-saturated cracked solids. *Journal of Geophysical Research*, *82*(36), 5719–5735.
30. Winkler, K., & Nur, A. (1979). Pore fluids and seismic attenuation in rocks. *Geophysical Research Letter*, *6*(1), 1–4.
31. Gassmann, F. (1951b). Über die elastizität poröser medien. *Vierteljahrsschrift der Naturforschenden Gesellschaft in Zürich*, *96*, 1–23.
32. Siggins, A. F., & Dewhurst, D. N. (2003). Saturation, pore pressure and effective stress from sandstone acoustic properties. *Geophysical Research Letter*, *30*(2), 1089.
33. Eberhart-Phillips, D., Han, D. H., & Zoback, M. D. (1989). Empirical relationships among seismic velocity, effective pressure, porosity, and clay content in sandstone. *Geophysics*, *54*(1), 82–89.
34. Al-Wardy, W., & Zimmerman, R. W. (2004). Effective stress law for the permeability of clay-rich sandstones. *Journal of Geophysical Research*, *109*(B4), B04203.
35. Wong, T-f, David, C., & Zhu, W. (1997). he transition from brittle faulting to cataclastic flow in porous sandstones: Mechanical deformation. *Journal of Geophysical Research*, *102*(B2), 3009–3025.
36. Nur, A., & Simmons, G. (1969). The effect of viscosity of a fluid phase on velocity in low porosity rocks. *Earth and Planetary Science Letters*, *7*(2), 99–108.
37. Lu, C., & Jackson, I. (2006). Low-frequency seismic properties of thermally cracked and argon-saturated granite. *Geophysics*, *71*(6), F147–F159.
38. Mavko, G., & Vanorio, T. (2010). The influence of pore fluids and frequency on apparent effective stress behavior of seismic velocities. *Geophysics*, *75*(1), N1–N7.

Chapter 8
Conclusions

8.1 Summary

Anelastic relaxation processes in natural rocks (heterogeneous multi-phase assemblages) are more complicated, as seen in this study, than these in synthesised polycrystalline upper mantle minerals or silicate melts (single-phase homogeneous samples) that have formed the focus of many previous studies. Here, the thermally-activated mechanical characteristics of partially-molten rocks (with melts less than 2 %) show significant changes depending on the microstructure and thermal history as a function of temperature, under seismic frequency stresses (0.05–10 Hz) and at low strains ($10^{-4} - 10^{-6}$). Alongside studies of igneous rocks, the studies of analogue materials (crystalbond-saturated and water-saturated sandstones) reveal their potential and important roles to understand the underlying physical properties of solid-melt systems in the Earth's interior.

$\sim 10^{-2}$–10^{2} s^{-1} μ

In this study, several anelastic relaxation processes, superposed on the exponentially increasing high temperature background, are found in basalts (800–1,300 K) and gabbro (800–1,400 K) at stress frequency of 1 Hz. Gabbro has more complicate microstructure and a wide range of grain size distributions and results in more complicate shear modulus behaviours and more attenuation peaks than basalt does. The microstructural observations (pyroxene growth, domain wall development, partial melting and recrystallisation) and the complicate shear modulus behaviours (multi-stages of stiffening and softening) with the corresponding relaxation peaks of particular activation energies suggest the possible origins in terms of crack healing, diffusion, dislocation and diffusional creep. In addition, creep studies of basalt show that creep behaviour may not active below $\sim$974 K, that also imply that no high-temperature background is expected below this temperature.

Despite the different grain size in basalt and gabbro, the attenuation magnitude are not found to be significant related to the grain size, as suggested by previous studies of single-phase polycrystalline rocks. Similar internal friction magnitudes are measured in basalt and in gabbro, showing that grain size effects may not be important to the

S.-Y. Chien, *Rheological and Seismic Properties of Solid-Melt Systems*,
Springer Theses, DOI: 10.1007/978-3-319-03098-2_8,

attenuation at high temperatures (up to 1,400 K) and hence it can be assumed that the grain boundary sliding is likely less important to the seismic attenuation in the lithosphere. The mechanisms like crack healing, diffusion, dislocation and diffusional creep (or partial melting) may have more contributions to the attenuation than grain boundary sliding.

Small amount of melts were generated in this study when samples were heated to high temperatures (∼1 % in gabbro and ∼1.5 % in basalt). As temperature drops, melts may transform to glass during the rapid cooling and this encourages the development and propagation of fractures. With the presence of the glass and under the deviatoric stress, catastrophic brittle failure occurs (that is likely due to crack percolation) at temperatures between 0.5 and 0.6 T_m on cooling. This reproducible behaviour is also seen and more profound in the crystalbond-saturated sandstone with higher proportion of glass (up to 14 %) on cooling, measured by dynamic mechanical analyser. These measurements have informed our understanding of seismic patterns recently reported from episodically microseismicity in Iceland: as an upwards propagating dyke intrudes into the crust (with decreasing temperature), melts solidify and form blocks. The fractures are generated on cooling and results in brittle failure of the block (which causes small earthquakes). This process occurs repeatedly (and hence episodic seismicity is observed) on repeated thermal cycling driven by continuous uplifting melt from below.

An earthquake can be considered as a big crackling noise in the Earth. Like the Gutenberg-Richter Law, which states that small earthquakes are common and large earthquakes are rare, noise behaviours from shear modulus data (real part of the exponent) and internal friction data (imaginary part of the exponent) show a power law probability distribution, and both can be observed by inverted forced torsion pendulum. Although the microstructural changes in basalts and gabbro (complex heterogeneous solids) or the interference from the device may change the details of the exponents, the overall underlying physics remain, marked by universality and self-organised criticality.

The final part of this work is an attempt to extend the characterisation of mechanical response in fluid-bearing solids to high pressure. When viscous melts fill the crack tips in a propagating dyke, a pore pressure is provided at the fracture tip against the confining pressure from the country rock and overburden. Two stages of brittle failure (shear localisation at low confining pressure and cataclastic flow in high confining pressure) can occur associated with the pore pressure and the confining pressure. The presence of clay on grain surfaces (or pore surfaces) may also affect the analysis of the effective pressure coefficients, which is highly correlated to pore pressure. The analysis of the effective pressure coefficients in this study shows its potential to reveal the microstructural damage in the rocks at varying pore pressure and confining pressure. However, further detailed work on this topic should be undertaken to examine the reproducibility of the changes and to confirm the relation between the effective pressure coefficient and the sample's microstructure.

Despite many aspects that still require exploration, this study has provided the first detailed shear modulus and internal friction characteristics of partially-molten basalts and gabbro at seismic frequencies, identifying several relaxation process with

significant energy loss. Understanding the microstructural relation between fluid and solid states and its effect on the mechanical properties of minerals and rocks based on this study provide potential explanations for geophysical observations in the solid-melt systems, such as low velocity zones, dyke systems or partial melting in the Earth's interior.

8.2 Future Directions

This study has highlighted the many possible mechanisms that may play a role in controlling the mechanical properties of geomaterials. The over-riding conclusion is that real natural samples display complexity well in excess of the picture provided by earlier investigations of monomineralic systems. The problem in making such study is, however, the difficulty in isolating individual processes for further study. The development of good analogues to natural systems offers a way forward in this regard. Indeed, McCarthy and Takei [1] have demonstrated that aggregates of borneol-diphenylamine-melt systems provide an analogue of crystal-melt systems in which grain size can be controlled. The crystalbond-saturated sandstones of this study (Chap. 5) show surprising similarity to partially-molten basalt. A poly-phase analogue in which phase proportions and melt can be controlled may be the best approach to further identifying individual relaxation processes in basalt and gabbro.

Controls on crack networks in a solid could provide a rock to understand the role of crack healing in anelastic responses of brittle materials. One route to carry out such control would be to take a glassy sample and pre-anneal it just below the glass transition temperature to promote crack healing of initial cracks. Cracks may be developed by stresses applied within the apparatus, and healed in subsequent thermal treatments. In this case a well-formed glass with little propensity to recrystallise would be a good candidate for study.

To test the role of melt on grain boundaries, and to explore the possible influence of grain size in wetted samples, it would be instructive to compare samples with varying degrees of partial melting, or glass content. It has been suggested that grain boundaries are rigid and static in the deep Earth. However, grain boundary wetting might be expected at the deepest part of the mantle, the core-mantle boundary. In the study of Dobson et al. [2], computational mineralogy has a part to play in defining the important mechanisms controlling grain boundary dynamics at extreme pressure and temperature.

At more modest depths, it would be worth exploring the role of grain size, chemical composition, and thermal history (in particular cooling rates) on the mechanical stability of igneous rocks, to define the expected window in which episodic failure might be expected. The basaltic sample discussed in Chap. 5 correlates well with intrusions observed geophysically. Might similar processes be expected in andesitic intrusions, or at greater depth in gabbroic bodies?

Finally, while this study has shown that mechanical spectroscopy, a tool developed initially for metallurgical research, is very useful for the study of geomaterials, there

are undoubted opportunities for technical improvements in experimental design. In the realm of understanding noise behaviour, the augmentation of torsional pendulum studies by acoustic emission methods would be highly valuable for this reason. I suggest a high priority for future work in this area should be the addition of an acoustic emission system to the pendulum, where a sensor could easily be attached in close proximity to the clamped sample on the pendulum rod.

References

1. McCarthy, C., & Takei, Y. (2011). Anelasticity and viscosity of partially molten rock analogue: Toward seismic detection of small quantities of melt. *Geophysical Research Letters, 38*(18), L18306.
2. Dobson, D., Ammann, M., & Tackley, P. (2012). The grain size of the lower mantle. In: *European Mineralogical Conference, European Mineralogical Conference* (Vol 1, p. 403).

Appendix A
SEM Images and Microprobe Analysis of Basalts

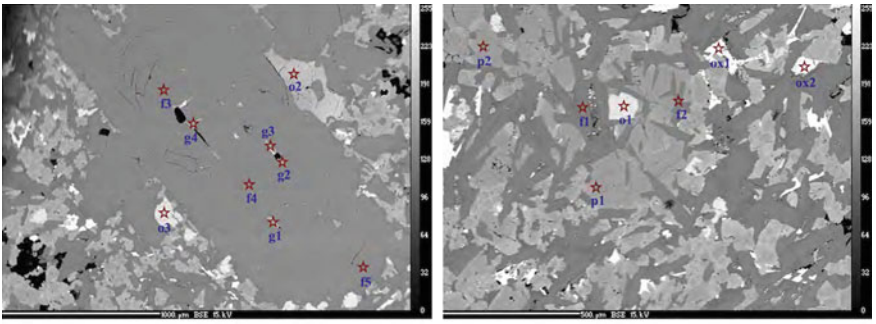

(wt%)	feldspar					pyroxene		glass			
Point	f1	f2	f3	f4	f5	p1	p2	g1	g2	g3	g4
SiO2	50.9	49.62	46.82	47.89	47.28	52.01	51.39	51.76	50.68	51.12	52.03
TiO2	0.09	0.04	0.03	0.04	0.03	0.56	0.49	0.8	0.91	1.19	0.72
Al2O3	29.25	30.05	32.55	32.19	32.08	2.26	1.92	1.95	2.19	2.00	2.01
Cr2O3						0.21	0.26	0.15	0.11	0.06	0.19
FeO	0.92	0.95	0.57	0.58	0.69	8.35	7.76	9.6	11.75	13.65	8.63
MnO	0.04	0.00	0.01	0.03	0.00	0.18	0.11	0.24	0.13	0.31	0.34
MgO	0.05	0.06	0.14	0.16	0.19	18.16	17.95	15.31	14.73	14.69	16.27
CaO	13.29	13.91	16.9	16.33	16.36	17.31	17.51	19.81	18.19	17.33	19.76
SrO	0.03	0.05	0.01	0.01	0.00						
BaO	0.19	0.12	0.08	0.06	0.09						
Na2O	3.92	3.55	1.93	2.22	2.16	0.21	0.19	0.25	0.16	0.22	0.28
K2O	0.20	0.17	0.04	0.02	0.04	0.01	0.00	0.00	0.03	0.03	0.00
NiO						0.10	0.00				
Total	98.88	98.52	99.08	99.53	98.92	99.36	97.58	99.87	98.88	100.59	100.23

(wt%)	olivine			oxides	
Point	o1	o2	o3	ox1	ox2
SiO2	32.52	36.56	33.38	0.02	0.03
TiO2	0.03	0.01	0.04	66.69	40.44
Al2O3	0.00	0.00	0.00	0.21	0.10
Cr2O3	0.03	0.00	0.00	0.03	0.03
P2O5	0.06	0.01	0.00		
FeO	47.76	31.1	45.58	27.87	52.93
MnO	0.61	0.46	0.60	0.13	0.46
MgO	18.57	31.41	20.18	1.20	1.82
CaO	0.28	0.29	0.29	0.07	0.03
NiO	0.00	0.02	0.07	0.01	0.03
Total	99.85	99.85	100.16	96.23	95.87

Fig. A.1 SEM images and representative microprobe analysis of I13_83493 basalt 'as received'

S.-Y. Chien, *Rheological and Seismic Properties of Solid-Melt Systems*,
Springer Theses, DOI: 10.1007/978-3-319-03098-2,

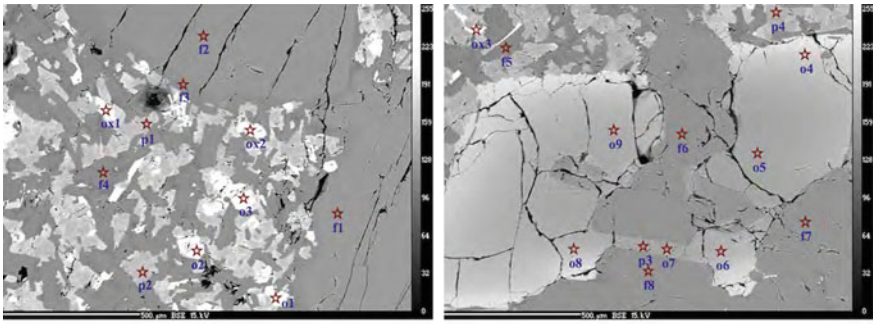

(wt%)	feldspar						pyroxene					
point	f1	f2	f3	f4	f5	f6	f7	f8	p1	p2	p3	p4
SiO2	46.14	46.31	54.86	50.92	53.94	47.09	46.76	46.96	52.45	51.03	39.08	51.88
TiO2	0.03	0.04	0.15	0.10	0.19	0.04	0.05	0.05	0.70	0.77	0.05	0.68
Al2O3	33.2	33.32	27.55	29.76	28.3	32.93	32.71	32.66	1.68	1.86	0.04	1.84
Cr2O3									0.01	0.07	0.00	0.02
FeO	0.59	0.43	1.13	1.03	1.18	0.68	0.52	0.62	9.00	9.19	18.11	9.16
MnO	0.00	0.00	0.02	0.05	0.00	0.01	0.00	0.04	0.26	0.23	0.31	0.23
MgO	0.15	0.16	0.06	0.06	0.06	0.17	0.17	0.17	15.63	15.32	42.03	15.67
CaO	17.28	17.5	10.98	13.43	11.32	16.75	16.98	16.76	19.18	19.01	0.28	19.37
SrO	0.01	0.03	0.01	0.01	0.03	0.01	0.00	0.05				
BaO	0.05	0.04	0.27	0.17	0.37	0.08	0.04	0.08				
Na2O	1.61	1.47	5.12	3.85	4.81	1.92	1.84	2.00	0.21	0.21	0.00	0.24
K2O	0.05	0.00	0.32	0.16	0.34	0.04	0.03	0.04	0.02	0.00	0.00	0.01
NiO									0.05	0.00	0.17	0.00
Total	99.11	99.28	100.49	99.53	100.54	99.71	99.10	99.41	99.20	97.69	100.06	99.09

(wt%)	olivine								oxides			
Point	o1	o2	o3	o4	o5	o6	o7	o8	o9	ox1	ox2	ox3
SiO2	33.38	34.22	33.14	35.84	39.51	38.58	39.19	38.22	38.73	0.05	33.32	0.03
TiO2	0.05	0.09	0.05	0.03	0.02	0.00	0.02	0.00	0.01	47.34	0.07	48.29
Al2O3	0.02	0.09	0.00	0.03	0.04	0.02	0.01	0.02	0.04	0.06	0.00	0.10
Cr2O3	0.00	0.00	0.00	0.01	0.04	0.09	0.07	0.09	0.01	0.00	0.00	0.01
P2O5	0.04	0.08	0.04	0.02	0.02	0.00	0.00	0.01	0.00			
FeO	50.06	48.52	49.82	36.3	17.85	21.23	18.11	24.07	22.03	48.38	50.84	47.75
MnO	0.77	0.66	0.67	0.43	0.16	0.33	0.24	0.35	0.32	0.79	0.62	0.44
MgO	16.16	16.22	16.33	27.63	42.24	39.4	42.07	37.84	39.05	2.49	16.07	2.04
CaO	0.30	0.43	0.29	0.23	0.31	0.28	0.27	0.29	0.29	0.07	0.23	0.16
NiO	0.00	0.12	0.00	0.08	0.15	0.13	0.10	0.13	0.09	0.00	0.01	0.01
Total	100.79	100.42	100.35	100.61	100.33	100.06	100.10	101.01	100.58	99.18	101.18	98.84

Fig. A.2 SEM images and representative microprobe analysis of I13_83493 basalt, as heated to 1250 K under stress

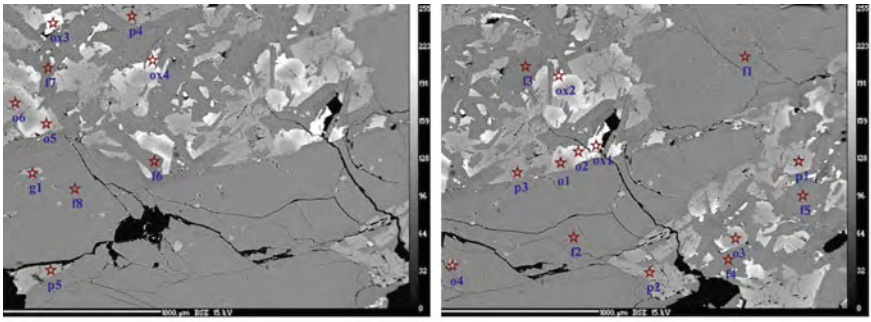

(wt%)	feldspar								glass	pyroxene				
Point	p1	p2	p3	p4	p5	p6	p7	p8	g1	p1	p2	p3	p4	p5
SiO2	47.48	36.94	48.57	46.52	46.11	53.53	53.10	55.55	49.14	52.09	53.34	51.40	53.67	52.00
TiO2	0.01	0.03	0.02	0.01	0.02	0.06	0.1	0.09	1.39	0.59	0.32	0.6	0.56	0.47
Al2O3	32.77	24.75	32.43	33.62	33.67	28.7	28.68	27.35	4.98	2.67	1.65	3.61	2.91	3.22
Cr2O3	0.00	0.03	0.03	0.02	0.01	0.00	0.00	0.00	0.00	0.03	0.24	0.57	0.07	0.81
FeO	0.47	0.27	0.64	0.38	0.46	0.75	0.70	0.72	15.57	7.61	5.70	5.93	6.63	5.20
MnO	0.04	0.02	0.00	0.01	0.00	0.04	0.03	0.00	0.23	0.25	0.19	0.14	0.13	0.13
MgO	0.26	0.15	0.15	0.23	0.23	0.15	0.16	0.11	14.24	16.57	17.85	16.56	17.14	16.85
CaO	16.79	13.24	15.9	17.6	17.61	12.26	12.26	10.58	12.28	19.79	20.14	20.56	20.42	20.46
SrO	0.03	0.00	0.01	0.03	0.00	0.00	0.02	0.02						
BaO	0.04	0.03	0.06	0.03	0.02	0.12	0.15	0.18						
Na2O	1.89	0.94	2.23	1.32	1.23	4.19	4.24	5.23	0.54	0.19	0.18	0.21	0.14	0.19
K2O	0.01	0.03	0.04	0.01	0.03	0.06	0.06	0.13	0.10	0.02	0.00	0.02	0.00	0.01
NiO	0.00	0.00	0.03	0.00	0.00	0.01	0.01	0.00		0.02	0.00	0.07	0.04	0.05
Total	99.79	76.44	100.11	99.77	99.38	99.88	99.51	99.96	98.48	99.84	99.62	99.67	101.69	99.40

(wt%)	olivine						oxides			
Point	o1	o2	o3	o4	o5	o6	ox1	ox2	ox3	ox4
SiO2	39.72	34.56	53.34	49.24	37.26	40.11	0.08	0.11	0.15	0.19
TiO2	0.01	0.05	0.38	1.19	0.05	0.01	2.93	6.11	24.01	40.69
Al2O3	0.07	0.15	1.42	5.25	0.06	0.05	3.90	2.38	1.47	1.01
Cr2O3	0.00	0.03	0.00	0.07	0.00	0.01	0.00	0.05	0.00	0.00
P2O5	0.06	0.03	0.02	0.10	0.03	0.03				
FeO	21.36	39.82	7.19	15.64	37.85	16.82	79.8	84.29	68.35	52.26
MnO	0.35	0.61	0.19	0.29	0.53	0.27	2.48	0.34	0.53	0.72
MgO	40.69	23.02	17.65	13.66	27.73	40.44	2.54	0.70	0.49	0.75
CaO	0.43	0.46	19.35	12.6	0.41	0.42	0.07	0.10	0.05	0.11
NiO	0.19	0.09	0.06	0.01	0.09	0.18	0.05	0.06	0.00	0.09
Total	102.89	98.84	99.59	98.03	104.01	98.34	91.83	94.14	95.04	95.80

Fig. A.3 SEM images and representative microprobe analysis of Iceland basalt ‘as received’

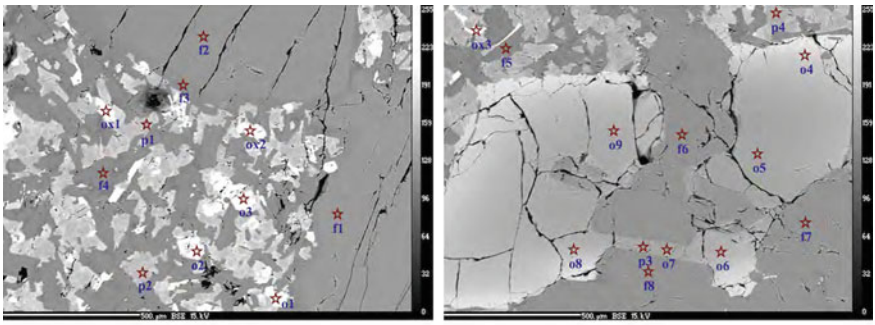

(wt%)	feldspar								pyroxene			
point	f1	f2	f3	f4	f5	f6	f7	f8	p1	p2	p3	p4
SiO2	46.14	46.31	54.86	50.92	53.94	47.09	46.76	46.96	52.45	51.03	39.08	51.88
TiO2	0.03	0.04	0.15	0.10	0.19	0.04	0.05	0.05	0.70	0.77	0.05	0.68
Al2O3	33.2	33.32	27.55	29.76	28.3	32.93	32.71	32.66	1.68	1.86	0.04	1.84
Cr2O3									0.01	0.07	0.00	0.02
FeO	0.59	0.43	1.13	1.03	1.18	0.68	0.52	0.62	9.00	9.19	18.11	9.16
MnO	0.00	0.00	0.02	0.05	0.00	0.01	0.00	0.04	0.26	0.23	0.31	0.23
MgO	0.15	0.16	0.06	0.06	0.06	0.17	0.17	0.17	15.63	15.32	42.03	15.67
CaO	17.28	17.5	10.98	13.43	11.32	16.75	16.98	16.76	19.18	19.01	0.28	19.37
SrO	0.01	0.03	0.01	0.01	0.03	0.01	0.00	0.05				
BaO	0.05	0.04	0.27	0.17	0.37	0.08	0.04	0.08				
Na2O	1.61	1.47	5.12	3.85	4.81	1.92	1.84	2.00	0.21	0.21	0.00	0.24
K2O	0.05	0.00	0.32	0.16	0.34	0.04	0.03	0.04	0.02	0.00	0.00	0.01
NiO									0.05	0.00	0.17	0.00
Total	99.11	99.28	100.49	99.53	100.54	99.71	99.10	99.41	99.20	97.69	100.06	99.09

(wt%)	olivine								oxides			
Point	o1	o2	o3	o4	o5	o6	o7	o8	o9	ox1	ox2	ox3
SiO2	33.38	34.22	33.14	35.84	39.51	38.58	39.19	38.22	38.73	0.05	33.32	0.03
TiO2	0.05	0.09	0.05	0.03	0.02	0.00	0.02	0.00	0.01	47.34	0.07	48.29
Al2O3	0.02	0.09	0.00	0.03	0.04	0.02	0.01	0.02	0.04	0.06	0.00	0.10
Cr2O3	0.00	0.00	0.00	0.01	0.04	0.09	0.07	0.09	0.01	0.00	0.00	0.01
P2O5	0.04	0.08	0.04	0.02	0.02	0.00	0.00	0.01	0.00			
FeO	50.06	48.52	49.82	36.3	17.85	21.23	18.11	24.07	22.03	48.38	50.84	47.75
MnO	0.77	0.66	0.67	0.43	0.16	0.33	0.24	0.35	0.32	0.79	0.62	0.44
MgO	16.16	16.22	16.33	27.63	42.24	39.4	42.07	37.84	39.05	2.49	16.07	2.04
CaO	0.30	0.43	0.29	0.23	0.31	0.28	0.27	0.29	0.29	0.07	0.23	0.16
NiO	0.00	0.12	0.00	0.08	0.15	0.13	0.10	0.13	0.09	0.00	0.01	0.01
Total	100.79	100.42	100.35	100.61	100.33	100.06	100.10	101.01	100.58	99.18	101.18	98.84

Fig. A.4 SEM images and representative microprobe analysis of Iceland basalt, as heated to 1300 K under stress

Appendix B
SEM Images and Microprobe Analysis of Gabbro

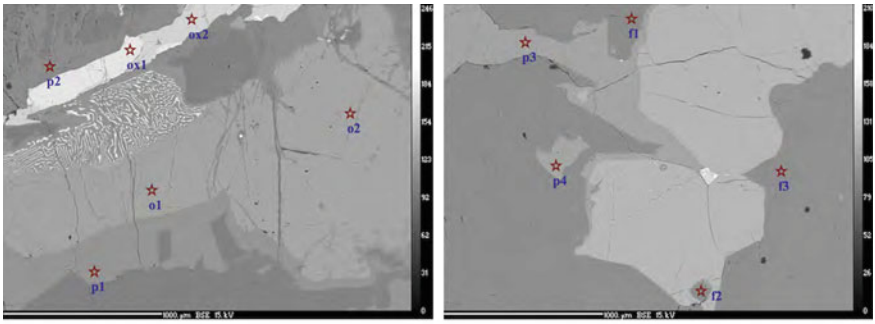

(wt%)	feldspar			pyroxene				olivine		oxides	
Point	f1	f2	f3	p1	p2	p3	p4	o1	o2	ox1	ox2
SiO2	53.48	53.72	53.57	52.58	38.61	52.89	52.82	36.12	36.04	0.03	0.03
TiO2	0.04	0.10	0.08	0.56	4.43	0.30	0.37	0.03	0.03	1.30	50.21
Al2O3	28.66	28.25	28.65	1.16	14.57	0.81	0.92	0.01	0.02	0.90	0.04
Cr2O3	0.06	0.01	0.04	0.00	0.00	0.00	0.00	0.00	0.05	0.02	0.00
P2O5								0.03	0.01		
FeO	0.48	0.64	0.35	20.76	10.95	21.16	21.63	34.68	34.78	90.90	47.88
MnO	0.05	0.05	0.00	0.54	0.09	0.40	0.50	0.48	0.49	0.05	0.45
MgO	0.04	0.03	0.03	23.54	18.44	23.72	23.07	29.60	29.71	0.21	2.28
CaO	11.51	11.08	11.56	1.33	0.08	1.02	1.42	0.07	0.06	0.00	0.01
SrO	0.01	0.00	0.04								
BaO	0.13	0.14	0.19								
Na2O	4.54	5.06	4.47	0.00	0.34	0.02	0.00				
K2O	0.36	0.24	0.40	0.02	9.38	0.00	0.00				
NiO	0.00	0.03	0.00	0.03	0.04	0.04	0.05	0.21	0.10	0.15	0.00
Total	99.35	99.36	99.39	100.52	96.93	100.36	100.78	101.24	101.29	93.56	100.90

Fig. B.1 SEM images and representative microprobe analysis of gabbro 'as received'

S.-Y. Chien, *Rheological and Seismic Properties of Solid-Melt Systems*,
Springer Theses, DOI: 10.1007/978-3-319-03098-2,

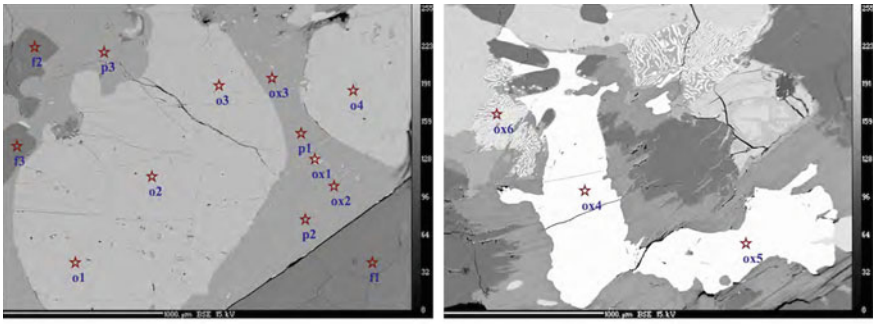

(wt%)	feldspar			pyroxene			olivine				oxides					
Point	f1	f2	f3	p1	p2	p3	o1	o2	o3	o4	ox1	ox2	ox4	line2	line3	line4
SiO2	55.21	53.00	53.57	52.09	51.26	52.74	36.31	36.42	36.15	36.52	0.01	15.95	27.47	0.03	0.01	14.66
TiO2	0.08	0.04	0.10	0.43	0.57	0.53	0.01	0.02	0.03	0.04	0.01	19.18	9.16	50.22	49.74	4.97
Al2O3	28.24	29.13	28.51	1.17	1.61	1.08	0.03	0.01	0.01	0.01	0.01	1.53	1.87	0.03	0.03	1.62
Cr2O3	0.01	0.00	0.01	0.02	0.00	0.00	0.00	0.00	0.02	0.01	0.02	0.05	0.01	0.00	0.01	0.03
P2O5							0.02	0.00	0.02	0.01						
FeO	0.35	0.33	0.38	15.92	13.15	20.17	33.76	34.08	34.43	33.91	40.38	53.78	50.87	47.08	47.21	69.74
MnO	0.02	0.00	0.00	0.43	0.23	0.39	0.50	0.48	0.46	0.44	0.01	0.34	0.44	0.48	0.46	0.32
MgO	0.05	0.01	0.03	18.51	16.33	23.35	29.35	29.58	29.46	29.36	0.00	6.68	14.56	2.06	2.18	9.68
CaO	10.50	12.03	11.27	10.80	14.05	1.85	0.06	0.06	0.08	0.06	0.09	4.59	1.06	0.01	0.02	0.16
SrO	0.02	0.03	0.04	0.00	0.00	0.00										
BaO	0.13	0.10	0.16	0.87	1.07	0.95										
Na2O	5.06	4.34	4.67	0.13	0.19	0.03										
K2O	0.36	0.33	0.33	0.00	0.00	0.01										
NiO	0.00	0.01	0.00	0.04	0.04	0.09	0.12	0.08	0.06	0.18	1.40	0.09	0.12	0.04	0.05	0.17
Total	100.02	99.36	99.06	100.40	98.51	101.18	100.15	100.73	100.72	100.54	41.92	102.19	105.56	99.94	99.69	101.34

Fig. B.2 SEM images and representative microprobe analysis of gabbro, as annealed at 900 K for 10 h without stress

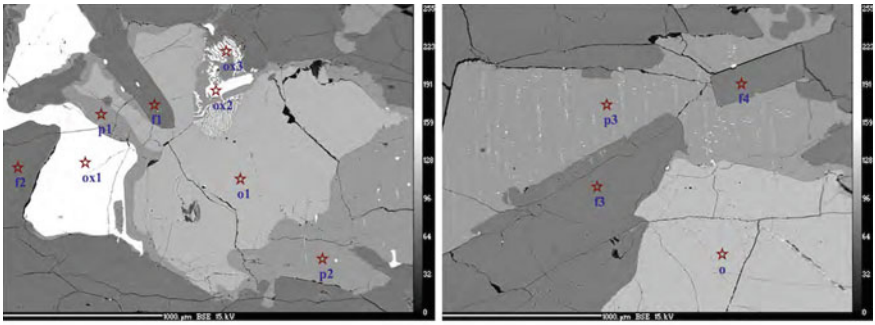

(wt%)	feldspar				pyroxene			olivine	oxides		
Point	f1	f2	f3	f4	p1	p2	p3	o1	ox1	ox2	ox3
SiO2	50.79	50.99	51.66	53.03	52.77	53.13	50.79	36.29	0.01	0.11	0.17
TiO2	0.05	0.09	0.07	0.09	0.61	0.37	0.92	0.03	49.43	5.06	6.70
Al2O3	30.85	30.44	30.08	29.11	1.07	0.97	2.75	0.02	0.07	2.40	2.43
Cr2O3	0.05	0.00	0.03	0.01	0.05	0.01	0.07	0.00	0.00	0.11	0.04
P2O5								0.01			
FeO	0.47	0.39	0.39	0.32	19.8	20.52	9.62	33.75	46.86	84.05	80.9
MnO	0.08	0.05	0.01	0.00	0.46	0.41	0.26	0.48	0.42	0.12	0.20
MgO	0.02	0.06	0.02	0.02	23.83	23.71	14.46	30.19	2.90	1.21	2.22
CaO	13.82	13.46	13.28	12.08	1.63	1.02	20.69	0.07	0.02	0.00	0.14
SrO	0.01	0.05	0.00	0.03							
BaO	0.07	0.15	0.17	0.16							
Na2O	3.29	3.44	3.85	4.32	0.01	0.03	0.42				
K2O	0.16	0.21	0.27	0.27	0.00	0.03	0.01				
NiO	0.06	0.00	0.00	0.01	0.07	0.02	0.00	0.12	0.03	0.18	0.12
Total	99.72	99.34	99.83	99.45	100.30	100.22	100.00	100.97	99.74	93.24	92.92

Fig. B.3 SEM images and representative microprobe analysis of gabbro, as annealed at 1250 K for 10 h without stress

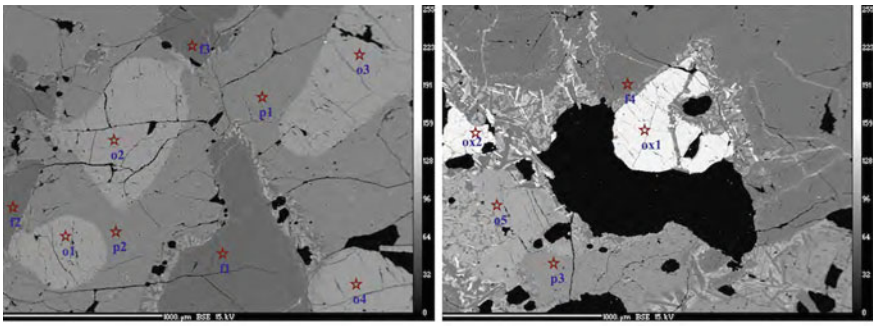

(wt%)	feldspar				pyroxene			olivine					oxides	
Point	f1	f2	f3	f4	p1	p2	p3	o1	o2	o3	o4	o5	ox1	ox2
SiO2	52.52	51.04	51.96	51.74	51.88	51.65	51.29	36.13	36.68	36.44	36.27	36.30	0.01	0.01
TiO2	0.10	0.07	0.08	0.08	0.74	0.91	0.57	0.04	0.02	0.04	0.02	0.03	51.62	52.64
Al2O3	29.7	30.39	29.66	30.16	1.91	2.20	1.80	0.02	0.02	0.00	0.01	0.04	0.21	0.64
Cr2O3	0.01	0.04	0.04	0.00	0.09	0.08	0.00	0.03	0.00	0.00	0.00	0.00	0.00	0.00
P2O5								0.09	0.03	0.01	0.02	0.02		
FeO	0.37	0.34	0.32	0.42	12.07	9.03	11.67	33.41	32.74	33.92	33.90	32.89	41.18	41.54
MnO	0.00	0.06	0.02	0.05	0.31	0.23	0.26	0.51	0.43	0.35	0.45	0.33	0.26	0.34
MgO	0.04	0.17	0.03	0.03	17.04	14.91	16.05	30.18	30.90	30.59	29.86	30.22	6.04	5.18
CaO	12.49	13.78	12.64	12.96	15.73	20.63	21.42	0.06	0.06	0.05	0.06	0.04	0.04	0.02
SrO	0.01	0.02	0.03	0.08										
BaO	0.19	0.14	0.18	0.20										
Na2O	4.05	3.14	3.93	3.56	0.21	0.27	0.31							
K2O	0.31	0.22	0.25	0.33	0.00	0.00	0.02							
NiO	0.01	0.00	0.03	0.00	0.00	0.09	0.01	0.16	0.12	0.20	0.18	0.18	0.07	0.02
Total	99.80	99.40	99.18	99.62	99.99	99.99	103.40	100.64	100.99	101.60	100.76	100.05	99.42	100.41

Fig. B.4 SEM images and representative microprobe analysis of gabbro, as repeatedly annealed at 1400 K twice without stress

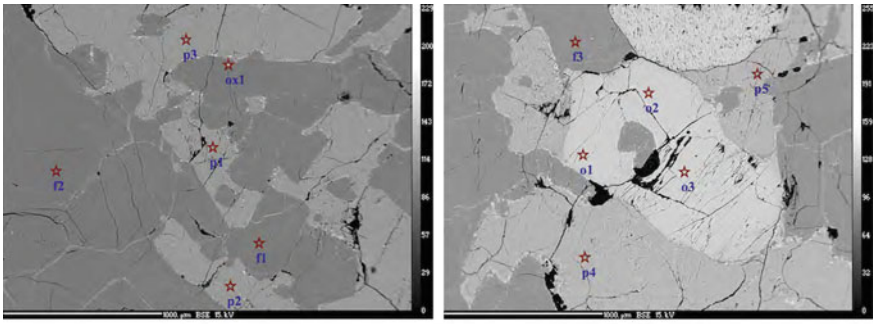

(wt%)	feldspar			pyroxene					olivine			
Point	f1	f2	f3	p1	p2	p3	p4	p5	o1	o2	o3	ox1
SiO2	50.87	54.13	50.36	53.9	51.52	52.87	51.61	51.74	36.75	36.47	36.32	0.27
TiO2	0.08	0.12	0.10	0.56	1.01	0.74	0.89	0.88	0.04	0.04	0.06	21.99
Al2O3	30.42	28.43	30.56	1.41	3.08	2.03	2.37	2.21	0.01	0.01	0.02	1.88
Cr2O3	0.06	0.02	0.00	0.00	0.07	0.07	0.14	0.13	0.05	0.04	0.00	0.02
P2O5									0.01	0.01	0.03	
FeO	0.33	0.36	0.43	14.88	9.39	10.49	8.17	7.88	32.57	32.47	32.71	70.35
MnO	0.02	0.04	0.03	0.34	0.26	0.30	0.23	0.15	0.38	0.49	0.46	0.47
MgO	0.04	0.04	0.03	19.67	14.25	16.54	15.11	14.81	30.83	30.76	30.76	0.82
CaO	13.97	11.31	13.96	10.84	19.01	18.09	20.65	21.42	0.08	0.07	0.07	0.42
SrO	0.04	0.04	0.04									
BaO	0.14	0.22	0.16									
Na2O	3.15	4.63	3.29	0.20	0.33	0.27	0.31	0.29				
K2O	0.24	0.36	0.15	0.02	0.13	0.00	0.02	0.00				
NiO	0.04	0.00	0.03	0.00	0.05	0.00	0.02	0.02	0.16	0.07	0.16	0.06
Total	99.39	99.70	99.15	101.81	99.10	101.41	99.52	99.53	100.89	100.44	100.60	96.28

Fig. B.5 SEM images and representative microprobe analysis of gabbro, as repeatedly heated to 1400 K under stress